THE UNIVERSITY *of* EDINBURGH

THE UNIVERSITY
of EDINBURGH

Organometallic Neptunium Complexes; Synthesis, Structure and Reduction Chemistry

A thesis submitted to the
UNIVERSITY OF EDINBURGH

for the degree of
DOCTOR OF PHILOSOPHY

Presented by
MICHAŁ SEWERYN DUTKIEWICZ
MSc. in Eng., Warsaw University of Technology
born on January 8th, 1987 in Warsaw
Citizen of the Republic of Poland

Accepted on the recommendation of
Prof. Dr Marinella Mazzanti, examiner
Dr Michael Cowley, co-examiner

2016

This thesis contains no material which has been submitted for any other degree or professional qualification, and comprises entirely the work of the author, except where due reference is made in the text

Michał Dutkiewicz
Karlsruhe, September

"The strong are the patient ones"

James Clavell, Shōgun

ACKNOWLEDGEMENTS

This work would not be possible without the support and contributions of the following people whom I would like to acknowledge with my deep gratitude. First of all, I would like to thank my supervisors, Prof. Dr Polly L. Arnold, University of Edinburgh, and Prof. Dr Roberto G. M. Caciuffo, European Commission (EC), Joint Research Centre (JRC), Institute for Transuranium Elements (ITU), for establishing an exceptional doctoral project under the auspices of EC-JRC ITU and giving me the opportunity to work at the forefront of the actinide research. They provided me with the freedom that I needed to pursue the quest into the no man's lands of chemistry and directed me towards the transnational actinide community. I am also indebted to Prof. Arnold for many helpful comments during this thesis preparation and proof-reading.

In particular, I would like to sincerely thank Dr Olaf Walter (ITU) who contributed the crystallographic determinations that he performed on behalf of my synthetic execution. His concomitant expertise on the advanced NMR spectroscopy has also helped to in-depth study of the solution structure of the transuranic molecules. I would like to thank Dr Christos Apostolidis (ITU) for sharing his distinguished experience on the synthetic actinide and lanthanide chemistry that stimulated the conducted research and also pointing me often into the right direction with his insight and scientific curiosity. I would like to thank Dr Eric Colineau, Dr Jean-Christophe Griveau and Dr Nicola Magnani (ITU) for measuring the DC magnetization isotherms and AC susceptibility analyses, modelling and interpreting of magnetization curves for several compounds of interest.

Last but not least I would like to thank Klaus Paris and colleagues of the glassblowing workshop at the Institute of Catalysis Research and Technology (IKFT) for their competence and outstanding service.

This work has been supported by the European FP7 Talisman project, under contract with the European Commission. I acknowledge the European Commission for support in the frame of the Training and Mobility of Researchers programme.

ABSTRACT

The aim of the work described in this thesis was to develop a more extensive knowledge of the chemistry of neptunium compounds by making rare, air- and moisture sensitive, low formal oxidation state neptunium compounds with full structural and synthetic characterization. The thesis contains three results chapters.

Chapter one introduces neptunium chemistry as a background to the results presented. The first review on the molecular non-aqueous neptunium chemistry is provided and the literature reports to date discussed in the context of this.

Chapter two describes exploratory synthetic and structural investigations of the organoneptunium complexes supported by the cyclopentadienyl anion, Cp = $(C_5H_5)^-$, and the (trimethylsilyl)cyclopentadienyl anion, Cp' = $(C_5H_4[Si(CH_3)_3])^-$. The syntheses of $[Np(Cp)_3]_n$ and $Np(Cp')_3$ complexes are detailed and the effect of the trimethylsilyl group of the ligand on the structure and reactivity have been investigated. Complexes were characterized by single crystal X-ray diffractometry, NMR and ATR(IR) spectroscopy. Both organoneptunium complexes were studied in reactions designed to expand the neptunium redox envelope. Notably, the complex $Np(Cp')_3$ is reduced by KC_8 in the presence of 2.2.2-cryptand to afford a product assigned as neptunium(II) complex, K(2.2.2-cryptand)$[Np(Cp')_3]$ that is thermally very unstable above approx. -10 ºC, in direct analogy to previously reported uranium, thorium and lanthanide complexes of the general formula, K(2.2.2-cryptand)$[M(Cp')_3]$. The reaction between $Np(Cp)_3Cl$ and KCp in THF afforded the unanticipated $K[Np^{III}(Cp)_4]$ product as a result of a single-electron reduction presumably arising from Np–C σ-bond homolysis reactivity. This behaviour appears to be unique amongst the actinides for the An(IV)/An(III) redox couple.

Chapter three focuses on oxo-bridged homo and heterometallic complexes. The reaction of $NpCp_3$ with dioxygen afforded not only the simple oxide, $(\mu\text{-}O)[An(Cp)_3]_2$, but also a small quantity of the unexpected new trinuclear oxo- neptunium(IV) compound $[\{(Cp_3Np)(\mu\text{-}O)\}_2\{Np(Cp)_2\}]$, which interestingly contains the rare C_{2v}-symetric $[An(Cp)_2]^{2+}$ structural moiety. This oxo-bridged environment is not paralleled in uranium chemistry. The two isostructural oxides, $(\mu\text{-}O)[An(Cp)_3]_2$ (An = U, Np), allow a comparative study of the magnetic exchange phenomena between the two actinide centres demonstrating an exceedingly strong

antiferromagnetic coupling, which is largely independent of the communicated Kramers Np^{IV} ($5f^3$, $^4I_{9/2}$) or non-Kramers U^{IV} ($5f^2$, $^3H_4$) ions. To design heterobimetallic systems, the uranyl(VI) complexes, $[(U^{VI}O_2)(THF)(H_2L)]$, supported by the calix[4]pyrrole Schiff base macrocycles, H_4L^{Oct} and H_4L^{Et}, were singly-reduced to uranyl(V) with either of the actinide complexes $Np(Cp)_3$ or $U(Cp)_3$, affording isostructural $[(Cp_3)An^{IV}OU^{V}O(THF)(H_2L)]$. Preliminary investigations of the magnetism of the An^{IV}-O-U^{V} are reported, although their analysis gave counterintuitive results.

Chapter four explores the redox chemistry and molecular and electronic structure of neptunium(III) complexes of the doubly deprotonated *trans*-calix[2]benzene[2]pyrrole, $H_2(L^{Ar})$, macrocycle which has a unique π-bonding potential and conformational flexibility. Interestingly, the reactions with neptunium(IV) chloride yielded mono- and dinuclear neptunium(III) complexes, $[(L^{Ar})NpCl]$ and $[(L^{Ar})Np_2Cl_4(THF)_3]$, with a subsequent elimination of the ligand radical; both complexes adopted $\eta^6{:}\kappa^1{:}\eta^6{:}\kappa^1$ bis(arene) sandwiched structural motif. In a direct analogy to the redox behaviour occurring in the salt metathesis between $Np(Cp)_3Cl$ and KCp, the spontaneous reduction derives from the favourable Np(IV)/Np(III) redox system. The reduction of complex $[(L^{Ar})NpCl]$ with NaK_3 in DME produces near-black solutions consistent with $[Np^{II}(L^{Ar})(DME)]$ that in the absence of excess NaK_3 gradually convert to the metallated $(L^{Ar\text{-}H})^{3-}$ neptunium(III) complex, $[K(DME)(L^{Ar\text{-}H})Np^{III}(OMe)]_2$, featuring the actinide centre bound with a 'metallocene-type' geometry provided by the two η^5-bound pyrrolides of the ligand. The neptunium(III) compounds were characterized in the solid state by single crystal X-ray diffractometry, ATR(IR) spectroscopy and in a solution by NMR and UV-Vis-NIR spectroscopy.

Table of Contents

ABBREVIATIONS

An	actinide, 5*f*-series element
Ar	aromatic, arene (generic)
atm	atmosphere, 1 atm = 1.01325×10^5 Pa
ATR	attenuated total reflectance
Å	Ångström, 1 Å = 10^{-10} m
°	degree
°C	degree Celsius
br	broad
Bu	butyl
CCI	cation-cation interactions
CN	coordination number
COSY	Homo-Nuclear Shift Correlation Spectroscopy
COT	cyclooctatetraenediyl dianion
Cp	cyclopentadienyl anion
Cp'	(trimethylsilyl)cyclopentadienyl anion
Cp''	1,3-bis(trimethylsilyl)cyclopentadienyl anion
Cp^*	pentamethylcyclopentadienyl anion
Ct	centroid, spatial center between
d	day (time unit), dublet (NMR)
DME	1,2-dimethoxyethane
$E_{1/2}$	half-wave potential
EA	elemental analysis
Et	ethyl
Et_2O	diethyl ether
eq	equivalent, stoichiometric ratio
Fc	ferrocene
gHMQC	gradient Heteronuclear Multiple Quantum Coherence (NMR)
h	hour
i-Pr	*iso*-propyl
IR	infrared
K	kelvin
L	ligand
Ln	lanthanide, 4-*f* series element

M	metal (generic formulae); molarity, mol dm^{-3} (concentration)
Me	methyl
MF	molecular formula
mg	milligram
min	minute
mL	millilitre
mmol	millimole
MW	molecular weight
min	minute
NMR	nuclear magnetic resonance
NOSY	nuclear Overhauser effect spectroscopy
ORTEP	Oak Ridge Thermal Ellipsoid Plot
ppb	parts per billion
ppm	parts per million
Py	pyridine
r.p.m	rounds per minute
r.t.	room temperature
$t_{1/2}$	half-life
*t*Bu	*tert*-butyl, 1,1-dimethylethyl
TDDFT	time-dependant density functional theory
THF	tetrahydrofuran
u	unified atomic mass unit
UV	ultraviolet
Vis	visible spectrum
X	halogen atom
y	calendar year, 365.25 days
δ	chemical shift
λ	wavelength
ν	frequency

1 Introduction

1.1 General Considerations

Neptunium ($_{93}$Np) is an artificial element having twenty four characterized radioisotopes including four metastable isomers with the relative isotopic mass numbers ranging from 225.03391(8) to 244.06785(32) u.[1] The most stable isotopes are ^{237}Np ($t_{1/2}$ = 2.144(7) × 10^6 y), ^{236}Np ($t_{1/2}$ = 1.54(6) × 10^5 y) and ^{235}Np ($t_{1/2}$ = 396.1(12) d), whilst all the remaining have half-lives that are less than 4.5 days, with a majority below 50 min.[2] The longest-lived neptunium nuclide, ^{237}Np, has the half-life of 2117(24) times shorter than the age of the Earth, 4.54(5) billion years[3], thus no primordial neptunium is present today. This notwithstanding, accurate α-ray measurements of concentrated uranium ores allowed the direct detection of natural ^{237}Np at the maximum mass ratio to ^{238}U of 1.8 × 10^{-12}; the result of the neutron activation and decay products arising thereof.[4] The other two short-lived isotopes, ^{239}Np ($t_{1/2}$ = 2.356(3) d) and ^{240}Np ($t_{1/2}$ = 61.9(2) min), are incapable to establish concentration equilibria in ores but their occurrence has been acknowledged indirectly by their decay to the longer half-life plutonium isotopes.[2]

In spite of the various neptunium isotopes that are artificially synthesized in nuclear fuels by transmutation reactions and the concomitant radioactive decay chain products, essentially pure ^{237}Np isotope is extracted from the spent fuel rods after the cooling period. This is explained by the large difference in the thermal-neutron fission cross-sections between ^{236}Np and ^{237}Np, and the favourable distribution of the neptunium isotopes half-lives. The ^{237}Np radiosotope is typically produced from the β decay of ^{237}U ($t_{1/2}$ = 6.749(16) d) fissioning of commercial uranium fuels (Scheme 1). Another portions arises from the 4n + 1 decay chain, the 'neptunium-series', of the ^{241}Am ($t_{1/2}$ = 432.2(7) y) radioisotope by α decay. A chemical removal ('*milking*') of the accumulated ^{237}Np isotope from ^{241}Am material provides ultra-pure samples.

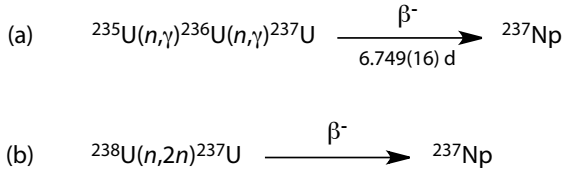

Scheme 1.1. Neutron capture reactions producing ^{237}Np isotope in uranium fuels; (a) using slow (thermal) neutrons, (b) using fast neutrons (above 5 MeV).

Although the neptunium content in spent nuclear fuel is approximately only 5 % of that of plutonium and 0.03 % of the total discharge, over 50 000 kg of the element is produced annually. At this level, the long-lived ^{237}Np is an important by-product of the recovery of plutonium from spent fuel dissolution-liquor in nitric acid, which is conducted on industrial scale by liquid-liquid solvent extraction. The process called PUREX (**P**lutonium **U**ranium **R**edox **E**xtraction)[5] delivers essentially pure U and Pu streams from reprocessed nuclear fuels, although the feed contains not only the desirable, non-extractable neptunyl(V) ions, $[NpO_2]^+$, but also their oxidation product, neptunyl(VI), $[NpO_2]^{2+}$. The high extractability of the Np^{VI} formed in the process conditions together with established kinetic equilibria between both species in nitric acid solutions[6] results in distribution of the Np element between the organic solvent product and aqueous raffinate. This difficult control over the neptunium speciation in actinide partitioning put high demands on PUREX technology, requiring complementary extraction loops for decontamination of the separated uranium and plutonium streams. In particular, the uranium product from the early stage partitioning was shown to co-extract about 75 % of the initial Np feed content, that must be completely removed in the purification cycle. The resulting raffinate of the purification loop was designed to remove 99.8 % of the essentially pure neptunyl(V) nitrate solution. In this form and also reprocessed to neptunium(IV) oxide[7] it is currently the most frequently used neptunium source for the chemical studies of the element and is also used in niche ^{237}Np isotope based technologies, i.e. methods for the production of ^{238}Pu radioisotope[8] and high-energy (MeV) neutron detection equipment.

The general and inorganic chemistry of the neptunium element was described by Yoshida *et al.*[9] within a comprehensive and definitive, 6-vol. book series *The Chemistry of Actinide and Transactinide Elements*.[10] A more focussed monograph on the thermodynamics and chemistry of Np and Pu species was reported by Lemire

and colleagues.[11] Mishin *et al.*[12] provided a review over the volatile Np and Pu compounds. The information therein may be consulted for background material and a more detailed discussion. The current knowledge of neptunium chemistry is largely defined by the national nuclear programmes and pertains to specific political interests and technological challenges. A common denominator is, however, research towards effective preservation of the biosphere from the nuclear waste disposal, where ^{237}Np radionuclide speciation control is fundamentally important.[13] In its so-called 'pentavalent' form, $[NpO_2]^+$, neptunium shows an easier ability to migrate than other actinides under environmentally relevant conditions, thus potentially increasing its long-term radiotoxicity hazards.[14] The latter combine with the gradual accumulation of the long-lived ^{237}Np radioisotope in the unseparated nuclear wastes which extends both the total volume and period of their containment over 10 000 years,[15] an operating time of the predicted engineered barriers in geological repositories. Therefore, contemporary neptunium chemistry research has taken an intense interest in providing detailed understanding of the 1) management of the element in nuclear fuel cycles and 2) how it interacts with the natural barriers under repository conditions and their geological surroundings; the two challenges being a key provision of sustainable nuclear energy production. These issues translate into the scientific investigations elucidating fundamental bonding properties, covalency and periodicity trends amongst the f-block elements.

In 2010 a percipient note on "*Neglected neptunium*" was published by Ibers, who outlined the importance of the lacking solid-state characterization of the element and its compounds and indicates the disproportionate relative attention that the different actinide elements have received.[16] In fact, there is much more to be discovered about the non-aqueous neptunium chemistry, especially through the systematic studies of relevant early actinide complexes in series. Furthermore, there is a great scope for a much larger number of research groups to potentially engage in neptunium chemistry, albeit ever more stringent rules pertaining to radioprotection and safety conditions must be observed.

As a context for the synthetic and structural studies on the neptunium complexes containing organic ligands, the following sections in the introduction will describe the relevant prior studies to date on molecular and organometallic Np chemistry,

with a focus on the redox properties and bonding interactions. A separate subsection describes the technical aspects of safe working practicalities.

1.2 Safety and Control Measures for Handling Neptunium Complexes

The hazards of handling ^{237}Np radionuclide closely resemble those of the lighter radioactive elements, taking into account a discrete change in greater risk due to severe radiotoxic effects when incorporated.[4,17] Despite the expected lower radiotoxicity of the neptunium than plutonium (specific activities for α decaying isotopes: $a(^{237}\text{Np})$ = 25.9 MBq · g^{-1} and $a(^{239}\text{Pu})$ = 2.30 GBq · g^{-1}), various studies on microorganisms indicated a higher chemical and thus overall toxicity of the neptunium element.[15] The analysis of the physics of radiation protection principles for the ^{237}Np isotope suggests several key findings, although these are rarely addressed in the precaution sections in the synthetic chemical literature. The ^{237}Np radioisotope shows primarily α emission (Qα = 4.958 MeV), although this is limited by the long half-life of the radionuclide ($t_{1/2}$ = 2.14 × 10^6 years) and its resulting low specific activity. The accompanying γ-ray radiation is weak and the two characteristic energy maxima, used in γ-ray spectroscopy determinations, are depicted red on Figure 1.1.

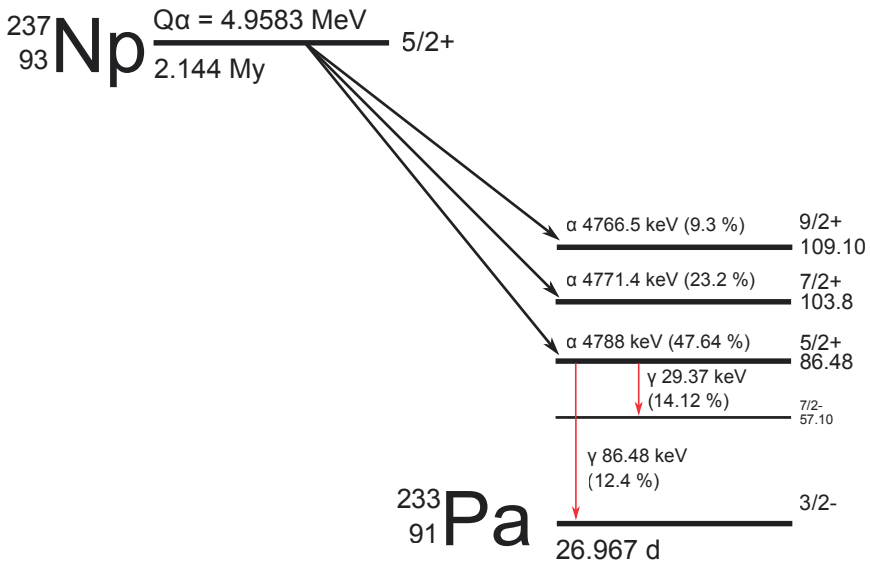

Figure 1.1. Schematic representation of the simplified ^{237}Np isotope decay, adapted from ref. [18].

More importantly, ^{237}Np decays to ^{233}Pa ($t_{1/2}$ = 26.97 days, a = 21 kCi · g^{-1}), which in turn is a potent β emitter (Q^- = 0.570 MeV) and exhibit strong γ-ray emission

due to its decay to ^{233}U. These radiations can result in exposure due to penetration of the gloves and skin. The long-lived ^{233}U isotope ($t_{1/2}$ = 1.592(2) × 10^5 y) and its minute amounts in the ^{237}Np materials do not essentially add to the parent radioactivity. Because of its short half-life the ^{233}Pa daughter quickly comes into secular equilibrium with its ^{237}Np parent and after approx. 189 days (7 half-lives) the concentration of ^{233}Pa asymptotically approaches 34.6 ppb. Accordingly, the ^{237}Np/^{233}Pa system should be analysed collectively in terms of the relevant safety and control measures. Health-physics calculations supported by Nucleonica GmbH[19] produce fast and definitive radiation hazard pictures for each specific radionuclide sample. Using the ^{237}Np/^{233}Pa example, the equilibrium concentration of the daughter nuclide (34.6 ppb) gives rise to about 83% of the total produced tissue-absorptive γ-radiation. The equivalent gamma dose rates in tissue for the ^{233}Pa isotope content is also 4.98 times higher than in the parent isotope. Finally, the large half- and tenth value attenuation thickness of lead (0.18 and 0.62 cm) limit the effective shielding of ^{237}Np/^{233}Pa sources with common thin lead linings.

Not surprisingly the synthetic scale neptunium chemistry programme must be organized within nuclear establishments and pertain to the radioprotection, extensive control measures and legal requirements in force. This 'built-in' safety is based on extremely low maximum permissible concentrations of the transuranium elements in air for continuous operational exposure and thus provide multiple levels of containment for the neptunium compounds at all stages of manipulations. The preparative work is carried out in the negative pressure radiological gloveboxes equipped with combined HEPA (**H**igh **E**fficiency **P**articulate **A**ir filters) and activated charcoal filters which trap potential radioactive particles released in the box chamber as the gas circulates through the exchange/purification systems. The gloveboxes are usually operated under an inert gas atmosphere to provide explosion and fireproof environment, although operating conditions (negative pressure, multiple glove-ports) makes back diffusion of oxygen and moisture significant compared to a standard glove box. The organometallic neptunium chemistry described in this thesis places exceptional demands on the purity of the atmosphere for the manipulation of air- and moisture sensitive complexes, pyrophoric reagents and using organic solvents. Radioactive residues arising from these synthetic practicalities are utilized for efficient ^{237}Np radionuclide recycling (cf. section 1.3.3.2), which allows

to comprise radioactive waste minimizing and scaling up the synthetic operations, where more product enables broader characterization not accessible with smaller amounts. The experimental design is commonly based on the overall performance and efficiency of using the ^{237}Np isotope, whilst the radiotoxicity hazard is of paramount consideration and key to sustainability of operations. The latter criteria frequently require the use of different hazardous reagents in the synthetic work, however, these can be safely handled under full containment regime, and the produced mixed hazardous waste streams generally comply with the rules for the standard radioactive waste incineration.

All necessary analyses of the complexes are carried out exclusively using either the apparatuses or their sample compartments embedded in the radiological gloveboxes or doubly encapsulated with at least one barrier having sufficient mechanical properties to withstand an accidental drop without loss of primary containment. The intrinsic structure degradation of the ^{237}Np coordination and organometallic complexes due to autoradiolysis is typically not observed throughout the periods of several months to years and Np^{4+} ion exhibits indefinite radioresistance.[20] The ^{237}Np isotope has been proven fissile, however, the respective criticality mass was determined as 63.6 kg,[21] and does not present a practical danger.

1.3 Organometallic Neptunium Chemistry

1.3.1 Relevance of the non-aqueous actinide studies

There is a growing body of literature that recognizes the importance of non-aqueous actinide chemistry. Element-specific surveys have been recently published for non-aqueous uranium chemistry, by Liddle,[22] and for plutonium chemistry by Gaunt *et al.*,[23] who also provided a broader analysis of the synthetic and structural actinide studies.[24] This chemistry *ab initio* can operate outside of the solvent exchange and metal hydrolysis constrains of the aqueous systems and thus is capable to enhance the fundamental understanding of the extent and nature (5*f vs.* 6*d*) of covalency in actinide bonding, and their correlation with the reactivity and physico-chemical properties. The term 'non-aqueous' is somewhat open to interpretation and may refer to anhydrous compounds prepared in organic solvent solutions either using hydrated starting materials or under a strict air- and moisture sensitivity regime. This ambiguity translates

largely into the two distinct functions of the actinide chemistry: the first one is significant in developing new extractant systems for the partitioning of actinides and lanthanides in spent nuclear fuel, through selective actinide-ligand complex formation in organic phases,[25,26] whilst the second attempts to answer more fundamental questions about M-L bonding. In both domains the quantification of the metal–ligand covalency in complexes holding *f*-element open-shell centres is of paramount importance.[27,28] Despite its importance to this, and observable progress in recent years, computational analysis of metal-ligand interactions still struggles with providing the exact contributions of *f*-orbitals and the extent of covalency in actinide complexes, which is the matter of current discussions.[28,29,30] On the other hand, the recent quantitative X-ray absorption spectroscopy (XAS) analyses at the carbon K-edge of the organometallic thorium and uranium complexes, $[An(COT)_2]$ (An = Th, U), "actinocenes", revealed experimentally the unconventional carbon 1s to the Th-C antibonding $2e_{3u}$ ($5f$–ϕ) transition for thorocene and its substantially smaller amount in analogous orbital mixing in the uranium homologue.[31] This multiconfigurational character of mixing of the An 5*f* and C orbitals in organoactinide complexes continues to be an active area of debate and covalent bonding does not essentially appear to increase uniformly across the series, contrasting with the earlier proposals.[27,30,32] This example suggests the soft-donor, multiply bounded organometallic ligands provide an excellent platform for advanced studies and potentially allow exploiting of different levels of *f*-block elements covalency. A good illustration of this is provided by the emerging field of the actinide based single molecule magnets (SMMs), which potentially combine the advantage of stronger anisotropy and enhanced covalent interactions over the lanthanide systems, especially in combination with transition metals.[33–36] The majority of currently published *f*-element systems that exhibit slow relaxation of magnetization result from a single-ion or slightly modified single-ion property, which concurrently yields larger spin-orbit coupling of actinide ions of considerable interest. In fact, the first experimental proof of allowing stronger magnetic anisotropy and larger coercive fields by the 5*f*- *vs.* 4*f*-element based SMM was presented in 2011 for the rigorously D_{8h} symmetrical, 'neptunocene' complex, $[Np(COT)_2]$ **1**, which exhibits intriguing magnetic memory effects at low temperatures, Figure 1.2.[37] Even at the maximum field of 14 T and the lowest attainable temperature of 1.8 K, the resultant magnetic moment

(0.8 μ_B) remains largely unsaturated and corresponds to *ca.* half of the expected value for $J_z = \pm 5/2$ doublet. At temperatures above 10 K and applied fields of below 2 T, the graph of the function $\ln(\tau) = f(1/T)$ become essentially linear and a surprisingly low thermal activation barrier of $\Delta = 41$ K and $\tau_0 = 1.1 \times 10^{-5}$ s was obtained. One possibility for this is the field induced nuclear spin mediated crossings of electron, which is not observable above 2 T. At 1.8 K and applied fields of 5 T and above, the slow relaxation of magnetization becomes independent of frequency and butterfly-shaped hysteresis loops develop (14 T), suggesting that the primary mechanism of relaxation at low temperatures is nuclear spin-induced quantum tunnelling, (Figure 1.2). Finally, the other isoelectronic actinide complex K[U(COT)$_2$] **2**, containing an f^3 U^{III} centre, shows no detectable SMM behaviour,[38] presumably due to the net difference in crystal field splitting and the possible molecular symmetry distortions.

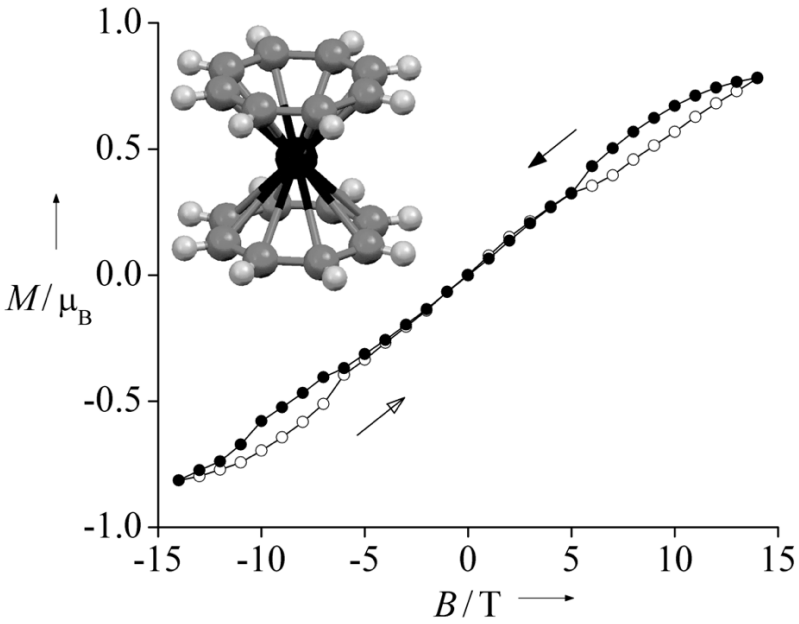

Figure 1.2. Hystereses of isothermal magnetization of **1** at 1.8 K; the traces in increasing (decreasing) magnetic field were depicted with empty (full) circles. The molecular structure was depicted on the inset; neptunium (black), carbon (grey), hydrogen (light-grey). Adapted from ref. [37].

Compared to the overwhelming prevalence of the less radioactive uranium and thorium complexes, anhydrous transuranic chemistry trails far behind. This is a consequence of the limited number of appropriate radiological research facilities worldwide, scarcity of the available transuranic elements in their pure forms and skills shortage due to the retirement of exceptionally qualified

personnel. In the past (1956-1986) the field had developed more slowly than chemistry of the less radioactive actinide complexes, and did not enjoy the same sort of remarkable and definite progress mainly due to radioactivity concerns in the research methodology. Notably, the most powerful technique of the molecular structure determination, single crystal X-ray diffraction (XRD), has led to key advances in uranium and thorium chemistry that inform and strengthen the scientific interests in actinide chemistry. Even in modern days, when advanced instrumentation and sophisticated strategies for XRD data analysis allow almost routine crystal structure determination, this method for transuranic elements is technically more challenging for the long-lived neptunium and plutonium isotopes. One of the best indices of progress in the molecular actinide chemistry are structurally characterized complexes added into the *Cambridge Structural Database* (CSD). The analysis of total actinide records shows the practical difficulties associated with increasing radioactivity and diminishing availability of isotopes across the actinide series, Figure 1.3.a. The second correlation of specifically the organometallic actinide derivatives reflects additionally the exceptional level of technical proficiency required to manipulate such transuranic compounds, Figure 1.3.b. At the time of writing the most updated version of the CSD (22 Dec 2015) contains four organoneptunium crystal structures, but those related to only three individual compounds, as data for two of the entries were for the same compound at different temperatures. The desire to expand the portfolio of the structural chemistry of organometallic neptunium compounds was a key motivator for this thesis. The scope of the following sections will be limited to derivatives of the +4 and +3 oxidation states of actinide centres, focusing primarily on Np. The general progress in organo-*f*-element chemistry has been extensively reviewed by Edelman and co-workers,[39-59] covering the period of 1992 to 2014, and seminal contributions in organometallic actinide chemistry up to 2013 were summarized by Behre and Walensky.[60]

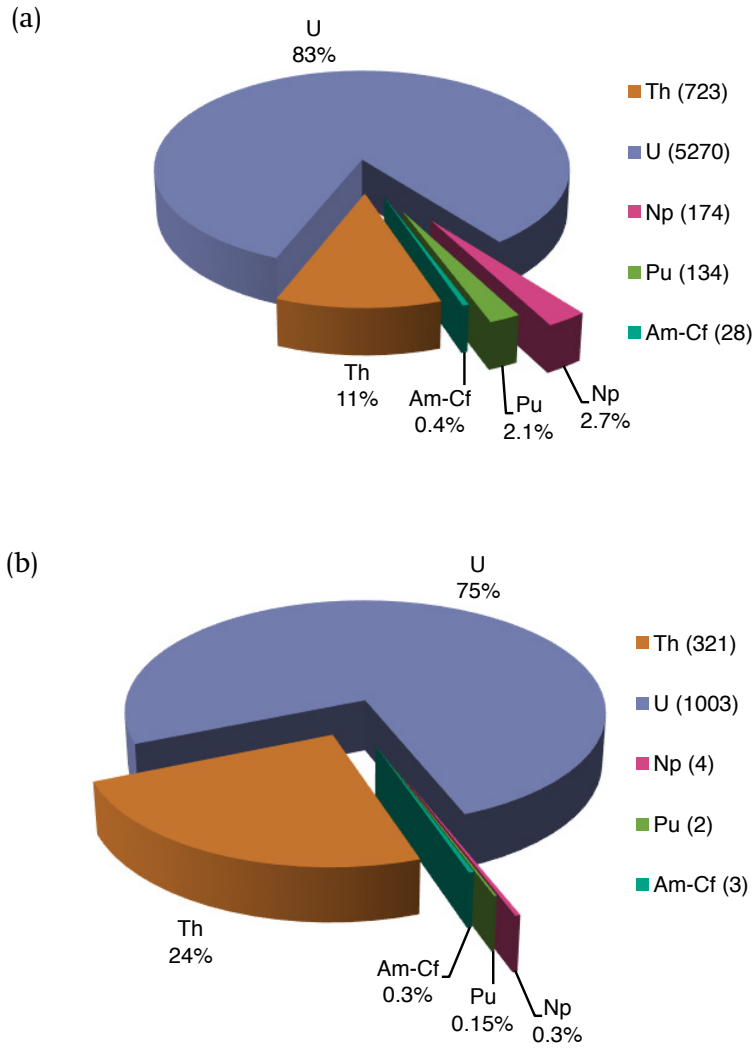

Figure 1.3. Pie-charts demonstrating the differences in the percentage breakdown of actinide entries in the Cambridge Structural Database (WebCSD, update 22 Dec 2015) by: (a) element, (b) element entries that contain An-C bond.

1.3.2 Redox properties of the neptunium element

The redox properties of the element play a pivotal role in neptunium chemistry and distinguish many of the chemical behaviours amongst the actinide series. Neptunium exhibits five oxidation states in compounds, +3 to +7, with the most prevailed being +5. The +3 and +4 oxidation numbers are associated with simple ions, whereas further oxidation of the metal centre commonly leads to the formation of two or three stable oxo- functionalities ('yl' groups) which enable more effective lowering of the formal positive charge on the metal cation. The energy separation between the oxidation states of Np is comparable with that

of U, and substantively higher to Pu, however, the reversible An(IV)/An(III) redox system properties diverge widely. Although there are hardly any reports of measured redox potentials for transuranium complexes in non-aqueous media, the available data suggest that the Np^{IV}/Np^{III} couple is intermediate in value between U and Pu in the triad; a selection of reported formal potentials summarized in Table 1.1.

Table 1.1. Formal potentials (V, *vs.* SHE) of An(IV)/An(III) couples in aqueous solutions.[61]

Couple	Formal potential, $E^{o\prime}$, in V *vs.* SHE		
	1 M $HClO_4$	pH 8	1 M NaOH
U^{IV}/U^{III}	-0.631	-1.95(17)	-2.78(35)
Np^{IV}/Np^{III}	0.155(10)	-1.13(14)	-1.88(24)
Pu^{IV}/Pu^{III}	0.9821(5)	-0.39(15)	-1.04(24)

The standard redox potential of Np^{IV}/Np^{III} (I = 0, T = 25 °C) derived from the measurements under acidic conditions equals to E^o = 0.219(10) V *vs.* SHE,[11] which closely matches the potential of the reference silver chloride electrode (E^o = 0.222(13) V *vs.* SHE)[62] and suggests the isolated Np^{4+} ion has oxidation properties similar to that of AgCl. The electrochemical properties of actinide centres in organoactinides usually differ considerably on the particular ligand environments,[63] however the Np^{IV}/Np^{III} couple in organoneptunium(IV) complexes appears surprisingly insusceptible to the ligand-induced changes.[64] The relatively high oxidative potential of the Np^{IV} ion adds to the chemical stability trends of the isostructural series of non-aqueous actinide complexes $[An^{IV}(Cp)_4]$[20,65] or isotypic $[An^{IV}(BH_4)_4]$[12,66] series. On the contrary, early actinide elements (An = Th-Np) demonstrate a thermodynamic preference for the +4 oxidation state and disproportion reactions of the trivalent U and Np complexes into 0.75 eq of An^{IV} and 0.25 eq of An^0 were reported (*cf.* Scheme 1.5).[67]

1.3.3 Neptunium halide starting materials

The major difference between the uranium and transuranic starting materials is the accessibility to the element of the latter. This means that synthetic methods for the An^{III} halides that uses reduction reactions of higher oxidation state precursors (An = Np) have to be used instead of the more convenient

and well-developed strategies for controlled oxidation of metals with elemental halogens or alkyl halides in organic solvents.[68] Although the neptunium(III) iodide precursor $[NpI_3(THF)_4]$ **6a** made from the metal is considered most efficient in terms of good solubility in organic media and favourable salt metathesis reactions, this and related salts are generally unavailable at present due to the lack of access of most transuranic labs to neptunium metal. Additionally, NpI_4 is thermodynamically unstable at ambient conditions, thus effectively limiting its potential reaction chemistry. Therefore, mainly $NpCl_4$ **4** and its recently reported 1,2-dimethoxyethane adduct, $[NpCl_4(DME)_2]$ **4a** are of greatest synthetic use as the relevant Np^{IV} synthons.

1.3.3.1 Neptunium(III)

Several methods were developed for the synthesis of anhydrous neptunium(III) halide precursors, Scheme 1.2. In 1966 Laubereau detailed the first preparation of $NpCl_3$ **3**, by contacting the solid $NpCl_4$ **4**, with hydrogen gas, Scheme 1.2.a.[67] Although quantitative in nature, this reaction requires harsh reaction conditions (450 °C, 2 h) and more importantly extreme purity of the reagents. Compound **3** was characterized as a grey-green solid crystallizing in the hexagonal system, isostructural with UCl_3 and $PuCl_3$, and water-insoluble. Further investigations by others identified other more convenient solid-state routes to neptunium(III) halides, NpX_3 (X = Cl (**3**), Br (**5**), I (**6**)), that avoid the use of dihydrogen and do not produce corrosive HX by-products. These include reduction of the neptunium(IV) halides, NpX_4 (X = Cl (**4**), Br (**7**)), with excess zinc (Scheme 1.2.b), a direct combination of the elements, neptunium metal and excess iodine (Scheme 1.2.b),[69] or a stoichiometric reaction between $^{237}NpO_2$, Al metal and AlX_3 (X = Br, I) (Scheme 1.2.d).[70] All these protocols necessitate sealing the reactants under vacuum in quartz tubes, prolonged heating above 500 °C and product isolation by the high temperature (fractional) vacuum sublimation.

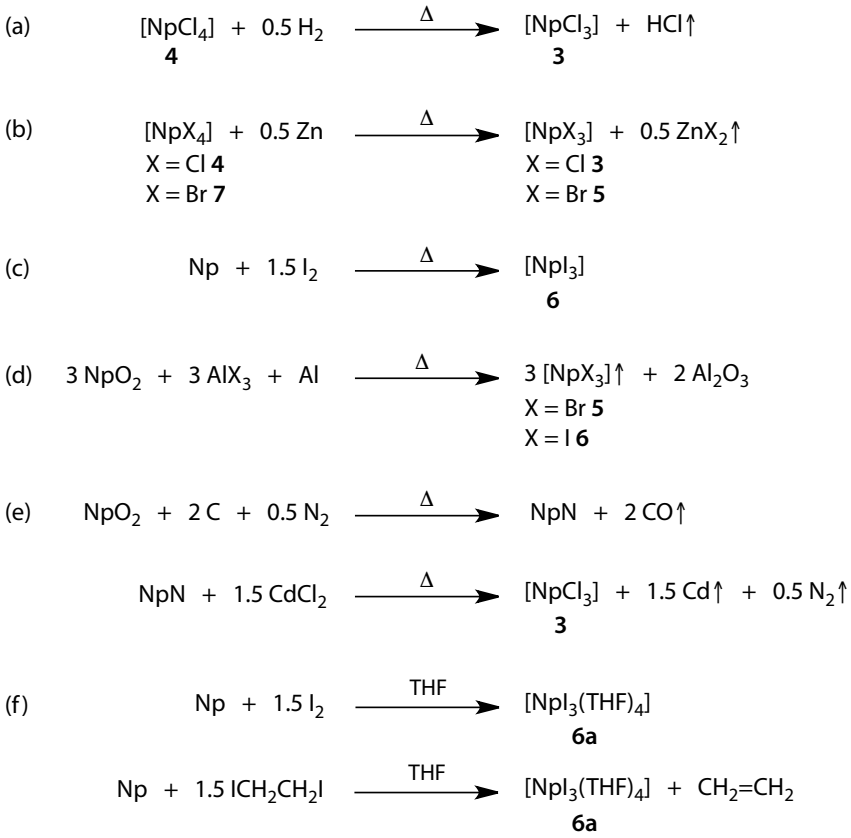

Scheme 1.2. Syntheses of neptunium(III) halides, NpX_3, X = Cl **3**, Br **5**, I **6**, and THF adduct **6a**.

In 2013 Hayashi *et al.* reported the state-of-the-art reaction of neptunium nitride, NpN, with cadmium chloride that gives high-purity **3** (Scheme 1.2.e).[71] This method is based upon research to make advanced nitride fuels *via* carbothermic reduction of oxides, which uses $^{237}NpO_2$ to afford the clean NpN product containing below 1000 ppm of total carbon/oxygen impurities. The NpN was ground with cadmium chloride and heated under dynamic vacuum up to 465 ºC, producing a dark green powder of **3** in the 97-100 % isolated yield, based on $^{237}NpO_2$. The cumulative advantage of constricted corrosion hazards, avoiding molten-salt baths in the radiological facilities and perhaps more importantly, the relevance to fuel programme and existing specialized research installations may all influence the desirability of compound **3** as a precursor to low valent neptunium chemistry.

Anhydrous actinide(III) halides form polymeric structures in the solid-state,[72,73] which leads to their insolubility in common organic solvents and decreased reactivity.[74] To avoid solid-state methods and the subsequent limitations of the precursors, solution based methods that would give solvated metal halides

were elaborated independently by Karraker[75] and Zwick *et al.*[76] The two routes are based on neptunium metal oxidation with stoichiometric quantities of either of 1,2-diiodoethane or elemental iodine in THF; both produce solid $[NpI_3(THF)_4]$ **6a**, at ambient temperature for 16-24 h (Scheme 1.2.f). Unlike the original synthesis of $[UI_3(THF)_4]$,[77] the reactions involving neptunium proceed cleanly without prior metal activation, affording **6a** as a robust yellow orange powder in very good yields; uranium and thorium metals were found unreactive towards 1,2-diiodoethane under similar conditions.[75] Despite the scarcity of the neptunium metal, the soluble complex **6a** has proven to be a competent precursor to new and existing compounds.

The ever growing safety envelopes for the radiological installations inspired Foropoulus *et al.*[78] to patent a low-hazard method for the production of **3** directly from an aqueous solution. The method claims involve oxidation-state control over the Np^{III} in a chloride solution with hydroxylamine hydrochloride followed by a two-stage dehydration process; the solid **3** is obtained by evaporation of the solvent and contacting the residue with excess thionyl chloride ($SOCl_2$) at elevated temperatures. Despite the simple approach and waste minimization practice, the 'essentially pure' product appears to be contaminated with some sulfur-containing side-products due to reduction of trace amounts of higher metal chlorides and oxychlorides with $SOCl_2$. This is paralleled by the results from the chlorination of uranium oxides[79] by the $SOCl_2$ reagent.[80]

1.3.3.2 Neptunium(IV)

Neptunium tetrachloride, $[NpCl_4]$ **4**, is the most commonly used neptunium halide starting material and proved to be the foundation of numerous studies over the last 60 years. Due to the early development of the $^{237}NpO_2$ production method and the process optimization up to the plant-scale,[7] the chlorination of the readily accessible neptunium dioxide with CCl_4 vapour became the method of choice for the synthesis of **4**,[67,81] Scheme 1.3.b.

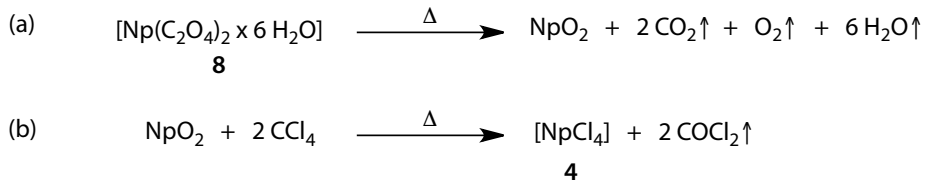

Scheme 1.3. Synthesis of **4** *via* thermal chlorination of complex **8**.

Despite harsh reaction conditions (500-650 °C) and corrosive environment, the major advance of this reaction lies in the scope of the method to recycle and purify the neptunium element from mixed waste streams in 98-99% yield, and thus potentially closing the operation loop of the element at the radiological facility. The neptunium gravimetry is routinely used to separate the Np^{IV} oxalate hexahydrate from 1-4 M nitric acid solution with oxalic acid. Hydrazine and ascorbic acid are used for complete reduction to Np^{IV} and stabilizing this oxidation state in the solution, which is to ensure quantitative precipitation of the $[Np(C_2O_4)_2 \cdot 6H_2O]$ **8**. Unlike the moderate to high distribution coefficients between many ionic impurities and neptunium, the method essentially does not separate the actinide elements. The green microcrystalline **8** dissociates thermally to give high surface area NpO_2 prior to the chlorination; both processes are usually coupled in a one-pot synthesis (Scheme 1.3). The crude **4** vaporizes out of the reaction zone at 650 °C and condenses onto the cooler parts of the apparatus as dark red crystals or an orange-red deposit. The sublimation of **4** enables the isolation of pure product from $PuCl_3$ and other less volatile metal chlorides, showing the partition constant of about 3×10^3 for the sample initially containing 4% Pu; yield ~96%. To avoid the potential $NpOCl_2$ impurity formation the reaction gas mixture frequently uses a small percentage of premixed chlorine with the CCl_4/Ar main stream.

The other synthetic method is derived from the uranium chemistry and uses the reaction of $(NpO_2)OH$ with hexachloropropene to afford **4** in ~50% yield.[82] The major difficulty arises here with the isolation technique by sublimation which causes the organic impurities to react with the crude product and its concomitant reduction to **3**. The analogous method represents arguably the most convenient route for the production of UCl_4, but this preparation for the Np congener awaits further developments.[83]

The preparative difficulties of the previous methods resulted in the introduction of bis(tetraethylammonium) hexachloroneptunate(IV), $[(NEt_4)_2(NpCl_6)]$ **9**,[84]

as an air stable alternative to **4**. The yellow microcrystalline precipitate of **6** forms easily from an aqueous solution containing Np^{IV} and $[NEt_4]Cl$ in hydrochloric acid solution, but presence of traces of different oxidation states strongly influence the colour and quality of the resulting product. The precursor proved its utility in the metathesis reaction with dipotassium salt of a COT derivative in THF, giving 1,1'-di-*tert*-butylneptunocene, $[Np(COT^{tBu})_2]$ **10**, in 36 % yield.

A more recent strategy provides the solvent adduct $[NpCl_4(DME)_2]$ **4a**, as an alternative precursor derived from drying of Np^{IV} chloride solution and extraction of the '$NpCl_4$' residue into the 1,2-dimethoxyethane solution containing trimethylsilyl chloride.[85] Work-up of the resulting pink solution afforded solid complex **4a** in an isolated 75 % yield. This complex is one of the few structurally authenticated and forms an isostructural series with Th, U and Pu analogues which all occupy the monoclinic $P2_1/c$ space group. The Np coordination in complex **4a** is distorted away from the idealized square antiprismatic geometry (CN = 8), showing average Np–Cl and Np–O bond distances of 2.608 and 2.55 Å, respectively, Figure 1.4. Comparison of the bonding parameters around the metal centres indicates shortening of the respective distances across the series of the isostructural complexes, signalling actinide contraction phenomena; the mean values for the An–Cl/An–O distances (in Å) support the trend: Th 2.690/2.596,[86] U 2.62/2.57,[87] Pu 2.592/2.54.[85] Additionally, transmission and reflection Vis-NIR spectroscopic studies of **4a** showed corresponding band patterns, suggestive of the structural identity in both DME solution and the solid-state. Finally, the DME solvate continues to prove its utility as a versatile Np^{IV} synthon in the most recent non-aqueous coordination chemistry studies.[88,89]

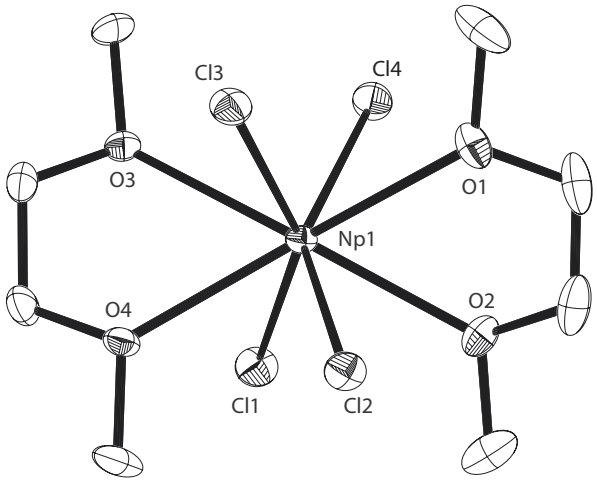

Figure 1.4. Molecular structure of **4a**. Thermal ellipsoids are drawn at 50% ellipsoid probability and hydrogen atoms are omitted for clarity. The crystallographic data was obtained from the Cambridge Structural Database (refcode: *BIPVUT*).

1.3.4 Organoneptunium complexes

Exactly 60 years have passed since the foundation of the chemistry of neptunium complexes containing hydrocarbyl ligands. Remarkably, the field has originated not from the chemical but the radiochemical synthesis account, using the organometallic complex, [^{238}UCl(Cp)$_3$] **11**, as a precursor to the transmutation of the metallic centre into neptunium element and thus resulting in the pioneering synthesis of complex [^{239}NpCl(Cp)$_3$] **12**.[90] Further research efforts followed exclusively the studies of complexes using the ^{237}Np isotope, being the only one accessible in weighable amounts.

The prior advances in uranium and thorium organometallics largely envisaged the potential targets for neptunium complexes, of which some were synthesized. This resulted in an isostructural series of compounds. Despite the largely missing structural characterization of modern day standards, the evolving field of ^{237}Np Mößbauer spectroscopy provided early a powerful experimental measure of interaction of ligand environment about the neptunium ion on its electronic and magnetic properties. Karraker summarized the fundamentals of Mössbauer spectroscopy of ^{237}Np isotope in his book chapter demonstrating 5*f*-electron structure and covalent effects in organometallic neptunium complexes.[91] To date, the majority of reported syntheses are of neptunium(IV) complexes that retain the +4 oxidation state, and throughout the course of reactions and exploratory reduction chemistry it remains scarce, with no structural data available for any

Np^{III} organometallics. In spite of the recent discovery of fascinating magnetic bistability properties of **1** (see Chapter 1.3.1), the last three decades have witnessed little progress in the field and no synthetic accounts reported. On the other hand, it is safe to predict that recent advances in the isolation of novel formally divalent lanthanide and early actinide complexes,[92–95] all supported by the ligands containing π-aromatic functionalities, will provide necessary impetus for the development of low-valent organometallic transuranium chemistry.[96]

1.3.4.1 Cyclopentadienyl complexes

Early organoactinide chemistry relied on the ubiquitous cyclopentadienyl ligand, $Cp = (C_5H_5)^-$, due to its enormous success in transition metal chemistry. This might be also attributed to both the rich structural and electronic diversity through ready ligand functionalization and the related robust coordination complexes with high Cp-An bond dissociation energy. Importantly, the π-aromatic cyclopentadienyl anions typically occupy approximately three coordination sites and thus are frequently employed as spectating ligands, that also possess excellent NMR spectral characteristics, due to the low rotational barriers around the An-Cp(centroid) axis reducing the complexity of the spectra, even for low-symmetry complexes.

In 1965 Baumgärtner, Fischer and Laubereau provided evidence for the formation of $[^{239}Np(Cp)_3X]$, where X = Cl **12**, F **13**, as a result of subjecting $[^{238}U(Cp)_3X]$ to thermal neutrons irradiation (Scheme 1.4).[90]

$$[^{238}U(Cp)_3X]\ (n,\gamma)\ [^{239}U(Cp)_3X] \xrightarrow[23.45(2)\ min]{\beta^-} [^{239}Np(Cp)_3X]$$

~ 90% isol. after 4h
X = Cl **12**
X = F **13**

Scheme 1.4. Radiochemical synthesis of **12** and **13** complexes.

The activation reaction $^{238}U(n,\gamma)^{239}U$ followed by β-decay of the latter nuclei was believed to proceed cleanly according to ^{239}Np γ-ray spectrometry. Interestingly, the potentially viable nuclear recoil displacement effect[97] of the emergent ^{239}U radioisotope did not affect chemical bonding and the parent structure and the isolation of the sublimates **12** and **13** with *ca.* 90% overall yield with respect to neptunium was achieved. This radiochemical synthesis has originated the field of organometallic neptunium compounds

and demonstrated volatility and thermal stability of the $[Np(Cp)_3X]$ complexes. At the same time, the very first chemical preparations of the analogous $[^{237}Np(Cp)_3X]$ (X = Cl (**14**) and F (**15**)) complexes, were outlined by Laubereau, who used molten $Be(Cp)_2$ as a reactant and a reaction medium.[67] Under these conditions the halide precursors **3**, **4** and neptunium trifluoride, NpF_3, all cleanly formed thermodynamically preferred +4 oxidation state products of the generic formula $[Np(Cp)_3X]$, which is not fully paralleled in uranium chemistry.

Although the $[U(Cp)_3X]$ complexes were primarily isolated, a ready salt metathesis reaction of the remaining halide ligands with cyclopentadienyl anion lead to the formation of the homoleptic complex, tetrakis(η^5-cyclopentadienyl)uranium(IV), $[U(Cp)_4]$ **16**; complex **16** can be isolated as a sole organometallic product; the two equations depicting the reactivity change were shown in Scheme 1.5.

$$4\ [UCl_3] + 6\ Be(Cp)_2 \xrightarrow[20\ h]{60\ ^oC} \underset{\mathbf{16}}{3\ [U(Cp)_4]} + U + 6\ BeCl_2$$

$$\underset{\mathbf{3}}{8\ [NpCl_3]} + 9\ Be(Cp)_2 \xrightarrow[3.5\ h]{60\ ^oC} \underset{\mathbf{14}}{6\ [Np(Cp)_3Cl]} + 2\ Np + 9\ BeCl_2$$

Scheme 1.5. Solvent-free syntheses of cyclopentadienyl uranium and neptunium complexes from $AnCl_3$ starting materials under thermodynamic control.

The chemical properties of complex **14** were found to closely match those of its uranium analogue.[65,98] The reported reactivity of **14** was delineated in Scheme 1.6. Additionally, complex **14** dissociates into stable, hydrated $(Cp)_3Np^+$ cation and Cl^- anion in dilute or semi-concentrated aqueous mineral acids under strict oxygen-free conditions. The resulting red-brown solutions or THF solutions of **14** react with ferric chloride only very sluggishly to produce ferrocene, suggestive of the similar degree of covalency in An^{IV}-(η^5-Cp) interaction for An = U, Np, and contrasts with the rapid ligand exchange of the Th analogue.

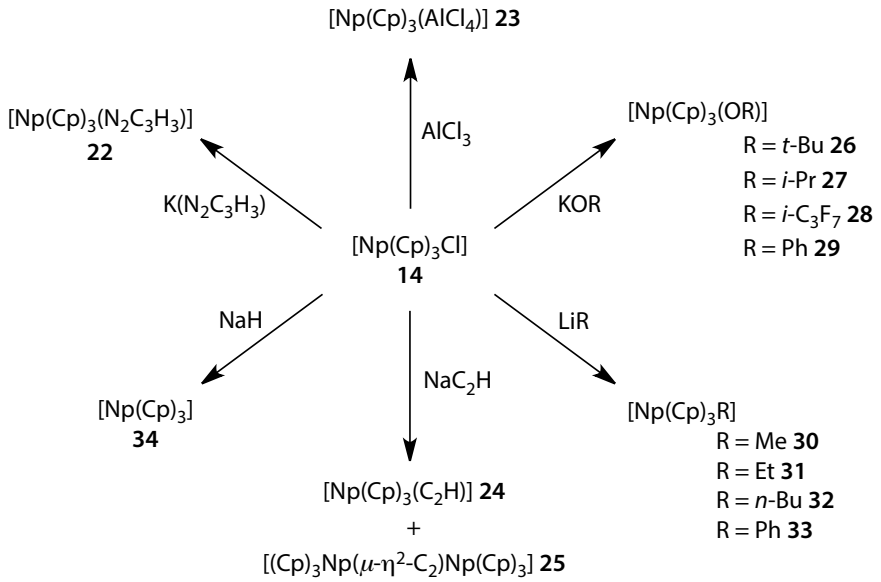

Scheme 1.6. Overview of the reactivity of **14**.

To date, there is only a single record of the structural authentication of a complex containing the {Cp_3Np} fragment. The molecular structure of [$Np(Cp)_3(OPh)$] **29** was determined from single crystal X-ray diffraction analysis;[99] the ORTEP plot is shown in Figure 1.5. Complex **29** is isostructural with the previously reported uranium analogue by the same authors, [$U(Cp)_3(OPh)$] **35**.[100] Assuming that the coordination polyhedron of either actinide centre contains a phenoxy oxygen atom and three Cp ring centroids the coordination geometry is best described as a flattened tetrahedron, showing approximately C_{3v} symmetry at the metal site with the O donor at the C_3 axis and the Cp-rings shifted towards the less sterically encumbered phenoxy ligand. Hence, this geometry is reflected in the modified tetrahedral angle values in **29**, which are for Ct(η^5-Cp)-Np-Ct(η^5-Cp) and O-Np-Ct(η^5-Cp), 116.1(2) to 117.6(2) Å and 97.6(3) to 102.3(3) Å respectively. The Np-O bond length is 2.136(7) Å and the Np-Ct(η^5-Cp) separations range from 2.460(7) to 2.477(8) Å. The unit cell dimensions and the cell volume in both homologues **29** and **35** are comparable, but somewhat higher in **29** (1745.2(7) *vs.* 1730(2) $Å^3$). Matching the root-mean-square positions of non-H atoms of **29** *vs.* **35** gives the value of 0.06 Å, which can be ascribed to slightly higher steric hindrance in **29**.

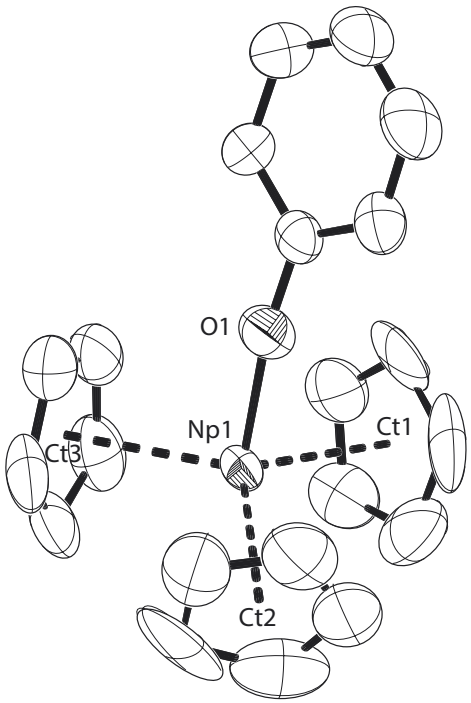

Figure 1.5. Molecular structure of **29**. Thermal ellipsoids are drawn at 50 % ellipsoid probability and hydrogen atoms are omitted for clarity. The crystallographic data was obtained from the Cambridge Structural Database (refcode: *HIHFEJ*).

Baumgärtner *et al.* reported the first homoleptic organoneptunium complex, tetrakis(η^5-cyclopentadienyl)neptunium(IV), $[Np(Cp)_4]$, **17,** using the reaction of **4** with excess of KCp in benzene solvent, Scheme 1.7.[101]

$$\underset{\mathbf{4}}{[NpCl_4]} + 4\,KCp \xrightarrow[80\,^{o}C,\,160\,h]{C_6H_6} \underset{\mathbf{17}}{[Np(Cp)_4]} + 4\,KCl$$

Scheme 1.7. Synthesis of complex **17**.

The pure reddish brown crystals were isolated and combined IR[65,101] and FIR[65] spectroscopic and powder X-Ray diffraction[102] data indicated four identical Cp rings arranged in a S_4 symmetric coordination mode around the Np^{IV} centre; a molecular arrangement later confirmed by the single-crystal structure of $[U(Cp)_4]$, **16**.[103] However, the amount of covalency in (η^5-Cp)-Np^{IV} bonding interaction is still a matter for conjecture, and Mößbauer isomer shifts for complexes **14** and **17** are a classic example of inconsistency in the reported data. Karraker[104,98] observed smaller covalent contributions in complex **17** than **14**, whereas Adrian[105,106] concluded the opposite. The latter provided spectra of **17** that contain two relaxation-broadened lines, which were further fitted assuming an anisotropic

cubic environment around the Np centre. The given isomeric shift values of the tetravalent neptunium complexes supported by cyclopentadienyl ligands were listed in Table 1.2.

Table 1.2 Isomer shifts for Np^{IV} complexes containing Cp ligands; data reported at 4.2 K by Karraker *et al.*[104,98] and Adrian.[105,106]

Compound	Isomer shift, δ, in mm s^{-1} vs. $NpAl_2$ (δ = 0)	
	Ref. [98, 104]	Ref. [105, 106]
$NpCl_3$ (**3**)	35.4[107]	
$[Np(COT)_2]$ (**1**)	19.4	19.1(2)
$[Np(Cp)_4]$ (**17**)	7.2(2)	17.9(1)
$[Np(Cp^{Me})_4]$	7.1(7)	—
$[Np(Cp)_3Ph]$ (**33**)	—	17.4
$[Np(Cp^{Me})_3(BH_4)]$	14.5(40)	—
$[Np(Cp)_3(p\text{-}(C_6H_4C_2H_5))]$	4.2(28)	—
$[Np(Cp)_3C_2H]$ (**24**)	—	11.0
$[Np(Cp^{Me})_3(O^iPr)]$	9.3(7)	—
$[Np(Cp)_3(O^tBu)]$ (**26**)	8.6(30)	—
$[Np(Cp)_3(O^iPr)]$ (**27**)	8.6(20)	—
$[Np(Cp)_3(NCS)]$ (**20**)	—	8.1
$[Np(Cp)_3(O^iC_3F_7)]$ (**28**)	7.9(20)	—
$[(Np(Cp)_3)_2C_2]$ (**25**)	—	5.7(1)
$[Np(Cp)_3(NC_4H_4)]$	—	5.0
$[Np(Cp)_3(n\text{-}Bu)]$ (**32**)	2.7(7)	—
$[Np(Cp)_3(N_2C_3H_3)]$ (**22**)	—	2.4
$[\{(Cp)_3Np\}_2SO_4]$ (**21**)	—	1.9
$[Np(Cp)_3Cl]$ (**14**)	14(10)	0.6
$[Np(Cp^{Me})Cl_3 \cdot 2THF]$	-3.1(7)	—
$[Np(Cp)_3I]$ (**19**)	—	-3.9
$NpCl_4$ (**4**)	-3.4[108]	

Nevertheless, a comparison of isomeric shifts for **17** and **4** follow a minimum difference of +10.6 mm s^{-1}, suggestive of the significant shielding of 6s orbitals in **17**

and appreciable covalency in Np-Cp bonding. Bohlander[65] demonstrated further that complex **2** reacts with ammonium salts to form the stable Cp_3Np^+ conjugated Brønsted acid, which binds concomitantly with the corresponding inorganic anions. The series of tris(cyclopentadienyl)neptunium(IV) halides (Cl (**14**), Br (**18**), I (**19**)), thiocyanate **20** and sulfate **21** were obtained and characterized with UV-Vis-NIR, IR, FIR and ^{237}Np Mößbauer spectroscopy techniques.

1.3.4.2 Complexes with σ-bound hydrocarbyl ligands

Although tetraalkylactinides(IV), $[AnR_4]$, are known to be highly unstable and contain coordinatively unsaturated An^{IV} sites, which can induce α- and β-hydride elimination reactions, the sterically protected σ-bound organometallic complexes containing cyclopentadienyl ligands are accessible. The salt metathesis reactions between $[An(Cp)_3Cl]$, and alkyl- and aryl- alkalides, MR, in appropriate solvents produce room temperature-stable complexes of the general formula $[An^{IV}(Cp)_3R]$; the reaction equilibria are shifted towards the products by precipitation of the MCl by-products, Scheme 1.8.

$$[An^{IV}(Cp)_3Cl] + M^{I}R \xrightarrow{\text{solvent}} [An^{IV}(Cp)_3R] + M^{I}Cl$$

An = Th, U, Np
M^{I} = Li, Na
R = hydrocarbyl group

Scheme 1.8. Synthesis of $[An(Cp)_3R]$ complexes from the appropriate chlorides.

Unlike the readily prepared Th^{IV} and U^{IV} analogues, the selective reactions of Np^{IV} involve precise stoichiometry and the addition rate of the organolithium reagents, avoiding coordinating solvents to force the LiCl precipitation and reactions at low temperatures. Karraker reported when THF was used as solvent for the synthesis of complexes $[Np(Cp)_3(n\text{-Bu})]$ **32** and $[Np(Cp)_3Ph]$ **33** the concomitant reduction reactions consume 40-60% of the generated Np-R species.[109] Even with the above precautions, some reduction to the Np^{III} side-products occur, presumably including the homoleptic complex $[Np(Cp)_3]$ **34**, and lower yields are typically observed.[65] To ensure the high purity of the resulting $[Np(Cp)_3R]$ samples, recrystallization from *n*-pentane can be used, provided the Np^{III} decomposition products are insoluble. Studies on the thermal decomposition of the solid complexes $[An(Cp)_3Me]$, where An = Th, U, Np (**30**), have indicated the stability series: Th >> U > Np, which follows the decreasing trend in An^{IV}/An^{III} reduction potential.[65] More

interestingly, the kinetics of the alcoholysis reactions (R'OH) of complexes $[An(Cp)_3R]$ containing the same R and R' substituents show the opposite trend and in the case of neptunium, the IR bands for both product $[Np(Cp)_3(OEt)]$ and the unreacted **30** are still seen after 15 h, upon dissolution of the latter in ethanol at room temperature.[65,110–112] This reactivity mirrors the results of the hydrolytic behaviour of bis([8]annulene) complexes of early actinides.[113,114]

1.3.4.3 Cyclooctatetraene and substituted cyclooctatetraene complexes

The chemistry of the ligand itself and the early actinide complexes supported by the cyclooctatetraene dianion, COT = $C_8H_8^{2-}$, and its alkyl- and silyl- substituted derivatives was reviewed extensively by Legin, who covered the initial study period of 1968 - 1976.[115] Further progress in bis([8]annulene)neptunium chemistry was associated with Bohlander's spectroscopic investigations of $[Np(COT)_2]$ **1** using IR, FIR, UV-Vis-NIR, and magnetic susceptibility measurements.[65] Interestingly, the newly acquired FIR spectra supported the strongest (covalent) bonding interaction in **1** withn respect to analogous $[U(COT)_2]$ and $[Th(COT)_2]$ complexes. At the same time, Adrian[106] reported a well-resolved ^{237}Np Mößbauer spectrum of **1**, indicating the largest isomer shift of 19.1(2) mm s^{-1} amongst the organoneptunium complexes and consistent with that previously reported by Karraker[116] (19.4 mm · s^{-1}, corresponding oxidation state of Np ~3.5). The observed magnetic splitting in ^{237}Np Mößbauer spectroscopy in between 4.2 and 40 K inspired only recently the modern dynamic susceptibility measurements under applied magnetic field, which indicated the unique SMM behaviour in complex **1** (*cf.* Chapter1.3.1).[37] In this study, also the available room temperature single-crystal X-ray diffraction data[117] of complex **1** was replaced by the state-of-art analysis.

1.4 Objectives of this thesis

In the realm of the molecular design in the formally low-valent neptunium chemistry, π-donor aromatic systems capable of potentially reactive neptunium-ligand linkages are envisaged to produce substantial results. Despite the fact that organoneptunium chemistry was established as early as 1965, structurally authenticated organometallic Np(III) complexes are still absent. Additionally, the long-term interest in the periodicity and covalency trends, and also more recently, expanding the available formal oxidation state range

for the *f*-elements have focused on the investigations towards missing studies of the tris(cyclopentadienyl)neptunium derivatives. Towards these goals the two homoleptic neptunium(III) complexes of the cyclopentadienyl, $(Cp)^-$ and the (trimethylsilyl)cyclopentadienyl, $(Cp')^-$, ligands are proposed as highly reactive Np^{III} starting materials in molecular non-aqueous neptunium chemistry, that can be isolated without the use of neptunium metal; the efforts in this vein are discussed in Chapter 2.

The given $\{(Cp)_3\}^{3-}$ ligand set is considered to impose a demanding steric profile to the central ion and provide directionality of the resulting structural arrangements within the reactivity studies. These are primarily directed towards the synthesis of the intrinsically axial, oxo-bridged homo- and heterobimetallic actinide complexes, which should become interesting model compounds for probing the magnetic interactions between communicating actinide ions; this work is covered in Chapter 3.

The work presented in chapter 4 provides an investigation into enhancing the fundamental understanding of the subtlest actinide π- and σ-(back)bonding interactions in the Np^{III} and Np^{IV} complexes derived from the doubly deprotonated *trans*-calix[2]benzene[2]pyrrole, $H_2(L^{Ar})$, which can structurally and electronically mimic the bis(cyclopentadienyl) ligand system, i.e. bis(η^5-pyrrolyl), or a bis(η^6-arene) sandwich form. This conformational flexibility and unique π- bonding potential of the ligand scaffold paves the way towards understanding prototypical reactivity and binding preferences of early actinide ions. Metathesis reactions involving Np^{IV} and Np^{III} precursors were followed and expected to induce prototypical reactivity and structural discrimination amongst other low-valent early actinide ions. The target complex $[(L^{Ar})NpCl_2]$ could also exhibit magnetic bistability at low temperature due to the presence of the Kramers Np^{IV} ($5f^3$, $^4I_{9/2}$) centre inside a 'metallocene-type' geometry of the η^5-pyrrolide binding mode, isotypic with U^{IV} and Th^{IV} complexes.

The potential isolation of the first formally Np^{II} neptunium complexes was initially examined through the stabilization of the higher-lying 6d orbitals by the two different ligand fields, generated by the three $(Cp')^-$ anions or encapsulated within $(LAr)^{2-}$ dianion framework. This work is also presented in Chapter 3 and 4 respectively.

2 Reduction Chemistry of Neptunium Cyclopentadienyl Complexes

2.1 Introduction

This section discusses homoleptic low valent neptunium complexes supported by the cyclopentadienyl anion, Cp^- and the trimethylsilyl(cyclopentadienyl) anion, $(Cp')^-$, focusing on representative syntheses and structural characterization. The complexes of each of the two ligands are discussed in decreasing Np oxidation state and single crystal X-ray diffraction analyses are discussed in a section of their own. Although this thesis does not focus on uranium organometallic chemistry, analogues of this element were used in complementary structural studies of $[An(Cp)_3]$ complexes (*cf.* Chapter 2.3.1) and their systematic oxo-functionalization (*cf.* Chapter 3.3). The experimental difficulties in handling more ionic organometallic complexes of the trivalent actinides means that no single crystal structural authentication has been reported for any neptunium(III) species prior to this work.

So far, four synthetic routes to $[An^{III}(Cp)_3]$ complexes have been developed starting from UCl_3,[74] $[U(Cp)_4]$ **16**,[74] $[U(Cp)_3Cl]$, **38**[104,118] and $[Np(Cp)_3Cl]$ **14**[104]; the respective reactions and reaction conditions are presented in Scheme 2.1. Attempts to desolvate complex **39a** (Scheme 2.1.c) by thermal dissociation in a vacuum have resulted in vast decomposition and either unchanged crystalline sublimate of **39a** (closed ampoule method) or trace amounts of **39** (flash pyrolysis under molecular flow conditions) were isolated.[20,104] A desire to study Mößbauer properties of the $[Np^{III}(Cp)_3]$ complexes has led Karraker and Stone[104] to the first exploratory synthesis affording a powder presumed to be a THF adduct $[Np(Cp)_3 \cdot 3THF]$ **34a**, although the metal content analyses that suggest three THF donors in the molecular structure may indicate the two of them being of a lattice solvent and not the proposed coordination number CN = 6 assigned for the central Np^{III} ion. Indeed, Bohlander showed that the olive brown product **34a** and **39a** are probably isostructural using IR, FIR and UV-Vis-NIR spectroscopies, with a distorted tetrahedral symmetry around the Np/U centre and the 1:1 Lewis base adduct constitution of both the complexes.[65] A slightly modified strategy of Zanella *et al.*[118] which uses weaker donor solvents can be employed for the synthesis of the unsolvated Np^{III} complex $[Np(Cp)_3]$ **34** (*cf.* Scheme 2.1.e).

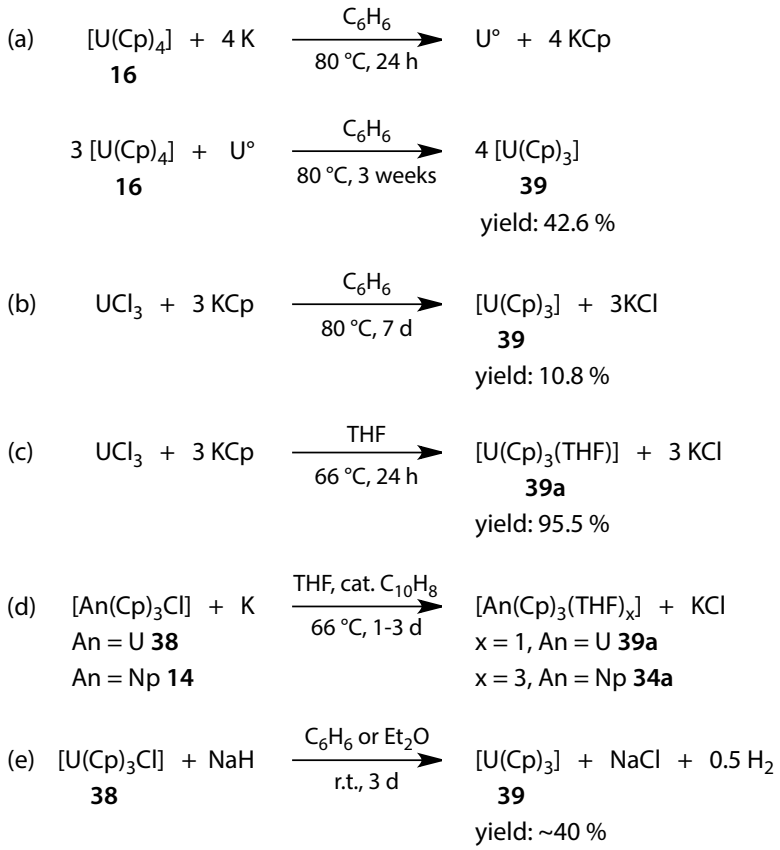

Scheme 2.1. Syntheses of $[An(Cp)_3]$ complexes, An = U (**39**),[74,118] Np (**34**) and their THF Lewis base adducts, $[An(Cp)_3(THF)_x]$, An = U, x = 1 (**39a**),[74,104,118] An = Np, x = 3 (**34a**).[104]

2.2 The Np^{IV} Precursors: $[NpCl_4]$ and $[Np(Cp)_3Cl]$

The homoleptic complexes $[Np(Cp)_3]$ **34** and $[Np(Cp')_3]$ **40** have been targeted using either a salt metathesis from an already reduced Np^{III} centre or a one-electron reduction of the complexes of the generic formulae $[Np^{IV}(Cp)_3X]$ and $[Np^{IV}(Cp')_3X]$, (*cf.* Scheme 2.1.b and Scheme 2.1.e). The first method offers the advantage that the *in situ* reduction of the well-known Np^{IV} precursor, $NpCl_4$ **4**, to $NpCl_3$ **3** can be followed in a one-pot reaction with the appropriate alkali or thallium cyclopentadienide reagent (Scheme 2.3 and Scheme 2.9). However, the poor solubility of **4** in non-coordinating solvents may present a synthetic problem, which could be minimized by the choice of weakly coordinating Et_2O solvent and prolonged reaction times. The other pathway involves the reduction of complex **14** with either metallic or hydridic reducing agents (Scheme 2.1.d and Scheme 2.1.e). This strategy is further supported by the preliminary studies on the isolation of the target complex **34** in the reaction of **14** with excess NaH

in Et_2O.[65] On the other hand, Ephritikhine *et al.*[119] showed later on that reactions with an excess of NaH can afford the hydride bridged complexes, i.e. $[Na(THF)_2](\mu\text{-}H)[U(Cp)_3]_2$, which may hamper the isolation of the desired neutral product $[An(Cp)_3]$ or influence its final purity. Therefore, only metallic reductants, KC_8 and liquid sodium amalgam, Na(Hg), were considered in this study; both synthetic routes were envisaged to produce expected complexes **34** and **40**.

Complex **14** was prepared readily from the reaction of **4** with slightly less than 3 eq of KCp in THF and purified by work-up from *n*-pentane (Scheme 2.2). The resulting deep brown, lustrous, single crystals of **14** were obtained in useful quantities and characterized crystallographically and by NMR spectroscopy in a C_6D_6 solution. Although previously well characterized by UV-Vis-NIR, IR, FIR, and Mößbauer spectroscopies, the molecular structure of **14** has not been reported prior to this work. The solid-state structure, Figure 2.4, consists of three η^5 bound Cp rings and an apical chloride ligand forming a flattened tetrahedral (approximately C_{3v}) arrangement about the Np^{IV} centre; the structure, bonding and its comparison with the uranium congener **38** in the solid-state are discussed in Chapter 2.5.1.

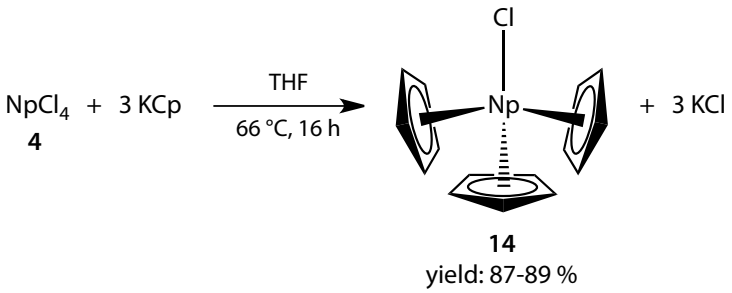

Scheme 2.2. Synthesis of complex **14**.

The ^1H and ^1H-^{13}C gHMQC NMR studies of **14** showed only one broadened signal for all the Cp rings at δ_H = -21.49 ppm (linewidth 31.22 Hz) and the respective ^{13}C shift of δ_C = 4.6 ppm, suggestive of the retention of the molecular structure in solution as in the solid-state. The ^1H NMR data correlate well with the previously reported isotropic shift[1] of Δ_H(**14**) = +27.4 ppm (30 Hz)[120] which was referenced to the diamagnetic complex $[Th(Cp)_3Cl]$ (Δ_H(Th) = 0, δ_H = 6.2 ppm[121]); these

[1] The origin of the reported positive sign of the isotropic shift within the original work remains unclear.

literature findings present the chemical shift value of δ_H(**14**) = -21.2 ppm, measured presumably at room temperature.

2.3 Neptunium(III) Complexes of the Cyclopentadienyl Ligand

2.3.1 Syntheses of [Np(Cp)$_3$] and [U(Cp)$_3$] complexes

The solid microcrystalline $NpCl_3$ **3** can be generated *in situ* from the quantitative reaction between $NpCl_4$ **4** and excess Na(Hg) in diethyl ether at room temperature, Scheme 2.3. The *in situ* formed **3** reacts rapidly with stoichiometric TlCp with the formation of a grey precipitate and a dark green-coloured solution, which is proposed to contain the target Np^{III} complex. However, the solution then darkens rapidly as the product reacts spontaneously with the TlCl by-product, and is oxidized to the dark brown Np^{IV} complex **14**. Interestingly, the latter reactivity demonstrates the strong preference of the +4 oxidation state for the complexes of cyclopentadienyl ligands, although the Np^{III} disproportionation mechanism already described in the literature (*cf.* Scheme 1.5)[67] has been modified by the presence of the thallium-amalgam|thallium(I) chloride, an equilibrium potential system which acts as an electron scavenger and precludes the precipitation of the higher activity Np metal. The reaction equations are presented in Scheme 2.3.

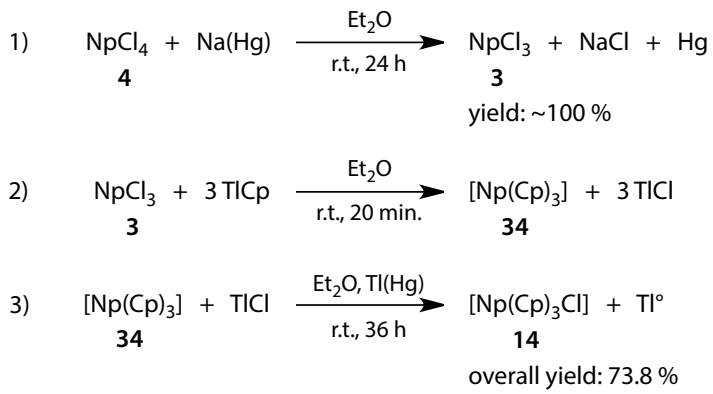

Scheme 2.3. Reactions of **4** with Na(Hg) and TlCp in diethyl ether.

Sonnenberger and Gaudiello demonstrated in cyclic voltammetry experiments that [An(Cp)$_3$Cl] (An = U **38**, Np **14**) complexes show reversible one-electron reduction waves without detectable Cl^- loss at $E_{1/2}$ = -1.80 V and -1.29 V in THF (*vs.* Fc/Fc^+, U^{IV}/U^{III} and Np^{IV}/Np^{III} respectively).[64] The value for Np is substantially less negative

and suggests the reductive chemistry could be more facile for the less studied Np(IV) complex **14** than compared to the U(IV) analogues.

The results of the reduction of **14** with 1.1 eq of KC_8 in Et_2O were inconclusive. Upon addition of KC_8 to a dark brown solution of **14**, the colour of the supernatant turned initially dark green-brown, which may indicate the formation of a Np^{III} species, Scheme 2.4.1. However, after a further reaction time of approx. 1.5 h, the gradual precipitation of the Np-containing products was observed and a clear, colourless solution formed over a period of 48 h at room temperature, Scheme 2.4.2. The Soxhlet extraction of the resulting black precipitate with Et_2O for 72 h gave only a yellowish solution containing trace amounts of an off-white precipitate, presumably of the KCp by-product, whilst the subsequent extraction with THF gave only a clear solution containing *ca.* 5 % of the total amount of KCp that could be formed, based on the initial quantity of **14** and was identified by a positive ferrous chloride test. These results imply the reductive cleavage of the Np-(η^5-Cp) bond and that any transiently formed soluble Np^{III} complex, i.e. $[\{Np(Cp)_2Cl\}_3]$, is susceptible to further ligand rearrangement reactions and conceivably polymerized due to bridging chloride ligands in the solid-state.

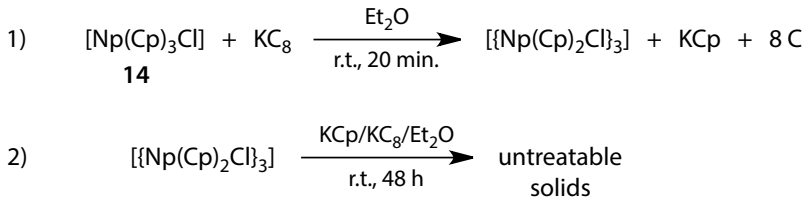

Scheme 2.4. Proposed reduction reaction of **14** with KC_8 in Et_2O solvent; suggested structural analogy between transiently formed Np^{III} species and the reported trimeric dark green uranium complex $[\{U(\eta^5\text{-}Cp^*)_2(\mu\text{-}Cl)\}_3]$.[122]

The tendency of the trivalent organoactinide complexes to form stable adducts with alkali halides under reducing conditions was first evidenced over three decades ago by Marks and colleagues,[122,123] who reported an insoluble complex $[(Cp^*)_2UCl(NaCl)]$ and its defined Lewis base adduct $[(Cp^*)_2U(\mu\text{-}Cl)_2Na(THF)_2]$. The electrochemical studies by Finke *et al.*[124] and later Sonnenberger and Gaudiello[64] concluded the complex $[(Cp^*)_2UCl_2]$ retains both the coordinated Cl^- ions in a fully-reversible, one-electron reduction process ($E_{1/2}$ = -1.22 V in THF vs. SCE or $E_{1/2}$ = -2.18 V *vs.* Fc/Fc^+). More importantly, the neptunium analogue, $[(Cp^*)_2NpCl_2]$, exhibits similar behaviour with the potential of $E_{1/2}$ = -1.38 V in THF

vs. Fc/Fc^{+}, thus implying the sensitivity of the Np^{IV}/Np^{III} couple to the ligand environment about the metal centre is greatly reduced.

Furthermore, Ephritikhine *et al.*[125] reported two anionic tris(cyclopentadienyl)uranium(III) complexes **41** and **42** bearing chloride ligands and incorporated sodium metal counterions. No ligand exchange reactions were detected between **39a** and NaCl in THF-d_8 by variable temperature ^{1}H NMR (Scheme 2.5.a), suggesting the reduction mechanism is key to the formation of coordination polymers. The anionic fragment of **42** adopts bent configuration consisting of the two Cp_3U units, which are interconnected with a bridging chloride atom, showing the U–Cl bond distances of 2.79(2) and 2.82(2) Å and U-Cl-U angle value of 156.5(7)°. This moiety is representative for the known $\{An^{III}(Cp)_2Cl\}$ motifs and the reduction product of **14** with KC_8 could have a similar structure.

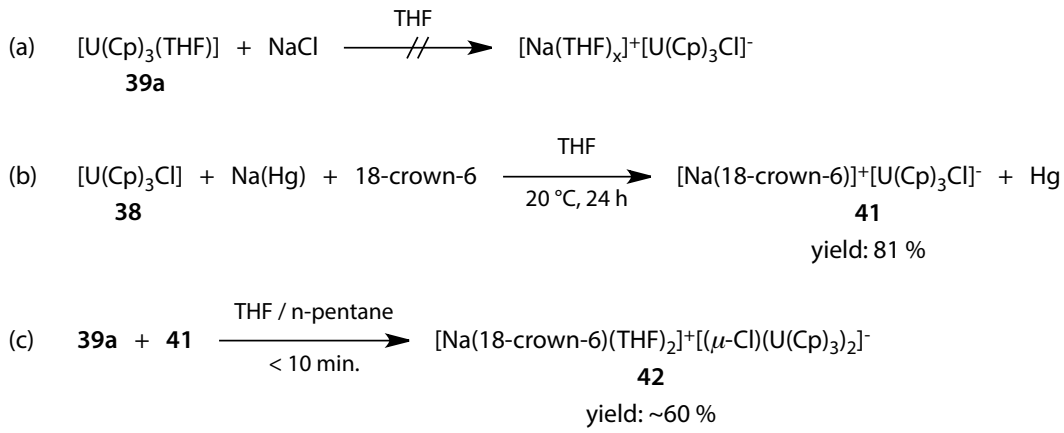

Scheme 2.5. Syntheses of anionic complexes **41** and **42** from the reduction of **38** in the presence of 18-crown-6 ether.[125]

Due to the lack of selectivity in the reaction between **14** and potassium graphite, milder reducing agents were envisaged to produce the expected molecular complex $[Np(Cp)_3]$ **34**. The analogous reduction reactions of **38** and **14** complexes using sodium amalgam are presented in Scheme 2.6. Both syntheses afforded cleanly the expected $[An(Cp)_3(OEt_2)]$, An = U (**39b**), Np (**34b**) complexes and subsequently the appropriate $[An(Cp)_3]$ products *via* controlled thermal dissociation reactions. The resulting Lewis base adducts readily lose the weakly coordinated oxygen donor solvent molecule *in vacuo*, or even on standing at room temperature under an argon atmosphere. The thermal dissociation of the Np^{III} congener **34b** is actually so facile that it precludes the analysis of the isolated pale green crystals of **34b,** due to quick darkening after transfer from the mother liquor to the perfluoroalkyl ether oil.

On the contrary, the isolated $[U(Cp)_3(OEt_2)]$ **39b** is more deeply coloured than the unsolvated complex **39**. The complex **39b** was characterized by single crystal X-ray diffractometry, showing not only the retention of the gross molecular configuration of the other tris(cyclopentadienyl)actinide(III) complexes, but also uniform An-C separations.[126]

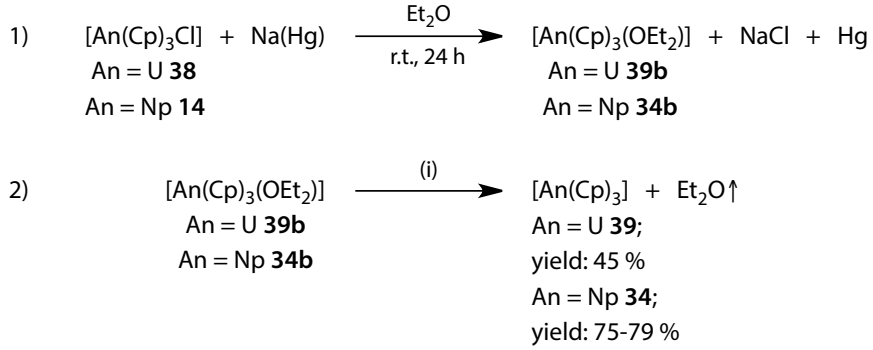

Scheme 2.6. Syntheses of neutral complexes $[An(Cp)_3(OEt_2)]$, An = U (**39b**), Np (**34b**), and $[An(Cp)_3]$, An = U (**39**), Np (**34**), from the reduction reactions of the corresponding chlorides **38** and **14** with Na(Hg) in diethyl ether; (i) desolvation conditions for **39b**: 40 °C, 3×10^{-3} mbar, 4 h; for **34b**: r.t., vacuum evaporation.

The solid-state structures of the unsolvated complexes **34** and **39** are isostructural and contain polymeric structures of the $\{An^{III}(\eta^5\text{-}Cp)_2\}$ units bridged through alternating $\mu\text{-}\eta^5,\eta^1$-bound cyclopentadienyl groups with the formation of infinite zig-zag chains (*cf.* Chapter 2.5.3). In this form both complexes are only very sparingly soluble in non-coordinating solvents but dissolve slowly in Et_2O or THF, forming molecular 1:1 adducts of the generic formula $[An(Cp)_3L]$. The ^1H and ^1H-^{13}C gHMQC NMR spectra of **34** in THF-d_8 show only one resonance for the Cp ring protons at δ_H = -9.65 ppm (linewidth 2.85 Hz) and the respective ^{13}C shift of δ_C = 150.4 ppm, suggesting that all the Cp rings are η^5 bound. The ^1H NMR study of complex **39** suggest the same structure as here, although the proton nuclei are higher shielded and signal broadened, δ_H = -15.41 ppm (linewidth 16.22 Hz), due to the contact with the more paramagnetic U^{III} ($5f^3$) centre.

Additionally, the ATR spectroscopy of complex **34** features several characteristic vibrations of the Cp rings (Figure 2.1, red trace), which correlate well with the previously reported IR data of the complexes $[M(Cp)_3]$ (M = U, Pu, Am, and Tm)[74] and the solvated adducts of $[Np(Cp)_3]$.[65] The closely matching vibrational peaks

for the entire series suggest appreciable ionic character of bonding in **34**, although different methods of reflection *vs.* transmission measurements preclude the comparison of the relative intensities of the bands and thus making potential discussion on the covalency component in Cp-M^{III} bonds difficult. The cyclopentadienyl ring vibrations were assigned using the general guideline of Aleksanyan and Lokshin[127] and are summarized in Chapter 5.3. Perhaps the most specific IR-active resonant vibrations of the Np^{III} tris-cyclopentadienyl complexes is the set of four absorptions at *ca.* 666, 611, 581 and 519 cm^{-1}, which is also visible in the ATR spectrum of **34**.

2.3.2 Synthesis and characterization of [K{Np(Cp)$_4$}], 43

The small quantities of extractable KCp and other low-molecular products from the reduction reaction of [Np(Cp)$_3$Cl] **14** with KC_8 (Scheme 2.4) are also consistent with the addition of KCp side-product to complex [Np(Cp)$_3$] **34**, which can result in the possible [K{Np(Cp)$_4$}] salt formation,

Scheme 2.7.

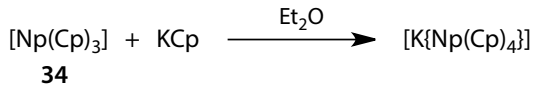

Scheme 2.7. Proposed reaction between **34** and KCp.

Although the neutral complex [Np(Cp)$_4$] was reported several times to form in the reaction between $NpCl_4$ and excess KCp in THF,[65] benzene,[65,101] or toluene[98] solution, the control reaction of the expected intermediate complex **14** with KCp may cast additional light on the reduction chemistry of neptunium cyclopentadienyl complexes. In fact, Adrian observed that Mössbauer spectra of the [Np(Cp)$_4$] targets provided by Bohlander contained the two low intensity bands arising from the unidentified impurities, which may provide an argument for this study.[105] Furthermore, the reduction properties of the cyclopentadienyl anions are well documented in preparative inorganic chemistry, and an additional equivalent(s) of either NaCp or [MgBr(Cp)] reagent are conveniently employed to reduce *in situ* the higher oxidation state transition metal and lanthanide precursors and produce metallocenes of the M^{II} centres i.e.: Cr,[128,129] V,[129,130] Ru,[131] Os,[132] or Eu.[133] However, in actinide chemistry this reactivity is rarer, and the only reported synthesis to date is the homoleptic complex [^{239}Pu(Cp)$_3$]

using caesium hexachloroplutonate(IV), $[Cs_2(^{239}PuCl_6)]$, and excess $Mg(Cp)_2$ in THF.[134]

In a reaction designed to reduce **14** with KCp according to the synthetic account for $[Np(Cp)_4]$ detailed by Bohlander a mixture of **14** and 1.1 eq of KCp was dissolved in THF and heated to gentle reflux for 96 h, Scheme 2.8. Initially, no precipitate formation was observed on contacting the reagents in the solvent at room temperature, but at elevated temperature the gradual accumulation of reddish brown solids corroborated the similar observations of $[Np(Cp)_4]$ product. However, a *n*-pentane extraction of the evaporated post-reaction mixture afforded 48.7 % of essentially pure dark brown, lustrous, crystals of **14**, while the subsequent prolonged extraction with Et_2O gave maroon single crystals of the postulated neptunate(III) complex of the molecular formula $[K\{Np(Cp)_4\}]$ **43**, which was identified by X-ray crystallography (Chapter 2.5) and NMR spectroscopy; the principal polymeric chain structure of **43** is also drawn in Scheme 2.8 for clarity.

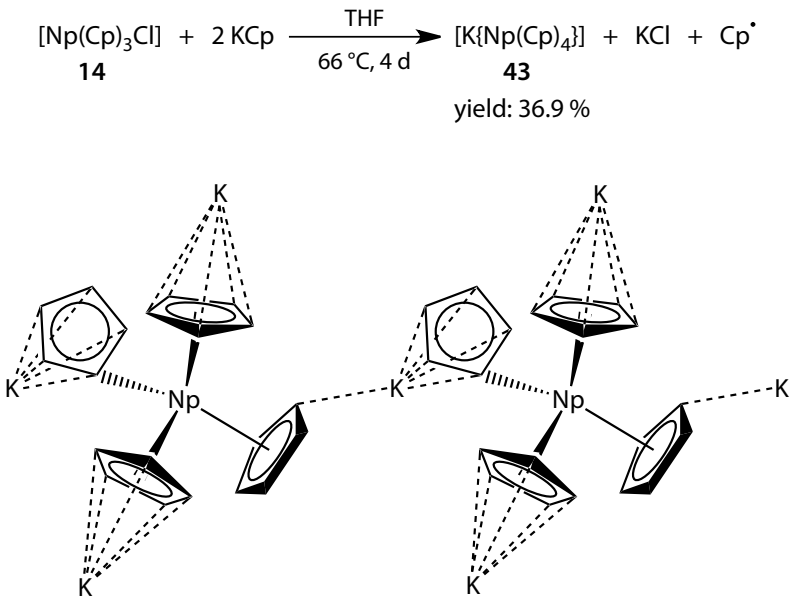

Scheme 2.8. Synthesis of $[K\{Np(Cp)_4\}]$ (**43**) from **14** and KCp and the principal structural fragment of the product in the-solid state, depicting η^1 and η^5 Cp ligand coordination modes around the Np^{III} centres.

The ^1H NMR spectrum of **43** in THF-d_8 contains only one broadened single resonance at -11.95 ppm (linewidth 18.05 Hz), suggesting that the Cp binding is fluxional at room temperature or the individual ion effectively dissociate in solution, and probably η^5-bound for the majority of time. Due to the very

low solubility of the 'ate-'complex **43** in THF at room temperature the UV-Vis-NIR spectra do not contain any absorptions with intensities visible above background using the optical chamber contained in the radiological glove-box. ATR analysis of solid samples of **43** showed very similar skeletal vibrations of the Cp rings, previously described for **34**, although the major difference is the different intensity ratios of several vibrational bands and the absence of the absorptions at 666, 611, 581 and 519 cm^{-1} in the fingerprint region for complex **34** and its Lewis base adducts **34a** and $[Np(Cp)_3(NCMe)_2]$[65,135]; the spectra are shown in Figure 2.1. The ATR spectra show a slight downshift of the vibrations in **43** *vs.* **34**, which is presumably due to the presence of the ionic K-Cp bonds in the solid-state structure (for comparison see Chapter 5.3).

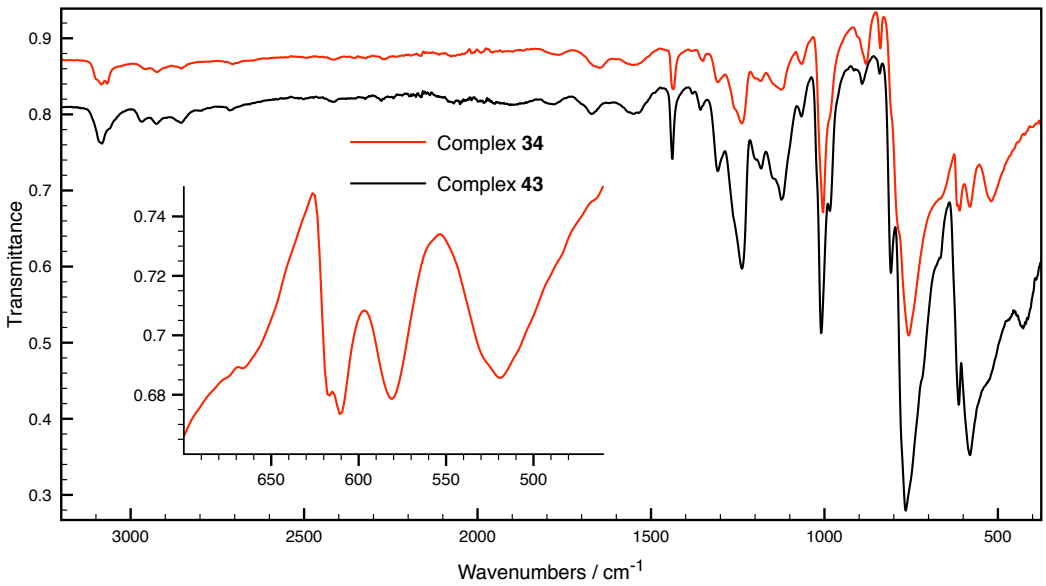

Figure 2.1. ATR spectra of complexes **34** (red trace) and **43** (black trace) measured using diamond ATR; the abundance ratio was constant for these measurements and reproducibility checked using multiple measurements of the peak-height ratio between the bands maxima near 1438 and 766 cm^{-1} and the one at 1009 cm^{-1}. The characteristic four of vibrations in **34** at 666, 611, 581 and 519 cm^{-1} for the Np^{III} cyclopentadienyl complexes is depicted on the inset.

2.4 Low-Valent Neptunium Complexes of the (Trimethylsilyl)-Cyclopentadienyl Ligand

2.4.1 Synthesis and characterization of $[Np(Cp')_3]$, 40

Due to potential loss of material during the room-temperature isolation/purification of the $[Np(Cp')_3Cl]$ intermediate, the one-pot synthesis

was targeted, envisaged to afford better yields of **40** (*cf.* Scheme 2.3). The complex [Np(Cp')$_3$] **40** was found to form a deliquescent crystalline solid, which dissolves slowly in the presence of 1 atm of *n*-pentane vapour at room temperature. The exploratory metathesis reaction of the *in situ* generated $NpCl_3$ **3** with 3 eq of TlCp resulted in the subsequent one-electron oxidation of the expected Np^{III} product, [Np(Cp)$_3$] to [Np(Cp)$_3$Cl] (*cf.* Scheme 2.3), thus a more reducing cyclopentadienyl salt was chosen. The precursor KCp' was synthesized according to a modified literature procedure (*cf.* Chapter 2.3) and isolated in the form of large single crystals of the known unsolvated form already structurally authenticated by Jutzi *et al.*[136] Complex **40** can be obtained in a straightforward reaction between **3** and the stoichiometric amount of KCp' in diethyl ether at room temperature (Scheme 2.9), however **40** is extremely soluble in common solvents and difficult to isolate in crystalline form. A flash vacuum evaporation was found to be the method of choice for reproducible isolation of **40**.

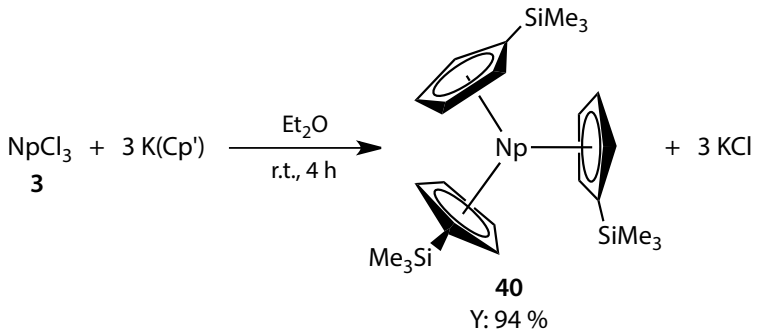

Scheme 2.9. Synthesis of complex **40** from *in situ* generated $NpCl_3$ **3** and K(Cp').

The ^{1}H NMR spectrum of **40** in toluene-d_8 solution shows Np^{III} ($5f^4$) contact shifted resonances at δ_H = -1.38 ppm for the $C_5H_4Si(C\underline{H_3})_3$ protons, and δ_H = -8.60 and δ_H = -9.51 ppm for the $C_5\underline{H_4}Si(CH_3)_3$ protons, in the overall 9:2:2 ratio, suggestive of all the ligands being η^5 bound to the metal centre. The spectrum of **40** acquired in THF-d_8 solution shows an analogous solution structure but the resonances are slightly shifted downfield (δ_H = -0.62, -8.81, -8.98 ppm), which may suggest adduct formation with the oxygen donor THF molecule, however without substantial change of the parent scaffold geometry. Unfortunately, solutions of complex **40** react with degassed commercial fluoropolymer NMR tube liner material, turning gradually from green to red after storing the solutions for up to 3 hours at room temperature and the new resonances appear or grow

in intensity in the relevant ^{1}H NMR spectra at -1.45, -2.78 (only for THF-d_8) and *ca.* -4 ppm, Figures 7 and 8. Although COSY, ^{1}H-^{13}C gHMQC (*cf.* Chapter 5.3) and ge-2D NOESY experiments provided no useful information to help further assignment of the decomposition products, one can assume the abstraction of a fluoride ion from the polymer by the coordinatively unsaturated Np^{III} centre of **40** to form various neptunium fluoride species.[137]

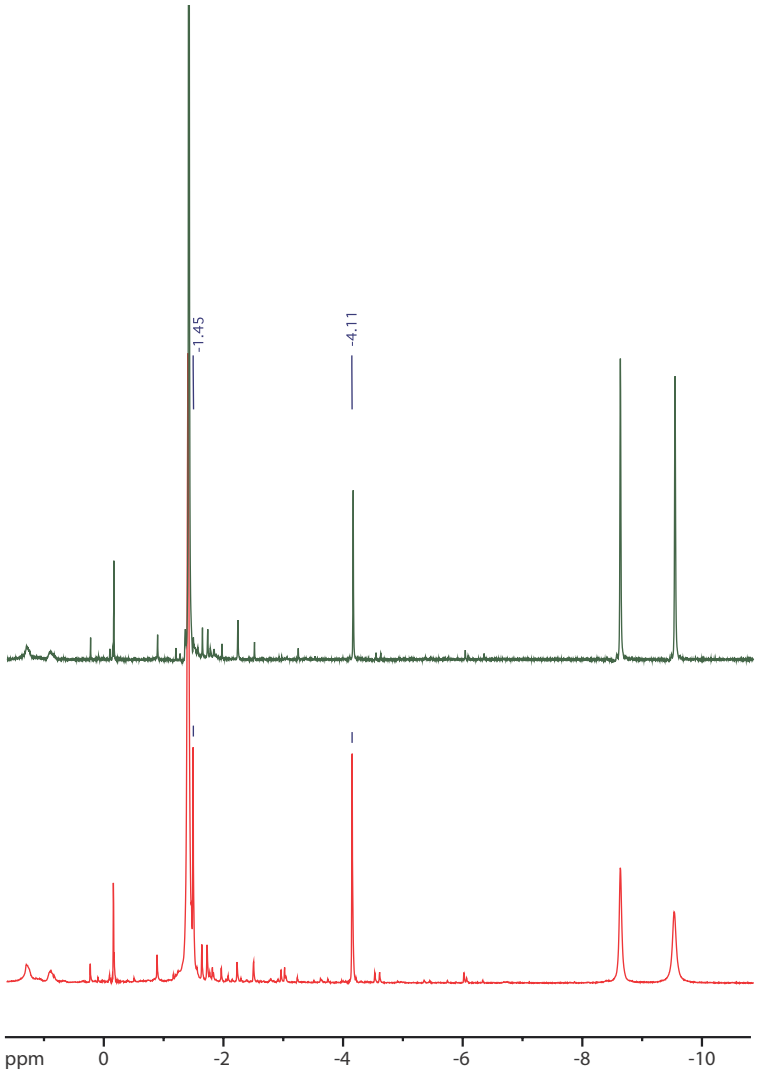

Figure 2.2. Sections of the ^{1}H NMR spectra of **40** in toluene-d_8 after loading the 7.6 mM solution into the 4 mm O.D. fluoropolymer NMR tube liner (*ca.* 10 min, green trace) and followed by storage at room temperature 105 min. (red trace). The highest intensity resonance at -1.38 ppm was cut off for clarity and signal intensities were normalized against the residual protio-solvent signal at 2.08 ppm, showing the gradual decomposition of **40** and concomitant formation of the two paramagnetically shifted resonances of presumably fluorine-containing neptunium species (labelled with exact δ_H values).

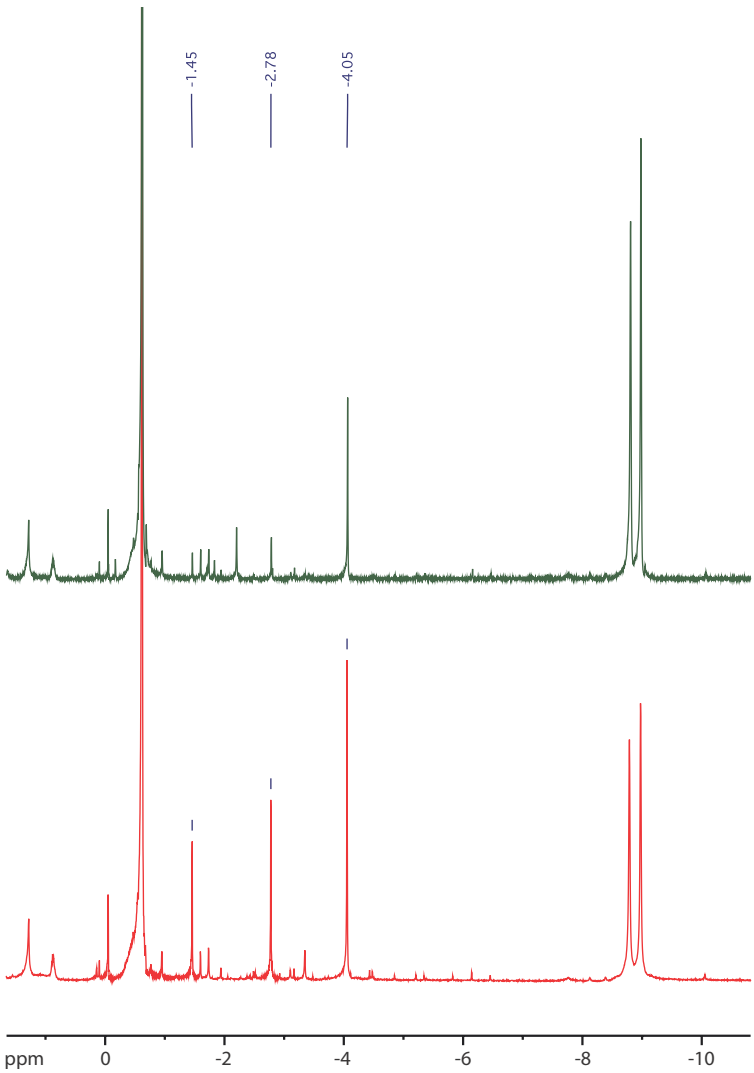

Figure 2.3. Sections of the ^{1}H NMR spectra of **40** in THF-d_8 after loading the 8.1 mM solution into the 4 mm O.D. fluoropolymer NMR tube liner at room temperature (*ca.* 15 min, green trace) and after the following 100 min. (red trace). The highest intensity resonance at -0.62 ppm was cut off for clarity and signal intensities were normalized against the residual protio-THF resonace at 3.57 ppm, showing the gradual decomposition of **40** and concomitant formation of the three paramagnetically shifted resonances of presumably fluorine-containing neptunium complexes (labelled with exact δ_H values).

2.4.2 Synthesis of [K(2.2.2-cryptand)][Np^{II}(Cp')$_3$] 79

After the first structural account in 2013 on the +2 oxidation state for uranium in a molecular complex [K(2.2.2-cryptand)][U(Cp')$_3$] **46** by Evans *et al.*,[93] the synthesis of the neptunium homologue **79** of this 'ate-' complex was examined. Due to the current technical limitations of the prolonged cooling operations and the need of safe manipulations conducted under stringent radiological,

inert-gas and low-temperature regimes, simultaneously, all restricted the scope of this research to the synthesis and crystallographic analysis only.

$$\underset{\mathbf{40}}{[Np(Cp')_3]} + KC_8 + 2.2.2\text{-cryptand} \xrightarrow[-35\ °C,\ 10\ min.]{THF/Et_2O} \underset{\mathbf{79}}{[K(2.2.2\text{-cryptand})][Np(Cp')_3]} + 8\,C$$

Scheme 2.10. Reaction of $[Np(Cp')_3]$ **40** with KC_8 in the presence of equimolar amount of 2.2.2-cryptand.

The reduction of complex **40** with KC_8 was carried out using the original method described for uranium, but the crystallization temperature modified to -78 °C, Scheme 2.10. The brownish-green solution of **40** and 2.2.2-cryptand in THF/Et_2O mixture turns immediately very intense dark brown to black on contact with the solid reducing agent, and the small, shiny black crystallites appear in the filtrate after approx. 1h of storage at -78 °C. Several potentially single crystals of suitable size for X-ray diffraction study were analysed but only very weak diffraction was observed. The putative Np^{II} crystals begin to deteriorate at room temperature within 1 minute of contact with the perfluoroalkyl ether oil, although the colour changes suggest first the loss of lattice solvent before oxidation. Unfortunately, none of the crystals that survived the filling into the capillary tubes of Lindemann glass and subsequent fixing of the radioactive surface contamination procedure have maintained the sufficient quality for the X-ray diffractometry.

2.5 Structural Analyses by Single Crystal X-ray Diffraction

2.5.1 Molecular structure of $[Np(Cp)_3Cl]$, 14

The large, lustrous, deep brown single crystals of **14** suitable for X-ray crystal structure determination were obtained from an *n*-pentane solution over 24 h. The crystals were refined in the monoclinic space group $P2_1/n$ (No. 14), a = 8.1172(6), b = 12.2727(8), c = 13.6606(9) Å, β = 90.5280(10)°, with 4 independent molecules in the unit cell; the asymmetric unit consists of 1 molecule of $[Np(Cp)_3Cl]$.

The molecular structure of **14** is presented in the Figure 2.4 and features a set of three η^5 bound Cp ligands and an apical σ-bound chloride ligand to the Np^{IV} centre. The two cyclopentadienyl rings and a chloride ligand are distorted away from the idealized C_{3v} molecular symmetry, indicating similar retention of the irregular geometry with the solid-state structure of its uranium congener,

$[U(Cp)_3Cl]$ **38**. The literature already contains lower resolution datasets for the crystal structure of **38** collected at room temperatures;[138–140] the revised studies of **38** at 103(2) K show both structures are practically superimposable with the structure of **14** obtained at 173(2) K. The corresponding root-mean-square distances of the non-hydrogen atoms in both U and Np complexes equals to RMS = 0.038 Å, which can be accounted for by the smaller ionic radii of Np^{3+} than U^{3+} (1.025 *vs.* 1.01 Å), as based on the available values for the six-coordinate ions.[141] The symmetry related distortions are frequently encountered in the whole series of the isotypic, but not necessarily isostructural, $[An(Cp)_3X]$ (An = Th, U, X = F, Cl, Br, I) complexes.

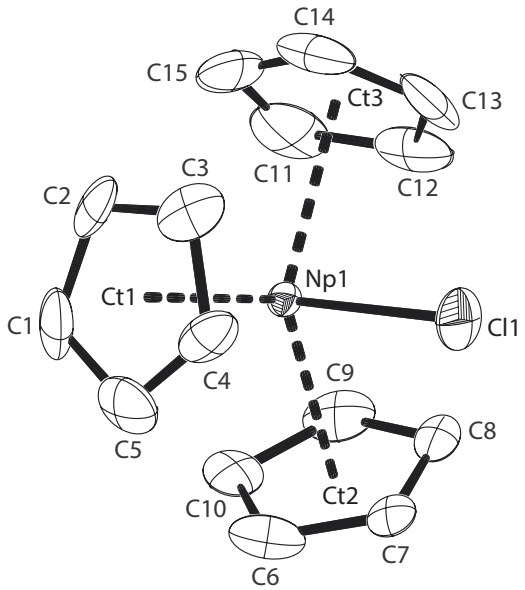

Figure 2.4. ORTEP drawing of complex **14** with thermal ellipsoids plot (50 % probability for non-H atoms). All hydrogen atoms were omitted for clarity. Selected bond lengths [Å] and angles [°] for **14**: Np1-Cl1 2.642(5), Np1-Ct1 2.433(14), Np1-Ct2 2.437(7), Np1-Ct3 2.436(4), Np1-C_{ar} 2.68(2) to 2.73(4), Ct1-Np1-Ct2 125.0(3), Ct1-Np1-Ct3 115.3(3), Ct2-Np1-Ct3 116.7(2), Ct1-Np1-Cl1 89.1(4), Ct2-Np1-Cl1 99.0(2), Ct3-Np1-Cl1 99.39(19); for the isostructural complex **38**: U1-Cl1 2.675(6), U1-Ct1 2.453(15), U1-Ct2 2.453(8), U1-Ct3 2.456(5), U1-C_{ar} 2.68(3) to 2.76(2), Ct1-U1-Ct2 125.8(4), Ct1-U1-Ct3 114.9(4), Ct2-U1-Ct3 116.9(2), Ct1-U1-Cl1 87.3(4), Ct2-U1-Cl1 99.5(3), Ct3-U1-Cl1 98.8(2).

2.5.2 Molecular structure of $[U(Cp)_3(OEt_2)]$, 39b

The large, lustrous, black single crystals of $[U(Cp)_3(OEt_2)]$ **39b** suitable for X-ray crystal structure determination were obtained from a diethyl ether solution over 6 h. The crystals were refined in the monoclinic space group $P2_1/m$ (No. 11), a = 8.1286(6), b = 13.3807(10), c = 8.3441(6) Å, β = 112.4590(10)°, with 2 molecules

in the unit cell; the asymmetric unit consists of 0.5 molecule of $[U(Cp)_3(OEt_2)]$, which lies on the mirror plane (x, ½ - y, z) perpendicular to the crystallographic *b*-axis.

The molecular structure of **39b** is presented in Figure 2.5 and contains a set of three η^5 bound Cp ligands and a σ-bound diethyl ether ligand to the U^{III} centre. The diethyl ether and two cyclopentadienyl ligands (C1-C5 and C11-C15) show positional disorder about the mirror plane which is crossing the U1 and C1 atoms; the oxygen donor atom and the C4 atom are in superposition. Not surprisingly, the comparison of the important U1–O1 bond length in the two different ethereal complexes **39a**[126] and **39b** showed significantly shorter distance of the THF adduct (2.551(10) *vs.* 2.643(6) Å), which is indicative of the higher Lewis basicity of that donor.

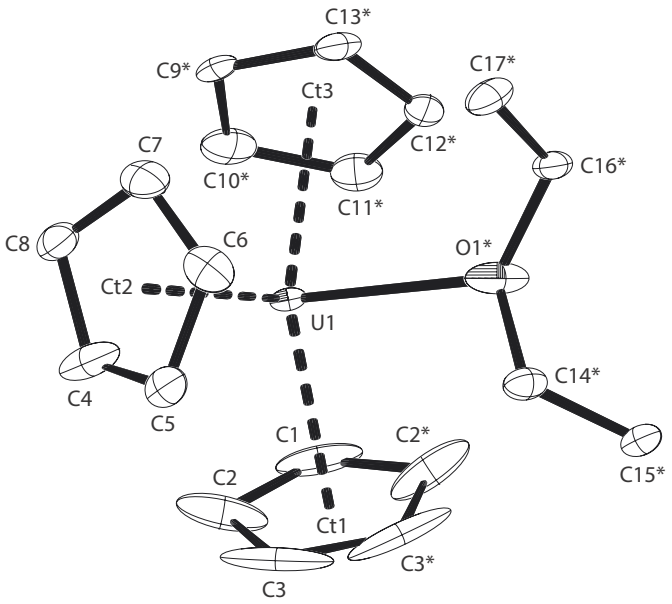

Figure 2.5. ORTEP drawing of complex **39b** with thermal ellipsoids plot (50 % probability for non-H atoms). All hydrogen atoms and complementary fragments were omitted for clarity and mirror symmetry related atom names are labelled with asterisks; selected bond lengths [Å] and angles [°]: U1-O1 2.643(6), U1-Ct1 2.545(4), U1-Ct2 2.510(5), U1-Ct3 2.532(4), U1-C_{ar} 2.643(6) to 2.831(9), Ct1-U1-Ct2 119.46(18), Ct1-U1-Ct3 116.03(12), Ct2-U1-Ct3 117.27(17), Ct1-U1-O1 99.00(17), Ct2-U1-O1 100.12(16), Ct3-U1-O1 97.91(16).

2.5.3 Molecular structure of $[Np(Cp)_3]$, 34

Dark brown, almost black single crystals of **34** suitable for X-ray crystal structure determination were obtained from a 3.5%$_{v/v}$ diethyl ether in *n*-pentane solution

for 160 h. The crystals belong to the orthorhombic space group $Pmc2_1$ (No. 26), a = 14.1208(6), b = 8.7037(6), c = 9.5917(5) Å, with four molecular units (forming two dinuclear $C_{30}H_{30}Np_2$ assemblies) in the unit cell; one molecular unit is situated in the asymmetric unit cell.

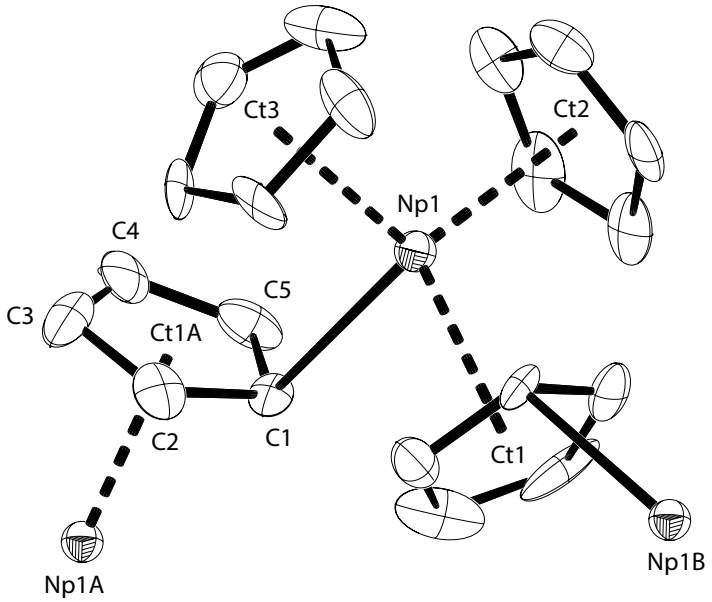

Figure 2.6. ORTEP drawing of a portion of the polymeric chain formed by **34** in the solid state with thermal ellipsoids at 50% ellipsoid probability for non-H atoms. All hydrogen atoms and complementary fragments were omitted for clarity and symmetry generated atom names are labelled with A and B. Selected bond lengths [Å] and angles [°] for **34**: Np1-C1 2.815(11), Np1-Ct1 2.587(5), Np1-Ct2 2.419(6), Np1-Ct3 2.561(10), Ct1-Np1-Ct2 112.23(19), Ct1-Np1-Ct3 113.66(19), Ct2-Np1-C3 115.1(2), Ct1-Np1-C1 94.5(3), Ct2-Np1-C1 110.7(3), Ct3-Np1-C1 108.7(2), Np1-C1-Np1A 167.5(3), ϕ(C1-Np1-Ct1∠Ct2-Np1-Ct3) 91.30(18), ϕ(C1-Np1-Ct3∠Ct1-Np1-Ct2) 82.9(2); for **39**: U1-C1 2.84(2), U1-Ct1 2.588(10), U1-Ct2 2.447(17), U1-Ct3 2.63(2), Ct1-U1-Ct2 120.9(5), Ct1-U1-Ct3 114.3(5), Ct2-U1-Ct3 114.6(4), Ct1-U1-C1 93.2(4), Ct2-U1-C1 103.5(6), Ct3-U1-C1 105.7(7), U1-C1-U1A 165.4(12), ϕ(C1-U1-Ct1∠Ct2-U1-Ct3) 92.7(6), ϕ(C1-U1-Ct3∠Ct1-U1-Ct2) 95.1(4).

The molecular structure of **34** is shown in Figure 2.6. The solid state structure comprises polymeric chains of the $[Np(Cp)_3]$ fragment formed through one in every three Cp ligands binding η^1 to one Np atom and η^5 to the next in the chain. An irregular tetrahedral geometry about the Np^{III} centre results from the coordination sphere consisting of the two η^5 bound. The coordination sphere consists of the two positionally disordered η^5 bound Cp ligands (C6-C10 and C11-C15) and two other symmetry related Cp rings bound in alternating $\eta^1(\pi)$ fashion. The distance between the Np1 atom and the carbon atoms C2 (3.266(9) Å) and C5 (3.552(10) Å) may be considered non-bonding, especially the latter.

The two alternating Cp rings that bridge Np1 with adjacent neptunium atoms Np1A and Np1B (formed by atoms C1-C5 and their symmetry generated equivalent C1B-C5B) can be approximately described as μ-η^1:η^5 bonded, with a Np1-C1 separation (2.815(11) Å) and Np1-C1-ring plane of 156.9(5)°. Therefore, a formal coordination number of CN = 10 can be assigned for the Np^{III} metal site. The Np1-C1-Np1A angle is close to 170° and emerge the zig-zag chainlike structure along cell axis *b*; the side projection of the infinite chain structure is depicted in Figure 2.7.

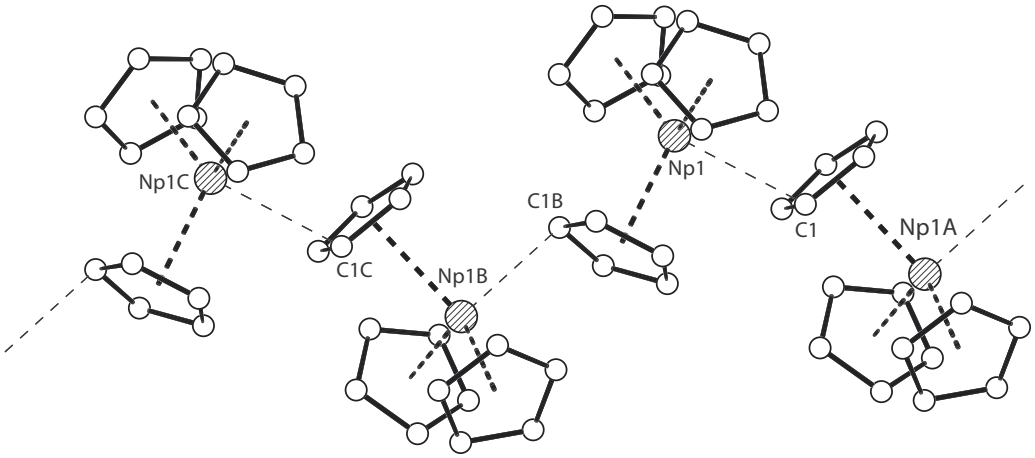

Figure 2.7. Representation of the zig-zag chain arrangement in $[Np(Cp)_3]$ **34**; symmetry generated atom names are indexed with A, B and C.

Complex **34** was found isostructural with the two known $P2_1$ crystal phases of the lanthanide congeners of the generic formula $[Ln^{III}(Cp)_3]$, where Ln = La[142] and Pr[143]. Both the reported crystal structures are of room temperature measurements and the lower resolution made the exact comparative analysis of the old datasets difficult. However, it should be noticed that a more comparable M–C1 and M–C2 separations give rise to better developed μ-η^2:η^5 bonding mode of the bridging Cp rings, which subsequently expanded the formal coordination number to CN = 11 for the Ln^{III} centres. This mirrors the less effective covalent interaction between the aromatic Cp ring system (C1-C5) and the similar radii 4f-element ions. Furthermore, this work revealed also the crystal structure of the uranium complex $[U(Cp)_3]$ **39**, which closely matches **34**, despite the larger anisotropic displacement parameters with the 100(2) K data. The corresponding root-mean-square distances of the non-hydrogen atoms in both complexes are falling in the range of RMS = 0.03(6) to 0.10(5) Å.

2.5.4 Molecular structure of [K{Np(Cp)$_4$}], 43

Intense red-brown crystals of **43** suitable for single crystal X-ray diffraction analysis were grown from a diethyl ether solution over the period of *ca.* 100 h. The crystals belong to the monoclinic space group *C*2 (No. 5), a = 22.6093(10), b = 14.7125(10), c = 9.0155(5) Å and β = 90.4150(10)°, with 4 'ate'-complex molecules in the unit cell. The asymmetric unit consists of 1.5 molecules of [K{Np(Cp)$_4$}] (one full unit of **43-A** and a half of **43-B**, *vide infra*) in addition to 0.5 molecule of badly disordered diethyl ether molecule residing on the crystallographic C_2 axis.

Complex **43** forms a three-dimensional framework interconnected with the K-Cp bonds in the solid state and consists of double molecular arrangement of the formally two **43-A** and **43-B** chainlike substructures, which are both situated along the crystallographic *c*-axis. Interestingly, the coordination environment around the Np^{III} ion in the molecular structure of K[Np(η^5-Cp)$_3$(η^1-Cp)] **43-A** builds upon that of the parent complex **34**, but is subject to geometrical stabilization of the repeat units due to potassium (instead of neptunium) neighbouring ions. This results in shortening of the respective distances between the Np1 centres and carbon atom donors in **43-A** *vs.* **34** (*cf.* Figures 8 and 11a). Furthermore, the Np1-C1(C20)-ring plane angle changes from 157.4(4) to 149.8(3) ° in **43-A**. The latter value correlates well with the linearization of the zig-zag alignment of **34** and the subsequent formation of the formal 2D layered structure through an additional side bridging of the **43-A** chains with K2 atoms (Figure 11). The distances between the K2 atom and the three Cp rings fall in the range of 2.976(7) to 3.254(17) Å; these are separations typically observed for the ionic potassium complexes containing π-aromatic five-membered carbocyclic ligands. The second tetrakis-cyclopentadienyl fragment, K[Np(η^5-Cp)$_4$] **43-B**, displays a more traditional η^5 binding of all the Cp ligands arranged in an irregular tetrahedral fashion around the Np^{III} centre. The average separation between the Np atoms and the η^5-Cp ring centroids in both the **43-A** and **43-B** units is slightly longer for a more sterically encumbered **43-B** system (2.638(6) *vs.* 2.507(5) Å). The four Cp ligands fall into two groups, where the rings formed by atoms C21-C25 and their symmetry generated equivalents are η^5 bounded to the K1 centres (3.013(5) Å), forming an infinite chain structure. The second group of the Cp ligands (C26-C30) is η^5 bounded to the K2 atoms of the **43-A**, interconnecting the two paralleled **43-A** chains, which belong to two different formal sheets. The resulting extended

structure is complemented by the interaction of the K1 atoms and the neighbouring Cp rings (formed by atoms C11-C15 of **43-A)**, giving the overall backbone structure of complex **43** (Figure 13), which additionally hosts lose diethyl ether molecules in presented channels.

The preferred binding mode for the cyclopentadienyl complexes of the actinide ions is η^5, with only one structurally characterized uranium complex containing lower hapticity published in 2016; the anionic complex [K(2.2.2-cryptand)][U(Cp')$_4$] **44**.[95] The reported bonding parameters of the coordination sphere around the U^{III} centre correlate very well with that of the analogous structural unit in the **43-A** substructure. The An–C(η^1-Cp) bond distances of both the An^{III} complexes (2.776(2) *vs.* 2.752(7) Å) show slight shortening of the corresponding Np scaffold, which is consistent with the lowering ionic radius of the metal site, as accordingly to the available data for a six-coordinate U^{3+} (1.025 Å) and Np^{3+} (1.01 Å) ions.[141]

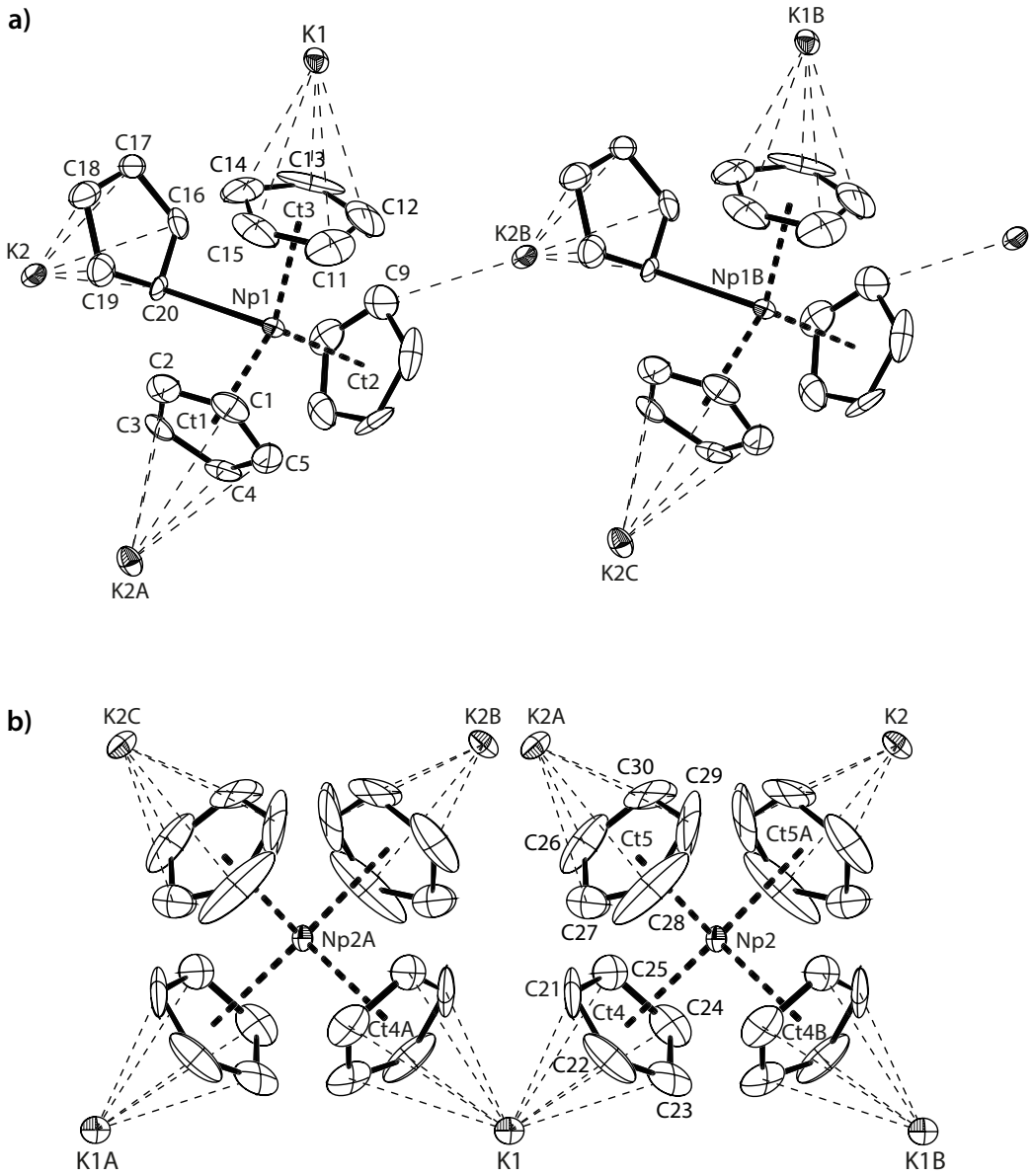

Figure 2.8. ORTEP drawing of a portion of the chain structures of K[Np(η^5-Cp)$_3$(η^1-Cp)] **43-A** (a) and K[Np(η^5-Cp)$_4$] **43-B** (b) with thermal ellipsoids at 50% probability for non-H atoms. All hydrogen atoms and lattice solvent molecules were omitted for clarity and symmetry generated atom names are indexed with A, B and C. Selected bond lengths [Å] and angles [°]; Np1-C20 2.752(7), Np1-Ct1 2.527(4), Np1-Ct2 2.516(4), Np1-Ct3 2.493(6), Np1-C_{ar} 2.732(13) to 2.842(9), K1-Ct3 3.067(6), K2-C9 3.197(10), K2-C16 3.049(8), K2-C17 3.136(9), K2-C18 3.121(7), K2-C19 3.022(9), K2-C20 2.976(7), K2A-Ct1 3.003(5), Ct1-Np1-Ct2 115.50(13), Ct1-Np1-Ct3 118.92(16), Ct2-Np1-Ct3 117.19(17), Ct1-Np1-C20 96.53(16), Ct2-Np1-C20 99.01(17), Ct3-Np1-C20 103.51(19), Np2-Ct4 2.631(5), Np2-Ct5 2.645(7), Np2-C_{ar} range 2.835(12) to 2.955(9), K1-Ct4 3.013(5), K2-Ct5A 2.884(7), Ct4-Np2-Ct5 109.2(2), Ct4-Np2-Ct4B 109.6(2), Ct4-Np2-Ct5A 110.5(2), Ct5-Np2-Ct5A 107.9(3), Ct4-K1-Ct4A 104.67(19), ϕ(Ct4-Np2-Ct5∠Ct4B-Np2-Ct5A) 88.7(2), ϕ(Ct4-Np2-Ct4B∠Ct5-Np2-Ct5A) 90.9(3).

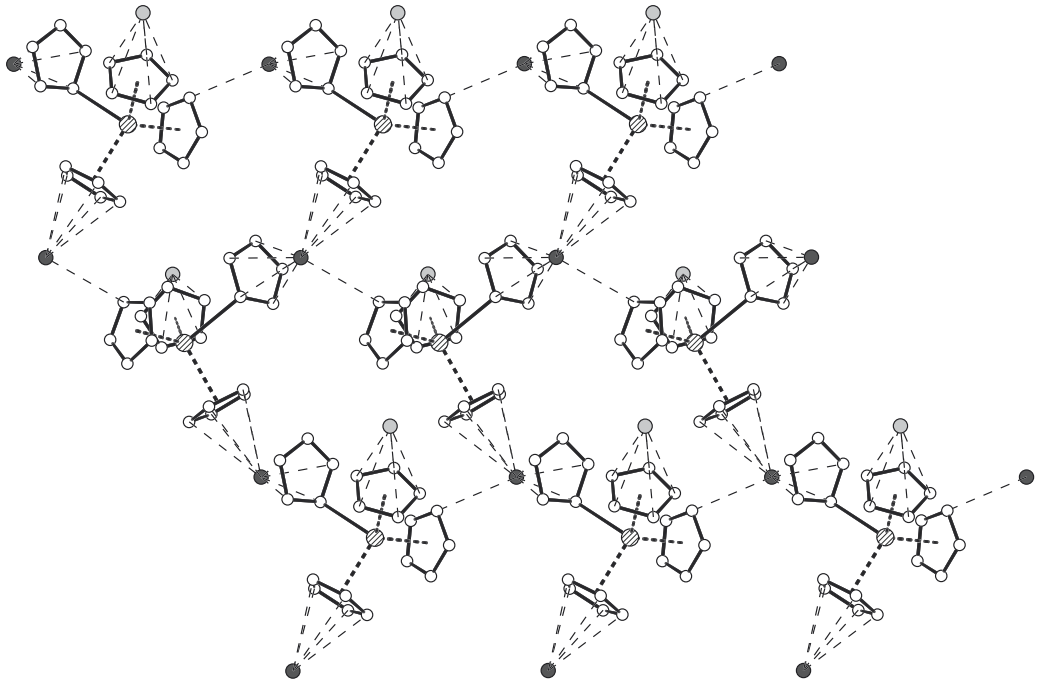

Figure 2.9. Representation of the 2D-sheet structure in K[Np(η^5-Cp)$_3$(η^1-Cp)] **43-A** formed by the formal bridging of the infinite chains of the [Np^{III}(η^5-Cp)$_3$(η^1-Cp)] units by K2 atoms; C (white), K1 (light grey), K2 (dark grey), Np1 (filled with lines).

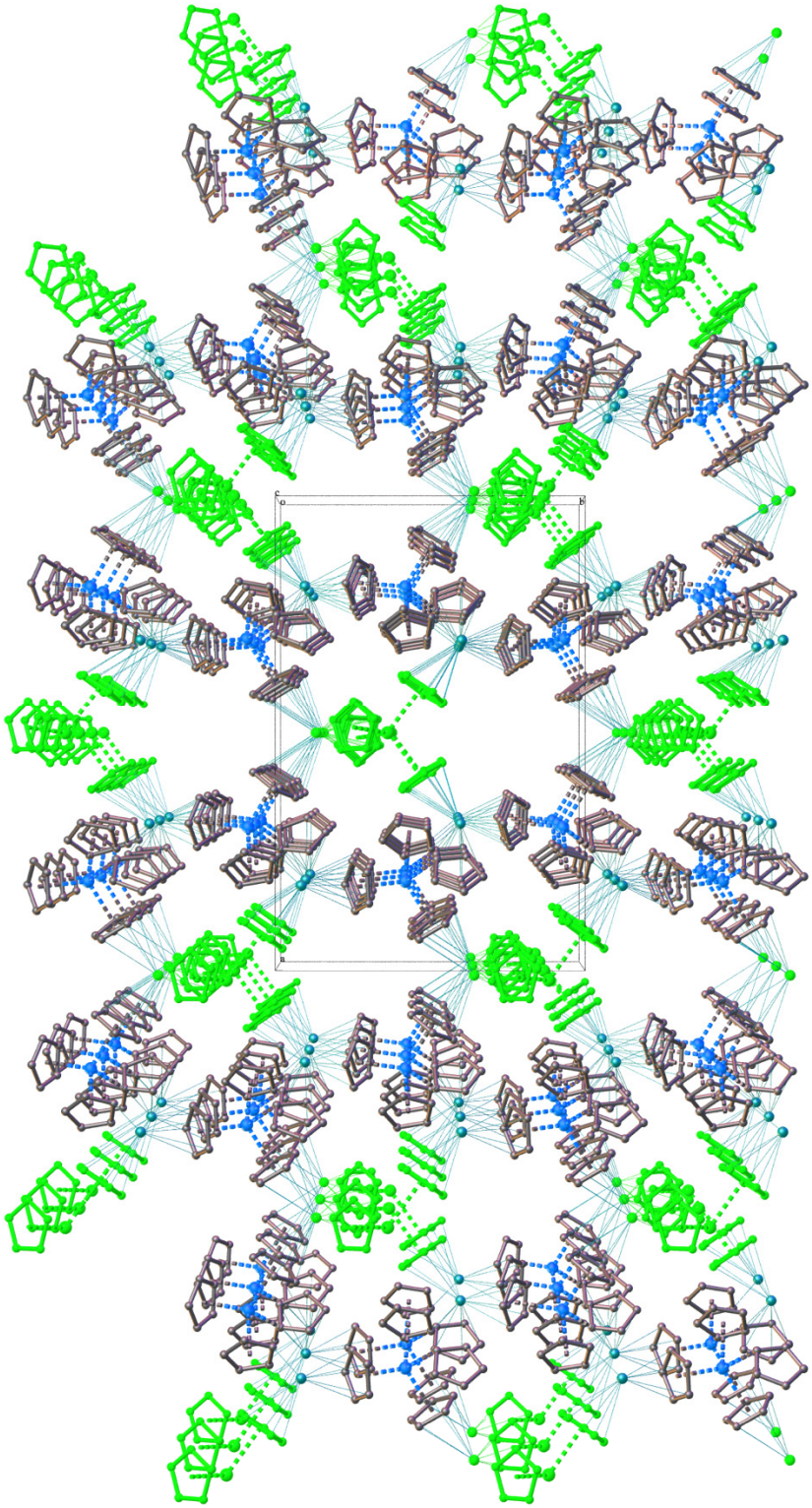

Figure 2.10. Representation of the crystal packing showing the channel structure of [K{Np(Cp)$_4$}] **43** down the *c*-axis. All hydrogen atoms and lattice solvent molecules were omitted for clarity. The K[Np(η^5-Cp)$_4$] **43-B** substructure was coloured green for emphasis; Np (blue), K (turquoise) and C (grey).

2.5.5 Molecular structure of [Np(Cp')$_3$], 40

The shiny, olive-green crystals of [Np(Cp')$_3$] **40** suitable for single crystal X-ray diffraction analysis were obtained on the flash vacuum evaporation of a *n*-pentane solution of **40**, with subsequent cooling to ca. -20 °C. The crystals were refined in the orthorhombic space group *Pbca* (No. 61), a = 8.2980(6), b = 22.1664(17), c = 28.917(2) Å, with 8 independent molecules in the unit cell; the asymmetric unit consists of a single molecule of [Np(Cp')$_3$].

The molecular structure of **40** is shown in Figure 2.11 and consists of the mononuclear Np^{III} complex containing three η^5 bound Cp' ligands, with all the Ct(η^5-Cp')-Np-Ct(η^5-Cp') angles close to 120° and the average Np-Ct(η^5-Cp') distance of 2.482(3) Å.

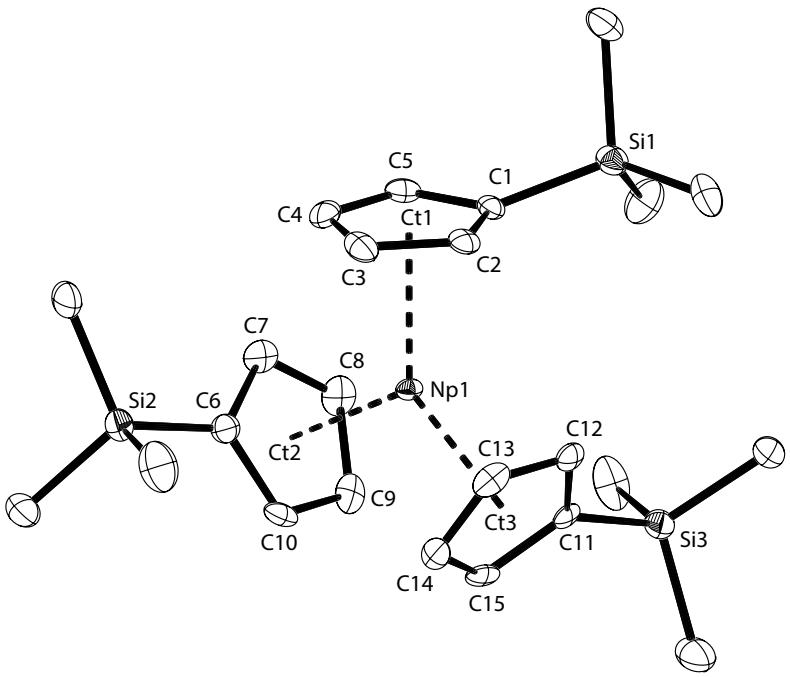

Figure 2.11. ORTEP drawing of [Np(Cp')$_3$] **40** with thermal ellipsoids plot (50% probability for non-H atoms). All hydrogen atoms were omitted for clarity; selected bond lengths [Å] and angles [°]: Np1-Ct1 2.485(2), Np1-Ct2 2.481(2), Np1-Ct3 2.479(2), Np1-C$_{ar}$ 2.734(6) to 2.786(4), Si1-(C1-C5) plane -0.382(8), Si2-(C6-C10) plane -0.109(8), Si3-(C11-C15) plane -0.169(8), Ct1-Np1-Ct2 119.86(8), Ct1-Np1-Ct3 120.46(7), Ct2-Np1-Ct3 119.06(8).

The Np1 atom lies in plane of the Cp ring centroids with only minor out-of-plane distortion (0.1133(13) Å), which is nearly identical with that of the theoretical plane centroid (0.1137(13) Å). Therefore, the molecular geometry about the central

Np atom closely matches a trigonal planar (D_{3h}) geometry and is isostructural with the previously reported uranium complex [U(Cp')$_3$] **45**.[144] Although the imprecision in the older dataset collected at room temperatures makes detailed analysis difficult, the average distances for the An–C separations (2.78(4) *vs.* 2.76(3) Å) and An-Ct(η^5-Cp') (2.51(3) *vs.* 2.482(3)) can be attributed to the actinide contraction effects.

2.6 Concluding Remarks

As anticipated prior to the experiments, the structural organoneptunium chemistry has many similarities with that of the uranium and the differences mainly being caused by the less negative reduction potential of the Np^{4+} ion. This work finds this property practical to the actinide molecular design by exploiting the oxidative coupling reactions of the electron rich π-substrates with Np^{IV} precursors to promise potentially unique Np^{III}–L complexes, which could be isolated without the use of any obvious or additional reducing agents. One such an example is the overlooked reactivity of the complex [Np(Cp)$_3$Cl] **14** with excess KCp, which results in the isolation of the first actinide(III) tetrakis-cyclopentadienyl complex, **43** under the synthetic conditions typically associated with the synthesis of the neutral complex [Np(Cp)$_4$] **17**. Remarkably, the solid-state structure of the [K{Np(Cp)$_4$}] **43** compound exhibits intracrystalline dimorphism, as the two chainlike components of a different binding modes of the one Cp ligand (η^1 for **43-A** *vs.* η^5 for **43-B**) combine to form the extended crystal lattice of **43.** Unexpectedly, this structure correlates well with the Mössbauer studies by Adrian, who reported two similar, but unidentified impurities present in samples of **17**. We now propose this is due to spontaneous reduction of Np^{IV} centre which fits the two-component structure of **43**.

Complexes [Np(Cp)$_3$] **34** and [Np(Cp')$_3$] **40** were synthesized reproducibly in useful quantities using a more traditional reduction and salt metathesis reactions. However, the attempts to employ KC_8 and TlCp reagents gave rise to unexpected reactivity. For the first time the solution based method for the quantitative *in situ* reduction of $NpCl_4$ **4** to an ill-defined, greenish precipitate of the formal equivalent of $NpCl_3$ **3** was demonstrated and the microcrystalline product exhibits substantial reactivity towards Cp transfer reagents, even in the absence of strongly coordinating solvents. In a reaction of **3** with the often more stable and mildly

reducing TlCp in place of the more commonly employed alkali metal cyclopentadienyl compounds the expected complex **34** reverts into the thermodynamically preferred **14**, which is due to the redox potential accessible electron scavenging Tl(Hg)|TlCl system.

In the quest for the neptunium analogue of the milestone U^{II} compound [K(2.2.2-cryptand)][$U(Cp')_3$] **46**, a similar reactivity was observed, although the reaction with the perfluoropolyalkylether oil in addition to the radiological concerns precluded mounting of the putative Np^{II} crystals on the diffractometer head at low temperatures. The investigated material showed insufficient crystal quality for the structure solution and further analyses. More recently, the greater thermal stability of the isotypic U^{II} and Th^{II} complexes was achieved by introducing the additional steric protection of the 1,3-bis(trimethylsilyl)cyclopentadienyl ligands, thus modifying the current scientific objective of the paralleled transuranic research.

3 Oxo-Functionalised Neptunium Cyclopentadienyl Complexes

Preamble

The studies of electronic communication in hetero(bimetallic) An(IV)-U(V) complexes An = (U-Pu), mediated by the uranyl oxo group were established concurrently with the fellow PhD research student Markus Zegke in the Arnold group (University of Edinburgh).[145] The subsection 3.3 note individual contribution to the project.

All molecular magnetism results presented in this chapter were obtained in collaboration with Drs Eric Colineau and Jean-Christophe Griveau who carried out the static and dynamic magnetisation studies at the Actinide Research Unit (E06) of the EC-JRC ITU, led by Prof. Dr Roberto G. M. Caciuffo. Dr Nicola Magnani (ITU) performed the corresponding data analysis and interpretation.

3.1 Introduction

The studies in oxo-binding and reactivity of the $[An(Cp)_3]$ complexes divide into two separate parts in this chapter. The first part is concerned with an aerobic oxidation of both the $[An(Cp)_3]$ (An = U **39**, Np **34**) complexes (*cf.* Chapter 2.3.1), whilst the second describes a systematic study on the ability of the $An^{III}(Cp)_3$ (An = U-Pu) complexes to reductively functionalize the *exo*-oxo group of the uranyl(VI) dication in $[(UO_2)(THF)(H_2L)]$, where $(H_2L)^{2-}$ is the doubly-deprotonated Schiff-base calix[4]pyrrole macrocycle. Furthermore, the structural characterization of the resulting model complexes is complemented by d.c. and a.c. magnetometry studies which provide an additional insight into the electronic configuration of the constituent actinide ions and any magnetic communication through the bridging oxo group.

The magnetic interactions between the metal centres can originate from a superexchange coupling through the oxo atom; this mechanism has been shown capable of reaching appreciable magnitudes. In the field of actinide-based molecular magnetism the reported polynuclear systems are dominated by those of actinyl ions, with the most prevalent based on the uranyl(V) monocation, $[UO_2]^+$ ($5f^1$, $^2F_{5/2}$).[36,146,147] For the lower oxidation state actinide oxo bridged complexes showing a clear maximum in the temperature-dependent magnetic susceptibility curves are limited to $[\{((^{t\text{-Bu}}ArO)_3tacn)U\}_2(\mu\text{-}O)]$ **47**,[148] $((^{t\text{-Bu}}ArO)_3tacn)H_3$ = 1,4,7-tris(3,5-di-*tert*-butyl-2-hydroxybenzyl)-1,4,7-triazacyclononane), Figure 3.1. The crystal field symmetry of complex **47** seems unique in supporting

antiferromagnetic communication between two U^{IV} ions, while the molecular geometry of other congeneric oxo bridged complexes is substantially different and thus precludes further analyses.[148]

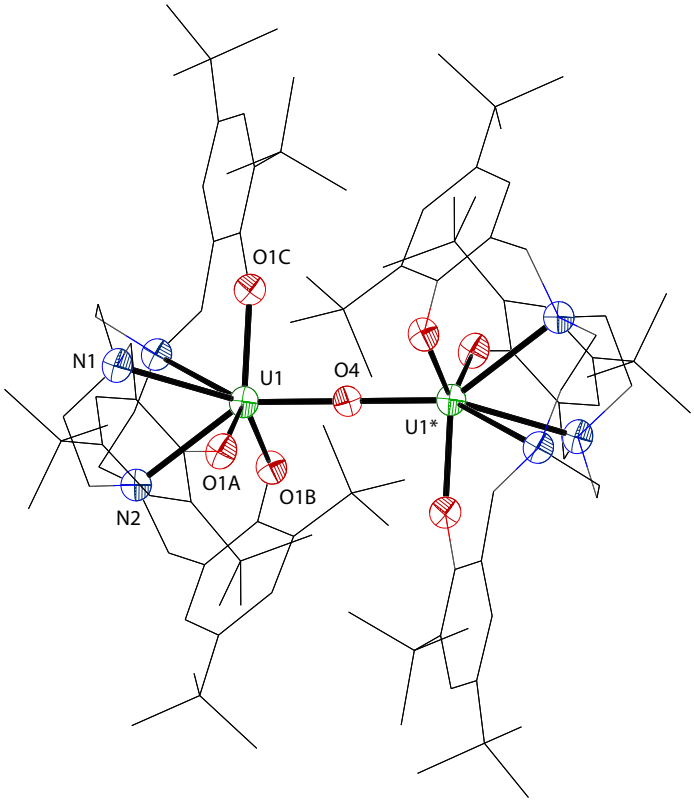

Figure 3.1 Molecular structure of [{((($^{t\text{-Bu}}$ArO)$_3$tacn)U}$_2$(μ-O)] **47**, Thermal ellipsoids are drawn at 50 % ellipsoid probability and hydrogen atoms and lattice solvent molecules are omitted for clarity. The crystallographic data was obtained from the Cambridge Structural Database (refcode: *AHAJUO*).

In fact, the systematic studies that enable scaling of the microscopic exchange constants for the An-(μ-O)-An bridges remain fundamentally unexplored and require the isostructural series of lower oxidation state actinide complexes, preferably of the single oxo-bridging ligand. This is perhaps due to the absence of suitable complexes of the higher spin-state Kramers ion Np^{IV} ($5f^3$, $^4I_{9/2}$), which is much less common than those of the abundant but often magnetically uninteresting U^{IV} ($5f^2$, $^3H_4$). Organometallic derivatives of the latter ions with oxo ligands are amongst the best existing (U) and potential (Np) molecular models, showing comparable chemical behaviour and binding to other ligands directionality of the remarkably robust $[An^{IV}(Cp)_3]^+$ (An = U, Np) cationic entities (*cf.* Chapter 1.3.4.1).

Organometallic uranium oxo complexes have been known in the literature since 1991.[149] Three distinct core structures $\{U_2O\}^{6+}$,[149–151] $\{U_2O_2\}^{4+}$[152] and $\{U_3O_3\}^{6+}$[150] have been identified to date and their formation depends on the organouranium precursor and synthetic route used. The resulting μ-oxo ligands derive from H_2O, O_2, N_2O and CO_2 small molecule activation by the U(III) complexes or by the hydrolytic cleavage of $[U(Cp)_4]$ **17** as shown in Scheme 3.1. The simplest and thermodynamically favoured complex $(\mu\text{-}O)[U(Cp)_3]_2$ **54** can be synthesized from each of the procedures listed.

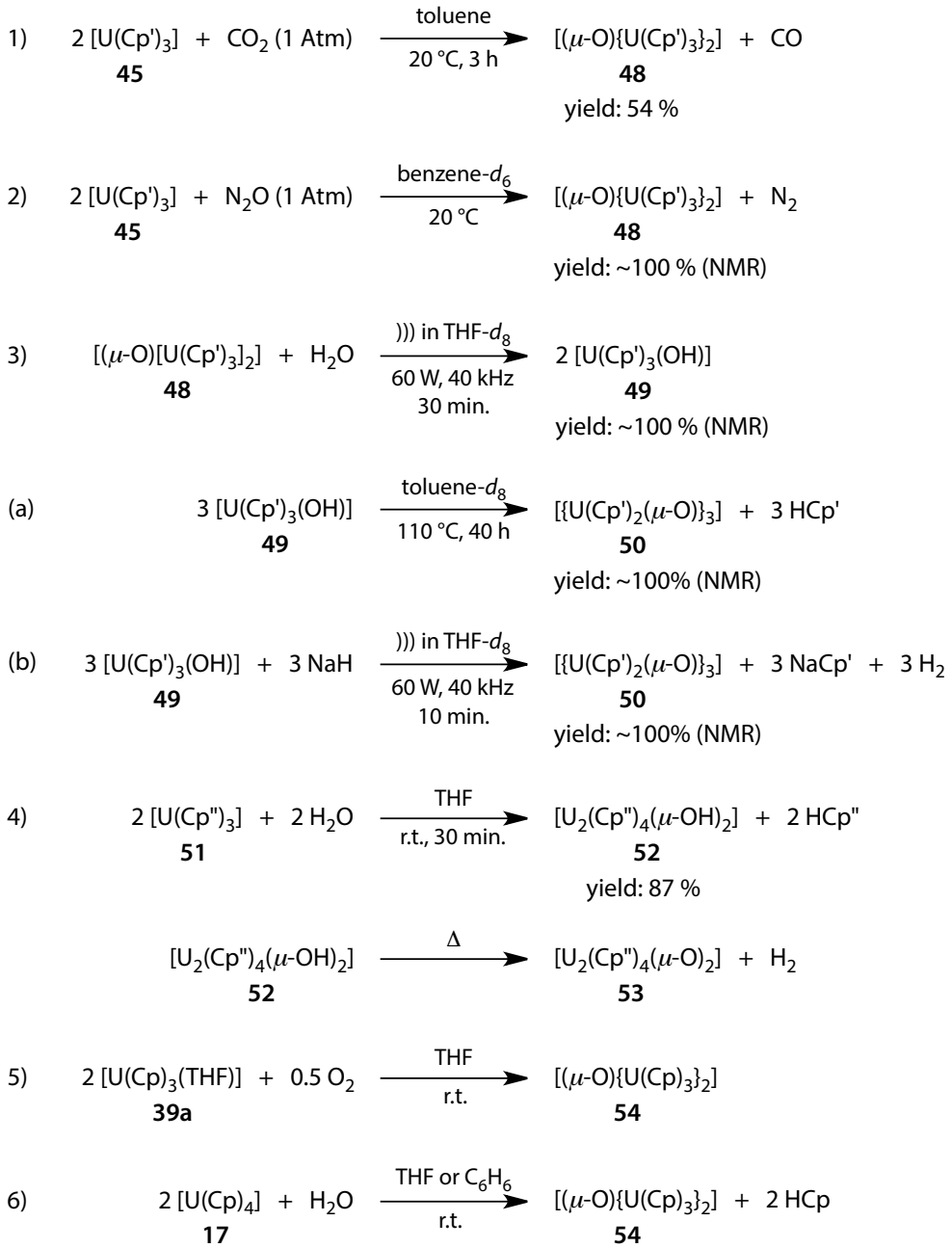

Scheme 3.1. Syntheses of the oxo-bridged uranium(IV) cyclopentadienyl complexes.[149–152]

The formation of mixed valent uranium(IV)-uranyl(V) intermediate was first evidenced by Berthet *et al.*[153] as a result of the prior-reduction step of the $[UO_2X_2]$ precursors with uranocene, $[U(COT)_2]$, which involves one-electron reductive capacity of the COT^{2-} ligand, rather than U^{IV} centre. Furthermore, Mazzanti and co-workers[154] reported the first structurally characterized uranium(IV)-uranyl(V) oxide clusters stabilized by the doubly-deprotonated *N,N'*-(2-aminomethyl)-

diethylenebis(salicyl-imine), mesaldienH_2, and a more sterically encumbered *N,N'*-phenylene-bis-(3,5-di-tert-butylsalicydene-imine), salophen-^{t}Bu$_2$H$_2$ ligands; the molecular structures contain the linear {[UO_2(mesaldien)-(U(mesaldien))]$_2$(μ-O)} **55**, Figure 3.2.a. and the quasi-planar {[UO_2(salen)][U(salophen-^{t}Bu$_2$)]$_2$[U(salen)]$_2$(μ-O)$_3$(μ$_3$-O)]} **56**, Figure 3.2.b. Remarkably, polynuclear complexes **55** and **56** result from the partial disproportionation of an otherwise stable uranyl(V) precursors in reactions with U^{IV} salts.

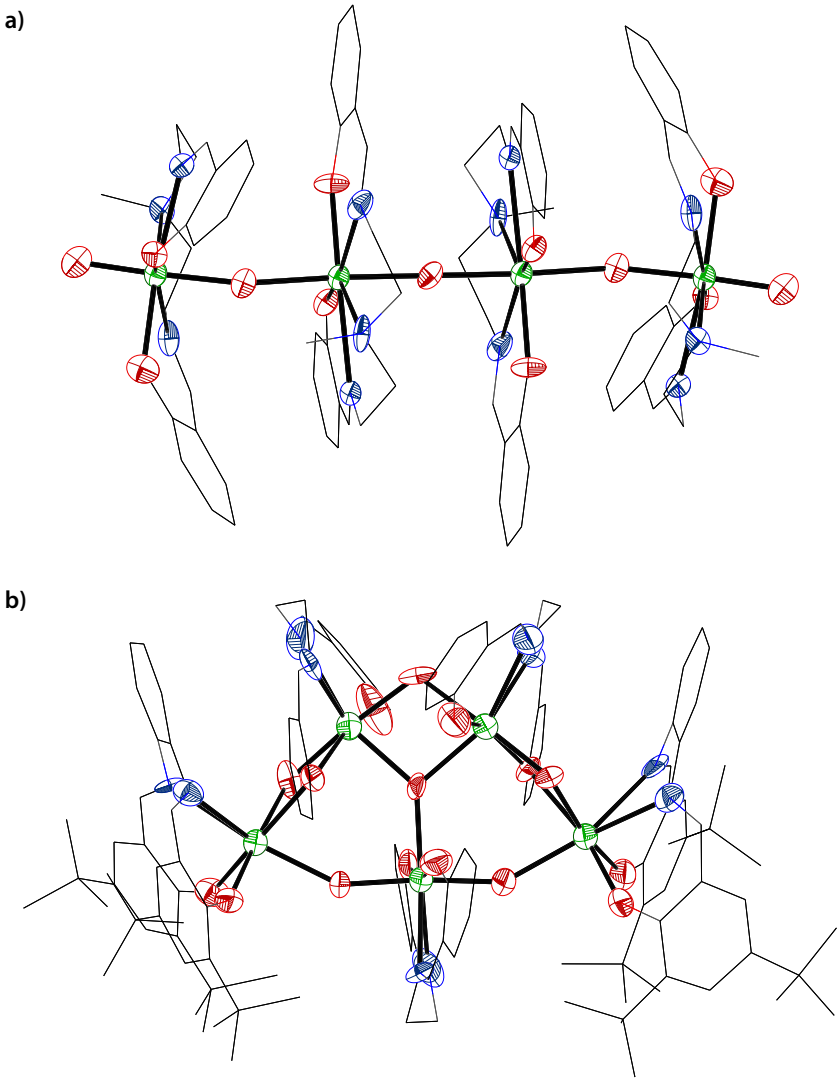

Figure 3.2 Molecular structures of {[UO_2(mesaldien)-(U(mesaldien))]$_2$(μ-O)} **55** (a), side-on view and {[UO_2(salen)][U(salophen-^{t}Bu$_2$)]$_2$[U(salen)]$_2$(μ-O)$_3$(μ$_3$-O)]} **56** (b), view down the *b*-axis. Thermal ellipsoids are drawn at 50 % ellipsoid probability and hydrogen atoms and lattice solvent molecules are omitted for clarity; U (green), O (red), N (blue), C (grey). The crystallographic data was obtained from the Cambridge Structural Database (refcode: *XALLON* and *XALMAA*).

3.2 Part I: Oxo-Bridged Di- and Trinuclear Neptunium(IV) Complexes

3.2.1 Reactivity of [$NpCp_3$] with air to make organoneptunium oxides

Building on the newly developed routes to the isostructural [$An^{III}(Cp)_3$], An = U, Np, complexes (*cf.* Chapter 2.3.1), the aerobic oxidation of [$Np(Cp)_3$] with air was studied as a route to molecular Np^{IV} oxo complexes. This approach proved rewarding as not only the expected dinuclear complex [(μ-O){$Np(Cp)_3$}$_2$] **58**, but also the unprecedented trinuclear μ-oxo bridged system [{$(Cp)_3Np(\mu\text{-}O)$}$_2${$Np(Cp)_2$}] **57** could be obtained (Scheme 3.2). Complex **58** is structurally very similar to previously authenticated uranium analogue **54**,[151] although it crystallizes in the non-centrosymmetric system due to the slightly distorted bimetallic bridge angle and polarized individual Np-O bond distances (cf. Chapter 3.2.3). The Gouy balance magnetic susceptibility measurements for **54** show both the low magnetic moment (μ_{eff} = 2.17 μ_B at 293 K) and any clear sign of the temperature-independent paramagnetism down to 4.2 K, which in addition to slight field-dependence of the susceptibility product at liquid helium temperatures was proposed to build in a weak U-U magnetic interaction. These studies were revisited in this work by using modern SQUID magnetometry but work on the detailed analyses of interactions is now in progress.

When slow diffusion of atmospheric gases into the THF or MeCN solution of [$Np(Cp)_3$] was employed, an unanticipated side reaction occurred, resulting in a formal elimination of the cyclopentadienyl radical and leading to the trinuclear complex [{$(Cp)_3Np(\mu\text{-}O)$}$_2${$Np(Cp)_2$}] **57**, which has a bent molecular geometry (approx. C_{2v}) across the An-O-An-O-An core which has yet to be observed in other *f*-block cyclopentadienyl chemistry. On the other hand, the same reaction performed in toluene or hexane solvent resulted in the expected [(μ-O){$Np(Cp)_3$}$_2$] **58** arrangement, analogous to the oxo-diactinide units found in U(IV) (**47** and **54**) and Th(IV)[135] chemistry. Interestingly, a rapid introduction of air into the solution of the starting material **34** leads to the exclusive formation of complex **58** in either solvent system.

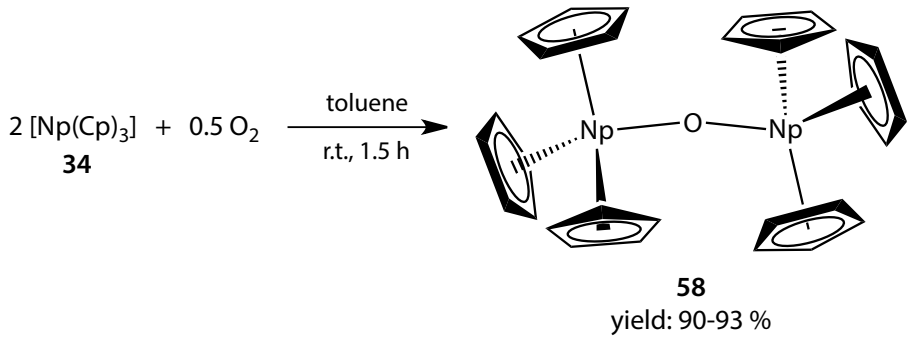

58
yield: 90-93 %

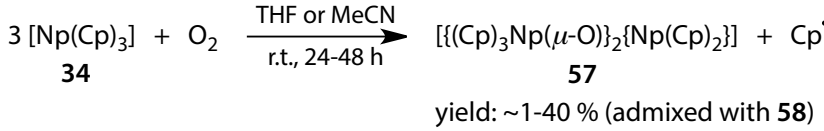

yield: ~1-40 % (admixed with **58**)

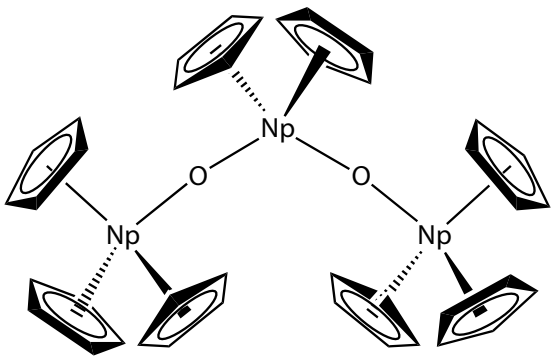

57

Scheme 3.2. Synthesis of μ-oxo bridged neptunium(IV) complexes $[\{(Cp)_3Np(\mu\text{-}O)\}_2\{Np(Cp)_2\}]$ **57** and $[(\mu\text{-}O)\{Np(Cp)_3\}_2]$ **58** starting from $[Np(Cp)_3]$ **34** and air; reactions in polar solvents are diffusion controlled.

Although the protonation mechanism required for the formation of the C_{2v}-symmetric $\{(Cp)_2Np\}^{2+}$ fragment in **57** is far from clear, the reactive hydroxo complex intermediate could be postulated. One may assume that traces of water act as a protonating agent at the Np^{III} centre in complex **34** and forms the reactive intermediate $\{(Cp)_2NpOH\}$, which is prone to subsequent dimerization and potential 1,2-hydride shift to one of the Np centres (Scheme 3.3). The latter event seems key in rationalizing the formation of **57** and is further supported by the excellent mechanistic work of Andersen *et al.*[152], who used similar but sterically congested uranium complexes to observe dihydrogen gas evolution from **52** (*cf.* Scheme 3.1.4). Unfortunately, the coordinatively unsaturated Np^{IV} and in particular

Np^{III} species are both susceptible to radical attack with dioxygen, which makes further mechanism proposal difficult.

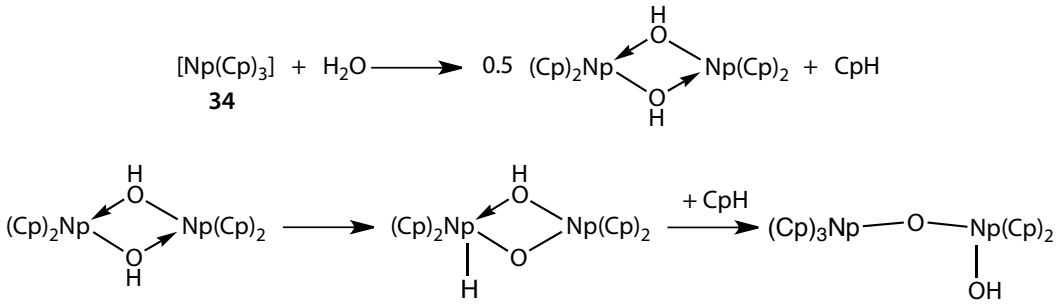

Scheme 3.3. Proposed acid-base reactions of $[Np^{III}(Cp)_3]$ **34** with water to produce $\{(Cp)_2Np^{IV}O_2\}^{2-}$ structural unit.

One may assume that traces of water act as a protonating agent at the Np^{III} centre in complex **34** and forms the reactive intermediate $\{(Cp)_2NpOH\}$, which is prone to subsequent dimerization and potential 1,2-hydride shift to one of the Np centres (Scheme 3.3). The latter event seems key in rationalizing the formation of **57** and is further supported by the excellent mechanistic work of Andersen *et al.*[152], who used similar but sterically congested uranium complexes to observe dihydrogen gas evolution from **52** (*cf.* Scheme 3.1.4). Unfortunately, the coordinatively unsaturated Np^{IV} and in particular Np^{III} species are both susceptible to radical attack with dioxygen, which makes further mechanism proposal difficult.

No separate studies have been performed to examine the reactivity of **34** with water or other potential protic impurities from the reaction systems. The use of air as an oxidant gave only mixtures containing microcrystalline forms of both the oxide complexes **57** and **58**; the product ratio was inspected visually using microscopy of the batches of solid-phases suspended in perfluoropolyalkyl ether oil. The resulting product ratio falls into a broad range from approximately 1 to 40 specimens / 100 (uncorrelated data), which seems to vastly limit the preparative utility of this method and further analyses of complex **57**.

Control experiments were designed to compare the aerobic oxidation process of **34** to **57** in THF solvent with the isostructural uranium complex $[U(Cp)_3]$, **39,** Scheme 3.1.5. These gave exclusively the well-known, microcrystalline complex $[(\mu\text{-}O)\{U(Cp)_3\}_2]$ **54**, regardless of the strictly paralleled amounts and concentrations of the reactants used (for details see Chapter 5.4).

The ^{1}H NMR spectrum of **58** in THF-d_8 contains only one broad resonance for the Cp rings at δ_H = -18.35 ppm (linewidth 13.45 Hz), suggestive of the retention of the molecular structure in solution as in the solid-state. Due to very low solubility of the **58** in THF at room temperature the UV-Vis-NIR spectra do not contain any absorption bands with intensities visible above background using the optical chamber contained in the radiological glove-box; the extremely low solubility of complex **54** precluded both the comparative spectroscopy studies in a solution. ATR analysis of solid samples of both **58** and **54** complexes showed very similar skeletal vibrations of the Cp rings, with the An-O-An asymmetrical stretching frequency identified at 599 and 586 cm^{-1} for **58** and **54**, respectively. The net vibrational frequency difference of this band for both U and Np complexes is higher than that of the characteristic absorption bands for the aromatic five membered rings (13 *vs. ca.* 3 - 4 cm^{-1}), which can be explained by the lowered molecular symmetry of the $\{Np_2O\}^{6+}$ core and the presence of different Np-O bond distances in the solid-state structure (*cf.* Chapter 3.2.3). Furthermore, bands assignments were confirmed using ^{18}O isotopically enriched complex $[(\mu\text{-}[^{18}O]O)\{U(Cp)_3\}_2]$ which allowed us not only to observe the expected downshift value of $\nu(U\text{-}^{18}O\text{-}U)$ = 556 cm^{-1} for $[^{18}O]^{16}O$ labelled derivative, but also a new shoulder at *ca.* 716 cm^{-1} to one of the bending vibration related to Cp ring system with the maximum at 765 cm^{-1}; the origin of the shift remains unclear.

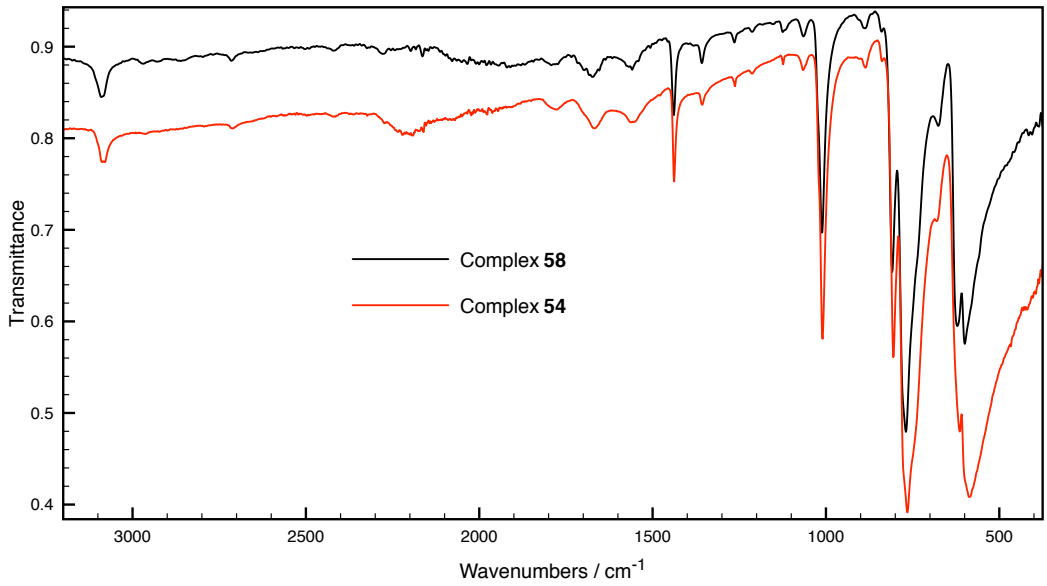

Figure 3.3. ATR spectra of complexes [(μ-O){U(Cp)$_3$}$_2$] **54** (red trace) and [(μ-O){Np(Cp)$_3$}$_2$] **58** (black trace) measured using diamond ATR; the abundance ratio was constant for these measurements and reproducibility checked using multiple measurements of the peak-height ratio between the bands maxima near 1439 and 769 cm^{-1} and that at 1011 cm^{-1}.

3.2.2 Molecular structure of [{(Cp)$_3$Np(*μ*-O)}$_2${Np(Cp)$_2$}], 57

Needle-like, red single crystals of **57** suitable for X-ray crystal structure determination were obtained from layering of a THF solution of **57** with *n*-hexane over 16 h. The diffraction data were refined in the monoclinic space group $P2_1/n$ (No. 14), a = 8.3917(4), b = 27.6278(12), c = 14.6608(6) Å, β = 90.7120(10)°, with 4 independent molecules in the unit cell; the asymmetric unit consists of a single molecule of [{(Cp)$_3$Np(μ-O)}$_2${Np(Cp)$_2$}] **57**.

The solid-state structure of **57** is composed of discrete trinuclear [{(Cp)$_3$Np(μ-O)}$_2${Np(Cp)$_2$}] molecules (Figure 3.4) of the gross molecular configuration that results from the central Np(η^5-Cp)$_2$(μ-O)$_2$ fragment, which adopts a *pseudo*-tetrahedral, C_{2v} coordination environment about the central Np^{IV} ion. The other two units are approx. C_3-symmetric Np(η^5-Cp)$_3$ groups, in which each Np^{IV} centre is apically σ-bonded to the single oxygen atom. Both doubly bridging oxo ligands maintain the planar {Np$_3$O$_2$}$^{8+}$ core geometry (within 0.093(4) and 0.024(4) Å for O1 and O2, respectively); in each case, the bridging oxo moieties are close to linear (Np-O-Np = 172.8(2) and 174.1(2) °). Perhaps, the most important structural parameter in **57** is the short mean Np-O(μ-oxo) distance of 2.085(9) Å,

which is significantly shorter than the Np-O(phenolato) bond length in [Np(Cp)$_3$(OPh)] **29** (2.136(7) Å) and remarkably similar to that of the linear μ-oxo diuranium complexes **47** and **54** (2.1095(4) and 2.0925(4) Å, respectively), suggesting the appreciable An-O π-bonding character in **57**. This is further supported by the presence in the structure of the 'bent-sandwich' An(Cp)$_2$X$_2$ geometry around the Np1 atom, which is stabilized electronically against ready ligand redistribution rather than by the increased steric congestion.

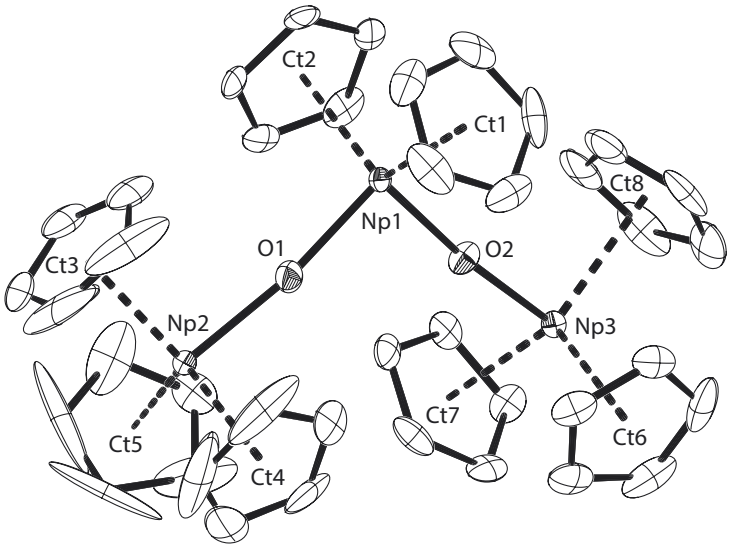

Figure 3.4. ORTEP drawing of complex **57** with thermal ellipsoids plot (50 % probability for non-H atoms). All hydrogen atoms were omitted for clarity; selected bond lengths [Å] and angles [°]: Np1-Ct1 2.469(4), Np1-Ct2 2.471(3), Np1-O1 2.076(4), Np1-O2 2.085(4), Np2-Ct3 2.467(5), Np2-Ct4 2.466(4), Np2-Ct5 2.465(5), Np2-O1 2.094(4), Np3-Ct6 2.474(3), Np3-Ct7 2.481(3), Np3-Ct8 2.479(3), Np3-O2 2.085(4), Np-C_{ar} 2.693(14) to 2.765(7), O1-Np1-O2 100.96(16), Ct1-Np1-Ct2 121.92(11), Ct1-Np1-O1 109.56(15), Ct1-Np1-O2 108.40(14), Ct2-Np1-O1 109.39(14), Ct2-Np1-O2 104.45(14), Np1-O1-Np2 172.8(2), Np1-O2-Np3 174.1(2), ϕ(O1-Np1-O2∠Ct1-Np1-Ct2) 88.54(12).

3.2.3 Molecular structure of [(*μ*-O){Np(Cp)$_3$}$_2$], 58

The golden-russet microcrystals of complex **58** usually grow as twins and crystals of a suitable size and quality for single crystal X-ray diffraction are exceedingly rare, regardless of the crystallization solvents (benzene, toluene, Et$_2$O, THF/*n*-hexane) and conditions used. The selected crystal was a hexagonal plate obtained from the toluene/heptane solution over *ca.* 150 h. The crystal structure belongs to the monoclinic space group *Cc* (No. 9), a = 14.4553(17), b = 8.2422(10), c = 21.434(3) Å and β = 108.284(2)°, with 4 independent molecules in the unit cell; the asymmetric unit consists of a single molecule of [(μ-O){Np(Cp)$_3$}$_2$] **58**.

Complex **58** is isotypic to $[(\mu\text{-O})\{U(Cp)_3\}_2]$ **54**[151] and can be seen as a distorted, non-centrosymmetric polymorph (Figure 3.5). Most significantly, the $\{Np_2O\}^{6+}$ core deviates from the ideally axial arrangement (173.0(13)°) and shows two distinct Np-O bonds (2.06(2) and 2.12(2) Å for Np1-O1 and Np2-O1, respectively), which lie in between the corresponding mean value found in **57** (2.085(9) Å). This diversity lowers in turn directionality of the mutual alignment of both the two $Np(\eta^5\text{-}Cp)_3$ groups around the oxometallic core structure and makes further bonding parameters analyses difficult.

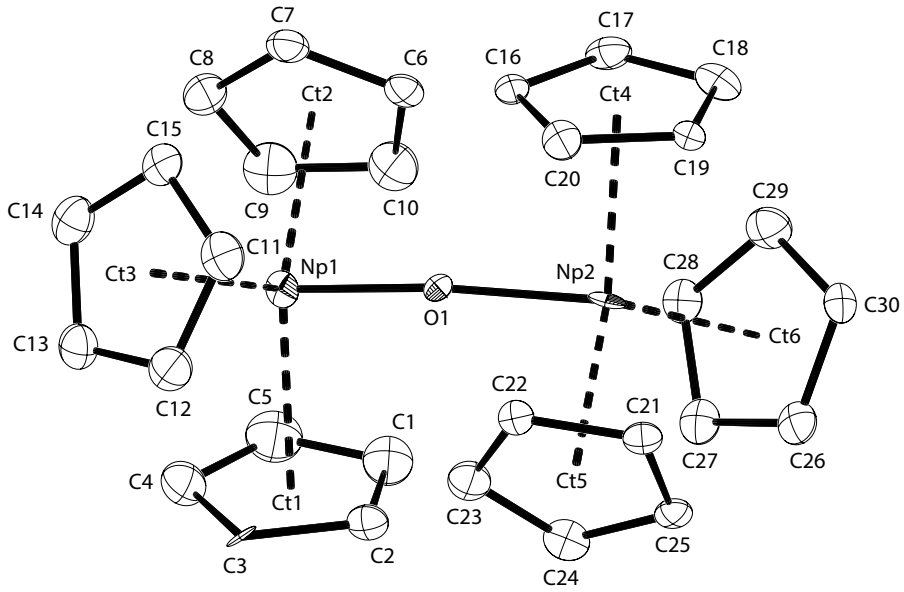

Figure 3.5. ORTEP drawing of of **58** with thermal ellipsoids plot (50 % probability for non-H atoms). All hydrogen atoms were omitted for clarity; selected bond lengths [Å] and angles [°]: Np1-O1 2.06(2), Np2-O1 2.12(2), Np1-Ct1 2.483(6), Np1-Ct2 2.509(7), Np1-Ct3 2.449(6), Np1-C_{ar} 2.714(11) to 2.821(10), Np2-Ct4 2.483(5), Np2-Ct5 2.448(6), Np2-Ct6 2.515(6), Np2-C_{ar} 2.71(1) to 2.813(17), Np1-O1-Np2 173.0(13), Ct1-Np1-Ct2 114.0(2), Ct1-Np1-Ct3 116.47(18), Ct2-Np1-Ct3 119.39(19), Ct1-Np1-O1 103.0(7), O1-Np2-Ct4 100.7(7), ϕ(Ct1-Np1-O1∠Ct4-Np2-O1) 4.2(10), ϕ(Ct1-Np1-O1∠Ct5-Np2-O1) 60.8(2), ϕ(Ct1-Np1-O1∠Ct6-Np2-O1) 123.0(2), ϕ(Ct2-Np1-O1∠Ct4-Np2-O1) 116.8(2), ϕ(Ct2-Np1-O1∠Ct5-Np2-O1) 58.8(3), ϕ(Ct2-Np1-O1∠Cg6-Np2-O1) 5.2(8), ϕ(Cg3-Np1-O1∠Cg4-Np2-O1) 59.1(3), ϕ(Cg3-Np1-O1∠Cg5-Np2-O1) 61.8(3), ϕ(Ct3-Np1-O1∠Cg6-Np2-O1) 7.0(13).

3.2.4 DC magnetometry studies of $[(\mu\text{-O})[An(Cp)_3]_2]$ complexes; An = U, Np

In the anticipation that the two isotypic complexes $[(\mu\text{-O})\{An(Cp)_3\}_2]$ (An = U **54**, Np **58**) could provide a molecular platform to investigate potentially strong and highly directional magnetic exchange phenomena between the two An^{IV} ions through the isolated bridging oxo group, we have studied

the variable temperature magnetic behaviour by SQUID magnetometry to probe the magnetism of the ground states and an *f*-electron occupancy of the participating actinide ions. The DC magnetic susceptibility curves ($\chi = f(T)$) for both complexes are collated in Figure 3.6.

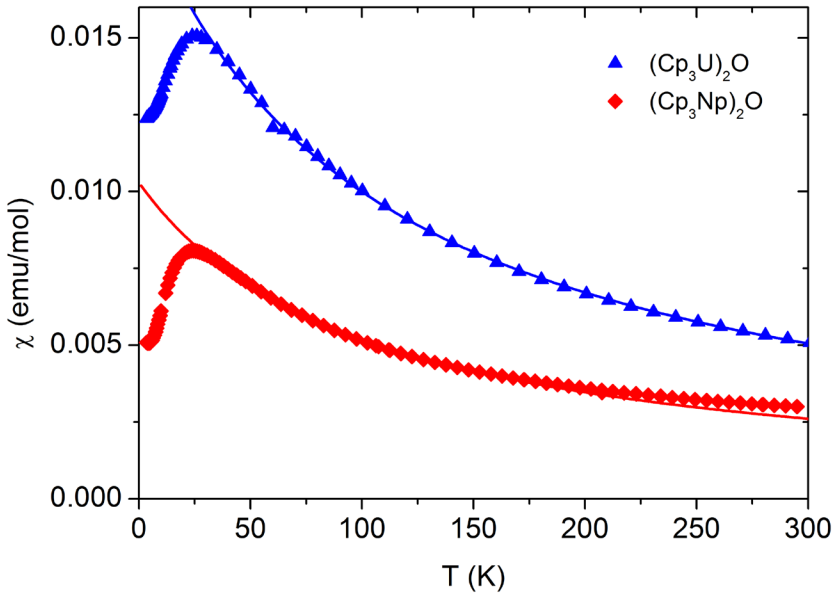

Figure 3.6. DC magnetic susceptibility (χ) curves measured as a function of temperature (T) for complexes **54** (red rhombohedra) and **58** (blue triangles). Data were collected with an applied field of 7 T. The solid lines show fitted values of the Curie-Weiss expression of $\chi = \mu_{eff}^2/8(T-\Theta)$ for the region between 40 and 200 K; the corresponding numerical parameters were extracted: μ_{eff}(**54**) = 2.86 μ_B/ion, Θ(**54**) = -104 K, μ_{eff}(**58**) = 2.05 μ_B/ion, Θ(**58**) = -102 K.

In the temperature region above 40 K both the experimental curves follow closely a Curie-Weiss behaviour, which indicates that these systems contain the single-ion ground states that are both magnetic. Unless time-reversal symmetry guarantees the complexes of the Kramers' ion Np^{IV} ($5f^3$, $^4I_{9/2}$) exhibit magnetic ground state of at least doubly-degenerate, the same behaviour is remarkable for the non-Kramers' U^{IV} ion which prefers a non-magnetic singlet ground state ($5f^2$, $^3H_4$) in most geometries. In complex **54** the relation of degeneracy with symmetry thus translates into the crystallographic component which generates a doublet ligand-field ground state. In fact, this can be attributed to the centrosymmetric molecular geometry of **54** in the solid-state with an inversion centre lying on the oxygen atom in $\{U_2O\}^{6+}$ core, which exhibits an ideal 180° alignment and both the $U(\eta^5\text{-Cp})_3$ groups are perfectly staggered about this axis. At lower temperatures, both the susceptibility curves exhibit maxima (26 and 24 K for **54** and **58**, respectively)

which indicate the presence of an antiferromagnetic coupling between the actinide ions, most likely due to superexchange interactions mediated by the bridging oxo unit. Remarkably, the peak temperatures and the extracted Curie-Weiss temperatures, Θ, are quantitatively similar in **54** and **58** and detailed calculations are now in progress to evaluate how the microscopic exchange constants scale between formally +4 oxidation state U and Np ions within similar complex geometry.

Presented magnetic studies of **54** and **58** closely match those reported for the centrosymmetric complex [{((($^{t\text{-Bu}}$ArO)$_3$tacn)U}$_2$(μ-O)] **47** which shows analogous magnetization susceptibility curves in the whole temperature range with the peak temperature maximum at *ca*. 20 K. Despite this qualitatively similar behaviour a very different ancillary [N_3O_4]-ligand field environment in **47** precludes a more detailed comparison.

3.3 Part II: Subtle Actinide(IV)-Uranium(V) Interactions Mediated by the Uranyl Oxo-Group

Organometallic complexes containing sterically unsaturated U^{III} and Th^{III} ions can reduce and activate inert small molecules, but there is no precedent of such reactivity for the transuranic molecules that display substantially less negative An^{IV}/An^{III} redox potentials. A handful of studies on the reduction of the d^0f^0 uranyl ion $[UO_2]^{2+}$ to the singly-reduced d^0f^1 uranyl monocation $[UO_2]^{+}$ often involve the concomitant oxo-group functionalization with main Group[155–157], 3*d*- and 4*f*-block metal cations.[36,146,147]

Additionally, the rigorously axial oxo ligand geometry of the $[UO_2]^{+}$ ion, which contains the Kramers' ion U^{V} ($5f^1$) centre, has become recently an excellent design-element for SMMs since it enables the simultaneous control over the directionality of both the magnetic vector and the supramolecular assembly with other magnetically relevant cations.[36] Actinides exhibit increased covalency in bonding compared to the analogous metal-ligand interactions with the lanthanide elements and thus should produce stronger magnetically coupled systems.

3.3.1 Molecular precursors for reductive oxo-metallation of $[UO_2]^{2+}$ ion with An^{III} cations; An = U, Np, Pu

To study the ability of the An^{III} (An = U, Np, Pu) ions to oxo-bind and reduce the uranyl(VI) ion, the use of well-tailored molecular precursors is critical. The isostructural $[An^{III}(Cp)_3]$ complexes are considered reactive Lewis acidic precursors which impose a steric protection to a bound molecule and the capacity for one-electron oxidation; the oxidation product $[An^{IV}(Cp)_3]$ should be relatively inert. The complex $[Pu(Cp)_3(THF)]$ **59** used in the study was prepared and purified by Dr Christos Apostolidis (ITU).

The well-defined crystalline uranyl(VI) complex $[(UO_2)(THF)(H_2L^{Et})]$ **60**, (Figure 3.7) was obtained in a straightforward manner from the reported complex $[UO_2(py)(H_2L^{Et})]$[147] by solvent exchange *via* Soxhlet extraction with *n*-hexane / THF mixture (*cf.* Chapter 5.1). Complex **60** is structurally similar to the previously reported octamethyl derivative $[(UO_2)(THF)(H_2L^{Oct})]$ **61**[158] but is more soluble in aprotic solvents; The molecular structure of complex **60** is shown in Figure 3.7. The uranyl ion is bound by only one of the two N_4-donor sets of the macrocycle and has an approximately D_{5h}-symmetric coordination environment around the uranium atom. This consists of four N donors occupying the equatorial positions alongside with one O donor from the coordinated THF molecule, and the two axial positions occupied by the uranyl oxo groups. The remaining vacant N_4-compartment of the Schiff-base calix[4]pyrrole macrocycle retains the two protonated pyrrole nitrogens which interact through strong hydrogen bonding to the *endo*-oxo group of the accommodated uranyl ion. This differentiates both the U=O distances (U1-O1 1.768(3) Å, U1-O2 1.790(3) Å) and presumably imparts a greater *exo*-oxo group reactivity.

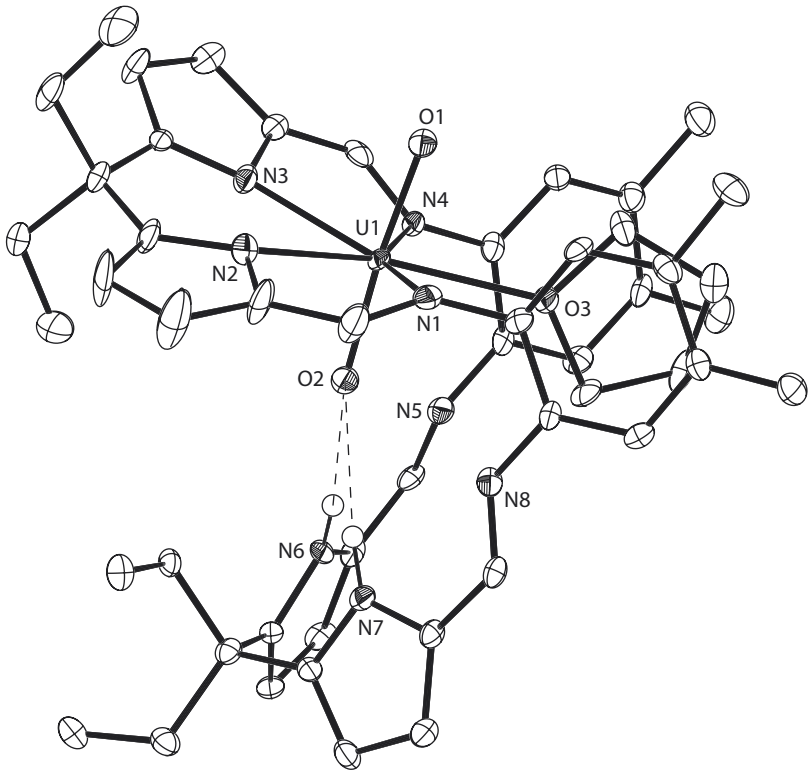

Figure 3.7. ORTEP drawing of the side-on view of [$(UO_2)(THF)(H_2L^{Et})$] **60** with thermal ellipsoids plot (50% probability for non-H atoms). All hydrogen atoms (except for pyrrolic nitrogens) and crystallization solvent molecules were omitted for clarity; selected bond lengths [Å] and angles [°]; U1-O1 1.768(3), U1-O2 1.791(3), U1-O3 2.423(5), U1-N1 2.526(4), U1-N2 2.439(4), U1-N3 2.430(6), U1-N4 2.544(4), O1-U1-O2 175.10(17).

3.3.2 Synthesis of actinide-functionalized uranyl(V) complexes

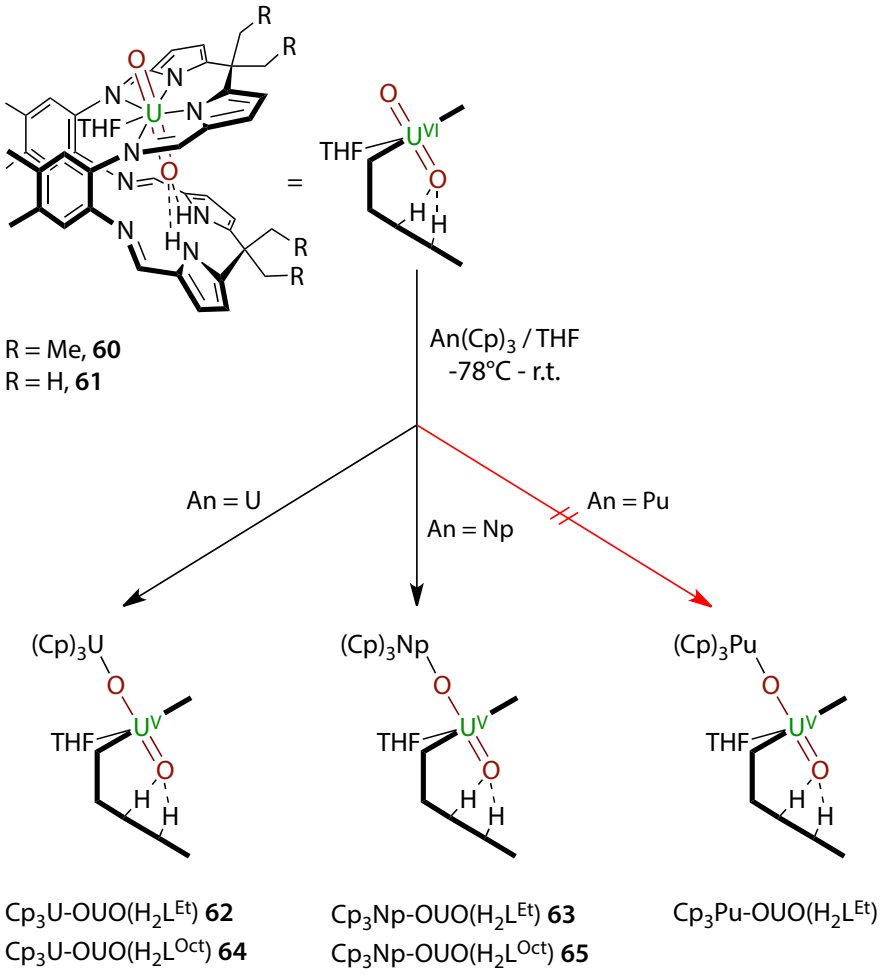

Scheme 3.4. Reductive oxo-metallation of uranyl(VI) complexes **60** and **61** by the Lewis acidic uranium and transuranic complexes [An(Cp)$_3$] (An = U (**39**), Np (**34**), and Pu (**59**)).

The reactivity of the [An^{III}Cp$_3$] (An = U (**39**), Np (**34**), and Pu (**59**)) complexes towards complex [(UO$_2$)(THF)(H$_2$L^{Et})] **60** was initially described in the PhD thesis of Zegke,[145] Scheme 3.4. All three reactions were conducted similarly by contacting the equimolar solid reactants in thawing or cold THF and the reaction mixtures allowed to slowly reach room temperature. The colours of the solutions have changed from initially brownish-green to brown (U) and reddish-brown (Np), but no observable reaction for the Pu^{III} analogue, presumably due to insufficient reducing potential of the cation and the competitive THF solvent donor strength over uranyl oxo coordination. The resulting complexes of the general formula [(Cp)$_3$An^{IV}OU^{V}O(THF)(H$_2$L^{Et})] (An = U (**62**), Np (**63**)) were obtained after work-up

(*cf.* Chapter 5.4) and crystallographically characterized, although the low thermal stability of the solid phases at room temperature, especially for the complex **62**, precluded detailed analyses that correlate structure and physicochemical properties. In a solution, complex **62** undergoes rapid decomposition upon dissolving the crystals of **62** in THF-d_8, leading to the formation of a complex mixture of products containing the parent uranyl(VI) complex **60** (^{1}H NMR). This is consistent with the observation that U^{4+} can promote the disproportionation reaction of the otherwise stable sterically protected $(UO_2)^+$ complexes[154] and further supported by the smaller decomposition rate of the isostructural Np-OUO complex **63**. To assess the potential for the additional stabilization given to the resulting bimetallic complexes, the use of differently alkyl-substituted macrocyclic ligand appeared to be the viable strategy for the fine modification of the crystal lattice structure and the crystal growth mechanism. We therefore decided to explore similar reactivity of the known complex $[(UO_2)(THF)(H_2L^{Oct})]$ **61**[158] towards the same potential reductants **39** and **34**, Scheme 3.4. These reactions can be interpreted as the formal addition of the *exo*-oxo group of the uranyl(VI) moiety in **61** to appropriate Lewis acidic An^{III} ions of $[An(Cp)_3]$ complexes. Both reactions in THF solvent result in complete consumption of green (**61**) and brown (**39** or **34**) solids on allowing the stirred reaction mixture to reach room temperature and the concomitant colour change of the solution to brown (An = U) and red-brown (Np), respectively; the resulting crystalline complexes, golden-brown **64** and dark red-brown **65** were isolated after the work-up in yields of around 20 and 30 %, respectively, Scheme 3.4. Both reactions are always accompanied with the formation of a small quantity of an ochre (An = U) or golden russet (Np) microcrystalline by-products, which are identified as the appropriate $[(\mu\text{-}O)\{An(Cp)_3\}_2]$ complexes; the latter are insoluble in the reaction medium, which facilitates the isolation of the main product. It is worth noting that in a reaction set between **60** and 1.5 eq of **34** we reported previously the formation of a clear red solution affording complex $[\{(Cp)_3Np(\mu\text{-}O)\}_2\{Np(Cp)_2\}]$ **57**, as a sole Np-containing product. To date, this result was not repeatable and almost certainly appeared from a serendipitous oxygen containing impurity reactions of either the excess **34** or the expected oxo-metallated complex **63**. In a view of the latter oxidation studies of **34** with trace air impurities in THF solutions (*cf.* Chapter 3.2.1), the unexpected and highly selective transformation of the isolated solution of **63** to complex **57** implies the possible different hydrolytic reactivity of the tris(cyclopentadienyl)

fragments of the heterobimetallic uranium-neptunium complexes. In fact, all An-OUO complexes are exceedingly air-sensitive, but the octamethyl derivatives, **64** and **65,** are much easier to isolate in the pure form than **62** and **63**, as the crystal growth is less anisotropic and large, block crystals result without visible surface impurity and occlusion.

3.3.3 Characterization of the actinide-functionalised uranyl(V) complexes

Both series of homo- and heterobimetallic complexes are exclusively *exo*-oxo metalated, as characterized in a solution by ^{1}H NMR, and Vis-NIR spectroscopy and in the solid-state by ATR spectroscopy and single crystal X-ray diffractometry. In general, the solution stability of the octamethyl An-OUO complexes, **64** and **65**, exceeds that of the tetraethyl derivatives **65** and **63**, and enables complete solution-structure elucidation by NMR in correlation to the molecular geometry of the complexes obtained from the solid-state data. Despite several following measurement attempts the resulting spectra of **63** are complicated by the formation of impurities during the preparation of the encapsulated NMR samples (*cf.* Chapter 5.4).

The ^{1}H NMR spectra of complexes **64** and **65** in THF-d_8 contain paramagnetically broadened and contact shifted resonances, which can be ascribed for both the doubly deprotonated octamethyl macrocyclic ligand, $(H_2L^{Oct})^{2-}$, and the three equivalent cyclopentadienyl groups in each case. The former sets are suggestive of the retention of the approximately C_2-symmetrical 'wedge-shaped' geometry of the macrocycle (*cf.* Figure 3.7) and the two pyrrolic NHs of the vacant N_4-donor compartment, resonating at δ_H(**64**) = +51.1 and δ_H(**65**) = +54.8 ppm. These resonances are specifically shifted due to the strong H-bonding interactions to the *endo*-oxo group of the uranyl,[159,160] which exhibits a potent paramagnetic character of the U^V ($5f^1$) ion and in turn strongly implies complete or close to complete electron transfer between both pairs of reagents to form An^{IV}-O-U^V complexes. On the other hand, the proton chemical shift of the Cp ligands does not necessary differentiate the electronic environment around the coordinated An^{IV} and An^{III} metal sites, and predictions about the paramagnetic tensor orientation in NMR are often erroneous, especially in case of the U^{IV} ion (*vide infra*). The Cp-ring protons in **62** and **64** resonate at a high frequency chemical shift

of δ_H(**62**) = +3.17 ppm δ_H(**64**) = +3.30 ppm, close to the resonance of $[U^{IV}(Cp)_3Cl]$ δ_H (**38**) = -3.48 ppm and significantly lower in energy than the resonance in $[U^{III}(Cp)_3(THF)]$ δ_H (**39**) = -15.41 ppm. However, complexes of the general formula $[U^{IV}(Cp)_3(OR)]$ exhibit lower frequency Cp resonances, i.e. δ_H (**35**) = -8.8 ppm for OR = OPh, and δ_H = -18.4 ppm for OR = OEt.[126] Furthermore, both the heterobimetallic complexes show the chemical shifts of the Cp-ring protons at δ_H(**63**) = -12.1 ppm and δ_H(**65**) = -11.1 ppm, which are remarkably similar to those measured in the isotypic $[Np^{III}(Cp)_3]$ fragments at δ_H(**43**) = -11.95 ppm in $[K\{Np^{III}(Cp)_4\}]$ and δ_H (**34a**) = -9.65 ppm for $[Np^{III}(Cp)_3(THF\text{-}d_8)]$. All these resonances are several ppm lower in frequency as compared to the analogous Np^{IV} complexes showing Cp-ring protons shifts at δ_H(**14**) = -21.49 ppm in $[Np^{IV}(Cp)_3Cl]$ and δ_H(**58**) = -18.35 ppm for $[(\mu\text{-}O)\{Np^{IV}(Cp)_3\}_2]$. This contrasts with the previously assigned Np^{IV}-O-U^V formal oxidation states in complex **65**, since it suggests only partial reduction of the uranyl group if any, and potential Np^{III} character, with the uranyl oxo acting more as a Lewis base donor than oxidant.

The ATR and FTIR spectra of all four complexes show the absorption for the uranyl asymmetric stretch at 893 cm^{-1} (**62**), 897 cm^{-1} (**63**), 892 cm^{-1} (**64**), and 891 cm^{-1} (**65**), which are in agreement with a lowering of the oxo bond order of the parent uranyl(VI) complexes (906 and 907 cm^{-1} for **60** and **61**, respectively). The ATR spectrum of **65** (Figure 3.8) shows the characteristic sharp absorption at 3367 cm^{-1} of the pyrrole N-H stretching vibration involved in the intramolecular hydrogen bonding with *endo*-oxo group of uranyl(VI) cation (**61**) significantly lowers in energy and to 3267 cm^{-1} in **65** and concomitantly broadens. The spectrum also contains a broad absorption at 3102 cm^{-1} which is the characteristic ν(CH) skeletal vibration of the Cp-rings; for comparison, the corresponding values of 3084 and 3082 cm^{-1} were previously assigned for the Np^{III} containing complexes **34** and **43**, respectively. A shoulder at 758 cm^{-1} is attributed to a δ(CH) twisting vibration and a similar broadened vibrational band of the identical frequency is observed in the spectrum of parent complex **34**. The three vibrational peaks at 612 (sh), 605 (sh), 571 (s) cm^{-1} belong to a very characteristic set of four vibrations discussed previously for the Np^{III} cyclopentadienyl complexes, Figure 2.1. Finally, the broad band with a maximum at *ca.* 519 cm^{-1} is indistinct, as the expected characteristic Cp-ring band in that region is overlapping with a series of other fingerprint absorptions of the aromatic Schiff-base calix[2]pyrrole fragment.

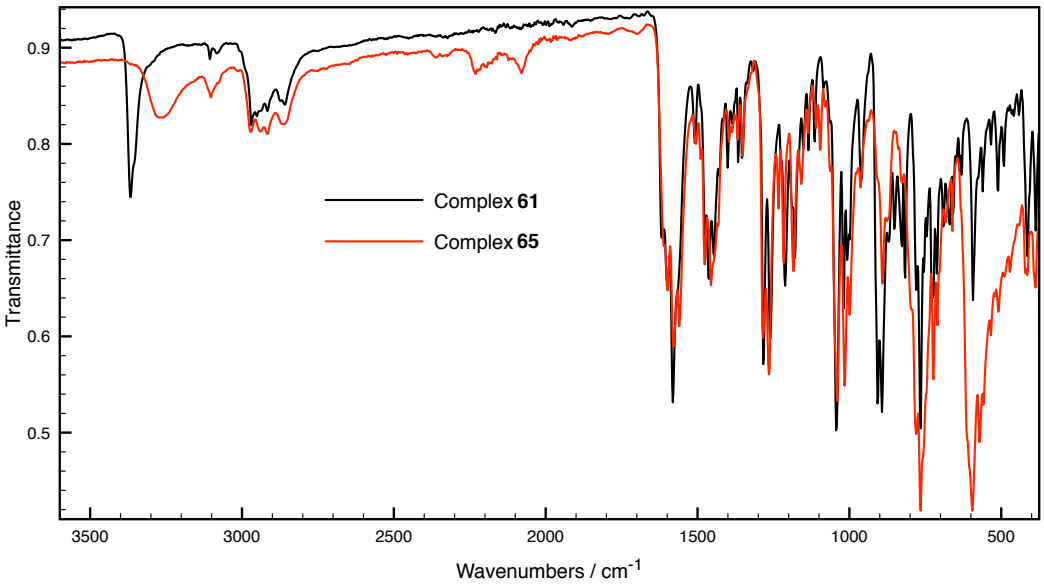

Figure 3.8. ATR spectrum of complexes $[(UO_2)(THF)(H_2L^{Oct})]$ **61** and $[(Cp)_3NpOUO(THF)(H_2L^{Oct})]$ **65** measured using diamond ATR; spectra are not normalized.

In spite of the drastic changes in solution stability between the complexes **63** and **65** and the resulting NMR spectra, the Vis-NIR spectroscopic characterization of both heterobimetallic systems show essentially identical sets of absorptions (Figure 3.9 and Figure 3.10). This may suggest that complex **63** reacts quickly with the fluoropolymer NMR tube liner material required for radiological encapsulation of the NMR sample, forming an impurity which appears to have a very similar solution structure to parent complex **63** as evidenced by the C_2 symmetric $(H_2L^{Et})^{2-}$ environment. The two overlapping sets of resonances make unambiguous assignment of the smaller resonances for **63** not possible (for details see Chapter 5.2). The Vis-NIR spectra of **63** and **61** contain both the absorptions at 1066 and 987 nm, which are the part of the characteristic band manifold of around 1060 and 1010 nm attributed to the *pseudo*-tetrahedral $Np^{IV}(Cp)_3$ groups and are not seen for any Np^{III} analogues.[65] There is also no evidence of the absorption around 1260 nm, which is the most characteristic and highest intensity band for the reported $[Np^{III}(Cp)_3]$ systems. There are several bands below 1000 nm that may further support to Np^{IV} character but imprecision in the older data for neptunium complexes currently makes further analysis difficult.[65]

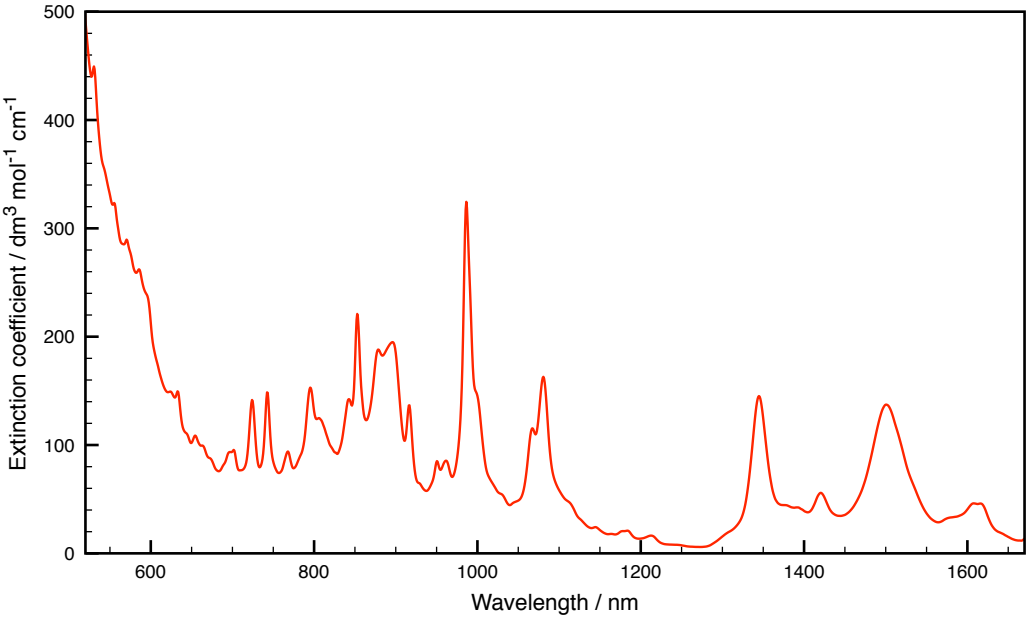

Figure 3.9. Vis-NIR spectrum of $[(Cp)_3NpOUO(THF)(H_2L^{Et})]$ **63** dissolved in THF (^{237}Np concentration 2.93 mM).

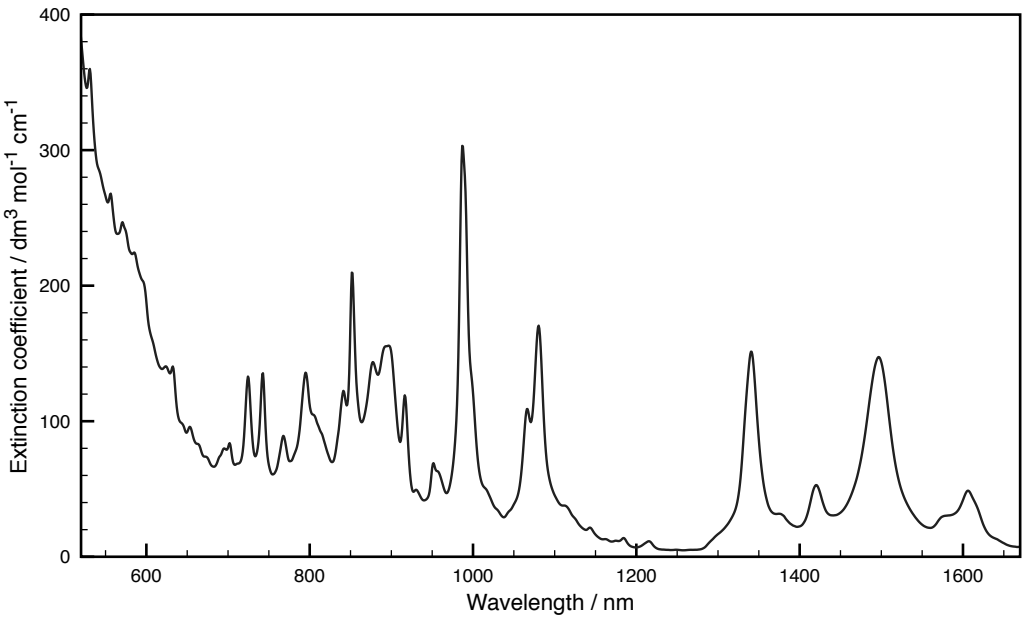

Figure 3.10. Vis-NIR spectrum of $[(Cp)_3NpOUO(THF)(H_2L^{Oct})]$ **65** dissolved in THF (^{237}Np concentration 3.42 mM).

3.3.4 Molecular structures of [(Cp)$_3$NpOUO(THF)(H$_2$L^{Oct})], 65

Dark-red brown, rhombohedra crystals of **65** suitable for X-ray crystal structure determination were obtained by diffusion of *n*-pentane into a THF solution at room temperature. The crystals were refined in the monoclinic space group $P2_1/n$ (No. 14), a = 15.6568(10), b = 19.1455(13), c = 23.72780(16) Å, β = 106.9890(10)°, with 4 independent molecules in the unit cell; the asymmetric unit consists of a single molecule of [(Cp)$_3$NpOUO(THF)(H$_2$L^{Oct})].

The molecular structure of **65** is shown in Figure 3.11 and consists of the heterobimetallic uranium-neptunium complex showing metrical parameters of the two oxo-groups of the uranyl cation, which are fully consistent with the singly-reduced uranyl cation and consequently the complete electron-transfer from the Np^{III}(Cp)$_3$ fragment; complex **65** is isostructural to its diuranium analogue **64**. In each complex, the uranyl unit is linear (O_{exo}-U1-O_{endo} = 178.02(17) and 178.10(18) °, for **64** and **65**, respectively) and the An-O_{exo}-U has an approximately linear geometry (171.0(2) in **64** and 171.2(2) ° in **65**). The uranium atom of both the uranyl complexes still resides inside one set of N$_4$-donors of the macrocyclic ligand occupying the four equatorial positions alongside with the fifth of the O3 donor of the coordinated THF molecule in an overall pentagonal bipyramidal environment, which is further distorted by the asymmetrical lengthening of the axial oxygen-uranium bonds. The metalated *exo*-oxo group elongation is more significant than the corresponding *endo*-oxo (U1-O_{exo} = 1.975(5) *vs.* U1-O_{endo} 1.843(5) in **65**) and supports the assignment of the U^V uranyl attached to both U(Cp)$_3$ and Np(Cp)$_3$ fragments. Both organoactinide units exhibit approximately C_{3v} symmetry around the An ions with the mean An–C(η^5-Cp) separations of 2.74(2) and 2.717(9) Å for **64** and **65**, respectively. This is consistent with a formal oxidation state of U^{IV} but unequivocal for Np. In comparison, the average Np-C distance for C_{3v}-symmetric groups in complex [{(Cp)$_3$Np(μ-O)}$_2${Np(Cp)$_2$}] **57** are similar but unremarkable (2.722(18) and 2.747(21) Å) and the old, room temperature data for [Np(Cp)$_3$(OPh)] **29** shows the interim average Np–C separation of 2.733(3) Å. More importantly, the Np-O_{exo} distance in **65** (2.256(6) Å) is close to that of the dative Np^{IV}-O bond of diphenylmethylphosphine oxide in the reported complex [NpCl$_3$(Cp)(OP(Me)Ph$_2$)$_2$][161] (2.277(12) Å) and significantly greater than the single covalent Np-O(phenolato) bond length in **29** (2.136(7) Å), or the Np$_2$(μ-O) bimetallic bridges in **58** (2.06(2) and 2.12(2) Å for Np1-O1 and Np2-O1)

and the average value in **57** (2.085(9) Å). There are no structurally authenticated C_{3v}-symmetric $Np^{III}(Cp)_3$ complexes yet, which makes further analysis of bonding difficult.

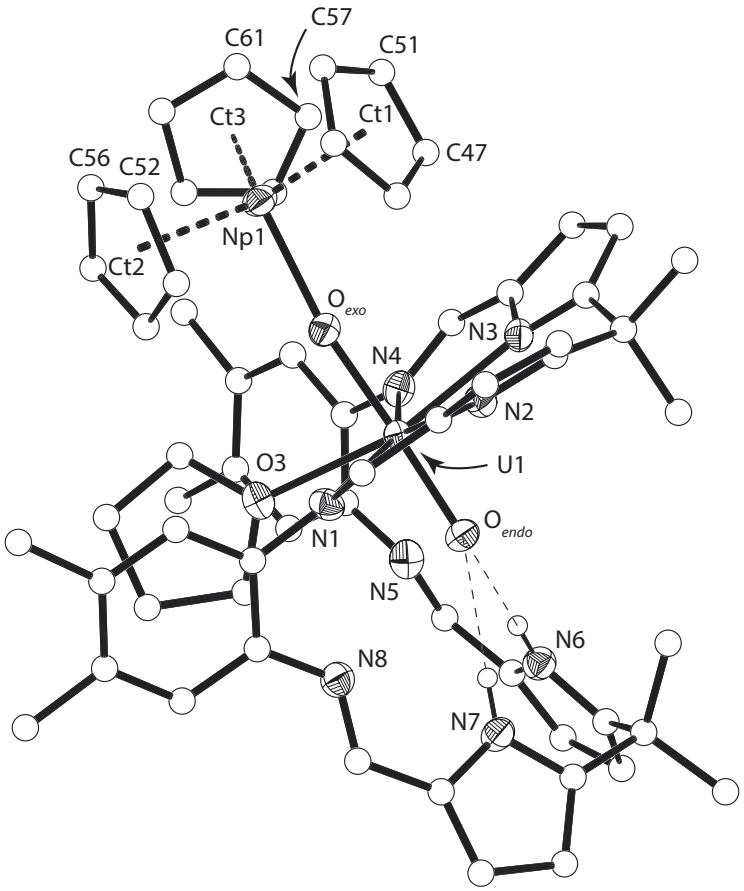

Figure 3.11. Molecular structure of $[(Cp)_3NpOUO(THF)(H_2L^{Oct})]$ **65** with thermal ellipsoids drawn at 50 % ellipsoid probability for non-H/C atoms. All hydrogen atoms (except for pyrrolic nitrogens) and lattice solvent molecules were omitted for clarity; selected bond lengths [Å] and angles [°] for **65**: U1-O_{endo} 1.843(5), U1-O_{exo} 1.975(5), U1-O3 2.519(4), U1-N1 2.651(4), U1-N2 2.466(5), U1-N3 2.455(4), U1-N4 2.670(4), Np1-O_{exo} 2.256(6), Np1-Ct1 2.440(4), Np1-Ct2 2.444(5), Np1-Ct3 2.454(5), Np1-C_{ar} 2.690(8) to 2.752(10), O_{endo}-N6 3.043(7), O_{endo}-N7 3.174(6), O_{exo}-U1-O_{endo} 178.10(18), Np1-O_{exo}-U1 171.2(2), Ct1-Np1-Ct2 116.98(15), Ct1-Np1-Ct3 114.93(17), Ct2-Np1-Ct3 115.66(16), Ct1-Np1-O_{exo} 102.72(13), Ct2-Np1-O_{exo} 100.69(14), Ct3-Np1-O_{exo} 102.34(15); for **64**: U1-O_{endo} 1.844(5), U1-O_{exo} 1.984(3), U1-O3 2.535(4), U1-N1 2.676(4), U1-N2 2.454(5), U1-N3 2.480(5), U1-N4 2.647(4), U2-O_{exo} 2.260(3), U2-Ct1 2.465(3), U2-Ct2 2.480(4), U2-Ct3 2.469(4), U2-C_{ar} 2.718(7) to 2.771(9), O_{endo}-N6 3.297(12), O_{endo}-N7 3.124(12), O_{exo}-U1-O_{endo} 178.02(17), U2-O_{exo}-U1 171.0(2), Ct1-U2-Ct2 115.08(14), Ct1-U2-Ct3 116.9(12), Ct2-U1-Ct3 115.83(13), Ct1-U2-O_{exo} 102.43(12), Ct2-U2-O_{exo} 100.17(14), Ct3-U2-O_{exo} 102.78(13).

3.3.5 DC and AC magnetometry studies of $[(Cp)_3An(UO_2)(H_2L^{Oct})]$; An = U (64), Np (65)

The DC susceptibility curves for both the complexes **64** and **65** are collated in Figure 3.12 as a function of $\chi T = f(T)$. The lowest attainable temperature data show a very similar effective magnetic moment of *ca.* 2.4 μ_B for both complexes but upon reaching higher temperatures large differences in the magnetic behaviour of the two samples can be seen. The χT product for **64** quickly surpasses the upper theoretical limit expected for a U^{III}-U^{VI} couple and approaches the value of μ_{eff}(**64**) = 2.42 μ_B which is close to expected for a U^{IV}-U^{V} couple at room temperature, while the magnetic moment of **65** slowly reaches the saturation value that corresponds to Np^{III}-U^{V} system and equals to μ_{eff}(**65**) = 2.34 μ_B. Interestingly, this asymptotic analysis suggests that the two different electronic structures of the complexes a practically negligible electron-transfer in heterobimetallic complex **65** and a singly-reduced uranyl unit in diuranium complex **64** are present.

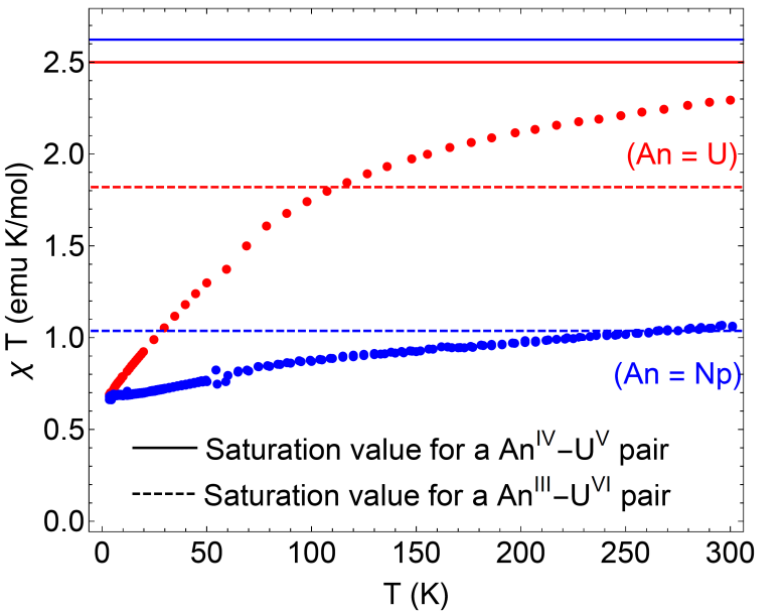

Figure 3.12. Variable temperature DC magnetic susceptibility curves measured for complexes **64** (red dots) and **65** (blue dots) with an applied field of 1 T; as a graph of the $\chi T = f(T)$ function. The expected magnetic saturation values for An^{IV}-U^{V} and An^{III}-U^{VI} ion couples are given as continuous and dashed lines, respectively; colour codes of the lines are according to main data.

Therefore, the dynamic magnetic properties of complex **64** were studied by AC magnetic susceptibility measurements, the results of which are summarized

in Figure 3.13. The out-of-phase component (χ") of the AC susceptibility contain a well-developed peaks from below 4 K, which are indicative of the SMMs behaviour of complex **64**. The dependence of temperature on the relaxation time (τ) can be modelled as a direct process with either a Raman or an Orbach relaxation pathway component. Both the extracted parameters of time $\tau_0 = 3.26 \times 10^{-8}$ s and thermal activation barrier $\Delta = 26.9$ K fall into the range specific to previously reported single-ion SMM, triamidoamine uranium(V) mono-oxo complex, [U(O)(Tren^{TIPS})] **66**.[162] The combined information of described SMM characteristics for **64**, which lack any visible sign of the magnetic interaction phenomena between the uranium ions in the DC magnetic susceptibility curves (i.e. maxima for antiferromagnetic exchange, as for **54** or **58**, Figure 3.6), and that U^{IV} ion often adopts the non-magnetic ground state in low-symmetric coordination spheres both imply the SMM property can be ascribed to a magnetically isolated single-ion uranyl(V). Although the majority of reported U^{V} SMMs derive from the more symmetrically relevant $(UO_2)^+$ cation rather than containing a single U^{V}=O moiety, to date, complex **66** remains the only one where the SMM behaviour can be attributed solely to the U^{V} centre. Most of the known U^{V} SMMs are heterometallic complexes containing for example Mn centres, whose complexes are very well known for their peculiar magnetic properties.[36] It is worth noting here that the more symmetrical heterobimetallic U^{V}-Mn^{II} system exhibits to date the highest reported thermal activation barrier of $\Delta = 81.0(5)$ K for a mono-uranyl complex, seemingly due to specific intramolecular interaction between both magnetically relevant actinide and transition metal ions.[36]

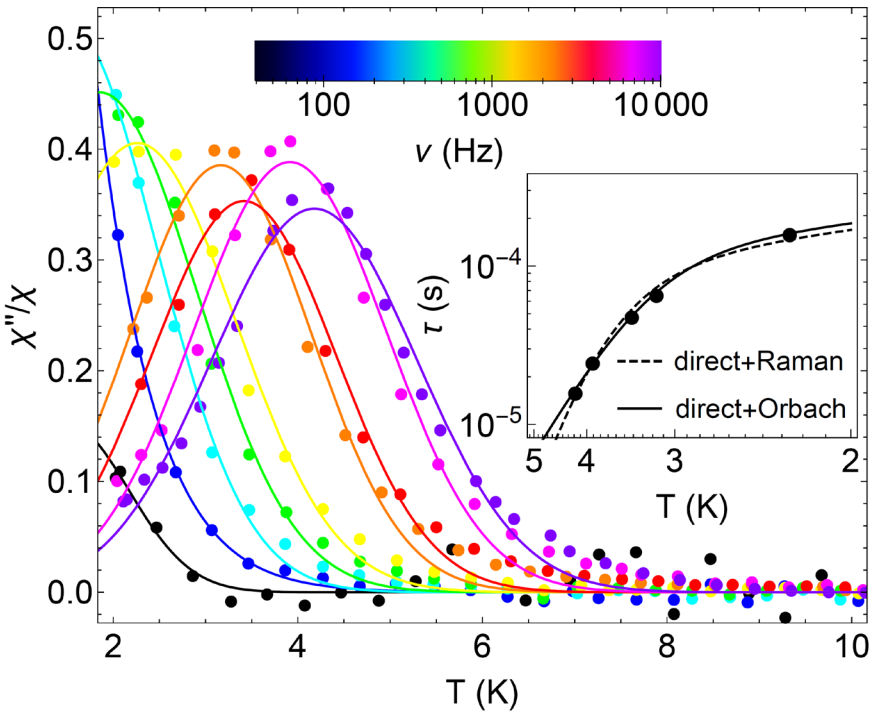

Figure 3.13. Imaginary component of the AC magnetic susceptibility for $[(Cp)_3UOUO(THF)(H_2L^{Oct})]$ **64** as a function of $\chi''/\chi_{dc} = f(T)$) and for different values of the frequency ν of the 5 G driving field; inset: temperature-dependant relaxation times τ showing two possible fits obtained by considering an Orbach (continuous line) and a Raman (dashed line) relaxation path combined each with a direct process.

3.4 Concluding remarks

A quarter-century has passed since the discovery of the first organouranium oxide complex and this period has seen a substantial progress in different directions of the structural, acid-base reactivity, small molecule activation and mechanistic studies thereof. In contrast to this, the neptunium analogues of the oxo-bridging groups have not yet appeared in the literature and this work describes the pioneering complexes $[\{(Cp)_3Np(\mu\text{-}O)\}_2\{Np(Cp)_2\}]$ **57** and $[(\mu\text{-}O)\{Np(Cp)_3\}_2]$ **58**. The crystal structure of the trinuclear complex **57** shows the 'bent metallocene' geometry around the central $Np^{IV}O_2$ group, with short average Np-O distances (2.085(9) Å). Furthermore, the comparison of the metrical parameters for the bimetallic bridges, An-(μ-O)-An (An = U, Np), indicates the strong preference of the uranium congeners to form centrosymmetric units, with an inversion centre positioned on the bridging O atom (**54**) or the planar ring-centroids in U_2O_2 and U_3O_3 metallacycles, whereas both Np complexes show

non-centrosymmetric geometry and polarised Np-O bond distances, which may suggest complex electronic structures.

In order to cast light on the *f*-electron occupancy of each actinide ion in the isotypic complexes **54** and **58**, we have performed preliminary DC susceptibility measurements. Remarkably, the gross magnetic properties in both samples are quantitatively similar in spite of the different magnetic ground state of the actinide metal sites. The susceptibility curves closely follow the Curie-Weiss law above 40 K and demonstrate antiferromagnetic exchange around 25 K, although the detailed analysis of the microscopic exchange constants is still in progress.

The second part of this chapter describes the first selective uranyl oxo-metalation and concomitant reduction of the uranyl oxo group by another actinide complex, featuring the redox reaction capable to produce the first heterobimetallic transuranic complex $[(Cp)_3NpOUO(THF)(H_2L^{Oct})]$ **65**. The bridging oxo group between the two actinide ions provides an efficient electron transfer pathway for uranyl reduction by the more reducing U^{III} ion and to a smaller degree Np^{III}, but the extent of electron transfer is not clear cut according to the characterization methods used. The relative stability of the Pu^{III} oxidation state does not allow the formation of a similar oxo-bridged heterobimetallic in a competing donor solvent, such as THF. The molecular magnetism analyses at low temperatures for the two isostructural An-OUO (An = U (**64**) and Np (**65**)) systems are perhaps the most at-odds with the other data, suggesting that the bimetallic interaction in **65** is more like the donor-acceptor complex in the solid-state. Despite there being no apparent magnetic communication between the actinide ions, the U^{IV}-U^{V} system exhibits a single-ion based (U^{V}, $5f^1$) slow magnetic relaxation behaviour with a relaxation barrier of 19 cm^{-1} and relaxation time of 2.5×10^{-8} s at infinite temperature.

To support additionally a theorem of a decreased electron transfer to uranyl group from organoactinide, on traversing the latter series of complexes from U to Pu, the DFT calculations of Hirshfeld charge and spin density analyses are now in progress with the help of the research group of Prof. H. Georg Schreckenbach (University of Manitoba).

4 Neptunium Coordination Chemistry of the *trans*-Calix[2]Benzene[2]Pyrrolide Macrocycle

Preamble

This Chapter covers the synthetic project carried out by the author under the supervision of Prof. Dr Polly L. Arnold (University of Edinburgh) and published recently as an article in *Nature Chem.* (Section 6.3 of this thesis). The original manuscript can be consulted for the additional molecular magnetism investigations and computational bonding analyses, which were designed, performed and analysed by the group of Prof. Dr Roberto G. M. Caciuffo (personal contributions as detailed in Preamble section to Chapter 3) and by Prof. Dr Nikolas Kaltsoyannis (University College London), respectively.

4.2 Introduction

The strong and potentially useful *f*-block arene π- and δ-(back)bonding interactions have been used to generate both new C-H bond activation and functionalization reactions[163] and to stabilise the reactive metal sites, for example in the recent mono-arene complex of the formal U^{II} cation.[94] Although metal-bis(arene) complexes are widely recognised in almost all areas of the periodic table, for actinide elements only predictions of the stability are available.[164]

The possibility to better understand the potential for the actinides to participate in the subtlest of π- and δ-symmetry bonding interactions has led us to explore the coordination chemistry of the conformationally flexible, small-cavity, dianionic macrocycle *trans*-calix[2]benzene[2]pyrrolide, $(L^{Ar})^{2-}$, which has a notable capacity to bind *two* U^{III} cations forming the very unusual dinuclear complex $[(L^{Ar})U^{III}{}_2I_4]$ **67**, which contains a U^{III} cation in the bis(η^5-pyrrolyl) and one in bis(η^6-arene) sandwich forms, Chart 4.1.[165,166] The mononuclear adducts showed a remarkable structural preference for the $\eta^6{:}\kappa^1{:}\eta^6{:}\kappa^1$ metal-ligand binding of the softer U^{III} centre, i.e. $[(L^{Ar})U^{III}X]$ (X = I (**68**), BH_4 (**69**), $N(SiMe_3)_2$ (**70**), O-2,6-*t*-Bu_2-C_6H_3 (**71**)), whilst smaller, harder U^{IV} and Th^{IV} cations are typically bound in the $\kappa^5{:}\kappa^5$ metallocene-type geometry. However, an exception to this geometry was found recently in the U^{IV} complex $[(L^{Ar})U(BH_4)][B(C_6F_5)_4]$ **74**, that is a one-electron oxidation product of complex **69**, showing the small $\{U((\eta\text{-}H)_3BH)\}^{3+}$ cationic entity is located deeper within the *endo* cavity of the macrocycle and results in $\eta^1{:}\eta^5{:}\eta^1{:}\eta^5$ metal-ligand binding.

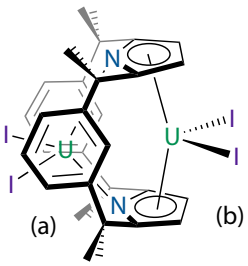

$[(L^{Ar})U^{III}{}_2I_4]$ **67**

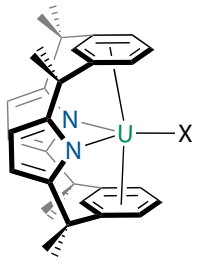

$[(L^{Ar})U^{III}X]$
X = I, **68**; X = (BH_4), **69**
X = $N(SiMe_3)_2$, **70**
X = O-2,6-*t*-Bu_2-C_6H_3, **71**

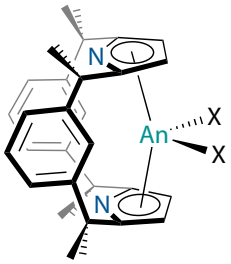

$[(L^{Ar})An^{IV}X_2]$
An = Th, X = Cl, **72**
An = U, X = I, **73**

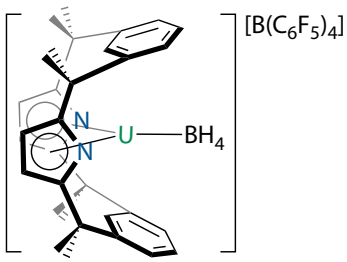

$[(L^{Ar})U^{IV}(BH_4)][B(C_6F_5)_4]$ **74**

Chart 4.1. Low-oxidation-state actinide complexes of the small-cavity macrocyclic ligand *trans*-calix[2]benzene[2]pyrrolide, $(L^{Ar})^{2-}$. Dinuclear complex $[(L^{Ar})U^{III}{}_2I_4]$ **67** shows the concomitant coordination in either the two isoelectronic (a) bis(η^6-arene) and (b) bis(η^5-pyrrolide) compartments.

Herein, we report on the range of Np^{III} complexes, which contain organometallic ligands other than historically important cyclopentadienyl and cyclooctatetraenyl anions. The dianionic macrocycle, $(L^{Ar})^{2-}$, can structurally and electronically mimic the bis(cyclopentadienyl) ligand system with unique π-bonding potential, which in turn may enable greater stabilization of the coordinated Np^{III} ions and explorative reduction chemistry.

4.3 Synthesis and Characterization of the Mono- and Dinuclear Neptunium(III) Complexes

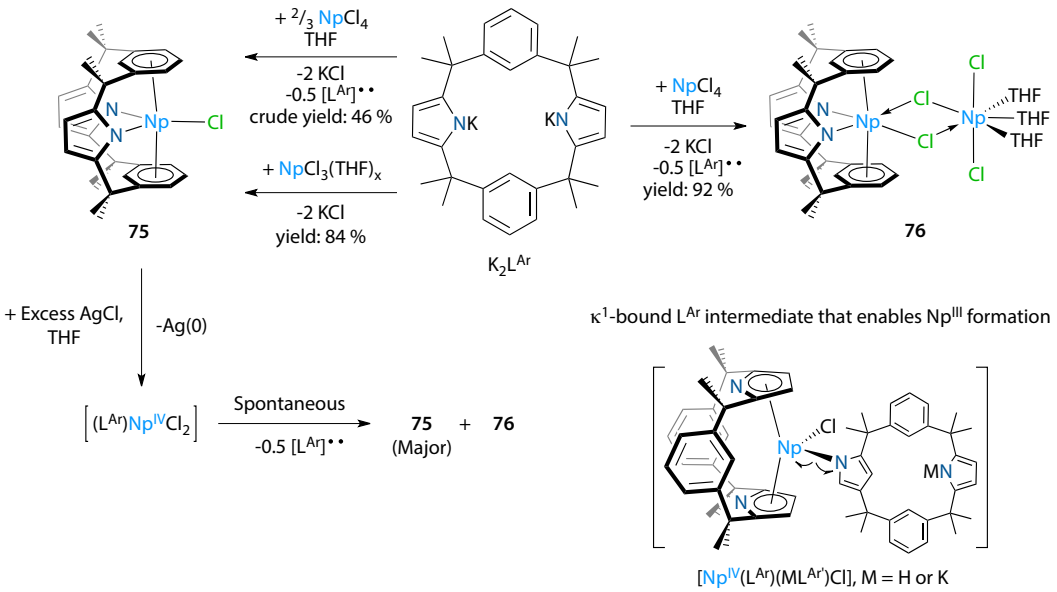

Scheme 4.1. Syntheses of Np^{III} L^{Ar} adducts $[(L^{Ar})NpCl]$ **72** and $[(L^{Ar})Np_2Cl_4(THF)_3]$ **73** from the spontaneous reduction of the Np^{IV} precursor.

The reaction between $NpCl_4$ **4** and 1.5 eq of K_2L^{Ar}, the dipotassium salt of *trans*-calix[2]benzene[2]pyrrole,[165] affords the new mononuclear complex of Np^{III} $[(L^{Ar})NpCl]$ **75** in 46 % crude yield, in the form of a red-orange solid after work-up (Scheme 4.1). The product was formed alongside organic by-products that were difficult to remove even after fractional recrystallization. However, analytically pure **75** was obtained from the equimolar reaction between the *in situ* generated $[NpCl_3(THF)_x]$ **3a** and K_2L^{Ar} and isolated as a dark-red single-crystalline material in very good yield, 84 %. Interestingly, the equimolar reaction between **4** and K_2L^{Ar} in THF at ambient temperature, followed by work-up to remove KCl and off-white organic residues result in dinuclear Np^{III} complex $[(L^{Ar})Np_2Cl_4(THF)_3]$ **76** in 92% yield, as analytically pure dark-red crystals.

The ^1H and ^{13}C NMR spectra of **75** shows the macrocyclic ligand to adopt C_{2v} symmetry and the resonances are broadened and contact-shifted owing to the presence of the paramagnetic Np^{III} ($5f^4$) centre, but enabling complete assignments, which confirms the practical utility of the multinuclear NMR spectroscopy to determine the solution-structure of the Np^{III} organometallics.

The aryl proton resonances bound with carbons C9, C11/13, and C12 in Figure 4.5 were assigned based on the ^{1}H-^{1}H COSY correlation peaks, and agree with the presumed molecular C_2-symmetry information, as three signals at 4.26, -0.38 and 4.95 ppm (relative intensity 1:2:1), respectively. The protons of the pyrrole groups associated with carbons atoms C2 and C3 in Figure 4.5 appear as one resonance at 7.07 ppm, whilst four methyl groups split into two resonances at 3.20 and 0.15 ppm, of equal intensity (6H) each. Each of these resonances show different cross peaks in the ^{1}H-^{13}C gHMQC spectrum (Figure 4.1), which allows the assignment of the ^{1}H and ^{13}C spectra. The assignments were further refined by the 500 ms 2D-ge NOESY spectrum (Figure 4.2) which shows the nOe correlation peaks for hydrogen atom of C9 (aromatic ring) and the methyl group protons adjacent to carbons C7, C16, which are more perpendicular to the aryl planes and pointed outside of the metal centre. The above analysis also correlates well with the close interaction (~0.28 Å) between the hydrogen atoms involved.

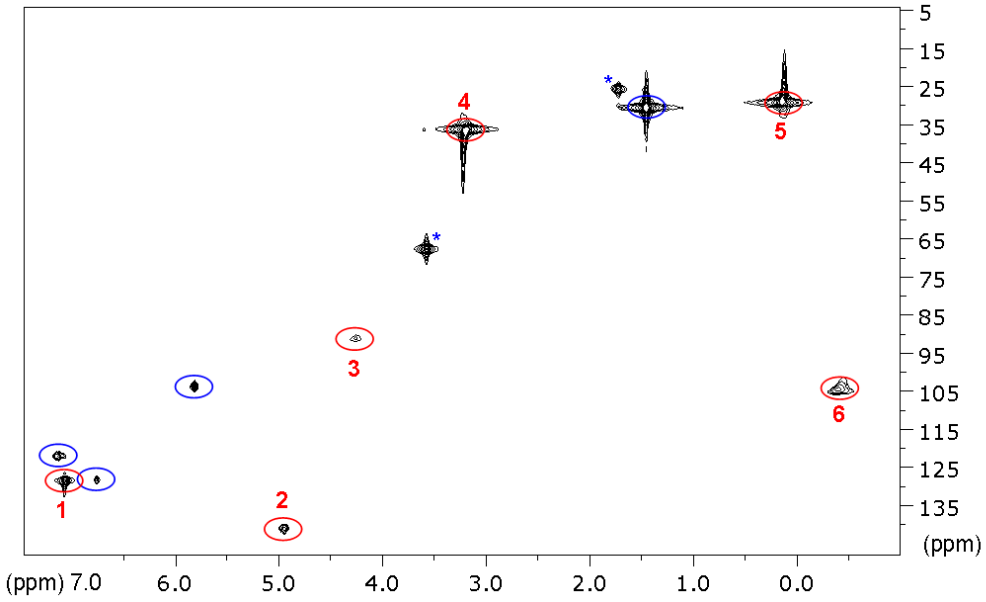

Figure 4.1. Section of the ^{1}H-^{13}C gHMQC spectrum of [(L^{Ar})NpCl] **75**. Resonances marked in red are assigned to **75**, according to the numbering scheme in Figure 4.5 (δ_H (no. of H)/ δ_C, C atom labelling): {7.07 (2H), 128.6 C2/C3}, {4.95 (1H), 141.2, C9}, {4.26 (1H), 91.1, C12}, {3.20 (6H), 36.6, C7/C16}; {0.15 (6H), 28.7, C6/C15}, {-0.39 (2H), 104.6, C11/C13}. Resonances marked in blue are of free organic-base macrocycle, H_2L^{Ar}, and the residual protio solvent resonances are marked with an asterisk.

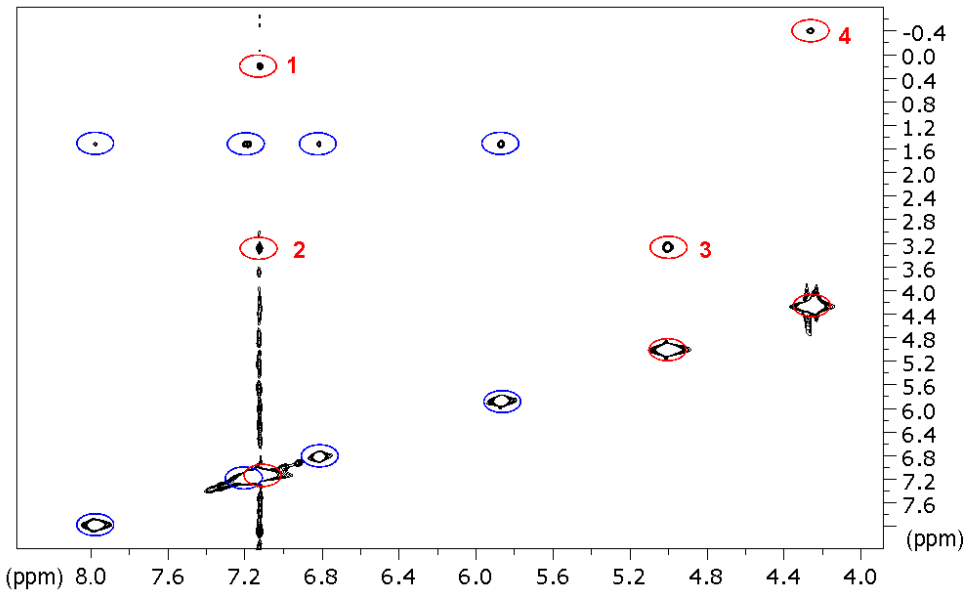

Figure 4.2. Section of the 1H 2D-ge NOESY spectrum of [(L^{Ar})NpCl] **75**. Resonances marked in red are assigned to **75**, according to the numbering scheme in Figure 4.5; cross peaks (δ_{H1}/ δ_{H2}, C atom(s) 1 to C atom(s) 2): no.1 {7.07/0.15, C2/C3 to C6/C15}, no. 2 {7.07/3.20, C2/C3 to C7/C16}, no. 3 {4.95/3.20, C9 to C7/C16}, no. 4 {4.26/-0.39, C12 to C11/C13}. Resonances marked in blue are of free organic-base macrocycle, H_2L^{Ar}.

The low solubility of complex **76** in THF-d_8 solvent precludes any analyses in a solution. Additionally, the room temperature Vis-NIR spectra of **75** in THF and DME solutions are both indistinguishable, showing identical set of sharp absorptions with the low molar absorptivity values ($\varepsilon \sim 10^1$ $dm^3 \cdot mol^{-1} \cdot cm^{-1}$) in the nIR range, as expected for *f–f* transitions (Figure 4.3). Interestingly, complex **75** exhibits reversible thermally induced solvatochromism in DME solutions, changing the colour from orange to pink on cooling from 19 to -78 °C; the solutions in THF solvent of similar **75** concentrations are pink at room temperature. The two colours for the solutions are depicted in Figure 4.4.

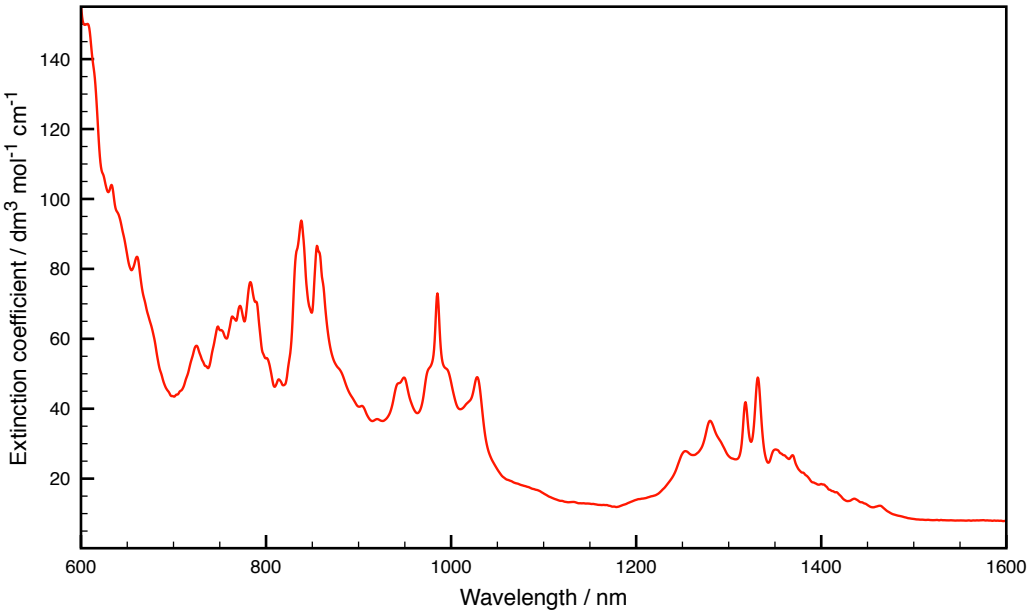

Figure 4.3. Vis-NIR spectrum of [(L^{Ar})NpCl] **75** dissolved in THF (^{237}Np concentration 2.31 mM).

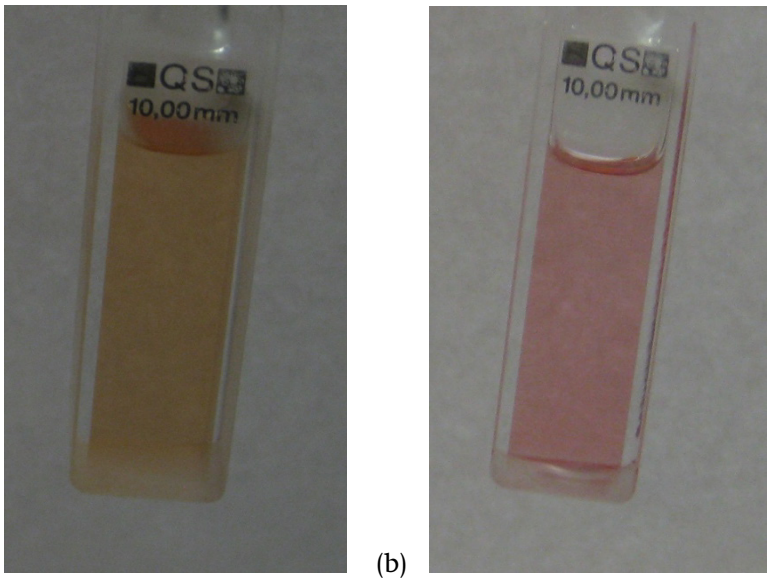

(a) (b)

Figure 4.4. Photographs of the same solution of [(L^{Ar})NpCl] **75** in DME at 19 °C (a) and cooled to -78 °C (b) demonstrating thermally induced solvatochromism; ^{237}Np concentration 0.70 mM.

The molecular structures of **75** and **76** (Figure 4.5 and Figure 4.6) both confirm binding of a single Np^{III} ion in the bis(η^6-arene) pocket of the macrocycle, which is similar to the previously reported complexes of Sm^{III} and U^{III}, whereas complex **76** formally contains an additional equivalent of $NpCl_3(THF)_3$ bound through chloride-bridging, rather than participating in ligand bridging.

The notable feature of these reactions is the reduction of Np^{IV} to Np^{III}, which can be accounted for by considering the metal-ligand binding in a κ^1-pyrrolide conformation that supports the σ-bond homolysis, providing a reducing electron to the Np ion and releasing the ligand as a radical (Scheme 4.1). The present THF donor solvent may have facilitated the required substitution of the chloride ligand by the κ^1-pyrrolide coordinated $(L^{Ar})^{2-}$ scaffold. This spontaneous reduction chemistry for Np^{IV} complexes was not reported prior to this work, but was also observed in Chapter 2.3.2 for the cyclopentadienyl ligand, which has shown a rare binding flexibility to large actinide ions and diverts from the η^5 into η^1 coordination mode. Both reduction processes are consistent with the yields and nature of the by-products and further the N-confused macrocyclic fragment κ^1-bound-$(HL^{Ar'})^-$ was demonstrated in a samarium complex $[(L^{Ar})(HL^{Ar'})SmCl]$, that is a decomposition product in Sm^{III} chemistry of the flexible macrocycle.[167] Attempts to identify the formation of $[D]_2L^{Ar}$ as a by-product from preparations carried out in THF-d_8, which would be expected for the ligand radical species abstracting the H(D) atoms from the solvent, were inconclusive.

4.3.1 Molecular structure of $[(L^{Ar})NpCl]$, 75

Red crystals of **75** suitable for X-ray crystal structure determination were obtained by diffusion of *n*-pentane into a THF solution at room temperature. The diffraction data were refined in the monoclinic space group *C*2/c (No. 15), *a* = 18.9910(14), *b* = 14.9865(11), *c* = 10.1443(8) Å, β = 110.321(1)°, with four independent molecules in the unit cell; the asymmetric unit consists of a half of a molecule of $[(L^{Ar})NpCl]$, in which the Np atom resides on the crystallographic centre of inversion.

The molecular structure of $[(L^{Ar})NpCl]$ **75**, is shown in Figure 4.5. In this complex, Np centre display η^6:κ^1:η^6:κ^1 binding modes to the benzene and pyrrolide units alternatively, as found for the isotypic Sm^{III} and U^{III} complexes. The arene sandwich Ct_{Ar}-Np-Ct_{Ar} angle, 174.20(4)° in **75** is essentially linear and features similar metrics to analogous complexes: $[(L^{Ar})UX]$ (**68-71**, range 173.4(3)-174.4(2)°) and $[(L^{Ar})SmCl]$ (175.95(8)°). The mean Np-C_{Ar} separation in **75** (2.95 Å) correlates well with those in the isostructural complex $[(L^{Ar})UI]$ **68** (range 2.95-2.98 Å) and $[(L^{Ar})SmCl]$ (2.98 Å). The uniformly short C_{Ar}-C_{Ar} distances in **75** (range 1.380(4)-1.425(4) Å) are similar to those found in **68** (1.36(2)-1.43(2) Å) and $[(L^{Ar})SmCl]$ (range 1.364(6)-1.439(6) Å), indicated that arene reduction had not taken place and considerable arene-metal

π-bonding interactions occur. The comparison of An^{III}-arene centroid distances found in **75** (2.601(1) Å) and also later in **76** (2.666(3) and 2.609(3) Å) with that of the weakly-bound U^{III} arene complex $[U(BH_4)_3(\eta^6\text{-}C_6Me_6)]$[168] (2.581(8) Å). After correction for the larger ionic radius of the six-coordinated ions U^{3+} than Np^{3+} (1.025 *vs.* 1.01 Å),[141] these data clearly demonstrate only minimal metal-arene interaction in both Np^{III} complexes. The difference in M-Cl bond lengths between $[(L^{Ar})SmCl]$ (2.618(3) Å) and **75** (2.6688(9) Å), corrected for ionic radii of the six-coordinated Sm^{3+} and Np^{3+} metal ions, [141] is the same within standard uncertainties (-0.0012 Å).

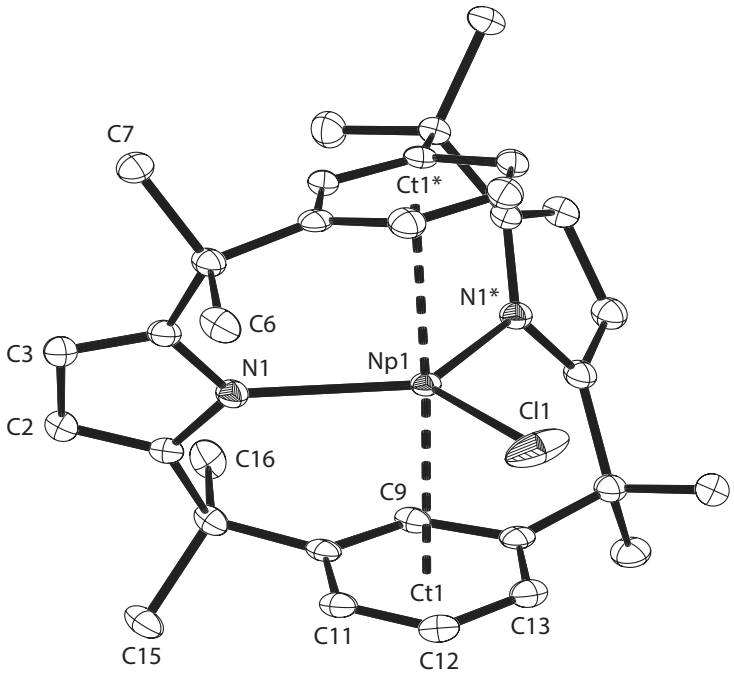

Figure 4.5. ORTEP drawing of $[(L^{Ar})NpCl]$ **75** with thermal ellipsoids plot (50 % probability for non-H atoms). All hydrogen atoms were omitted for clarity. The mirror symmetry related atom and centroids names are labelled with asterisks; selected bond lengths [Å] and angles [°] for **75**: Np1-Cl1 2.6694(9), Np1-N1 2.447(2), Np1-C_{aryl} range 2.853(2) to 3.010(3), Ct1-Np1-Ct1* 174.20(4), N1-Np1-Cl1 120.50(4), N1-Np1-N1* 118.97(8), N1*-Np-Cl1 120.51(4).

4.3.2 Molecular structure of $[(L^{Ar})Np_2Cl_4(THF)_3]$, 76

Dark-red, block crystals of **76** suitable for X-ray crystal structure determination were obtained by layering of a THF solution with *n*-hexane at room temperature. The diffraction data were refined in the triclinic space group *P-1* (No. 2), a = 10.5639(7), b = 13.6771(8), c = 18.1083(11) Å, α = 75.147(1), β = 75.732(1),

γ = 84.334° with two independent molecules in the unit cell; the asymmetric unit consists of a single molecule of $[(L^{Ar})Np_2Cl_4(THF)_3]$, containing additional half of the uncoordinated THF molecule in the lattice.

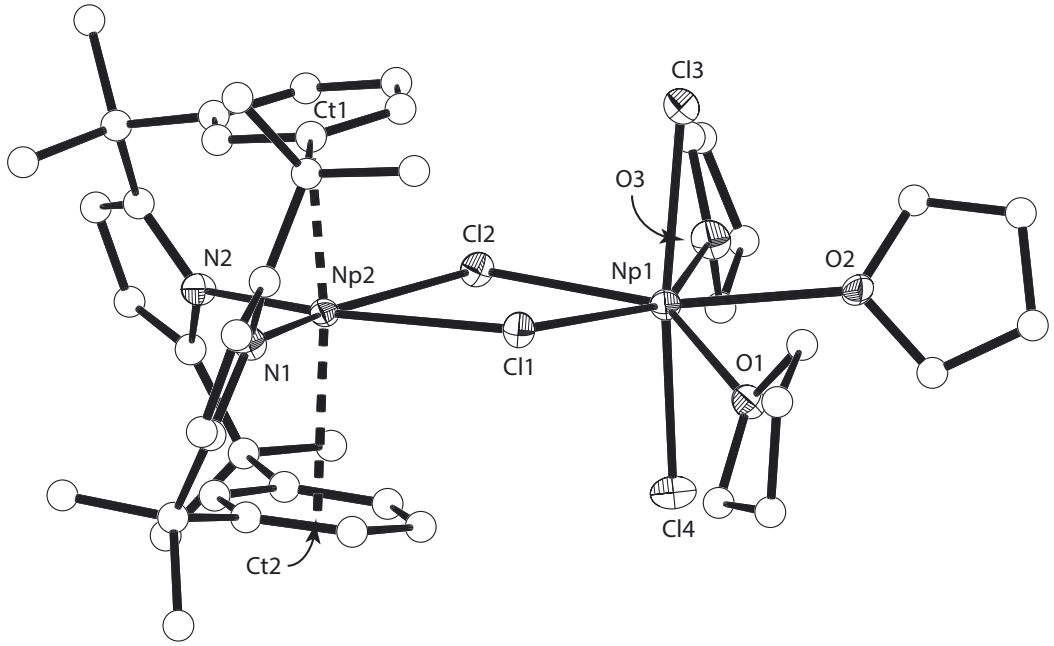

Figure 4.6. Molecular structure of $[(L^{Ar})Np_2Cl_4(THF)_4]$ **76** with thermal ellipsoids drawn at 50 % ellipsoid probability for non-H/C atoms. All hydrogen atoms and lattice solvent molecules were omitted for clarity; selected bond lengths [Å] and angles [°] for **76**: Np1-Cl1 2.814(2), Np1-Cl2 2.796(2), Np1-Cl3 2.723(2), Np1-Cl4 2.683(2), Np1-O1 2.493(4), Np1-O2 2.510(4), Np1-O3 2.537(4), Np2-Cl1 2.864(2), Np2-Cl2 2.871(2), Np2-N1 2.496(6), Np2-N2 2.487(5), Np2-Ct1 2.667, Np2-Ct2 2.609, Np2-C_{aryl} range 2.854(6) to 3.022(6), Cl1-Np1-Cl2 76.10(5), Cl1-Np2-Cl2 74.14(5), Np1-Cl1-Np2 104.51(5), Np1-Cl2-Np2 104.82(6), N1-Np2-N2 115.8(2), Cl3-Np1-Cl4 170.93(6), Ct1-Np2-Ct2 173.2(1).

The molecular structure of dinuclear $[(L^{Ar})Np_2Cl_4(THF)_3]$ **76** is best described as a formal adduct of complex **75** with one equivalent of $NpCl_3(THF)_3$. The presence of the two chlorido ligands bound to Np^{III} ion residing in the bis(η^6-arene) pocket in **76**, instead of one for **75** bears only minimal influence on the conformation of the macrocyclic scaffold. All metrical parameters of the metal-macrocycle interactions in **76** closely resemble those of $[(L^{Ar})NpCl]$ **75**, with only slightly longer Np-N bond distances (2.486(5) and 2.496(6) Å in **76** *vs.* 2.447(2) Å for **75**). The $NpCl_3(THF)_3$ coordination entity shows an irregular pentagonal bipyramidal geometry around the Np^{III} centre, with the two axial chlorine atoms distorted away from linear configuration by *ca.* 9.0°. The Np^{III}-Cl distances are very similar to those

reported for other structurally authenticated Np^{III} complexes, and longer than in molecular Np^{IV} complexes.[161,169]

4.4 One-Electron Oxidation and Reduction Reactions of [(L^{Ar})NpCl]

4.4.1 Oxidation studies of [(L^{Ar})NpCl], 75, with AgCl

With the goal to isolate the intermediate Np^{IV} adduct of L^{Ar}, complex [(L^{Ar})Np^{III}Cl] **75** was reacted with a convenient one-electron, solid-state oxidant, AgCl, in a THF solution, Scheme 4.1. This approach was advantageous as it not only allowed monitoring the progress of the reaction in a solution by colour change, but also because of the formation of solids. In fact, an instantaneous colour change of the solution from red to maroon and concomitant precipitation of the shiny needles of metallic silver suggested the successful re-oxidation of the Np^{III} centre in **75** and *in situ* formation of [(L^{Ar})$Np^{IV}Cl_2$]. However, as before, even at -78 °C the gradual precipitation of organic decomposition products and the colour change of the solution back to red validated both the instability of the Np^{IV} centre bound to $(L^{Ar})^{2-}$. A number of the resulting red single crystals were analysed by measurement of the unit cell parameters and indicated the formation of a small amount of the complex [(L^{Ar})Np_2Cl_2(THF)] **76**, which is consistent with the decomposition reaction of the unstable product [(L^{Ar})$Np^{IV}Cl_2$].

4.4.2 Reduction studies of [(L^{Ar})NpCl], 75, with NaK_3

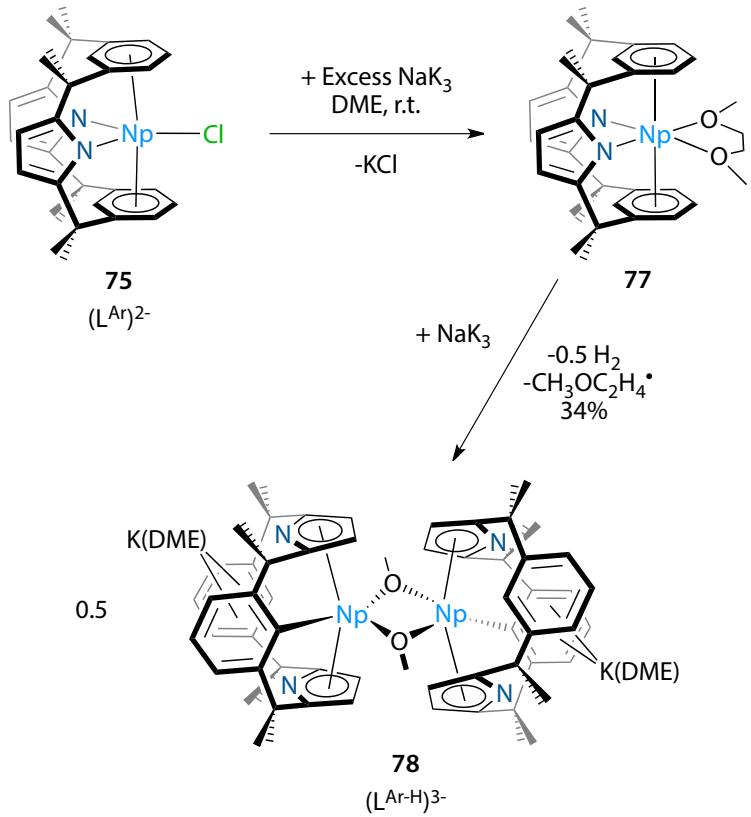

Scheme 4.2. Reduction of [(L^{Ar})NpCl] **75** with NaK_3 to form thermally unstable Np^{II} complex [(L^{Ar})Np^{II}(DME)] **77**, which gradually decompose into the triply deprotonated (L^{Ar-H})$^{3-}$ Np^{III} aryl complex [K(DME)(L^{Ar-H})Np(OMe)]$_2$ **78**.

In a reaction designed to reduce the Np^{III} centre in complex [(L^{Ar})NpCl] **75**, a suspension of **75** in DME was orbitally shaken (2800 r.p.m.) with NaK_3 alloy for a short period of 20 seconds, during which time the reddish starting material was consumed and the colour of the solution changed to brown and later to purple-black and KCl precipitated (Scheme 4.2). The solution of product was isolated from the excess of NaK_3 and solid by-products by passage through a silylated glass fibre membrane and analysed within minutes by optical spectroscopy. The obtained spectrum (Figure 4.7, black trace) shows strong absorption peak centred at 540 nm and a single broad band in between 1100 and 1420 nm with λ_{max} = 1275 nm. The extremely strong absorption in the UV-Vis region of the spectrum shows the predominant $d \rightarrow d$ and $d \rightarrow \pi^*$ character and can be further assigned to the formation of the new formal oxidation state Np^{II} in the neutral bis(arene) complex [(L^{Ar})Np^{II}(DME)] **77**. Similar

spectroscopic features were recently observed on the reduction of organometallic Ln^{III} and An^{III} precursors to the complexes of the general formula $[K(2.2.2\text{-cryptand})][M^{II}(\eta^5\text{-Cp}')_3]$; the uranium homologue **46** displays a broad absorption at 600 nm (ε = 750 $dm^3 \cdot mol^{-1} \cdot cm^{-1}$) and ink-black complex $[K(2.2.2\text{-cryptand})][Th^{II}(\eta^5\text{-Cp''})_3]$ at 650 nm (ε = 23 000 $dm^3 \cdot mol^{-1} \cdot cm^{-1}$). Furthermore, time-dependent spectra of the same solution of **77** were measured in which initial broad band at 1275 nm quickly bleached and a new set of low-intensity line-like absorptions falling in the range of 780 to 1350 nm grew over 12 h period, Figure 4.7. These changes were also accompanied by lightening of the bulk of the investigated solution to a reddish-brown colour, which together with optical spectroscopy measurements, supports the formation of the kinetically unstable formally Np^{II} complex of $(L^{Ar})^{2-}$.

To provide more detailed insight into the formation of complex **77** with UV-Vis-NIR spectroscopy by minimizing the effects of potential side-reactions and time delay due to sample preparation, a precooled (-30 °C) solution of $[(L^{Ar})NpCl]$ **75** and NaK_3 was measured in time intervals as the sample was allowed to warm to room temperature in the spectrometer chamber which is maintained at 19 °C; the resulting stacked spectra are shown in Figure 4.8. Unlike the appearance and further growth in intensity of the similar absorption at 1275 nm is confirmed, the sharp absorption at 540 nm is considerably flattened and being one of the triad of considerably broadened second two maxima at *ca.* 590 and 630 nm. The multicentre character of the latter band is, however very similar to those found previously in the UV-Vis spectra of 'ate-'type complexes of the formally Th^{II} and U^{II} centres.

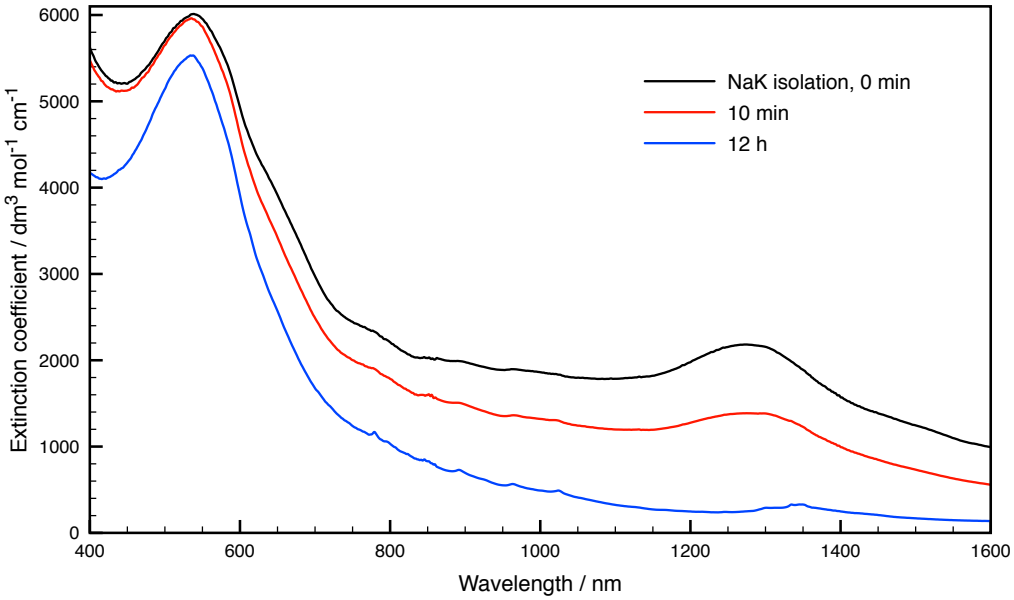

Figure 4.7. Vis-NIR spectra of *in situ* generated [(L^{Ar})Np^{II}(DME)] **77** in DME solution; legend indicate the time period after the isolation of the crude supernatant (^{237}Np concentration 2.47 mM).

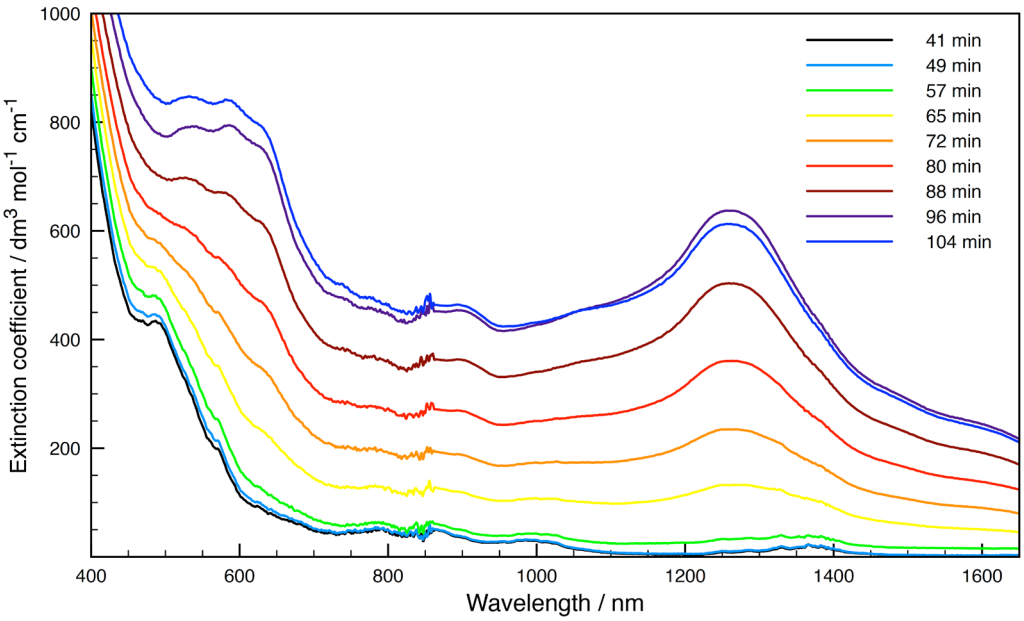

Figure 4.8. Time-dependent Vis-NIR spectra of DME solutions of **75** and NaK_3 showing the formation of [(L^{Ar})Np^{II}(DME)] **77**; legend indicate the time period between the introduction of the reductant and spectrum acquisition (^{237}Np concentration 0.56 mM).

In order to additionally prove the position of the reducing electron on the metal centre rather than on the ligand, the UV-Vis spectra of the dipotassium salt K_2L^{Ar}

contacted with NaK_3 in DME solvent were acquired, which show only a single broad absorption at 716 nm, characteristic for the very unstable, deep blue electride solution of the NaK_3/DME system alone, Figure 4.9.

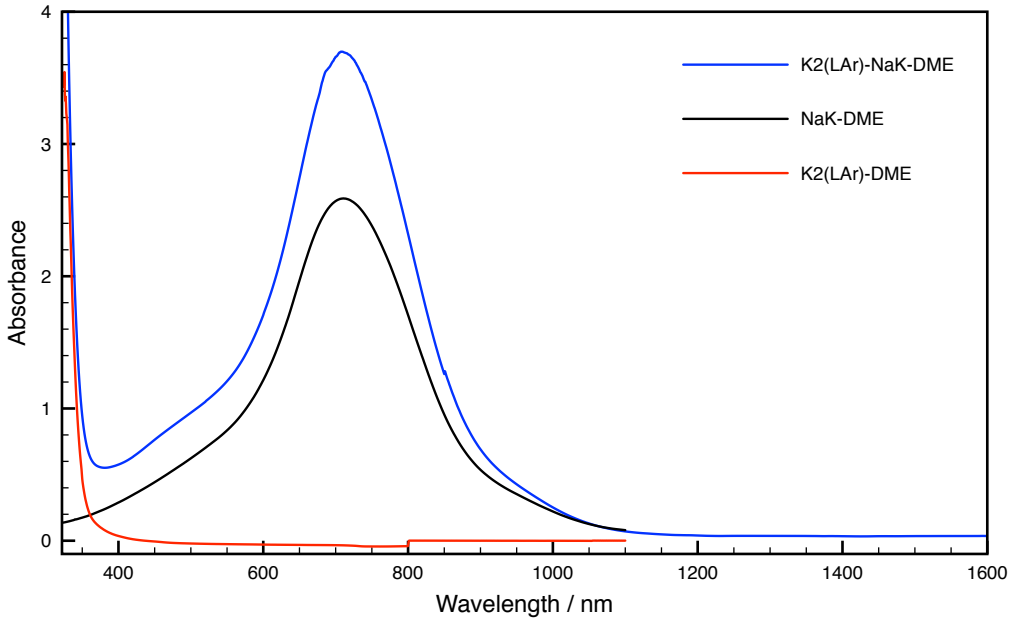

Figure 4.9. Vis-NIR spectra of DME solutions of $[K_2(L^{Ar})]$ (red trace; 9.69 mM) and an electride generated from NaK_3 in DME at 20 °C (black trace) and in $[K_2(L^{Ar})]$ solution in DME at 20 °C (blue trace, 9.69 mM L^{Ar}).

On two occasions, small black plate-shaped crystals that had grown in the product solution were analysed by single crystal X-ray diffraction but only weak diffraction was measured and the crystals showed signs of considerable surface degradation so further analysis was not possible. However, diffusion of *n*-pentane into the parent filtrate yielded long needle-shaped reddish brown single crystals over 48 h which were characterised by single crystal X-ray diffractometry as $[K(DME)(L^{Ar\text{-}H})Np(OMe)]_2$ **78**, which would formally be the product of metalation of the ligand associated with re-oxidation back to Np^{III}. The proposed mechanism for the formation of both **77** and **78** complexes, and observed persistence of the **77** in the presence of excess NaK_3 are shown in Scheme 4.3 and the latter feature also demonstrated in Figure 4.10.

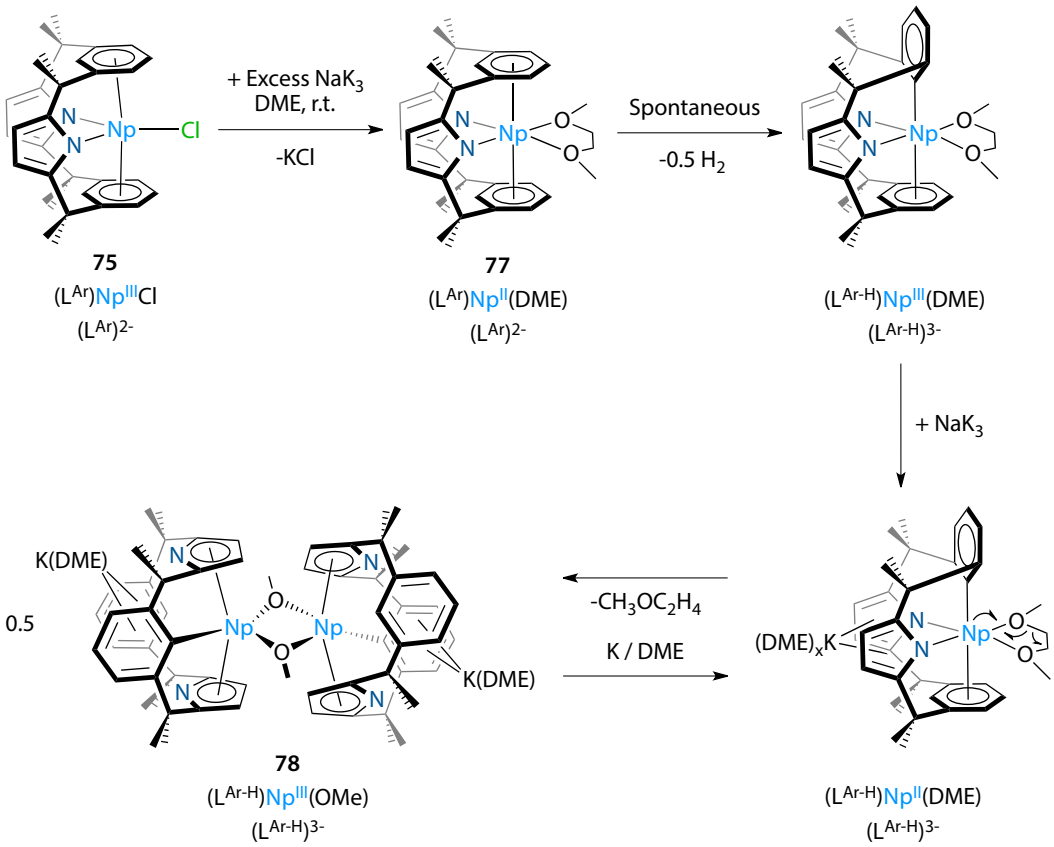

75
$(L^{Ar})Np^{III}Cl$
$(L^{Ar})^{2-}$

77
$(L^{Ar})Np^{II}(DME)$
$(L^{Ar})^{2-}$

$(L^{Ar-H})Np^{III}(DME)$
$(L^{Ar-H})^{3-}$

78
$(L^{Ar-H})Np^{III}(OMe)$
$(L^{Ar-H})^{3-}$

$(L^{Ar-H})Np^{II}(DME)$
$(L^{Ar-H})^{3-}$

Scheme 4.3. Proposed reaction pathway for the reduction reaction of [(LAr)NpCl] **75** with NaK_3 to target [(LAr)Np^{II}(DME)] **77** and the subsequent isolation of the complex [K(DME)(L^{Ar-H})Np(OMe)]$_2$ **78**.

(a) 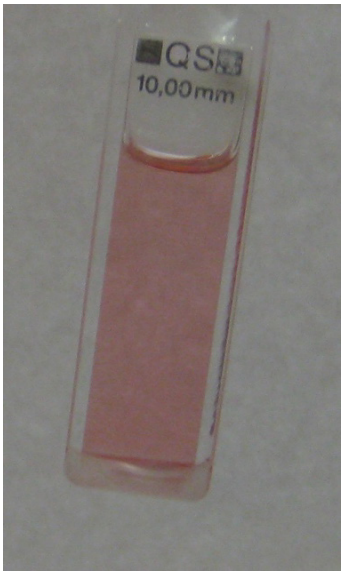 (b) 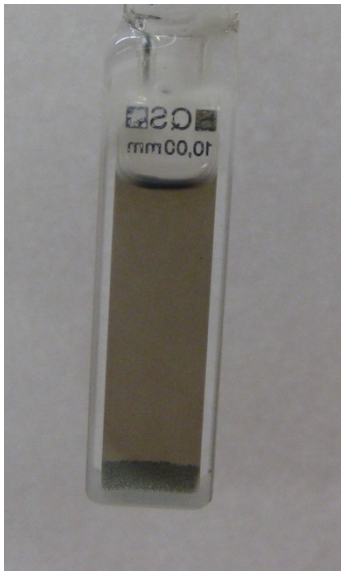

Figure 4.10. Photographs of DME solutions of (a) [(L^{Ar})NpCl] **75** at -78 °C and (b) the same solution after one hour of conditioning with NaK_3 at 19 °C; ^{237}Np concentration 0.70 mM.

4.4.3 Molecular structure of [K(DME)(L^{Ar-H})Np(OMe)]$_2$, 78

Intense red-brown crystals of **78** suitable for X-ray crystal structure determination were obtained by diffusion of *n*-pentane vapour into DME solution at room temperature. The diffraction data were refined in the monoclinic space group $P2_1/n$ (No. 4), a = 10.205(3), b = 20.025(5), c = 17.800(4) Å, β = 105.645(5)°, with 2 dinuclear molecules (or 4 mononuclear fragments) in the unit cell; the asymmetric unit consists of a half of the independent dinuclear fragment, [K(DME)(L^{Ar-H})Np(OMe)], which forms a dimer about the two-fold rotoinversion axis localized in the centre of gravity and perpendicular to the Np_2O_2 bridging unit.

The molecular structure of [K(DME)(L^{Ar-H})Np(OMe)]$_2$ **78** (Figure 4.11) features the novel trianionic form of the macrocyclic ligand, (L^{Ar-H})$^{3-}$ due to presence of one singly-metalated arene ring and concomitant binding of the polarisable potassium counter-ion within the bis(η^6-arene) cavity. This confirms the 'ate-'character of the complex and indicates an asymmetrical coordination. The Lewis-acidic fragment [Np^{III}(OMe)] is bound through two pyrrolide groups in the resulting κ^5:κ^5 metallocene-type geometry, a conformation typically attained by the An^{IV} complexes of (L^{Ar})$^{2-}$ and observed only previously for the An^{III} in the highly-strained di-U^{III} complex [(L^{Ar})U_2I_4] **67**. The complementary Np-OMe linkages originated presumably from the C-O bond cleavage of the neutral DME

complex, which is congruent with the assignment of the transiently stable Np^{II} metallic centre in **77**. The structure of **78** is dimeric in the solid-state showing two methoxide groups form asymmetric bridges between molecular fragments; the shorter of the two Np-O distances (2.296(8) Å) is close to that of the dative Np^{IV}-O bond of diphenylmethylphosphine oxide in the reported complex $[NpCl_3(Cp)(OP(Me)Ph_2)_2]$[161] (2.277(12) Å) and significantly greater than the single covalent Np-O(phenolato) bond length in **29** (2.136(7) Å).

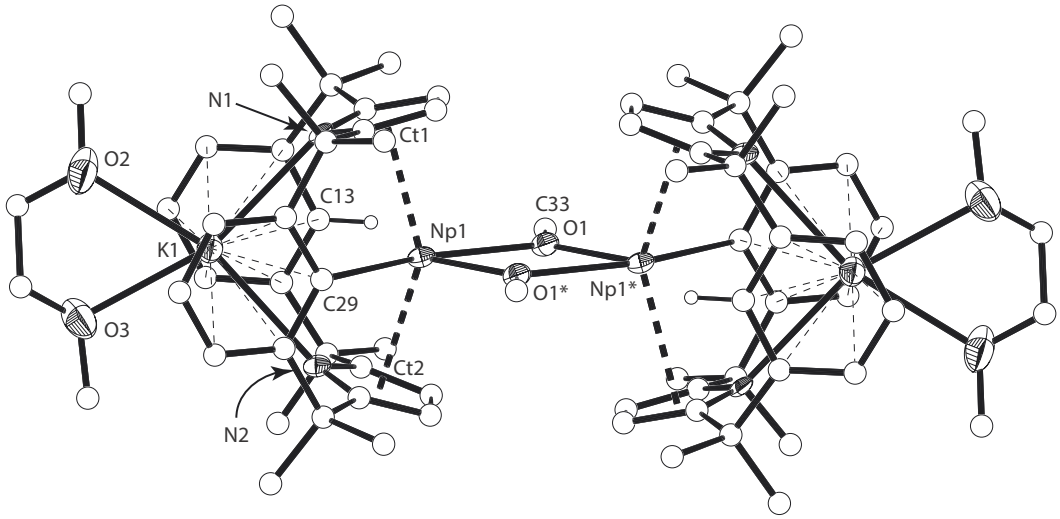

Figure 4.11. Molecular structure of $[K(DME)(L^{Ar\text{-}H})Np(OMe)]_2$ **78** with thermal ellipsoids drawn at 50% ellipsoid probability for non-H/C atoms. All hydrogen atoms (except that on C13) and lattice solvent molecules were omitted for clarity; selected bond lengths [Å] and angles [°] for **78**: Np1-O1 2.288(9), Np1-O1* 2.460(8), Np1-C29 2.660(13), Np1-Ct1 2.621(4), Np1-Ct2 2.652(4), Np1-C_{pyrr} range 2.757(12) to 2.998(11), K1-N1 2.913(11), K1-N2 2.886(11), K1-Ct3 3.059(5), K1-C_{aryl} range 3.051(13) to 3.366(15), K1-O2 2.727(11), O1-Np1-O1* 67.1(3), Np1-O1-Np1* 112.9(3), Ct1-Np1-Ct2 143.98(15),N1-K1-N2 95.4(3).

4.5 Concluding Remarks

Although the studies of transuranic π-aromatic organometallic complexes are historically and presently seminal to explore and validate the bonding theory in actinide compounds and to correlate their physicochemical properties, surprisingly only simple ligand systems i.e. either five- or eight-membered carbocyclic anions had been used to date. Prior to this work no transuranic metal-arene interactions have been reported.

The experimental work discussed in this chapter shows a number of unprecedented chemical and electronic behaviours for the organometallic Np^{III} complexes supported by the *trans*-calix[2]benzene[2]pyrrolide ligand, $(L^{Ar})^{2-}$.

In strong contrast to recently investigated thorium and uranium L^{Ar} complexes, the salt metathesis reactions of $NpCl_4$ with K_2L^{Ar} lead to the isolation of two novel Np^{III} complexes, $[(L^{Ar})NpCl]$ **75** and $[(L^{Ar})Np_2Cl_4(THF)_3]$ **76**, depending on the stoichiometry of the reactants used; both resulting complexes are the first examples of the bis(arene) sandwich motif in transuranic chemistry. This spontaneous reduction to Np^{III} can be seen analogous to previously described for the $[K\{Np(Cp)_4\}]$ **43** (*cf.* Chapter 2.3.2) and in both cases accounted for by considering the ability of the ligand to attain either κ^1 or η^1 binding of the metal-ligand, which supports σ-bond homolysis. The exceptionally strong preference of L^{Ar} for Np^{III} centre was further evidenced in a redox transmetallation reaction between $[(L^{Ar})NpCl]$ **75** and AgCl, which produced solutions postulated to contain $[(L^{Ar})Np^{IV}Cl_2]$ and showed the remarkable instability of the Np^{IV}-L^{Ar} compound even at -78 °C, leading to the mixture containing **75** and **76** complexes.

Considering the significant stabilization given to the Np^{III} centre by the L^{Ar} scaffold and the recent advances in formally An^{II} organometallic complexes has led us to study the reductive chemistry of **75**. A reaction of **75** with excess NaK_3 in DME gave us the putative purple/black arene-Np^{II} neutral complex $[(L^{Ar})Np^{II}(DME)]$ **77**, which was characterized only by absorption spectroscopy in the solution. However, the isolated solutions of **77** quickly decay at room temperature, presumably due to fragmentation of the coordinated DME molecule, which produced the reddish-brown complex $[K(DME)(L^{Ar\text{-}H})Np(OMe)]_2$ **78**. The molecular structure of **78** evidenced two remarkable features: 1) an asymmetrical triply deprotonated ligand form due to metalation of one of the arene groups, $(L^{Ar\text{-}H})^{3-}$ and 2) the first crystallographically characterized 'metallocene-type' geometry measured for Np^{III}.

Additionally, the resulting complexes **75**-**78** provide more direct analysis of reactivity and spectral and structural properties as a function of actinide metal centre, its oxidation state and bonding. Complex **75** complemented the first isostructural set of f-block elements organometallics, enabling computational analysis of the extent of covalency in the bonding across the Sm^{III}, U^{III}, Np^{III} triad (Prof. Dr Nicolas Kaltsoyannis, University College London) and the molecular magnetism studies (Prof. Dr Roberto G. M. Caciuffo, ITU). The latter indicated the ratio between the out-of-phase component of the AC susceptibility

and DC susceptibility is negligible down to T = 10 K, and rises to the maximum of *ca.* 0.06 at the lowest attainable temperature, T = 2K, which can be attributed to slowing down the magnetization dynamics.

Notwithstanding the limitations related to work under full radiological regime, the study suggests new prospects for the low oxidation state, anaerobic chemistry of transuranium elements.

5 Experimental Details

Caution! Compounds of the ^{237}Np isotope represent a potential health risk owing to α emission ($Q\alpha$ = 4.958 MeV), although this is limited by the long half-life of the radionuclide ($t_{1/2}$ = 2.14 × 10^6 years) and its resulting low specific activity (a = 25.9 MBq g^{-1}). More importantly, ^{237}Np decays to ^{233}Pa ($t_{1/2}$ = 26.97 days, a = 777 TBq g^{-1}), which is a potent β emitter (Q^- = 0.570 MeV) which can result in radiation exposure due to penetration of the gloves and skin. Compounds of ^{239}Pu ($t_{1/2}$ = 2.411 × 10^4 years, a = 2.30 GBq g^{-1}) have a strong α emission ($Q\alpha$ = 5.157 MeV). Handling of both ^{237}Np and ^{239}Pu isotopes should be undertaken in a properly regulated and controlled radiological facility and a more detailed safety envelope was described in Chapter 1.2 of this thesis.

5.1 Chemicals

Commercially available reagents and solvents were obtained from Sigma-Aldrich Co., ACROS Organics, STREM Chemicals Inc. or ABCR GmbH & Co. KG and used as received unless otherwise stated. Oxygen 6.0N and argon 6.0 N were supplied by basi Schöberl GmbH & Co. KG and the latter purified with Agilent Technologies Big Moisture and Oxygen Traps to achieve sub-5 and sub-1 ppb levels of the corresponding impurities respectively. Anhydrous grade solvents *n*-pentane, *cyclo*-pentane, *n*-hexane, benzene, toluene, diethyl ether, 1,2-dimethoxyethane and tetrahydrofuran were purified immediately before use by distillation from NaK alloy (K_2Na, 77.28 % K, eutectic) under argon. Deuterated tetrahydrofuran (99.5 atom % D) was stirred with NaK alloy until a persistent pale blue colour of the solvated electrons remains, and vacuum-transferred prior to use. Commercial 2.2.2-cryptand (4,7,13,16,21,24-hexaoxa-1,10-diazabicyclo-[8.8.8]-hexacosane) was melted under vacuum (110 °C, 6 × 10^{-4} mbar, 1 h) and recrystallized on cooling the hot, concentrated *n*-hexane solution to -25 °C. High-potassium NaK alloy (K_3Na, 83.6 % K) used in the reduction studies was obtained by combining the oxide-free metallic sodium and potassium metals under argon in a self-driven liquefaction process. Anhydrous metal precursors $AnCl_4$ (An = ^{238}U, ^{237}Np) and $^{239}PuCl_3$, were prepared by chlorination of the corresponding dioxides with a Cl_2/CCl_4/Ar gas mixture according to minor modifications of literature methods.[7,67] Crystalline samples of [$^{238}U(Cp)_3Cl$] **38** and [$^{239}Pu(Cp)_3(THF)$] **59** were prepared according to protocols outlined by Marks *et al.*[170] and Crisler *et al.*,[134] which were further refined by Dr Christos Apostolidis (ITU). $[UO_2(py)(H_2L^{Et})]$[147] and $[UO_2(THF)(H_2L^{Oct})]$ **61**[158] were synthesized using literature methods and further purified by extraction with

n-hexane and *n*-hexane / THF mixture (6:4). The extraction process converted the pyridine adduct quantitatively into the crystalline THF adduct $[UO_2(THF)(H_2L^{Et})]$ **60** (having an additional $^1/_4$ molecule of THF in the crystal lattice), which was isolated in the form of a green monocrystalline solid, suitable for X-ray diffraction; Complex **61** formed large, dark green crystals containing one additional molecule of THF in the crystal lattice. KCp,[171] TlCp,[172] and $[K_2L^{Ar}]$[165] were prepared according to the literature.

5.2 Experimental Details

General notes

The manipulations with ^{237}Np and ^{239}Pu radionuclides were conducted in the radiochemical laboratories at the Joint Research Centre (JRC) – Institute for Transuranium Elements (ITU), Karlsruhe, Germany. The provisions and rules in the Institute Manual M0020/M4/R3 (ver. May 2013) pertaining to radiation protection and safety were observed. Unsealed transuranium compounds were manipulated in dinitrogen filled (99+%), negative-pressure radiological gloveboxes. The glovebox for preparative chemistry was fitted with an automated dual vacuum/argon manifold and standard Schlenk techniques were used. Extraction processes refer to continuous sinter-glass extraction according to the modified literature method for extremely reactive solids.[173] A UV-Vis-NIR optical chamber and an ATR-IR spectrometer were contained within radiological gloveboxes to enable direct measurements. ATR-IR spectra were obtained using Bruker ALPHA FT-IR spectrometer fitted with a single reflection Platinium-ATR (diamond) module. Absorption bands are assigned as very weak (vw), weak (w), medium (m) and strong (s). Electronic absorption spectra were acquired in the range of 250-1650 nm at 120 nm · min^{-1} scan rate using Perkin-Elmer Lambda 19 UV/Vis/NIR spectrometer and semi-micro quartz cells (Suprasil®) with a path-length of 10.00 mm. The Vis-NIR spectra of time depending investigations of the reduction products of **75** with NaK_3 alloy were recorded at room temperature from 400 to 1650 nm with the speed of 980 nm min^{-1}. The ^1H NMR spectra were recorded on the Bruker Ascent™ 400 MHz WB NMR/DNP spectrometer equipped with a Bruker Triple Resonance Broad Band Probe (TBI). Degassed fluoropolymer NMR tube liners (4 mm nominal O.D.; 140°C, 6×10^{-4} mbar, 12 h) were charged with the liquid samples ensuring that the outer surface remained free from contamination, and sealed. The sealed liner

was then transferred into a standard borosilicate glass NMR tube placed in a PVC bag, which was sealed by welding. Chemical shifts were calibrated against residual protio solvent signal and are reported relative to tetramethylsilane (δ = 0 ppm).

Owing to the negligible radiation exposure from depleted uranium (99.68% ^{238}U, a = 4.04 × 10^{-7} Ci g^{-1}), only committed dose precautions and environmental protection policies applied for uranium compounds. The manipulations of depleted uranium compounds were carried out in a fume cupboard equipped with a combined activated charcoal and HEPA class H14 filtration system using an appropriate hand protection (nitrile, neoprene) according to the actual chemical hazards. The preparative work was conducted under an argon atmosphere using standard Schlenk techniques. Elemental analyses were carried out by Mikroanalytisches Laboratorium Kolbe, Mülheim an der Ruhr, using co-incineration with vanadium pentoxide method.

The analyses of complexes $[U(Cp)_3]$ **39** and $[(Cp)_3UOUO(THF)(H_2L^{Oct})]$ **62** were carried out in the School of Chemistry at the University of Edinburgh by fellow PhD research students Markus Zegke and Marketa Suvova in the Arnold group. ^1H and $^{13}C\{^1H\}$ NMR spectra were recorded at 298 K on AVA500 spectrometer at operating frequencies of 500.23 and 125.77 MHz respectively, and were referenced internally to residual protio solvent signal and are reported relative to tetramethylsilane (δ = 0 ppm). The infrared spectrum of **62** was recorded on a Jasco 410 spectrophotometer. Electronic absorption spectra were measured in the range 900-2100 nm using JASCO V-770 UV-Visible/NIR spectrophotometer and macro quartz cell (Suprasil®, 10.0 mm path-length) fitted with J. Young's valve.

5.3 Compounds and Reactions of Chapter 2

$[Np(Cp)_3Cl]$ **14**

MF = $C_{15}H_{15}ClNp$

MW = 467.78(2) g mol^{-1}

oxygen sensitive

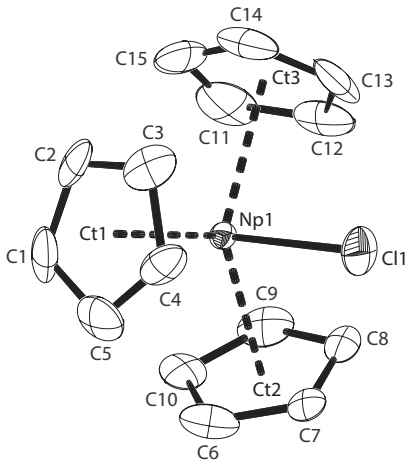

A 25-mL Schlenk flask was charged with $^{237}NpCl_4$ (481.0 mg, 1.27 mmol) and potassium cyclopentadienide (392.9 mg, 3.77 mmol). THF (18 mL) was added and the reaction mixture was stirred and heated under gentle reflux for 16 h. During this time an off-white precipitate formed and the colour of the supernatant changed to intense brown. The solvent was removed under reduced pressure and the resulting dark brown residue was extracted with *n*-pentane for 24 h. The large, metallic-lustrous, deep brown single crystals of $[^{237}Np(Cp)_3Cl]$ **14**, were collected, rinsed with pentane and dried shortly under vacuum (20 °C, $<5 \times 10^{-3}$ mbar); isol. yield 512.0-525.6 mg, 87.1-89.4 %.

^1H NMR (C_6D_6 ,293.1 K, 400.33 MHz): δ_H = -21.49 (s, 15H) ppm.
^1H-^{13}C gHMQC (C_6D_6 ,293.5 K, 400.34 MHz): $\{\delta_H, \delta_C\}$ = {-21.34, 4.6} ppm.

Radiological concerns prohibited combustion-based evaluation of the C and H content of **14**.

$[Np(Cp)_3]$ **34**

MF = $C_{15}H_{15}Np$

MW = 432.33(2) g mol^{-1}

pyrophoric

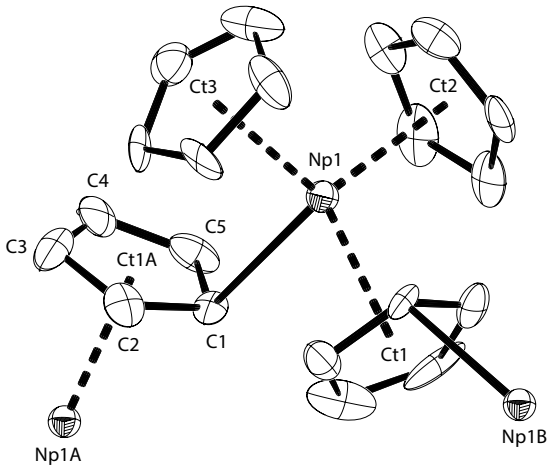

A 25-mL Schlenk tube was charged with $[^{237}Np(Cp)_3Cl]$, **14**, (230.6 mg, 0.493 mmol), solid sodium mercury amalgam (248 mg, 5.03%, 1.1 eqv.) and mercury metal (2.246 g). Diethyl ether (10 mL) was added and the reaction mixture was stirred vigorously for 12 h. During this time a dark green/grey suspension formed and the dichroic, dark brown to olive green supernatant isolated by filtration (fritted glass disk, 10-16 µm porosity). The filter cake was extracted with diethyl ether until no visible change in fresh eluent colour and the combined extracts evaporated to dryness under vacuum (i). The resulting bitumen-black solid was extracted with 3.5% $_{v/v}$ diethyl ether in *n*-pentane for 160 h (ii). The resulting dark brown, almost black single crystals of $[^{237}Np(Cp)_3]$, **34** were collected and dried shortly under vacuum (20 °C, $<5 \times 10^{-3}$ mbar); isol. yield 160-168 mg, 75-79 %.

Remarks: (i) The shiny pale green crystals deposited on concentration and cooling of the solutions. Attempts to isolate the crystals at room temperature resulted in instantaneous decomposition, which precluded further characterization of this material. (ii) Benzene and toluene solvents were found capable to extract the intrinsically contained complex $(\mu\text{-O})[Np(Cp)_3]_2$, **55**; a trace impurity appearing at the typical concentration of 1-2 % within the resulting crude product batches. This is quantitatively separated by using a dedicated eluent system.

^{1}H NMR (THF-d_8, 291.8 K, 400.34 MHz): δ_H = -9.65 (s, 15H) ppm.
^{1}H-^{13}C gHMQC (THF-d_8 ,293.4 K, 400.34 MHz): {δ_H, δ_C} = {-9.65, 150.4} ppm.

ATR-IR: ν = 3084 w (ν_{CH}), 3068 w, 2957 vw, 2957 vw, 2924 vw, 2852 vw, 1436 (ν_{CC}), 1350 w, 1307 w, 1238 m, 1184 w, 1125 w, 1065 w (δ_{CC}), 1004 m/s ($\delta_{CH//}$), 878 w, 839 w, 757 s ($\delta_{CH\perp}$), <u>666 m (sh)</u>, 617 m, <u>611 m</u>, <u>580 m</u>, <u>519 m</u> cm^{-1}. Underlined stretches attributed to characteristic fingerprint manifold for complexes containing $\{Np^{III}(Cp)_3\}$ unit.

Radiological concerns prohibited combustion-based evaluation of the C and H content of **34**.

$[U(Cp)_3]$ **39**

MF = $C_{15}H_{15}U$

MW = 433.31(2) g mol^{-1}

pyrophoric in powder form

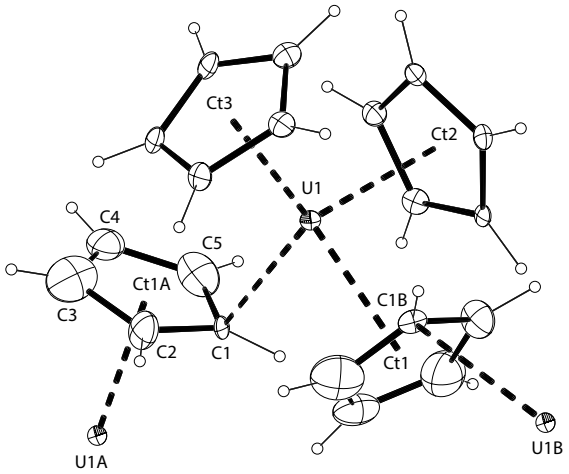

A 50-mL Schlenk tube was charged with $[^{238}U(Cp)_3Cl]$, **38** (1.3667 g, 2.916 mmol), solid sodium amalgam (1.399 g, 5.03 %, 1.05 eq) and mercury metal (12.677 g). Diethyl ether (35 mL) was added and the reaction mixture was stirred for 24 h. During this time a dark brown/grey suspension formed and the dark brown supernatant isolated by filtration (fritted glass disk, 10-16 µm porosity). The filter cake was extracted with diethyl ether until no visible change in fresh eluent colour and the combined extracts evaporated to dryness under vacuum (40 °C, 3×10^{-3} mbar, 4 h) (i). The resulting bitumen-black solid was extracted with 6 $\%_{v/v}$ diethyl ether in *n*-pentane for a total of 248 h (ii). The resulting dark brown, almost black single crystals of $[^{238}U(Cp)_3]$, **39** were collected and dried under vacuum (20 °C, 6×10^{-4} mbar, 6 h); isol. yield 569 mg, 45 %.

Remarks: (i) The extraction process afforded large, lustrous, black single crystals of $[^{238}U(Cp)_3(OEt_2)]$ **39b** according to single crystal X-ray diffractometric analysis. Due to the modest isolated yield (ca. 20 %), the material was used for establishing conditions for the thermal dissociation of the diethyl ether adduct and the raw product without additional solvent molecules combined with the main batch prior to the final extraction. (ii) The fractional extraction (1 × 48 h, 2 × 96 h) showed highest crystal quality specimens and theoretical C and H microanalysis specifications of the first batch, according to precision and accuracy of the methods of measurement. The second and third batches contained some tan coloured impurity, presumably due to the products of the ethereal solvent activation by U(III) centres.

^{1}H NMR (THF-d_8, 300.0 K, 600.75 MHz): δ_H = -15.41 (s, 15H) ppm.
^{1}H NMR (CD_3CN, 300.0 K, 600.75 MHz): δ_H = -13.62 (s, 15H) ppm.

EA (%) required for $C_{15}H_{15}U$: C 41.58, H 3.49; found: C 41.56, H 3.53 (first batch), C 40.80, H 3.78 (combined second and third batches).

[K(Cp')]

MF = $C_8H_{13}KSi$

MW = 176.373(8) g mol^{-1}

air sensitive

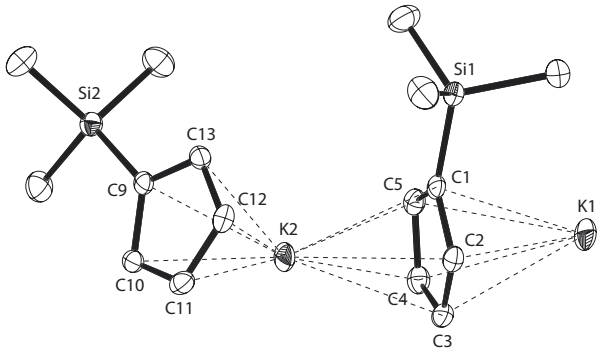

The following preparation is based upon an adaptation of the literature protocol of Evans *et al.*,[174] but the product showed to contain KCp impurity (*ca.* 3.5 $\%_{mol}$ by NMR, δ_H = 5.49 ppm), therefore the lower yielding but cleaner protocol of Evans *et al.*[175] is recommended.

A 100-mL Schlenk flask was charged with potassium bis(trimethylsilyl)amide (5.67 g, 28.4 mmol) and the solid dissolved in 50 mL of toluene. Trimethylsilylcyclopentadiene, mixture of isomers (3.57 g, 25.8 mmol) was added dropwise at room temperature over the period of 10 min. During this time the heat evolution was observed and the colour of the solution changed to dark red-brown. An off-white precipitate formed within 15 min after the addition, increasing in quantity during the course of reaction. The resulting suspension was allowed to stir for a further 16 h at room temperature and the volatiles were removed under reduced pressure. The resulting greyish mauve solid was purified by extraction with cyclopentane for *ca.* 10 h (washing) followed by extractive crystallization of [K(Cp')] from 12 $\%_{v/v}$ diethyl ether in *n*-pentane. The large colourless crystals of the product were collected, rinsed with pentane and dried under vacuum (20 °C, 8×10^{-4} mbar, 4 h); isol. yield 4.00 g, 88 %.

^{1}H NMR (THF-d_8, 400.34 MHz): δ_H = 5.76 (m, 2H, $C_5\underline{H_4}Si$), 5.66 (m, $C_5\underline{H_4}Si$ 2H), 0.06 (s, 9H, $Si(C\underline{H_3})_3$) ppm.
$^{13}C\{^1H\}$ NMR (THF-d_8, 100.68 MHz): δ_C = 112.6 ($\underline{C_4}H_4$), 111.0 ($\underline{C}SiCH_3$), 108.2 ($\underline{C_4}H_4$), 1.4 ($Si(\underline{C}H_3)_3$) ppm.

[Np(Cp')$_3$] **40**

MF = $C_{24}H_{39}NpSi_3$

MW = 648.87(3) g mol^{-1}

pyrophoric

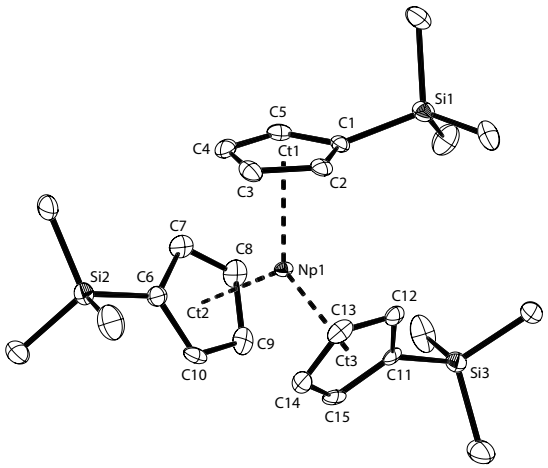

A suspension of $^{237}NpCl_3$ is first prepared *in situ*: A 25-mL Schlenk tube was charged with $^{237}NpCl_4$ (109.9 mg, 0.290 mmol), solid sodium mercury amalgam (139 mg, 5.03%, 1.05 eqv.) and mercury metal (1.262 g). Diethyl ether (8 mL) was added and the reaction mixture was stirred vigorously for 24 h. During this time the red-ochre solid was consumed and an insoluble greenish-grey precipitate formed.

To this suspension was added solid [K(Cp')] (153.4 mg, 0.870 mmol) at room temperature, leading to an immediate colour change of the reaction mixture to dark green. The reaction mixture was allowed to stir for further 4 h and the solvent stripped under reduced pressure. The resulting residue was extracted with *n*-pentane (12 mL) and the dark green supernatant isolated by syringe filtration (silanized glass fibre membrane, 1.0 µm porosity). Flash evaporation of the solvent under vacuum afforded [Np(Cp')$_3$], **40**, in the form of olive green crystalline solid. The crystals were collected and dried shortly under vacuum (20 °C, $<5 \times 10^{-3}$ mbar); isol. yield 177 mg, 94 %.

^{1}H NMR (THF-d_8 ,293.2 K, 400.34 MHz): δ_H = -0.62 (s, 27H, Si(C$\underline{H}_3$)$_3$), -8.81 (s, 6H, C$\underline{H}$), -8.98 (s, 6H, C$\underline{H}$) ppm. ^{1}H-^{13}C gHMQC (THF-d_8 ,293.5 K, 400.34 MHz): {δ_H, δ_C} = {-0.62, -6.1}, {-8.73, 154.6}, {-8.93, 158.6} ppm.
^{1}H NMR (toluene-d_8, 292.8 K, 400.34 MHz): δ_H = -1.38 (s, 27H, Si(C$\underline{H}_3$)$_3$), -8.60 (s, 6H, C$\underline{H}$), -9.51 (s, 6H, C$\underline{H}$) ppm. ^{1}H-^{13}C gHMQC (toluene-d_8, 293.1 K, 400.34 MHz): {δ_H, δ_C} = {-1.38, -14.1}, {-8.61, 165.1}, {-9.47, 166.9} ppm.

Radiological concerns prohibited combustion-based evaluation of the C and H content of **40**.

[K{Np(Cp)$_4$}] **43**

MF = $C_{20}H_{20}KNp$ ($C_4H_{10}O$)

MW = 610.64(3) g mol^{-1}

air sensitive

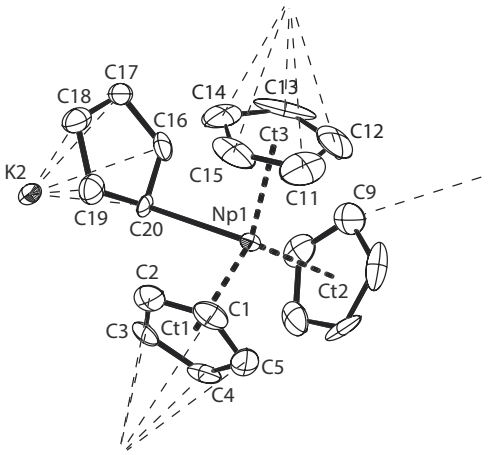

A 25-mL Schlenk flask was charged with [^{237}Np(Cp)$_3$Cl] (181.5 mg, 0.420 mmol) and potassium cyclopentadienide (48.1 mg, 0.462 mmol). THF (ca. 20 mL) was added and the reaction mixture was stirred vigorously for 1 h at room temperature. During this time no visible precipitate was produced and the reaction mixture was further heated under gentle reflux for a period of 96 h. A reddish brown precipitate formed and the colour of the supernatant changed to dark maroon. The suspension was evaporated to dryness under vacuum (25 °C, $<5 \times 10^{-3}$ mbar, 3 h) and the resulting dark brown solid extracted with *n*-pentane (36 h) and subsequently with diethyl ether (*ca.* 100 h). The *n*-pentane extraction separated essentially pure [Np(Cp)$_3$Cl] (88.4 mg, 48.7 %), whilst the following one afforded [K{Np(Cp)$_4$}] **43**, as maroon crystals suitable for single crystal X-ray diffractometry; isol. yield (94.6 mg, 36.9 %).

^{1}H NMR (THF-d_8 ,293.2 K, 400.34 MHz): δ_H = -11.95 (s, 20H) ppm.

ATR-IR: ν = 3084 w (ν_{CH}), 3059 w (sh), 2967 vw, 2925 vw, 2853 vw, 1438 (ν_{CC}), 1358 w, 1308 w, 1238 m, 1182 w, 1124 w, 1066 w (δ_{CC}), 1009 m/s ($\delta_{CH_{||}}$), 984 w, 891 w, 808 m, 766 s ($\delta_{CH_{\perp}}$), 666 m (sh), 613 m, 581 m cm^{-1}. Underlined stretches belong to the characteristic set of four vibrational peaks for complexes containing {Np^{III}(Cp)$_3$} unit.

Radiological concerns prohibited combustion-based evaluation of the C and H content of **43**.

Reaction of $[Np^{III}(Cp')_3]$ 40 with K (Chapter 2.4.2)

A glass column (6 mm I.D. × 80 mm L) equipped with fritted glass disc (10-16 µm porosity) and solvent reservoir (5 mL) was fitted with a straight-through PTFE-spindle valve (6 mm I.D.). A surrounding 'beaker-type' reservoir for liquid-cooling was fitted on top of a 25-mL Schlenk receiver flask. The apparatuses interior surfaces were silanized (exposure to dichloromethylsilane vapour) and heated *in vacuo* (160 °C, 6×10^{-4} mbar, 2 h) prior to use. The column was closely packed with a large excess of KC_8 (H = 70 mm) and secured with a glass fibre plug, also previously silanized. For the experiment both column and receiver vessels were precooled to -35 °C with methanol/dry-ice baths under argon. A brownish-green solution of $[Np(Cp')_3]$ **40** (88.1 mg, 0.136 mmol), and 2.2.2-cryptand (51.1 mg, 0.136 mmol) in 1:1 THF/Et_2O mixture (4.0 mL) was passed through the KC_8 bed with a slight-overpressure of Ar. The brownish-green solution become intensely coloured, and formed a dark brown/black solution upon passage through the column. The Schlenk containing the solution was capped and cooled to -78 °C for 1 h, affording small shiny black crystals. The mother liquor was decanted and the crystals of the target compound $[K(2.2.2cryptand)][Np^{II}(Cp')_3]$ **79** were rinsed with cold Et_2O (-30 °C, 2 × 2 mL). Batches of crystals were immersed in perfluoroalkyl ether oil and suitable crystals were selected for mounting inside Lindemann glass capillaries, which were manipulated through the process in a way to avoid outer surface contamination. The isolated tube was varnished by immersion in the cold (-10°C) solution of polycarbonate in dichloromethane and transferred to the goniometer head and crystals analysed by single crystal X-ray diffractometry, although only weak diffraction was observed.

Remarks: 1. Solutions of **79** in DME are thermally unstable above approx. -10 ºC, changing suddenly in colour to pale olive-green, precluding further solution analyses under the required radiological protection regimes. 2. Isolated crystalline samples of **79** begin to deteriorate at room temperature within 1 minute of contact with the degassed perfluoroalkyl ether oil, with the gradual deposition of an off-white crystalline solid, assumed to be liberated 2.2.2-cryptand observed.

5.4 Compounds and Reactions of Chapter 3

[(μ-O){U(Cp)$_3$}$_2$] **54**

MF = $C_{30}H_{30}OU_2$

MW = 882.62(3) g mol^{-1}

stable to dry air

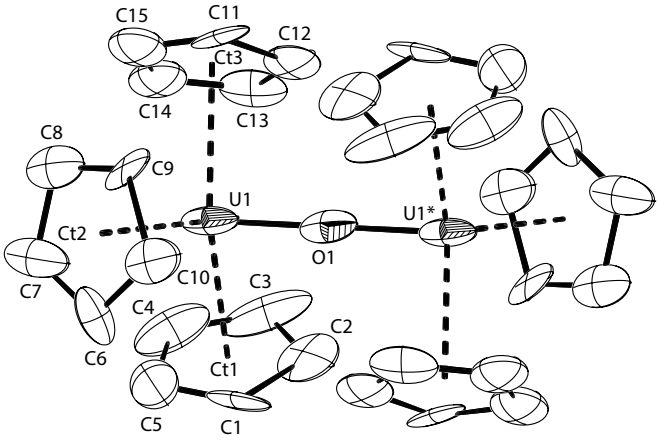

A suspension of [^{238}U(Cp)$_3$] (161.6 mg, 0.3729 mmol) in THF (16 mL) was exposed to dry air (drying tube with CaH_2) at room temperature and stirred vigorously for *ca.* 1 h at room temperature. During this time the colour of the supernatant turned greenish-brown and a yellow-ochre precipitate formed. The solid product was isolated by filtration (fritted glass disk, 10-16 μm porosity) and dried *in vacuo* (40 °C, 8 × 10^{-4} mbar, 2 h) and the resulting ochre residue was extracted with toluene for 275 h, affording **54** in the form of olive-green small crystals. The product was collected and dried under vacuum (20 °C, 8 × 10^{-3} mbar); isol. yield 135.8 mg, 82.5 %.

The low solubility of **54** in THF precludes solution-state studies.

ATR-IR: ν = 3088 w (ν_{CH}), 3080 w (ν_{CH}), 1776 w (br), 1561 w (br) 1438 w/m (ν_{CC}), 1357 w, 1262 w, 1212 vw, 1124 w, 1066 w (δ_{CC}), 1010 m ($\delta_{CH\parallel}$), 886 w (br), 806 m/s, 765 s ($\delta_{CH\perp}$, 716 for ^{18}O labelled), 679 m/s, 614 s, 586 s (U-O-U; 556 U-^{18}O-U) cm^{-1}.

EA (%) required for $C_{30}H_{30}OU_2$: C 40.82, H 3.43; found: C 40.97, H 3.51.

[(μ-O){Np(Cp)$_3$}$_2$] **58**

MF = $C_{30}H_{30}Np_2O$

MW = 880.66(3) g mol^{-1}

stable to dry air

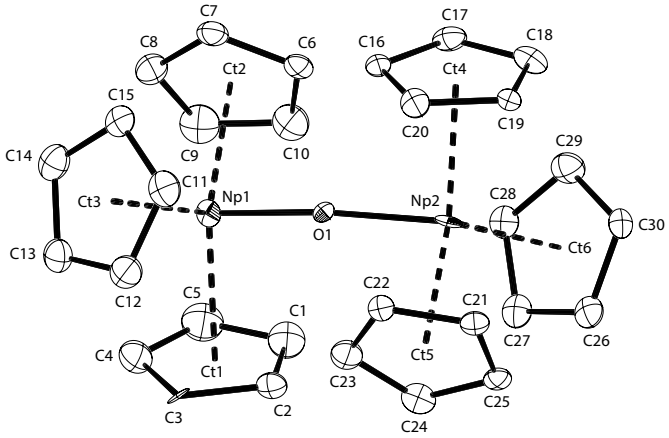

A suspension of [^{237}Np(Cp)$_3$] (37.0 mg, 0.086 mmol) in toluene (10 mL) was exposed to excess air at room temperature and stirred vigorously for 1.5 h. During this time the colour of the supernatant turned pale yellowish and the red-ochre precipitate formed. The suspension was evaporated to dryness (120 °C, <5 × 10^{-3} mbar, 2 h) and the resulting ochre residue extracted with benzene for 180 h, affording **58** in the form of a golden-russet microcrystalline solid. The product was collected and dried under vacuum (20 °C, <5 × 10^{-3} mbar); isol. yield 35.2 mg, 93.0 %.

^{1}H NMR (THF-d_8 ,293.2 K, 400.34 MHz): δ_H = -18.35 (s, 30H) ppm.

ATR-IR: ν = 3090 w (ν_{CH}), 3084 w (ν_{CH}), 2969 vw, 1674 w (br), 1559 w (br), 1438 (ν_{CC}), 1358 w, 1264 w, 1212 vw, 1124 w, 1065 w (δ_{CC}), 1011 m ($\delta_{CH_{||}}$), 888 w (br), 808 m/s, 769 s ($\delta_{CH_{\perp}}$), 676 m (sh), 620 s, 559 s (Np-O-Np) cm^{-1}.

Radiological concerns prohibited combustion-based evaluation of the C and H content of **58**.

$[(Cp)_3UOUO(THF)(H_2L^{Et})]$ **62**

MF = $C_{61}H_{65}N_8O_3U_2$ (1.75 C_4H_8O)

MW = 1560.46(7) g mol^{-1}

air sensitive

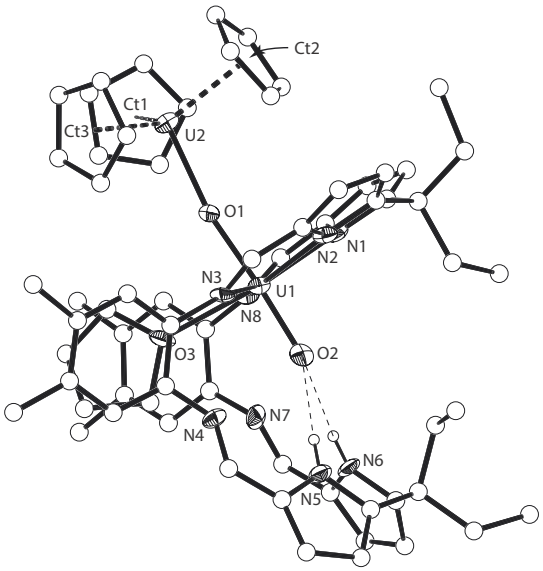

A 10-mL resealable glass ampoule was charged with $^{238}U(Cp)_3$ (48.6 mg, 0.096 mmol) and [$^{238}UO_2(THF)(H_2L^{Et})$ · ¼ THF] (103.6 mg, 0.096 mmol). THF (3.0 mL) was condensed onto the solids at -196 °C and the stirred reaction mixture allowed to warm to 20 °C over 4 h. During this time the dark brown and green solids were consumed and the colour of the solution turned brown. A small quantity of an ochre precipitate formed (i) and the supernatant was isolated by decantation and syringe filtration (PTFE membrane, 0.45µm porosity). Vapour diffusion of *n*-pentane into this solution in 21 h (ii) afforded $[(Cp)_3UOUO(THF)(H_2L^{Et})]$, **62**, in the form of small golden brown plates, suitable for X-ray diffraction. The crystals were collected, washed with *n*-pentane (1 × 0.5 mL) and dried under a stream of argon; isolated yield: 8.3 mg, 5.0 %.

Remarks: (i) The yellow-ochre powder sample was characterized as the structurally authenticated complex $(\mu\text{-}O)[U(Cp)_3]_2$ by both single-crystal X-ray diffractometry and ATR-IR analyses. (ii) Longer crystallization times afforded samples that co-crystallized with significant quantities of unreacted starting material, $[UO_2(THF)(H_2L^{Et})$ · ¼THF] and the ochre $(\mu\text{-}O)[U(Cp)_3]_2$ by-product.

^{1}H NMR (THF-d_8, 298 K, 500.12 MHz) δ_H = 51.4 (br, 2H, N*H*), 9.54 (s, 2H, pyrrole), 8.38 (s, 2H, pyrrole), 5.86 (m, 3H, C*H*$_3$), 3.92 (t, 3H, C*H*$_3$), 3.85 (s, 2H), 3.69 (s, 6H, C_6H_2(C*H*$_3$)), 3.48 (q, 2H, C*H*$_2$), 3.17 (s, 15H, U(C_5H_5)$_3$), 2.66 (t, 3H, C*H*$_3$), 2.14 (s, 2H), 1.37 (q, 2H, C*H*$_2$), 0.00 (s, 6H, C_6H_2(C*H*$_3$)), -2.72 (q, 2H, C*H*$_2$), -5.92 (t, 3H, C*H*$_3$), -7.88 (s, 2H), -9.43 (s, 2H) ppm.
$^{13}C\{^1H\}$ NMR (125.77 MHz) δ_C = 155.79, 147.71, 145.10, 141.32, 128.59, 128.12, 127.73, 120.30, 120.15, 113.79, 109.23, 53.92, 30.07, 23.06, 21.58, 17.57, 16.47, 12.93, 11.96, 11.52, 2.11, 1.75 ppm.

FTIR (Nujol) ν = 3583 (w, NH), 1581 (w, imine), 1462 (s, Nujol), 1377 (s, Nujol), 1304 (m, L), 1286 (w, L), 1154 (w, L), 1049 (m, L), 973 (s), 893 (s, asymm. UO_2 stretch), 770 (w, L), 722 (s, nujol) cm^{-1}. L = stretches attributed to the macrocyclic ligand.

EA (%) required for $C_{65}H_{73}N_8O_3U_2$: C 52.38, H 4.94, N 7.52; found: C 52.22, H 5.07, N 7.39.

$[(Cp)_3NpOUO(THF)(H_2L^{Et})]$ **63**

MF = $C_{61}H_{65}N_8NpO_3U$
(1.75 C_4H_8O)

MW = 1560.46(7) g mol^{-1}

air sensitive

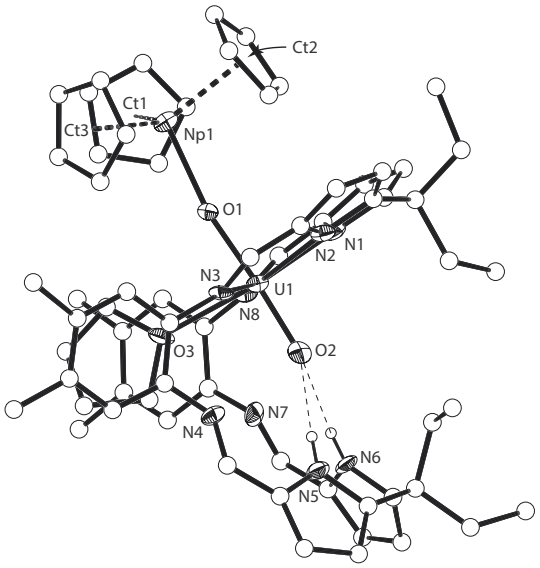

A 10-mL resealable glass ampoule was charged with $^{237}Np(Cp)_3$ (42.8 mg, 0.099 mmol), [$^{238}UO_2(THF)(H_2L^{Et})$ · ¼ THF] (71.0 mg, 0.066 mmol). THF (3 mL) was condensed onto the solids at -78°C and the resulting reaction mixture was allowed to warm to 20°C with stirring over 90 minutes. During this time the green crystallites were consumed and the colour of the solution changed to reddish brown. A golden russet precipitate formed and the supernatant was isolated by decantation and syringe filtration (PTFE membrane, 0.45 µm porosity). Vapour diffusion of *n*-pentane into this solution over 36 h (ii) afforded $[(Cp)_3NpOUO(THF)(H_2L^{Et})]$, **63**, in the form of dark red rhombic crystals suitable for single crystal X-ray diffraction. The crystals were collected, washed with *n*-pentane (3 × 1 mL) and dried under a stream of argon; isolated yield: 51.4 mg, 45.6 %.

Remarks: (i) The golden russet microcrystalline by-product was washed with THF (2 × 0.5 mL) and dried under vacuum (20 °C, $<5 \times 10^{-3}$ mbar, 4 h) and assigned as $(\mu\text{-}O)[Np(Cp)_3)]_2$ **58**, isolated yield: 8.9 mg, 27.7 % (based on $Np(Cp)_3$). A microscopic evaluation of this sample suspended in perfluoroalkylether oil (1800 cSt, degassed) confirmed the presence of a single crystalline phase. Although the crystals were too small to enable full crystallographic analyses, unit cell determinations showed the material to be isostructural with $(\mu\text{-}O)[Np(Cp)_3)]_2$ **58**. (ii) Longer crystallization times afforded samples that were contaminated with co-crystallized unreacted starting material, [$UO_2(THF)(H_2L^{Et})$ · ¼ THF], and presumably also small quantities of $(\mu\text{-}O)[Np(Cp)_3)]_2$.

^{1}H NMR (THF-d_8, 293 K, 400.34 MHz): δ_H = 55.5 (br, 2H, N<u>*H*</u>), -11.79 (br, 15H, $Np(C_5\underline{H}_5)_3$) ppm.
Complex **63** is exceedingly reactive in the solution state, presumably with the fluoropolymer liner required for radiological protection, forming an impurity which appears to have a very similar solution structure to **63** as evidenced by the C_2 symmetric $(H_2L^{Et})^{2-}$ environment. The two overlapping sets of resonances make an unambiguous assignment of the smaller resonances for **63** not possible. The reactivity of **63** precludes a definitive assignment from longer-duration NMR spectroscopic experiments such as correlation or heteronucleus experiments.

The resonances of the impurity: δ_H = 51.31 (br, 2H, N$\underline{H}$), -12.48 (br, 15H, Np($C_5\underline{H}_5$)$_3$) ppm.

ATR-IR: ν = 3414 w, 3275 w (br, NH), 3100 w, 2962 w, 2927 w, 2871 w, 1601 m, 1578 (ms imine), 1563 m, 1514 w, 1468 m, 1449 m, 1393 w, 1377 w, 1354 w, 1338 w, 1282 (ms, L), 1258 ms, 1201 wm, 1179 m, 1129 w, 1108 w, 1046 (ms, L), 1012 ms, 978 (w, L), 960 w, 892 (ms, assym. UO_2 strech), 869 wm, 759 s, 714 m, 617 s, 598 s, 565 ms, 512 ms, 416 ms, 403 ms cm^{-1}. L = stretches attributed to the macrocyclic ligand.

Vis-NIR (THF, 293 K): λ_{max} / nm (ε / dm^3 mol^{-1} cm^{-1}) = 1616 (46.0), 1608 (46.1), 1500 (137), 1420 (55.9), 1212 (16.4), 1183 (20.9), 1178 (20.5), 1081 (163), 1067 (115), 1000 sh (146), 986 (324), 962 (85.6), 950 (85.1), 916 (137), 896 (195), 879 (188), 853 (220), 842 (142), 806 (125), 795 (152), 767 (93.9), 743 (149), 724 (142), 702 (95.5), 697 (93.5), 654 (109), 633 (150), 586 (262), 570 (290), 555 (323), 530 (449).

Radiological concerns prohibited combustion-based evaluation of the C, H and N content of **63**.

$[(Cp)_3UOUO(THF)(H_2L^{Oct})]$ **64**

MF = $C_{61}H_{65}N_8O_3U_2$ (2.1 C_4H_8O)

MW = 1585.70(7) g mol^{-1}

air sensitive

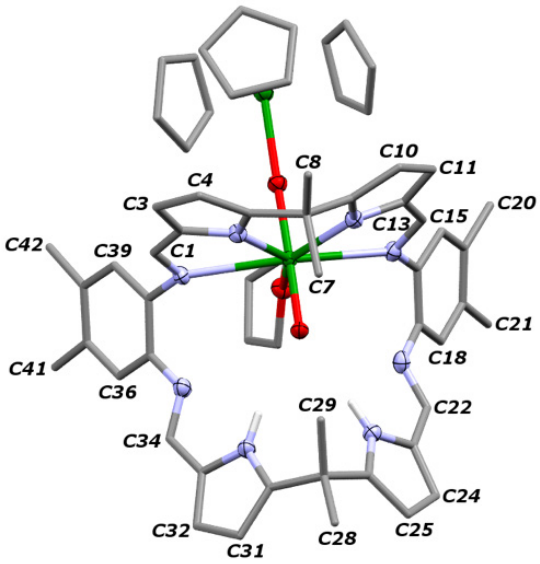

A 25-mL resealable glass ampoule was charged with $^{238}U(Cp)_3$ (83.5 mg, 0.193 mmol) and [$^{238}UO_2(THF)(H_2L^{Oct})$ · THF] (206.8 mg, 0.193 mmol). THF (6 mL) was condensed onto the solids at -196 °C and the stirred reaction mixture was allowed to warm to 20 °C over 4 h. During this time the dark brown and green solids were consumed and the colour of the solution turned brown. An ochre precipitate formed and the supernatant was isolated by decantation and syringe filtration (PTFE membrane, 0.45µm porosity) (i). The solution was concentrated under reduced pressure until precipitation started (*ca.* 2.5 mL, -5 °C) followed by warming to redissolve particulates and syringe filtration (PTFE membrane, 0.45µm porosity). Vapour diffusion of *n*-pentane into this solution over 24 h (i) afforded $[(Cp)_3UOUO(THF)(H_2L^{Oct})]$, **64**, as golden-brown, large block crystals, suitable for X-ray diffraction. The crystals were collected, washed with *n*-pentane (2 × 1 mL) and dried under a stream of argon; isolated yield: 60.0 mg, 19.6 %.

Remarks: (i) The ochre precipitate was identified again as $[^{238}U(Cp)_3]_2(\mu\text{-}O)$, the same by-product observed during the preparation of **62**. (ii) Longer crystallization times afforded impure samples containing the by-product, which were difficult to separate.

^{1}H NMR (THF-d_8, 298 K, 500.12 MHz): δ_H = 51.09 (br, 2H, N<u>H</u>), 12.49 (s, 3H, C29), 9.29 (s, 2H, C25(31)), 8.12 (s, 2H, C24(32)), 6.32 (s, 2H, C22(34)), 4.99 (s, 3H, C28), 3.39 (s, 6H, C21(41)), 3.30 (br, 15H, Np(C_5<u>H_5</u>)$_3$), 2.70 (s, 2H, C3(11)), 2.54 (s, 2H, C15(39)), 2.11 (s, 2H, C4(10)), 1.07 (s, 2H, C18(36)), -1.80 (s, 3H, C7), -7.62 (s, 2H, C1(13)), -8.48 (s, 3H, C8) ppm.
^{1}H-^{13}C HSQC {δ_H, δ_C}: {12.49, 45.2}, {9.29, 111.1}, {8.12, 118.7}, {6.32, 148.0}, {4.99, 29.7}, {3.39, 18.2}, {3.30, 232.3}, {2.70, 118.9} {2.54, 112.7}, {2.11, 108.9}, {1.07, 109.3} {-1.80, 18.6}, {-7.62, 66.6}, {-8.48, 15.3} ppm.

ATR-IR: ν = 3443 w, (3373 mw, NH), 3106 w, 2967 m, 2923 m, 2871 wm, 1712 w, 1617 s, 1604 s (sh), 1584 (s, imine), 1564 m, 1476 m, 1464 m (sh), 1400 w, 1366 w, 1355 w, 1339 w, 1282 (s, L), 1263 ms, 1214 m, 1184 wm, 1154 (w, L), 1132 w, 1047 s, 1019 m, 959 w, 907 m (UO_2 asymm. stretch), 897 m (sh), 871 w, 781 m, 725 w cm^{-1}. L = stretches attributed to the Pacman ligand.

Vis-NIR (THF, 293 K): λ_{max} / nm (ε / dm^3 mol^{-1} cm^{-1}) = 1948 (25.6), 1872 (25.8), 1826 (29.1), 1738 (45.3), 1625 (54.9), 1606 sh (51.9), 1544 (47.3), 1494 (110), 1291 (70.1), 1200 (89.0), 1144 (98.3), 1066 (84.4), 1023 (106), 1008 sh (87.5), 911 (86.0), 324, 213.

EA (%) required for $C_{61}H_{65}N_8O_3U_2$: C 51.08, H 4.57, N 7.81; found: C 50.67, H 4.33, N 7.71.

$[(Cp)_3NpOUO(THF)(H_2L^{Oct})]$ **65**

MF = $C_{61}H_{65}N_8NpO_3U$
(1.75 C_4H_8O)

MW = 1559.48(7) g mol^{-1}

air sensitive

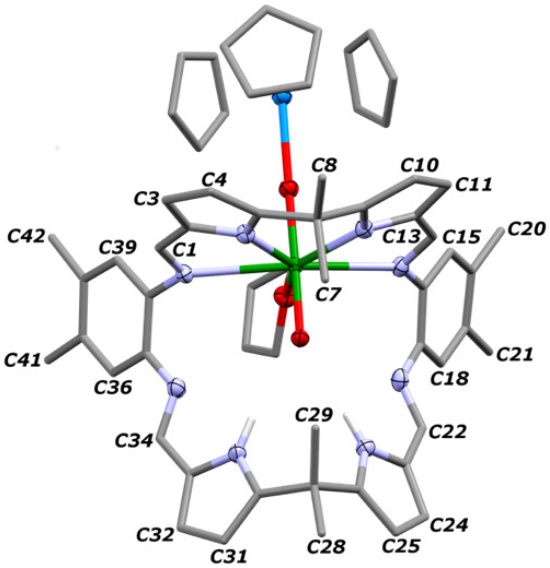

A 10-mL resealable glass ampoule was charged with $^{237}Np(Cp)_3$ (64.3 mg, 0.149 mmol), [$^{238}UO_2(THF)(H_2L^{Oct})$ · THF] (159.6 mg, 0.149 mmol) and a stirrer bar. THF (4 mL) was condensed onto the solids at -78 °C and the resulting reaction mixture was allowed to warm to 20°C with stirring over 100 min. During this time the dark green solid was consumed and the solution changed colour to red-brown with the formation of a small quantity of a golden russet precipitate. An analogous isolation strategy to that described for the compound **62** yielded $[(Cp)_3NpOUO(THF)(H_2L^{Oct})]$, **65**, in the form of dark red-brown single crystals suitable for X-ray diffraction; isol. yield: 71.0 mg, 30.6 %.

Remarks: The solution stability of **65** is greater than that of **54**, enabling a full NMR spectroscopic assignment. An X-ray unit cell analysis of the golden russet precipitate again indicates the formation of $(\mu\text{-}O)[^{237}Np(Cp)_3)]_2$ **58** as a by-product, as was seen in the synthesis of **63**; isolated yield: 8.1 mg, 9.5 % (based on $Np(Cp)_3$).

^{1}H NMR (THF-d_8, 293 K, 400.34 MHz): δ_H = 54.8 (br, 2H, N*H*), 14.55 (s, 3H, C29), 10.12 (s, 2H, C25(31)), 8.87 (s, 2H, C24(32)), 7.26 (s, 2H, C22(34)), 5.84 (s, 3H, C28), 2.66 (s, 2H, C18(36)), 1.96 (s, 6H, C21(41)), 1.68 (s, 2H, C3(11)), 0.74 (s, 2H, C15(39)), 0.21 (s, 2H, C4(10)), -2.88 (s, 3H, C7), -6.96 (s, 3H, C8), -7.07 (s, 2H, C1(13)), -12.05 (br, 15H, $Np(C_5H_5)_3$) ppm.
^{1}H-^{13}C gHMQC: {δ_H, δ_C} = {14.55, 46.7}, {10.12, 111.7}, {8.87, 119.7}, {7.26, 149.7}, {5.84, 30.7}, {2.66, 109.2}, {1.96, 25.7}, {1.68, 118.2}, {0.74, 113.2}, {0.21, 108.7}, {-2.88, 18.2}, {-6.96, 15.7}, {-7.07, 69.2} {-12.03, 263.2} ppm.

ATR-IR: ν = 3267 w (br, NH), 3102 w, 2971 w, 2938 w, 2916 w, 2863 w, 1611 wm (sh), 1599 m, 1579 (ms, imine), 1560 m, 1506 w, 1489 w, 1476 m, 1456 m, 1432 wm (sh), 1397 w, 1387 w, 1368 w, 1351 w, 1284 (m, L), 1264 m, 1233 wm, 1217 m, 1184 m, 1158 (w, L), 1136 w, 1110 w, 1096 w, 1080 w, 1063 w, 1040 (s, L), 1015 ms, 999 ms, 963 w, 891 ms (asymm. UO stretch), 876 wm, 870 wm (sh), 840 w, 827 w, 796 m (sh), 780 ms, 766 (s, L), 758 s (sh), 746 ms (sh), 724 ms, 711 ms, 683 wm, 661 wm, 612 s (sh), 605 s (sh), 595 s, 571 s, 558 ms, 534 m, 509 m, 471 m, 421 m, 414 m, 387 m cm^{-1}. L = stretches attributed to the Pacman ligand.

Vis-NIR (THF, 293 K): λ_{max} / nm (ε / dm^3 mol^{-1} cm^{-1}) = 1606 (48.8), 1497 (147), 1420 (52.9), 1341 (152), 1215 (11.4), 1184 (13.8), 1143 (21.5), 1080 (170), 1066 (109), 987 (304), 952 (69.1), 930 (49.4), 916 (119), 897 (156), 893 (155), 878 (144), 852 (211), 841 (122), 795 (136), 768 (89.2), 742 (136), 725 (133), 702 (83.8), 695 (79.9), 653 (95.9), 632 (140), 624 (140), 585 (224), 571 (247), 556 (268), 531 (360).

Radiological concerns prohibited combustion-based evaluation of the C and H content of **65**.

Oxidation studies of $[Np(Cp)_3]$ 34 and $[U(Cp)_3]$ 39 with air (Chapter 3.2.1)

4-mL glass vials equipped with PTFE-faced silicone septa were dried *in vacuo* (110 °C, 6 × 10^{-4} mbar, 12 h) and filled with 0.8 mL aliquots of the respective $[An^{III}(Cp)_3]$ solutions in both THF or MeCN under argon at 20 °C. The septa were punctured with 18G × 1.5"-long hypodermic needles enabling diffusion of the dinitrogen gas containing *ca.* 3000 ppm of O_2 and sub-10 ppm of H_2O (radiological glovebox atmosphere) into the solutions. All experiments were conducted in parallel and monitored over a period of 24-48 h; each reaction was stopped at the point at which the colour of the solution shows no further change within a 6 h period, or when they became almost colourless. Precipitates formed in each case and were collected by decantation, rinsed with a mixture of THF and *n*-hexane (1:2, 2 × 0.5 mL) and dried briefly under vacuum (20 °C, <5 × 10^{-3} mbar). Experiments using different concentrations of both starting materials **34** and **39** (range 0.25-10.3 mg · mL^{-1}) and the identity of the solvent used (THF, MeCN) were inconclusive as to the effect on the nature or yield of the product formed. All uranium-containing batches contained exclusively $[(\mu\text{-}O)\{^{238}U(Cp)_3\}_2]$ **54** in the form of an orange-ochre microcrystalline solid, regardless of the concentration of the starting material used. However, the oxidation of **34** produced reproducibly the two different products $[\{(Cp)_3{}^{237}Np(\mu\text{-}O)\}_2\{^{237}Np(Cp)_2\}]$ **57** and $[(\mu\text{-}O)\{^{237}Np(Cp)_3\}_2]$ **58**, admixed together, both as microcrystalline red and golden-russet solids. Complex **57** is moderately soluble in THF, which precludes quantitative confirmation of the product ratio from analysis of just the precipitate. However, optical microscopy inspection of batches of precipitates of **57** and **58** suspended in perfluoropolyalkyl ether oil suggests a ratio in the precipitated samples of 54:55 in the range 1 – 40 :100. Attempts to separate **57** from **58** by means of fractional recrystallization (THF, toluene) were unsuccessful.

The analogous aerobic oxidations of **34** and **39** with air were conducted by opening the vials in a closed 150-mL polyethylene zip-lock bags, filled previously with untreated air. All crude product batches were isolated similarly as described above and the homogeneity of the microcrystalline samples was confirmed by the visual inspection using microscopy to contain only $[(\mu\text{-}O)\{An(Cp)_3\}_2]$ complexes; isol. yield of 95-98 %. Complexes **54** to **58** decompose only slowly in moist air and are indefinitely stable in the absence of traces of water.

Reaction of $[Pu(Cp)_3(THF)]$ (59) with $[UO_2(THF)(H_2L^{Et})]$ (60) to target $[(Cp)_3PuOUO(THF)(H_2L^{Et})]$ (Chapter 3.3.2)

A 10-mL resealable glass ampoule was charged with $[^{239}Pu(THF)(Cp)_3]$ (23.2 mg, 0.046 mmol) and $[UO_2(THF)(H_2L^{Et}) \cdot ¼\ THF]$ (49.3 mg, 0.046 mmol). THF-d_8 (3 mL) was condensed onto the solids at -78°C and the resulting stirred reaction mixture allowed to warm to 20 °C over 75 min. No visible changes of the resulting mixture occurred during this time or during further storage of the solution at room temperature for 16 h. The contents of the ampoule were freeze-pump-thaw degassed (3 cycles) and the sealed, secured reaction vessel placed in an aluminium heating block maintained at 80 °C for 4 h. No reaction change was observed as further confirmed by ^{1}H NMR spectroscopy of an aliquot of the crude reaction mixture.

5.5 Compounds and Reactions of Chapter 4

$[(L^{Ar})^{237}NpCl]$ **75**

MF = $C_{32}H_{36}ClN_2Np$

MW = 721.14(4) g mol^{-1}

air sensitive

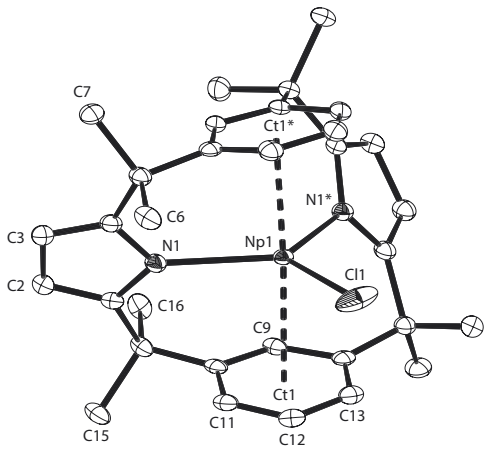

Method A, from Np^{IV}

A 10-mL resealable glass ampoule was charged with $^{237}NpCl_4$ (46.0 mg, 0.121 mmol) and $K_2(L^{Ar})$ (95.9 mg, 0.182 mmol). THF (3 mL) was condensed onto the solids at -78 °C and the resulting reaction mixture allowed to warm to 20 °C with stirring, over a 90 min. period. During this time the red-ochre solid was consumed and the colour of the solution changed to maroon and then to intense red. An off-white precipitate formed above -45 °C, increasing in quantity during the course of the reaction. The resulting suspension was allowed to stir for a further 16 h at room temperature and the red supernatant was isolated by syringe filtration (PTFE membrane, 0.45µm porosity). Slow vapour diffusion of *n*-pentane into this solution yielded $[(L^{Ar})NpCl]$, **75**, in the form of dark red crystals and a pale yellow powder, which was characterized as organic by-products based on γ-ray spectroscopy (<0.1 mg ^{237}Np radioassay). Attempts to purify the crude product *via* fractional crystallization were unsuccessful but mechanical separation of the fine yellowish powder, facilitated by repeated re-suspension of solids

in *n*-pentane, allowed the isolation of **75** as a coarse red precipitate; isolated yield: ~40 mg, 46 %.

Method B, from Np^{III}

A suspension of [$^{237}NpCl_3(THF)_x$] is first prepared *in situ*: A 25-mL Schlenk tube was charged with $^{237}NpCl_4$ (175.4 mg, 0.463 mmol), solid sodium mercury amalgam (222 mg, 5.03 %, 1.05 eqv.) and mercury metal (2.013 g). THF (8 mL) was added and the reaction mixture was stirred vigorously for 4 h. A greenish-grey suspension formed immediately, and was isolated from the mercury drop using a syringe (27 G hypodermic needle).

To this suspension solid $K_2(L^{Ar})$ (243.9 mg, 0.463 mmol) was added at room temperature, leading to an immediate colour change of the reaction mixture to intense red. The reaction mixture was allowed to stir for further 5 h, diluted with 10 mL of THF and the supernatant isolated by filtration (fritted glass disk, 10-16 µm porosity). The filter cake was washed with THF (2 × 4 mL) and the combined filtrates were evaporated to dryness under reduced pressure. The crude red product was solubilized in the minimum amount of THF (ca. 8-8.5 mL) and syringe-filtered (PTFE membrane, 0.45µm porosity). Slow vapour diffusion of *n*-pentane into the resulting solution afforded [(L^{Ar})NpCl], **75**, as red crystals, suitable for single crystal X-ray diffraction analysis. The crystals were collected, washed with *n*-pentane (4 × 1 mL) and dried under vacuum (20 °C, $<5 \times 10^{-3}$ mbar, 6 h); isolated yield: 281 mg, 84 %.

^{1}H NMR (THF-d_8, 291.8 K, 400.34 MHz): δ_H = 7.08 (s, 4H, C2/C3 pyrrolide C<u>*H*</u>), 4.96 (s, 2H, C9 $C_6\underline{H_4}$), 4.26 (br s, 2H, C12 $C_6\underline{H_4}$), 3.20 (s, 12H, C7/C16 $C\underline{H_3}$), 0.15 (s, 12H, C6/C15 $C\underline{H_3}$), -0.39 (br s, 4H, C11/C13 *meta*-$C_6\underline{H_4}$) ppm.
^{1}H-^{13}C gHMQC (THF-d_8 ,293.4 K, 400.34 MHz): {δ_H, δ_C} = {7.08, 128.6}, {4.96, 141.2}, {4.26, 91.1}, {3.20, 36.6}, {0.15, 28.7}, {-0.39, -104.6} ppm.

ATR-IR: ν = 3094 w, 3075 w, 2969 w/m, 2960 w, 2948 w, 2927 w, 2862 w, 1646 w, 1619 w, 1600 w, 1589 w, 1576 w, 1476 w/m, 1462 w/m, 1439 w, 1410 w/m, 1386 w, 1379 w, 1363 w/m, 1359 w/m, 1342 w, 1304 w, 1280 w, 1256 w/m, 1217 w/m, 1211 w/m, 1183 w, 1153 w, 1133 w/m, 1111 w, 1082 w, 1044 s, 1007 w, 985 w/m, 960 w, 935 w, 925 w, 902 w, 823 m, 809 w, 795 w, 748 s, 722 w/m, 715 m, 709 s, 677 w, 670 w, 644 w, 620 w/m, 677 w, 670 w, 645 w, 620 m, 580 m, 537 w/m, 511 w/m, 499 m, 459 w/m, 439 w/m, 429 w/m, 423 w/m, 410 m, 400 w/m, 386 w/m cm^{-1}.

Vis-NIR (THF, 293 K): λ_{max} / nm (ε / dm^3 mol^{-1} cm^{-1}) = 1351 (28.3), 1331 (48.9), 1318 (41.9), 1280 (36.6), 1253 (27.9), 1028 (49.0), 985 (73.0), 949 (48.9), 943 (47.3), 855 (86.6), 838 (93.8), 783 (76.2), 772 (69.4), 764 (66.4), 748 (63.5), 725 (58.0), 661 (83.5), 633 (104).

Radiological concerns prohibited combustion-based evaluation of the C and H content of **75**.

$[(L^{Ar})Np_2Cl_4(THF)_3]$ **76**

MF = $C_{44}H_{60}N_2Np_2O_3$ ($^1/_2$ C_4H_8O)

MW = 1316.92(6) g mol^{-1}

air sensitive

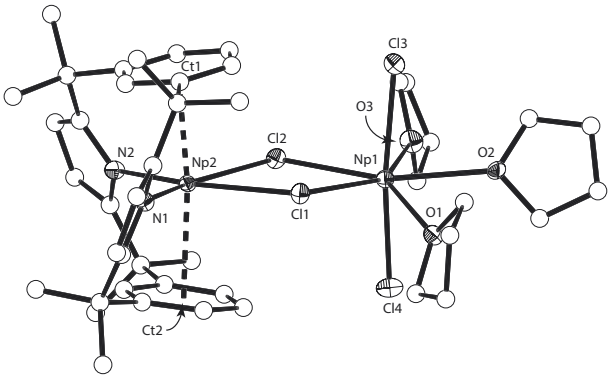

The solution of **76** was prepared as described for $[(L^{Ar})NpCl]$, **75**, (Method A), using an equimolar mixture of $^{237}NpCl_4$ (58.0 mg, 0.153 mmol) and $[K_2(L^{Ar})]$ (80.6 mg, 0.153 mmol) in 4 mL of THF. The red supernatant was isolated by syringe filtration (PTFE membrane, 0.45µm porosity) and subsequently concentrated to 2.1 mL under reduced pressure. Layering of aliquots of this solution in silylated NMR tubes with hexane afforded **76** in the form of very dark red crystals, suitable for single crystal X-ray diffraction analysis, and an off-white precipitate of organic by-products (<0.1 mg ^{237}Np radioassay). The clustered nature of crystal-growth of **76** enabled mechanical separation from the organic material. Washing with *n*-pentane (3 × 1 mL) and rapid drying under a stream of argon gave pure **76**; isolated yield: 92.6 mg, 91.9 %.

The low solubility of **76** in THF precludes solution-state studies.

ATR-IR: ν = 3106 w, 3069 w, 2965 w/m, 2928 w, 2868 w, 1599 w, 1579 w, 1484 w, 1462 w, 1413 w/m, 1381 w, 1359 w/m, 1307 w/m, 1238 s, 1209 m, 1180 m, 1131 m br, 1094 m, 1043 m, 981 m/s, 938 w/m, 915 w/m, 817 m, 795 m, 763 m/s, 747 m/s, 706 s, 666 m, 647 w/m, 615 m, 482 m/s, 463 m/s, 427 m/s, 406 m/s cm^{-1}.

Radiological concerns prohibited combustion-based evaluation of the C and H content of **76**.

$[K(DME)(L^{Ar\text{-}H})Np(OMe)]_2$
78

MF = $C_{74}H_{96}K_2N_4Np_2O_6$

MW = 1689.87(8) g mol^{-1}

air sensitive

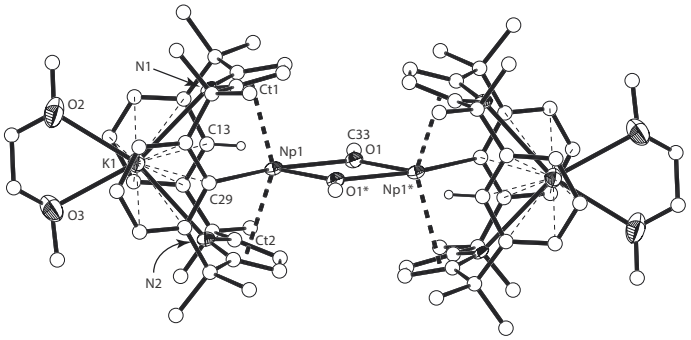

A 25-mL Schlenk tube was charged with $[(L^{Ar})NpCl]$, **75**, (43.2 mg, 0.060 mmol) and 8 mL of DME. An excess of NaK_3 alloy (0.24 mL) was added and the suspension was orbital shaken (2800 rpm) for 20 s. During this time the reddish solid was consumed and the colour of the solution changed to brown and later to intense purple black. The excess of the NaK alloy and any particulate matter were removed by syringe filtration (silylated glass fibre membrane in PE housing, 1.0 µm porosity) and the solution of **$[(L^{Ar})Np(DME)]$** (**77**) analysed for direct Vis-NIR measurements (340 µL load into 1.00 mm cell) and crystallization studies (7.4 mL).

On two occasions, small black plate-shaped crystals that had grown in the product solution were analysed by X-ray diffraction, but only weakly diffracted and the crystals showed signs of considerable surface degradation so further analysis was not possible.

Slow vapour diffusion of *n*-pentane into the isolated purple-black solution that was changing colour to red-brown with time yielded reddish brown crystals, suitable for single-crystal X-ray diffraction analysis that were characterised as $[K(DME)(L^{Ar\text{-}H})Np(OMe)]_2$, **78**. The crystals were collected, washed with *n*-pentane (4 × 1 mL) and dried under vacuum (20 °C, $<5 \times 10^{-3}$ mbar, 1 h); isolated yield: 16.1 mg, 34.4%.

ATR-IR: ν = 3088 vw, 3068 vw, 3054 vw, 3034 vw, 3013 vw, 2963 w/m, 2928 w/m, 2895 w, 2866 w/m, 2821 w, 2792 w, 1579 w, 1547 vw, 1523 vw, 1485 w, 1471 w, 1450 w/m, 1429 w, 1418 w, 1379 w, 1365 w, 1353 w, 1347 w, 1283 w, 1271 w, 1242 w/m, 1215 w/m, 1195 w, 1180 w, 1158 w/m, 1150 w/m, 1130 w/m, 1118 w/m, 1092 m/s, 1043 s, 1034 s, 1008 m/s, 990 w, 984 w, 964 w/m, 939 w, 917 w, 901 w, 857 m, 796 m, 773 s, 750 m, 734 m, 723 m, 714 m, 685 w/m, 646 w/m, 633 w, 614 w, 570 m, 554 w, 530 m, 488 w/m, 473 w/m, 428 w/m, 400 m, 380 m/s cm^{-1}.

Vis-NIR: (DME, 293 K): λ_{max} / nm (ε / dm^3 mol^{-1} cm^{-1}) = 1349 (329), 1345 (330), 1335 (328), 1300 (291), 1024 (490), 963 (566), 892 (730), 859 (796), 852 (829), 846 (850), 841 (847), 823 (913), 779 (1170).

Radiological concerns prohibited combustion-based evaluation of the C and H content of **78**. elements.

Reaction of [(L^{Ar})NpCl] 75 with AgCl to target [$Np^{IV}(L^{Ar})Cl_2$] (Chapter 4.4.1)

Method A

A 10-mL resealable glass ampoule was charged with [(L^{Ar})NpCl], **75**, (36.5 mg, 0.051 mmol) and dissolved in 4 mL of THF, affording an intense red-coloured solution. To this vigorously stirred solution was added AgCl (29.2 mg, 4.0 eq) in the absence of light. Brief inspection of the reaction mixture indicated an immediate colour change of the solution from red to maroon and the precipitation of shiny microcrystalline silver blades. After 3 minutes a pale-yellow powder had precipitated and the resulting maroon supernatant assigned as [(L^{Ar})$NpCl_2$], was isolated by syringe filtration (PTFE membrane, 0.45µm porosity). The filtrate colour turned back to red and copious amounts of an off-white solid precipitated (<0.05 mg ^{237}Np radioassay after pentane wash) over *ca.* 20-30 s period. Subsequent filtration (PTFE membrane, 0.45µm porosity) and concentration of the filtrate under reduced pressure afforded a red crystalline solid which comprises of a mixture of compounds **75** and **76**, as determined by single crystal X-ray diffraction.

Method B

One side of a double 10-mL resealable glass ampoule ('H-shaped', interconnected with a fritted glass disk, 10-16 µm porosity) was charged with [(L^{Ar})NpCl] **75**, (21.7 mg, 0.030 mmol) and AgCl (17.2 mg, 4.0 eq). THF (4 mL) was condensed onto the solids at -78 °C and the resulting stirred reaction mixture was stored at this temperature in the dark. Brief inspection of the reaction mixture indicated a gradual colour change of the suspension to light brown suggesting the formation of [(L^{Ar})$NpCl_2$]. Precipitation of the silver metal and a pale yellow organic by-product occurred during the period of 1 h. After that time the brown solution was filtered at -78 °C and the filtrate evaporated to dryness under reduced pressure. Orange-red coloured solids were isolated and found to contain crystallites of **75** (major) and **76** (minor) occluded in lighter-coloured organic by-products.

5.6 Crystallographic Analyses

Samples of crystals containing transuranium elements were immersed in perfluoropolyalkylether oil (1800 cSt, degassed) and suitable crystals were selected for mounting inside Lindemann glass capillaries, which were manipulated

throughout the process in a way to avoid outer surface contamination. The tube was sealed and varnished with a solution of polycarbonate in dichloromethane and transferred to the goniometer head. Single crystal XRD measurements were performed on a Bruker Apex II Quazar diffractometer collecting 4 full spheres of data.[176,177] The data were integrated with SAINT[176,177], corrected to Lorentz and polarisation effects and an empirical adsorption correction with SADABS[178] was applied. The structures were solved by direct methods and refined to the optimum R_1 value with SHELXL2013.[179,180] Hydrogen atom parameters were constrained. Visualization and rendering of the structures was performed with OLEX2.[181]

The crystallographic experimental data are collated in Chapter 7.2.2 (Appendix). Three already published structures have been deposited at The Cambridge Crystallographic Data Centre with the reference CCDC numbers 1423267-1423269. These data can be obtained free of charge from the CCDC *via* http://www.ccdc.cam.ac.uk/data_request/cif.

5.7 Magnetic Measurements and Analyses

The DC magnetization isotherms of the most stable oxo-containing complexes (**54**, **58**, **64**, **65**) were measured in the magnetic fields B of 0.1 to 7 T and in the temperature range of 2-300 K using Quantum Design MPMS-7T Superconducting Quantum Interference Device (SQUID). The powder samples of [(μ-O){U(Cp)$_3$}$_2$] **54** (m = 60.50(5) mg), [(μ-O){Np(Cp)$_3$}$_2$] **58** (m =59.80(5) mg), [(Cp)$_3$UOUO(THF)(H$_2$L^{Oct})] **64** (m = 18.70(5) mg), [(Cp)$_3$NpOUO(THF)(H$_2$L^{Oct})] **65** (m = 26.80(5) mg) were handheld compressed in a degassed PMMA sample holder of the cylindrical geometry (4.00 mm I.D.) and the fitted PMMA plunger rod was sealed under Ar by setting and fusing of the joint surface with chloroform solvent. The sample holder was further degassed to ensure removal of the solvent residue and quality control of the weld before measurement. The blank magnetization measurements of each sample holder were made and subtracted from the total signal. The DC magnetic susceptibility values have been determined by the longitudinal magnetization to the applied magnetic field ratio, which was calibrated against cylindrical palladium standard. The data correction for the diamagnetic contribution utilized tabulated Pascal's constants.

The effective magnetic moments of the ground states in complexes **64** and **65** were determined as a linear fits to low-temperature sections of the inverse DC susceptibility curves (B = 1 T); the fits passes through the origin of $\chi^{-1} = f(T)$. The obtained values are μ_{eff}(**64**) = 2.42 μ_B and μ_{eff}(**65**) = 2.34 μ_B, respectively. The corresponding data were collated in Chapter 6.2 (Appendix).

The AC susceptibility measurements were performed on the already encapsulated sample **64** using Quantum Design PPMS-14T platform. Magnetization dynamics were acquired on increasing the temperature from 2 to 20 K after zero-field cooling. Each measurement sequence used exclusively the applied AC field of 5 G fixed amplitude and frequencies in between 37 to 9887 Hz. The resulting data were presented in Figure 3.13.

6 Appendix

6.1 Crystallographic Data

[$Np(Cp)_3Cl$] **14**

Identification code	cait54	
Empirical formula	$C_{15}H_{15}ClNp$	
Formula weight	467.72	
Temperature	173(2) K	
Radiation	Mo Kα (λ = 0.71073 Å)	
Crystal system	Monoclinic	
Space group	$P2_1/n$	
Unit cell dimensions	a = 8.1172(6) Å	α = 90°
	b = 12.2727(8) Å	β = 90.5280(10)°
	c = 13.6606(9) Å	γ = 90°
Volume	1360.81(16) Å^3	
Z	4	
Density (calculated)	2.283 Mg/m^3	
Absorption coefficient	7.807 mm^{-1}	
F(000)	860	
Crystal size	0.192 × 0.119 × 0.044 mm^3	
Theta range for data collection	2.231 to 28.258°	
Index ranges	-10 ≤ h ≤ 10, -16 ≤ k ≤ 16, -17 ≤ l ≤ 18	
Reflections collected	23562	
Independent reflections	3217 [R(int) = 0.0180]	
Completeness to theta = 25.242°	100.0 %	
Absorption correction	multi-scan (SADABS)	
Refinement method	Full-matrix least-squares on F^2	
Data / restraints / parameters	3217 / 279 / 229	
Goodness-of-fit on F^2	1.553	
Final R indices [I>2sigma(I)]	R1 = 0.0384, wR2 = 0.1046	
R indices (all data)	R1 = 0.0390, wR2 = 0.1048	
Extinction coefficient	n/a	
Largest diff. peak and hole	2.084 and -2.588 e.Å^{-3}	

[$Np(Cp)_3$] **34**

Identification code	mdit34
Empirical formula	$C_{15}H_{15}Np$
Formula weight	432.27
Temperature	100(2) K
Radiation	Mo Kα (λ = 0.71073 Å)
Crystal system	Orthorhombic
Space group	$Pmc2_1$
Unit cell dimensions	a = 14.1208(6) Å α = 90°
	b = 8.7037(6) Å β = 90°
	c = 9.5917(5) Å γ = 90°
Volume	1178.85(11) $Å^3$
Z	4
Density (calculated)	2.436 Mg/m^3
Absorption coefficient	8.782 mm^{-1}
F(000)	792
Crystal size	0.133 × 0.103 × 0.074 mm^3
Theta range for data collection	2.749 to 28.355°
Index ranges	-18 ≤ h ≤ 18, -11 ≤ k ≤ 11, -12 ≤ l ≤ 12
Reflections collected	10413
Independent reflections	1483 [R(int) = 0.0211]
Completeness to theta = 25.000°	99.8 %
Absorption correction	multi-scan (SADABS)
Refinement method	Full-matrix least-squares on F^2
Data / restraints / parameters	1483 / 13 / 116
Goodness-of-fit on F^2	1.033
Final R indices [I>2sigma(I)]	R1 = 0.0141, wR2 = 0.0355
R indices (all data)	R1 = 0.0145, wR2 = 0.0359
Absolute structure parameter	0.47(7)
Extinction coefficient	n/a
Largest diff. peak and hole	1.045 and -1.123 e.$Å^{-3}$

[$U(Cp)_3Cl$] **38**

Identification code	cait112
Empirical formula	$C_{15}H_{15}ClU$
Formula weight	468.75
Temperature	103(2) K
Radiation	Mo Kα (λ = 0.71073 Å)
Crystal system	Monoclinic
Space group	$P2_1/n$
Unit cell dimensions	a = 8.1321(14) Å α = 90°
	b = 12.216(2) Å β = 90.707(2)°
	c = 13.654(2) Å γ = 90°
Volume	1356.2(4) $Å^3$
Z	4
Density (calculated)	2.296 Mg/m^3
Absorption coefficient	12.139 mm^{-1}
F(000)	856
Crystal size	0.120 × 0.090 × 0.010 mm^3
Theta range for data collection	2.237 to 26.487°
Index ranges	-10 ≤ h ≤ 10, -15 ≤ k ≤ 15, -17 ≤ l ≤ 17
Reflections collected	21900
Independent reflections	2799 [R(int) = 0.0670]
Completeness to theta = 25.242°	99.9 %
Absorption correction	multi-scan (SADABS)
Refinement method	Full-matrix least-squares on F^2
Data / restraints / parameters	2799 / 278 / 229
Goodness-of-fit on F^2	1.580
Final R indices [I>2sigma(I)]	R1 = 0.0494, wR2 = 0.1154
R indices (all data)	R1 = 0.0558, wR2 = 0.1171
Extinction coefficient	n/a
Largest diff. peak and hole	1.804 and -2.462 e.$Å^{-3}$

[$U(Cp)_3$] **39**

Identification code	mdit37	
Empirical formula	$C_{15}H_{15}U$	
Formula weight	433.30	
Temperature	100(2) K	
Radiation	Mo Kα (λ = 0.71073 Å)	
Crystal system	Monoclinic	
Space group	$P2_1$	
Unit cell dimensions	*a* = 8.3355(17) Å	α= 90°
	b = 9.5844(19) Å	β= 116.63(3)°
	c = 8.3355(17) Å	γ = 90°
Volume	595.3(3) $Å^3$	
Z	2	
Density (calculated)	2.417 Mg/m^3	
Absorption coefficient	13.600 mm^{-1}	
F(000)	394	
Crystal size	? × ? × ? mm^3	
Theta range for data collection	2.733 to 28.241°	
Index ranges	-10<=h<=10, -12<=k<=12, -11<=l<=10	
Reflections collected	10137	
Independent reflections	2740 [R(int) = 0.0305]	
Completeness to theta = 25.000°	99.9 %	
Absorption correction	multi-scan (SADABS)	
Refinement method	Full-matrix least-squares on F2	
Data / restraints / parameters	2740 / 151 / 193	
Goodness-of-fit on F^2	1.303	
Final R indices [I>2sigma(I)]	R1 = 0.0474, wR2 = 0.1064	
R indices (all data)	R1 = 0.0492, wR2 = 0.1076	
Absolute structure parameter	0.517(10)	
Extinction coefficient	n/a	
Largest diff. peak and hole	4.884 and -3.697 $e.Å^{-3}$	

$[U(Cp)_3(OEt_2)]$ **39b**

Identification code	mdit36a
Empirical formula	$C_{9.50}H_{12.50}O_{0.50}U_{0.50}$
Formula weight	253.71
Temperature	100(2) K
Radiation	Mo Kα (λ = 0.71073 Å)
Crystal system	Monoclinic
Space group	$P2_1/m$
Unit cell dimensions	*a* = 8.1286(6) Å α= 90°
	b = 13.3807(10) Å β= 112.4590(10)°
	c = 8.3441(6) Å γ = 90°
Volume	838.72(11) $Å^3$
Z	4
Density (calculated)	2.009 Mg/m^3
Absorption coefficient	9.673 mm^{-1}
F(000)	478
Crystal size	? × ? × ? mm^3
Theta range for data collection	2.641 to 28.449°
Index ranges	-10 ≤ h ≤ 10, -17 ≤ k ≤ 16, -11 ≤ l ≤ 10
Reflections collected	14764
Independent reflections	2076 [R(int) = 0.0349]
Completeness to theta = 25.000°	99.9 %
Absorption correction	multi-scan (SADABS)
Refinement method	Full-matrix least-squares on F^2
Data / restraints / parameters	2076 / 0 / 156
Goodness-of-fit on F^2	1.300
Final R indices [I>2sigma(I)]	R1 = 0.0282, wR2 = 0.0800
R indices (all data)	R1 = 0.0299, wR2 = 0.0807
Extinction coefficient	n/a
Largest diff. peak and hole	2.631 and -2.039 $e.Å^{-3}$

[Np(Cp')$_3$] **40**

Identification code	mdit46	
Empirical formula	$C_{24}H_{39}NpSi_3$	
Formula weight	648.82	
Temperature	100(2) K	
Radiation	Mo Kα (λ = 0.71073 Å)	
Crystal system	Orthorhombic	
Space group	*Pbca*	
Unit cell dimensions	*a* = 8.2980(6) Å	α = 90°
	b = 22.1664(17) Å	β = 90°
	c = 28.917(2) Å	γ = 90°
Volume	5318.8(7) Å^3	
Z	8	
Density (calculated)	1.620 Mg/m^3	
Absorption coefficient	4.051 mm^{-1}	
F(000)	2544	
Crystal size	0.075 × 0.025 × 0.012 mm^3	
Theta range for data collection	1.408 to 28.359°	
Index ranges	-11 ≤ h ≤ 9, -28 ≤ k ≤ 22, -38 ≤ l ≤ 37	
Reflections collected	42491	
Independent reflections	6360 [R(int) = 0.0919]	
Completeness to theta = 25.000°	100.0 %	
Absorption correction	mutli-scan method (SADABS)	
Refinement method	Full-matrix least-squares on F^2	
Data / restraints / parameters	6360 / 0 / 268	
Goodness-of-fit on F^2	1.027	
Final R indices [I>2sigma(I)]	R1 = 0.0393, wR2 = 0.0490	
R indices (all data)	R1 = 0.0866, wR2 = 0.0567	
Extinction coefficient	n/a	
Largest diff. peak and hole	1.200 and -1.276 e.Å^{-3}	

[K{Np(Cp)$_4$}] **43**

Identification code	mdit67	
Empirical formula	$C_{32}H_{35}K_{1.50}Np_{1.50}O_{0.50}$	
Formula weight	841.75	
Temperature	100(2) K	
Radiation	Mo Kα (λ = 0.71073 Å)	
Crystal system	Monoclinic	
Space group	C_2	
Unit cell dimensions	*a* = 22.6093(10) Å	α = 90°
	b = 14.7125(10) Å	β = 90.4150(10)°
	c = 9.0155(5) Å	γ = 90°
Volume	2998.8(3) Å^3	
Z	4	
Density (calculated)	1.864 Mg/m^3	
Absorption coefficient	5.406 mm^{-1}	
F(000)	1596	
Crystal size	0.044 × 0.032 × 0.024 mm^3	
Theta range for data collection	1.651 to 28.568°	
Index ranges	-30 ≤ h ≤ 29, -19 ≤ k ≤ 19, -12 ≤ l ≤ 11	
Reflections collected	27617	
Independent reflections	7071 [R(int) = 0.0474]	
Completeness to theta = 25.000°	100.0 %	
Absorption correction	mutli-scan method (SADABS)	
Refinement method	Full-matrix least-squares on F^2	
Data / restraints / parameters	7071 / 22 / 272	
Goodness-of-fit on F^2	1.062	
Final R indices [I>2sigma(I)]	R1 = 0.0330, wR2 = 0.0753	
R indices (all data)	R1 = 0.0399, wR2 = 0.0783	
Absolute structure parameter	0.000(11)	
Extinction coefficient	n/a	
Largest diff. peak and hole	1.304 and -0.868 e.Å^{-3}	

[(μ-O)[U(Cp)$_3$]] **54**

Identification code	mdit22	
Empirical formula	$C_{15}H_{15}O_{0.50}U$	
Formula weight	441.30	
Temperature	100(2) K	
Radiation	Mo Kα (λ = 0.71073 Å)	
Crystal system	Triclinic	
Space group	*P*-1	
Unit cell dimensions	*a* = 8.2562(7) Å	α = 72.5240(10)°
	b = 8.2838(7) Å	β = 88.3430(10)°
	c = 13.2887(11) Å	γ = 60.7640(10)°
Volume	748.86(11) Å^3	
Z	2	
Density (calculated)	1.957 Mg/m^3	
Absorption coefficient	10.816 mm^{-1}	
F(000)	402	
Crystal size	? × ? × ? mm^3	
Theta range for data collection	1.623 to 28.400°	
Index ranges	-10 ≤ h ≤ 11, -11 ≤ k ≤ 10, -17 ≤ l ≤ 17	
Reflections collected	13408	
Independent reflections	3501 [R(int) = 0.0254]	
Completeness to theta = 25.000°	99.9 %	
Absorption correction	multi-scan (SADABS)	
Refinement method	Full-matrix least-squares on F^2	
Data / restraints / parameters	3501 / 6 / 233	
Goodness-of-fit on F^2	1.117	
Final R indices [I>2sigma(I)]	R1 = 0.0337, wR2 = 0.0918	
R indices (all data)	R1 = 0.0507, wR2 = 0.1004	
Extinction coefficient	n/a	
Largest diff. peak and hole	2.301 and -2.093 e.Å^{-3}	

[{(Cp)$_3$Np(μ-O)}$_2${Np(Cp)$_2$}] **57**

Identification code	mdit75
Empirical formula	$C_{40}H_{40}Np_3O_2$
Formula weight	1263.72
Temperature	100(2) K
Radiation	Mo Kα (λ = 0.71073 Å)
Crystal system	Monoclinic
Space group	$P2_1/n$
Unit cell dimensions	a = 8.3917(4) Å α = 90°
	b = 27.6278(12) Å β = 90.7120(10)°
	c = 14.6608(6) Å γ = 90°
Volume	3398.8(3) Å^3
Z	4
Density (calculated)	2.470 Mg/m^3
Absorption coefficient	9.139 mm^{-1}
F(000)	2300
Crystal size	0.166 × 0.011 × 0.011 mm^3
Theta range for data collection	1.474 to 28.462°
Index ranges	-11 ≤ h ≤ 4, -36 ≤ k ≤ 36, -19 ≤ l ≤ 19
Reflections collected	29761
Independent reflections	7914 [R(int) = 0.0527]
Completeness to theta = 25.000°	100.0 %
Absorption correction	multi-scan (SADABS)
Refinement method	Full-matrix least-squares on F^2
Data / restraints / parameters	7914 / 0 / 409
Goodness-of-fit on F^2	1.000
Final R indices [I>2sigma(I)]	R1 = 0.0325, wR2 = 0.0509
R indices (all data)	R1 = 0.0589, wR2 = 0.0566
Extinction coefficient	n/a
Largest diff. peak and hole	1.567 and -1.537 e.Å^{-3}

[(μ-O){Np(Cp)$_3$}] **58**

Identification code	mdit68
Empirical formula	$C_{30}H_{30}Np_2O$
Formula weight	880.54
Temperature	100(2) K
Radiation	Mo Kα (λ = 0.71073 Å)
Crystal system	Monoclinic
Space group	*Cc*
Unit cell dimensions	*a* = 14.4553(17) Å α = 90°
	b = 8.2422(10) Å β = 108.284(2)°
	c = 21.434(3) Å γ = 90°
Volume	2424.8(5) Å^3
Z	4
Density (calculated)	2.412 Mg/m^3
Absorption coefficient	8.544 mm^{-1}
F(000)	1616
Crystal size	0.056 × 0.046 × 0.012 mm^3
Theta range for data collection	2.001 to 28.402°
Index ranges	-19 ≤ h ≤ 18, -10 ≤ k ≤ 11, -28 ≤ l ≤ 28
Reflections collected	21024
Independent reflections	5675 [R(int) = 0.0434]
Completeness to theta = 25.000°	100.0 %
Absorption correction	multi-scan (SADABS)
Refinement method	Full-matrix least-squares on F^2
Data / restraints / parameters	5675 / 188 / 245
Goodness-of-fit on F^2	1.262
Final R indices [I>2sigma(I)]	R1 = 0.0369, wR2 = 0.0676
R indices (all data)	R1 = 0.0441, wR2 = 0.0706
Absolute structure parameter	0.50(6)
Extinction coefficient	n/a
Largest diff. peak and hole	2.697 and -2.909 e.Å^{-3}

$[UO_2(THF)(H_2L^{Et})]$ **60**

Identification code	mdit18	
Empirical formula	$C_{30}H_{30}N_4O_4U$	
Formula weight	748.61	
Temperature	100(2) K	
Radiation	Mo Kα (λ = 0.71073 Å)	
Crystal system	Triclinic	
Space group	*P*-1	
Unit cell dimensions	*a* = 1151.44(18) pm	α = 84.478(2)°
	b = 1472.3(2) pm	β = 68.723(2)°
	c = 1566.6(2) pm	γ = 69.020(2)°
Volume	2.3089(6) nm^3	
Z	4	
Density (calculated)	2.154 Mg/m^3	
Absorption coefficient	7.081 mm^{-1}	
F(000)	1448	
Crystal size	0.057 × 0.040 × 0.039 mm^3	
Theta range for data collection	1.396 to 28.320°	
Index ranges	-15 ≤ h ≤ 15, -19 ≤ k ≤ 19, -19 ≤ l ≤19	
Reflections collected	24030	
Independent reflections	9356 [R(int) = 0.0580]	
Completeness to theta = 25.000°	92.2 %	
Absorption correction	multi-scan (SADABS)	
Refinement method	Full-matrix least-squares on F^2	
Data / restraints / parameters	9356 / 4 / 601	
Goodness-of-fit on F^2	1.031	
Final R indices [I>2sigma(I)]	R1 = 0.0417, wR2 = 0.0806	
R indices (all data)	R1 = 0.0644, wR2 = 0.0874	
Extinction coefficient	n/a	
Largest diff. peak and hole	1.823 and -1.973 e.$Å^{-3}$	

$[(Cp)_3NpOUO(THF)(H_2L^{Et})]$ **63**

Identification code	mdit51
Empirical formula	$C_{77}H_{97}N_8NpO_6U$
Formula weight	1705.65
Temperature	100(2) K
Radiation	Mo Kα (λ = 0.71073 Å)
Crystal system	Triclinic
Space group	*P*-1
Unit cell dimensions	*a* = 12.6253(15) Å α = 93.830(2)°
	b = 15.5437(18) Å β = 100.069(2)°
	c = 18.576(2) Å γ = 105.514(2)°
Volume	3433.6(7) $Å^3$
Z	2
Density (calculated)	1.650 Mg/m^3
Absorption coefficient	3.920 mm^{-1}
F(000)	1696
Crystal size	0.061 × 0.056 × 0.022 mm^3
Theta range for data collection	1.369 to 28.312°
Index ranges	-16 ≤ h ≤ 16, -20 ≤ k ≤ 20, -8 ≤ l ≤ 24
Reflections collected	29244
Independent reflections	15350 [R(int) = 0.0872]
Completeness to theta = 25.000°	99.6 %
Absorption correction	multi-scan (SADABS)
Refinement method	Full-matrix least-squares on F^2
Data / restraints / parameters	15350 / 204 / 866
Goodness-of-fit on F^2	0.951
Final R indices [I>2sigma(I)]	R1 = 0.0671, wR2 = 0.1317
R indices (all data)	R1 = 0.1589, wR2 = 0.1666
Extinction coefficient	n/a
Largest diff. peak and hole	2.720 and -3.032 $e.Å^{-3}$

$[(Cp)_3UOUO(THF)(H_2L^{Oct})]$ **64**

Identification code	mdit77a
Empirical formula	$C_{34.70}H_{40.90}N_4O_{2.55}U$
Formula weight	792.84
Temperature	100(2) K
Radiation	Mo Kα (λ = 0.71073 Å)
Crystal system	Monoclinic
Space group	$P2_1/n$
Unit cell dimensions	a = 15.6132(16) Å α = 90°
	b = 19.1552(19) Å β = 106.801(2)°
	c = 23.650(3) Å γ = 90°
Volume	6771.1(12) Å^3
Z	8
Density (calculated)	1.555 Mg/m^3
Absorption coefficient	4.831 mm^{-1}
F(000)	3116
Crystal size	0.151 × 0.121 × 0.096 mm^3
Theta range for data collection	1.392 to 28.382°
Index ranges	-20 ≤ h ≤ 20, -25 ≤ k ≤ 25, -31 ≤ l ≤ 31
Reflections collected	117266
Independent reflections	16065 [R(int) = 0.0510]
Completeness to theta = 25.000°	100.0 %
Refinement method	Full-matrix least-squares on F^2
Data / restraints / parameters	16065 / 0 / 823
Goodness-of-fit on F^2	1.107
Final R indices [I>2sigma(I)]	R1 = 0.0395, wR2 = 0.0980
R indices (all data)	R1 = 0.0671, wR2 = 0.1141
Extinction coefficient	n/a
Largest diff. peak and hole	3.406 and -1.754 e.Å^{-3}

[$(Cp)_3$NpOUO(THF)(H_2L^{Oct})] **65**

Identification code	mdit71
Empirical formula	$C_{68}H_{79}N_8NpO_{4.75}U$
Formula weight	1559.42
Temperature	100(2) K
Radiation	Mo Kα (λ = 0.71073 Å)
Crystal system	Monoclinic
Space group	$P2_1/n$
Unit cell dimensions	a = 15.6568(10) Å α = 90°
	b = 19.1455(13) Å β = 106.9890(10)°
	c = 23.7278(16) Å γ = 90°
Volume	6802.2(8) $Å^3$
Z	4
Density (calculated)	1.523 Mg/m^3
Absorption coefficient	3.948 mm^{-1}
F(000)	3064
Crystal size	0.151 × 0.131 × 0.059 mm^3
Theta range for data collection	1.392 to 28.477°
Index ranges	-20 ≤ h ≤ 20, -25 ≤ k ≤ 24, -31 ≤ l ≤ 31
Reflections collected	121427
Independent reflections	16294 [R(int) = 0.0320]
Completeness to theta = 25.000°	99.9 %
Absorption correction	multi-scan (SADABS)
Max. and min. transmission	0.786 and 0.699
Refinement method	Full-matrix least-squares on F^2
Data / restraints / parameters	16294 / 51 / 805
Goodness-of-fit on F^2	1.157
Final R indices [I>2sigma(I)]	R1 = 0.0397, wR2 = 0.1149
R indices (all data)	R1 = 0.0537, wR2 = 0.1237
Extinction coefficient	n/a
Largest diff. peak and hole	2.562 and -2.462 $e.Å^{-3}$

[(L^{Ar})NpCl] **75**

Identification code	mdit30 / CCDC 1423269
Empirical formula	$C_{16}H_{18}Cl_{0.50}NNp_{0.50}$
Formula weight	360.54
Temperature	100(2) K
Radiation	Mo Kα (λ = 0.71073 Å)
Crystal system	monoclinic
Space group	*C*2/*c*
Unit cell dimensions	*a* = 18.9910(14) Å α = 90°
	b = 14.9865(11) Å β = 110.3210(10)°
	c = 10.1443(8) Å γ = 90°
Volume	2707.5(4) $Å^3$
Z	8
Density (calculated)	1.769 Mg/m^3
Absorption coefficient	3.961 mm^{-1}
F(000)	1408
Crystal size	0.14 × 0.11 × 0.04 mm^3
Theta range for data collection	1.78 to 28.42°
Index ranges	-24 ≤ h ≤ 25, -19 ≤ k ≤ 19, -13 ≤ l ≤ 13
Reflections collected	24111
Independent reflections	3264 [R(int) = 0.0295]
Completeness to theta = 25.00°	100.0 %
Absorption correction	multi-scan (SADABS)
Max. and min. transmission	0.8545 and 0.6032
Refinement method	Full-matrix least-squares on F^2
Data / restraints / parameters	3264 / 0 / 172
Goodness-of-fit on F^2	0.759
Final R indices [I>2sigma(I)]	R1 = 0.0196, wR2 = 0.0509
R indices (all data)	R1 = 0.0204, wR2 = 0.0521
Largest diff. peak and hole	2.932 and -0.948 $e.Å^{-3}$

$[(L^{Ar})Np_2Cl_4(THF)_3]$ **76**

Identification code	mdit25 / CCDC 1423267
Empirical formula	$C_{46}H_{64}Cl_4N_2Np_2O_{3.50}$
Formula weight	1316.79
Temperature	100(2) K
Radiation	Mo Kα (λ = 0.71073 Å)
Crystal system	Triclinic
Space group	*P*-1
Unit cell dimensions	a = 10.5639(7) Å α= 75.1470(10)°
	b = 13.6771(8) Å β= 75.7320(10)°
	c = 18.1083(11) Å γ = 84.3340(10)°
Volume	2449.2(3) $Å^3$
Z	2
Density (calculated)	1.786 Mg/m^3
Absorption coefficient	4.478 mm^{-1}
F(000)	1272
Crystal size	0.084 × 0.065 × 0.015 mm^3
Theta range for data collection	1.195 to 28.497°
Index ranges	-14 ≤ h ≤ 9, -18 ≤ k ≤ 17, -23 ≤ l ≤ 20
Reflections collected	21593
Independent reflections	11033 [R(int) = 0.0416]
Completeness to theta = 25.000°	99.7 %
Absorption correction	multi-scan (SADABS)
Refinement method	Full-matrix least-squares on F^2
Data / restraints / parameters	11033 / 150 / 559
Goodness-of-fit on F^2	1.014
Final R indices [I>2sigma(I)]	R1 = 0.0415, wR2 = 0.0901
R indices (all data)	R1 = 0.0717, wR2 = 0.1026
Extinction coefficient	n/a
Largest diff. peak and hole	1.834 and -1.568 $e.Å^{-3}$

[K(DME)($L^{Ar\text{-}H}$)Np(OMe)]$_2$ **78**

Identification code	mdit78a / CCDC 1423268	
Empirical formula	$C_{37}H_{48}KN_2NpO_3$	
Formula weight	844.87	
Temperature	100(2) K	
Radiation	Mo Kα (λ = 0.71073 Å)	
Crystal system	Monoclinic	
Space group	$P2_1/n$	
Unit cell dimensions	a = 10.205(3) Å	α = 90°
	b = 20.025(5) Å	β = 105.645(5)°
	c = 17.800(4) Å	γ = 90°
Volume	3502.7(15) Å^3	
Z	4	
Density (calculated)	1.602 Mg/m^3	
Absorption coefficient	3.122 mm^{-1}	
F(000)	1680	
Crystal size	0.253 × 0.023 × 0.009 mm^3	
Theta range for data collection	1.564 to 28.421°	
Index ranges	-13 ≤ h ≤ 9, -26 ≤ k ≤ 26, -21 ≤ l ≤ 22	
Reflections collected	29155	
Independent reflections	8007 [R(int) = 0.1154]	
Completeness to theta = 25.000°	99.6 %	
Absorption correction	Semi-empirical from equivalents	
Max. and min. transmission	0.972 and 0.929	
Refinement method	Full-matrix least-squares on F^2	
Data / restraints / parameters	8007 / 0 / 418	
Goodness-of-fit on F^2	0.978	
Final R indices [I>2sigma(I)]	R1 = 0.0664, wR2 = 0.1108	
R indices (all data)	R1 = 0.1405, wR2 = 0.1250	
Largest diff. peak and hole	2.917 and -2.311 e.Å^{-3}	

6.2 Supplementary Magnetism Data

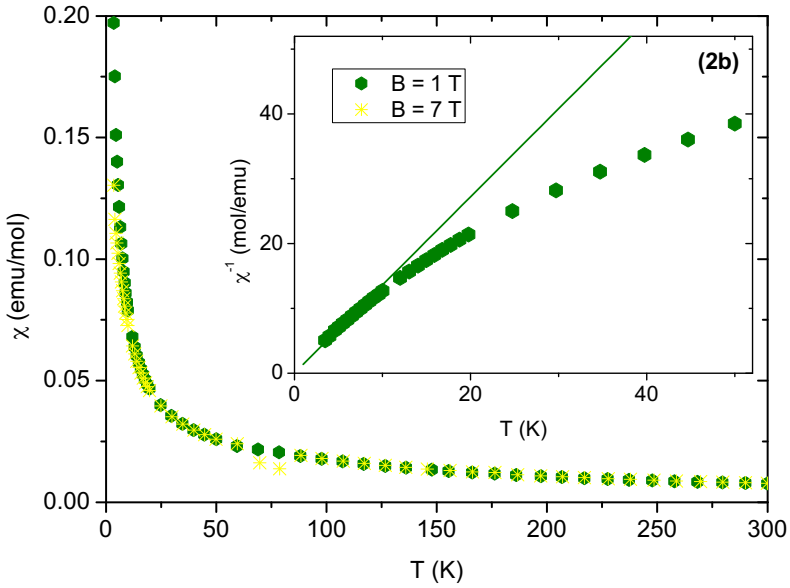

Figure 6.1. DC magnetic susceptibility (χ) of $[(Cp)_3UOUO(THF)(H_2L^{Oct})]$ **64** measured as a function of the temperature T, for different values of the magnetic field B (see legend). Inset: data for B = 1 T plotted as $\chi^{-1} = f(T)$, and fit of the low-temperature part with a Curie-Weiss law (line).

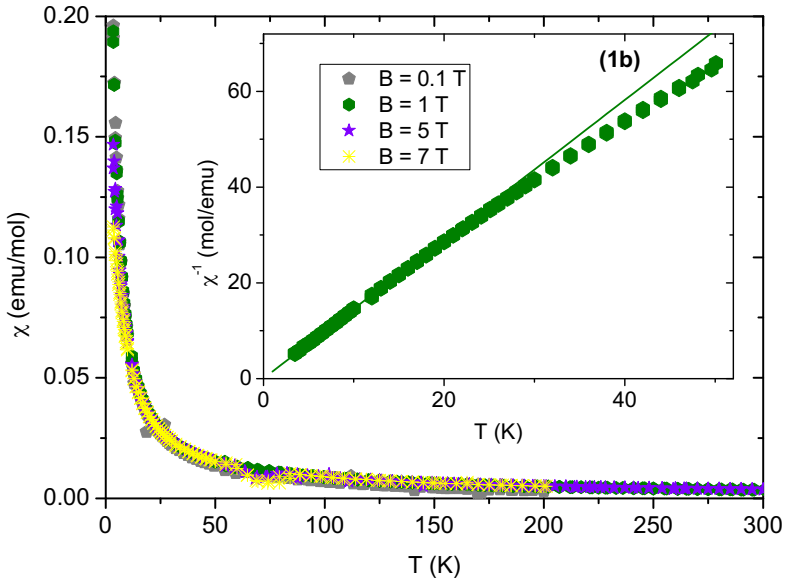

Figure 6.2. DC magnetic susceptibility (χ) of $[(Cp)_3NpOUO(THF)(H_2L^{Oct})]$ **65** measured as a function of the temperature T, for different values of the magnetic field B (see legend). Inset: data for B = 1 T plotted as $\chi^{-1} = f(T)$, and fit of the low-temperature part with a Curie-Weiss law (line).

6.3 Publications Related to this Thesis

M. S. Dutkiewicz, J. H. Farnaby, C. Apostolidis, E. Colineau, O. Walter, N. Magnani, M. G. Gardiner, J. B. Love, N. Kaltsoyannis, R. Caciuffo and P. L. Arnold *Nature Chemistry* **8**, 797-802 (2016); Organometallic neptunium(III) complexes.

P. L. Arnold, M. S. Dutkiewicz, M. Zegke, O. Walter, C. Apostolidis, Emmalina Hollis, A.-F. Pécharman, N. Magnani, J.-C. Griveau, R. Caciuffo, X. Zhang, G. Schreckenbach, J. B. Love *Angewandte Chemie International Edition* **2016**, *55* (41), 12797-12801; Subtle Interactions and Electron Transfer between U^{III}, Np^{III}, or Pu^{III} and Uranyl Mediated by the Oxo Group.

6.4 Public Presentations Related to this Thesis

45èmes Journées des Actinides (JDA), Prague, Czech Republic, **2015**; poster and oral presentations.

European F-Element Network (EUFEN-4) meeting, Lisbon, Portugal, **2015**; poster presentation. Award: *Outstanding Poster Presentation*.

Dalton Discussion 14: Advancing the chemistry of the f-elements, Edinburgh, UK, **2014**, Poster Presentation;

6.5 Fellowships Related to this Thesis

EC-JRC ITU Grantholder Cat. 20 Apr.2012 – Apr. 2015
Scientific/Technical Project Officer, E06

TALISMAN Joint Research Project C04-07 Apr.2015 – Aug.2015
Principal Investigator

7 Bibliography

[1] Wang, M.; Audi, G.; Wapstra, A. H.; Kondev, F. G.; MacCormick, M.; Xu, X.; Pfeiffer, B. *Chinese Phys. C* **2012**, *36* (12), 1603–2014.
[2] Bhat, M. R. In *Nuclear Data for Science and Technology*; Qaim, S. M., Ed.; Research Reports in Physics; Springer Berlin Heidelberg: Berlin, Heidelberg, 1992; pp 817–821.
[3] Dalrymple, G. B. *Geol. Soc. London, Spec. Publ.* **2001**, *190* (1), 205–221.
[4] Thompson, R. C. *Radiat. Res.* **1982**, *90* (1), 1–32.
[5] Herbst, R. S.; Baron, P.; Nilsson, M. *Advanced Separation Techniques for Nuclear Fuel Reprocessing and Radioactive Waste Treatment*; Elsevier, 2011.
[6] Drake, V. A. In *Science and Technology of Tributyl Phosphate Vol. III*; Schulz, W. W., Burger, L. L., Navratil, J. D., Eds.; CRC Press: Boca Rayton, Florida, 1990; pp 123–146.
[7] Porter, J. A. *Ind. Eng. Chem. Process Des. Dev.* **1964**, *3* (4), 289–292.
[8] Bertch, T.; Brown, L. *US Pat. App. 13/675,850* **2012**.
[9] Yoshida, Z.; Johnson, S. G.; Takaumi, K.; Krsul, J. R. In *The Chemistry of the Actinide and Transactinide Elements*; Morss, L. R., Edelstein, N. M., Fuger, J., Eds.; Springer Netherlands: Dordrecht, 2006; pp 699–812.
[10] *The Chemistry of the Actinide and Transactinide Elements*; Morss, L. R., Edelstein, N. M., Fuger, J., Eds.; Springer Netherlands: Dordrecht, 2011.
[11] Lemire, R. J.; Fuger, J.; Nitsche, H.; Potter, P.; Rand, M. H.; Rydberg, J.; Spahiu, K.; Sullivan, J. C.; Ullman, W. J.; Vitorge, P.; Wanner, H. *Chemical Thermodynamics of Neptunium and Plutonium*; OECD Nuclear Energy Agency, Ed.; Elsevier: Amsterdam, 2001.
[12] Mishin, V. Y.; Sidorenko, G. V.; Suglobov, D. N. *Sov. Radiochem. (Engl. Transl.); (United States)* **1987**, *28:3*, 293–300.
[13] Kienzler, B.; Vejmelka, P.; Römer, J.; Fanghänel, E.; Jansson, M.; Eriksen, T. E.; Wikberg, P. *J. Contam. Hydrol.* **2003**, *61* (1–4), 219–233.
[14] Dierking, S.; Amayri, S.; Reich, T. *J. Nucl. Sci. Technol.* **2008**, *45* (sup6), 133–137.
[15] Icopini, G. A.; Boukhalfa, H.; Neu, M. P. *Environ. Sci. Technol.* **2007**, *41* (8), 2764–2769.
[16] Ibers, J. *Nat. Chem.* **2010**, *2* (11), 996.
[17] Emsley, J. *Nature's Building Blocks: An A-Z Guide to the Elements*, New Editio.; Oxford University Press Inc.: New York, 2011.
[18] Neptunium-237-decay-scheme-simplified (c)Kays666. CC BY-SA 3.0.
[19] NucleonicaGmbH. Nucleonica GmbH: Karlsruhe, Germany 2014.
[20] Apostolidis, C. Private communication, 2015.
[21] Weiss, P. *Sci. News* **2002**, *162* (17), 259.
[22] Liddle, S. T. *Angew. Chem. Int. Ed. Engl.* **2015**, *54* (30), 8604–8641.
[23] Gaunt, A. J.; Neu, M. P. *Comptes Rendus Chim.* **2010**, *13* (6–7), 821–831.
[24] Jones, M. B.; Gaunt, A. J. *Chem. Rev.* **2013**, *113* (2), 1137–1198.
[25] Dam, H. H.; Reinhoudt, D. N.; Verboom, W. *Chem. Soc. Rev.* **2007**, *36* (2), 367–377.
[26] Lewis, F.; Hudson, M.; Harwood, L. *Synlett* **2011**, *2011* (18), 2609–2632.
[27] Neidig, M. L.; Clark, D. L.; Martin, R. L. *Coord. Chem. Rev.* **2013**, *257* (2), 394–406.
[28] Kaltsoyannis, N. *Inorg. Chem.* **2013**, *52* (7), 3407–3413.
[29] Bursten, B. E.; Rhodes, L. F.; Strittmatter, R. J. *J. Am. Chem. Soc.* **1989**, *111* (8), 2756–2758.
[30] Kirker, I.; Kaltsoyannis, N. *Dalton Trans.* **2011**, *40* (1), 124–131.
[31] Minasian, S. G.; Keith, J. M.; Batista, E. R.; Boland, K. S.; Clark, D. L.; Kozimor, S. A.; Martin, R. L.; Shuh, D. K.; Tyliszczak, T. *Chem. Sci.* **2014**, *5* (1), 351–359.
[32] Prodan, I. D.; Scuseria, G. E.; Martin, R. L. *Phys. Rev. B* **2007**, *76* (3), 33101.
[33] Meihaus, K. R.; Long, J. R. *Dalton Trans.* **2015**, *44* (6), 2517–2528.
[34] Liddle, S. T.; van Slageren, J. In *Lanthanides and Actinides in Molecular Magnetism*; Layfield, R. A., Murugesu, M., Eds.; Wiley-VCH Verlag GmbH & Co. KGaA: Weinheim, Germany, 2015; pp 315–339.
[35] Mougel, V.; Chatelain, L.; Pécaut, J.; Caciuffo, R.; Colineau, E.; Griveau, J.-C.;

Mazzanti, M. *Nat. Chem.* **2012**, *4* (12), 1011–1017.
[36] Chatelain, L.; Walsh, J. P. S.; Pécaut, J.; Tuna, F.; Mazzanti, M. *Angew. Chem. Int. Ed. Engl.* **2014**, *53* (49), 13434–13438.
[37] Magnani, N.; Apostolidis, C.; Morgenstern, A.; Colineau, E.; Griveau, J.-C.; Bolvin , H.; Walter, O.; Caciuffo, R. *Angew. Chemie Int. Ed.* **2011**, *50* (7), 1696–1698.
[38] Rinehart, J. D.; Long, J. R. *J. Am. Chem. Soc.* **2009**, *131* (35), 12558–12559.
[39] Edelmann, F. T. *Coord. Chem. Rev.* **2016**, *306*, 346–419.
[40] Edelmann, F. T.; Lorenz, V. *Coord. Chem. Rev.* **2000**, *209* (1), 99–160.
[41] Hyeon, J. *Coord. Chem. Rev.* **2003**, *241* (1–2), 249–272.
[42] Gottfriedsen, J.; Edelmann, F. T. *Coord. Chem. Rev.* **2005**, *249* (9–10), 919–969.
[43] Richter, J.; Edelmann, F. T. *Coord. Chem. Rev.* **1996**, *147*, 373–442.
[44] Hyeon, J. *Coord. Chem. Rev.* **2003**, *247* (1–2), 21–78.
[45] Kilimann, U.; Edelmann, F. T. *Coord. Chem. Rev.* **1995**, *141*, 1–61.
[46] Hyeon, J.-Y.; Gottfriedsen, J.; Edelmann, F. T. *Coord. Chem. Rev.* **2005**, *249* (24), 2787–2844.
[47] Edelmann, F. T. *Coord. Chem. Rev.* **2006**, *250* (19–20), 2511–2564.
[48] Gottfriedsen, J.; Edelmann, F. T. *Coord. Chem. Rev.* **2006**, *250* (19–20), 2347–2410.
[49] Gottfriedsen, J.; Edelmann, F. *Coord. Chem. Rev.* **2007**, *251* (1–2), 142–202.
[50] Edelmann, F. T.; Gun'ko, Y. K. *Coord. Chem. Rev.* **1997**, *165*, 163–237.
[51] Edelmann, F. T. *Coord. Chem. Rev.* **2009**, *253* (3–4), 343–409.
[52] Edelmann, F. T. *Coord. Chem. Rev.* **2009**, *253* (21–22), 2515–2587.
[53] Edelmann, F. T. *Coord. Chem. Rev.* **2011**, *255* (15–16), 1834–1920.
[54] Edelmann, F. T. *Coord. Chem. Rev.* **2012**, *256* (11–12), 1151–1228.
[55] Edelmann, F. T. *Coord. Chem. Rev.* **2012**, *256* (23–24), 2641–2740.
[56] Edelmann, F. T. *Coord. Chem. Rev.* **2013**, *257* (7–8), 1122–1231.
[57] Edelmann, F. T. *Coord. Chem. Rev.* **2014**, *261*, 73–155.
[58] Edelmann, F. T. *Coord. Chem. Rev.* **2015**, *284*, 124–205.
[59] Richter, J.; Edelmann, F. T.; Kilimann, U. *Coord. Chem. Rev.* **2003**, *256* (1–2), 99–160.
[60] Behrle, A. C.; Walensky, J. R. In *Encyclopedia of Inorganic and Bioinorganic Chemistry*; Scott, R. A., Ed.; John Wiley & Sons, Ltd: Chichester, UK, 2014; pp 1–41.
[61] Choppin, G.; Liljenzin, J.-O.; Rydberg, J.; Ekberg, C. *Radiochemistry and Nuclear Chemistry*; Elsevier, 2013.
[62] Bates, R. G.; Macaskill, J. B. *Pure Appl. Chem.* **1978**, *50* (11), 1701–1706.
[63] Marks, T. J.; Ernst, R. D. *Comprehensive Organometallic Chemistry*; Elsevier, 1982.
[64] Sonnenberger, D. C.; Gaudiello, J. G. *Inorg. Chem.* **1988**, *27* (15), 2747–2748.
[65] Bohlander, R. The organometallic chemistry of neptunium, Karlsruhe Univ. (T.H.), 1986.
[66] Banks, R. H.; Edelstein, N. M.; Spencer, B.; Templeton, D. H.; Zalkin, A. *J. Am. Chem. Soc.* **1980**, *102* (2), 620–623.
[67] Laubereau, P. Präparative und radiochemische Synthesen von Cyclopentadienylkomplexen der Actiniden und des Promethiums, sowie Untersuchungen zum Spaltprodukteinbau in Aromaten-Fängerkomplexe, Technischen Hochschule München, 1966.
[68] Baker, R. J. *Coord. Chem. Rev.* **2012**, *256* (23–24), 2843–2871.
[69] Brown, D.; Edwards, J. *J. Chem. Soc. Dalt. Trans.* **1972**, No. 16, 1757.
[70] Fried, S.; Davidson, N. *J. Am. Chem. Soc.* **1948**, *70* (11), 3539–3547.
[71] Hayashi, H.; Takano, M.; Kurata, M.; Minato, K. *J. Nucl. Mater.* **2013**, *440* (1–3), 477–479.
[72] Taylor, J. C.; Wilson, P. W. *Acta Crystallogr. Sect. B* **1974**, *30* (12), 2803–2805.
[73] Levy, J. H.; Taylor, J. C.; Wilson, P. W. *Acta Crystallogr. Sect. B* **1975**, *31* (3), 880–882.
[74] Kanellakopulos, B.; Fischer, E. O.; Dornberger, E.; Baumgärtner, F. *J. Organomet. Chem.* **1970**, *24* (2), 507–514.
[75] Karraker, D. G. *Inorganica Chim. Acta* **1987**, *139* (1–2), 189–191.
[76] Avens, L. R.; Bott, S. G.; Clark, D. L.; Sattelberger, A. P.; Watkin, J. G.; Zwick, B. D. *Inorg. Chem.* **1994**, *33* (10), 2248–2256.

[77] Clark, D. L.; Sattelberger, A. P.; Bott, S. G.; Vrtis, R. N. *Inorg. Chem.* **1989**, *28* (10), 1771–1773.
[78] Foropoulos, Jr., Jerry (Los Alamos, N.; Avens, Larry R. (Los Alamos, N.; Trujillo, Eddie A. (Espanola, N. Dehydration of plutonium or neptunium trichloride hydrate. US 5098682, 1992.
[79] Hecht, H.; Jander, G.; Schlapmann, H. *Zeitschrift für Anorg. Chemie* **1947**, *254* (5–6), 255–264.
[80] Hecht, H. *Zeitschrift für Anorg. Chemie* **1947**, *254* (1–2), 37–51.
[81] Choporov, D. Y.; Chudinov, E. G. *Radiokhimiya, 10 221-7(1968).* **1968**.
[82] Bagnall, K. W.; Laidler, J. B. *J. Chem. Soc. A Inorganic, Phys. Theor.* **1966**, 516.
[83] Patel, D.; Wooles, A. J.; Hashem, E.; Omorodion, H.; Baker, R. J.; Liddle, S. T. *New J. Chem.* **2015**, *39* (10), 7559–7562.
[84] Eisenberg, D. C.; Streitwieser, A.; Kot, W. K. *Inorg. Chem.* **1990**, *29* (1), 10–14.
[85] Reilly, S. D.; Brown, J. L.; Scott, B. L.; Gaunt, A. J. *Dalton Trans.* **2014**, *43* (4), 1498–1501.
[86] Cantat, T.; Scott, B. L.; Kiplinger, J. L. *Chem. Commun. (Camb).* **2010**, *46* (6), 919–921.
[87] Schnaars, D. D.; Wu, G.; Hayton, T. W. *Dalton Trans.* **2008**, No. 44, 6121–6126.
[88] Brown, J. L.; Batista, E. R.; Boncella, J. M.; Gaunt, A. J.; Reilly, S. D.; Scott, B. L.; Tomson, N. C. *J. Am. Chem. Soc.* **2015**, *137* (30), 9583–9586.
[89] Brown, J. L.; Gaunt, A.; King, D. M.; Liddle, S.; Reilly, S. D.; Scott, B.; Wooles, A. *Chem. Commun.* **2016**.
[90] Baumgärtner, F.; Fischer, E. O.; Laubereau, P. *Naturwissenschaften* **1965**, *52* (20), 560–560.
[91] Karraker, D. G. *Mössbauer Spectroscopy and Its Chemical Applications*; Stevens, J. G., Shenoy, G. K., Eds.; Advances in Chemistry; American Chemical Society: Washington, D. C., 1981; Vol. 194.
[92] Evans, W. J. *Inorg. Chem.* **2007**, *46* (9), 3435–3449.
[93] MacDonald, M. R.; Fieser, M. E.; Bates, J. E.; Ziller, J. W.; Furche, F.; Evans, W. J. *J. Am. Chem. Soc.* **2013**, *135* (36), 13310–13313.
[94] La Pierre, H. S.; Scheurer, A.; Heinemann, F. W.; Hieringer, W.; Meyer, K. *Angew. Chem. Int. Ed. Engl.* **2014**, *53* (28), 7158–7162.
[95] Windorff, C. J.; MacDonald, M. R.; Meihaus, K. R.; Ziller, J. W.; Long, J. R.; Evans, W. J. *Chem. - A Eur. J.* **2016**, *22* (2), 772–782.
[96] Wu, Q.-Y.; Lan, J.-H.; Wang, C.-Z.; Cheng, Z.-P.; Chai, Z.-F.; Gibson, J. K.; Shi, W.-Q. *Dalton Trans.* **2016**, *45* (7), 3102–3110.
[97] Harbottle, G.; Sutin, N. *J. Phys. Chem.* **1958**, *62* (11), 1344–1351.
[98] Karraker, D. G.; Stone, J. A. *Inorg. Chem.* **1979**, *18* (8), 2205–2207.
[99] De Ridder, D. J. A.; Apostolidis, C.; Rebizant, J.; Kanellakopulos, B.; Maier, R. *Acta Crystallogr. Sect. C Cryst. Struct. Commun.* **1996**, *52* (6), 1436–1438.
[100] Spirlet, M. R.; Rebizant, J.; Apostolidis, C.; Van den Bossche, G.; Kanellakopulos, B. *Acta Crystallogr. Sect. C Cryst. Struct. Commun.* **1990**, *46* (12), 2318–2320.
[101] Baumgärtner, F.; Fischer, E. O.; Kanellakopulos, B.; Laubereau, P. *Angew. Chemie Int. Ed. English* **1968**, *7* (8), 634–634.
[102] Kanellakopulos, B.; Bagnall, K. W. In *M.T.P. International Review of Science*; Bagnall, K. W., Ed.; MTP International Review of Science: Inorganic Chemistry; Butterworth & Co Publishers Ltd (February 1972), 1972; pp 299–322.
[103] Burns, J. H. *J. Organomet. Chem.* **1974**, *69* (2), 225–233.
[104] Karraker, D. G.; Stone, J. A. *Inorg. Chem.* **1972**, *11* (8), 1742–1746.
[105] Adrian, G. *Inorganica Chim. Acta* **1987**, *139* (1–2), 323–325.
[106] Adrian, G.; Appel, H.; Bohlander, R.; Haffner, H.; Kanellakopulos, B. *Hyperfine Interact.* **1988**, *40* (1–4), 275–278.
[107] Stone, J. A.; Pillinger, W. L. *Symp. Faraday Soc.* **1967**, *1*, 77.
[108] Stone, J. A.; Pillinger, W. L. *Phys. Rev.* **1968**, *165* (4), 1319–1326.
[109] Karraker, D. G. In *Organometallics of the f-Elements. Proceedings of the NATO Advanced Study Institute held at Sogesta, Urbino, Italy, September 11–22, 1978*; Marks, T. J.,

Fischer, R. D., Eds.; Springer Netherlands: Dordrecht, 1979; pp 395–420.
[110] Brandi, G.; Brunelli, M.; Lugli, G.; Mazzel, A. *Inorganica Chim. Acta* **1973**, *7*, 319–322.
[111] Marks, T. J.; Seyam, A. M.; Kolb, J. R. *J. Am. Chem. Soc.* **1973**, *95* (17), 5529–5539.
[112] Marks, T. J.; Wachter, W. A. *J. Am. Chem. Soc.* **1976**, *98* (3), 703–710.
[113] Streitwieser, A.; Yoshida, N. *J. Am. Chem. Soc.* **1969**, *91* (26), 7528–7528.
[114] Streitwieser, A.; Muller-Westerhoff, U.; Sonnichsen, G.; Mares, F.; Morrell, D. G.; Hodgson, K. O.; Harmon, C. A. *J. Am. Chem. Soc.* **1973**, *95* (26), 8644–8649.
[115] Legin, E. K. *Radiokhimiya* **1979**, *21* (4), 565–578.
[116] Karraker, D. G.; Stone, J. A.; Jones, E. R.; Edelstein, N. *J. Am. Chem. Soc.* **1970**, *92* (16), 4841–4845.
[117] De Ridder, D. J. A.; Rebizant, J.; Apostolidis, C.; Kanellakopulos, B.; Dornberger, E. *Acta Crystallogr. Sect. C Cryst. Struct. Commun.* **1996**, *52* (3), 597–600.
[118] Zanella, P.; Rossetto, G.; De Paoli, G.; Traverso, O. *Inorganica Chim. Acta* **1980**, *44*, L155–L156.
[119] Le Maréchal, J.-F.; Villiers, C.; Charpin, P.; Lance, M.; Nierlich, M.; Vigner, J.; Ephritikhine, M. *J. Chem. Soc. Chem. Commun.* **1989**, No. 5, 308.
[120] Fischer, R. D.; P., L.; Kanellakopulos, B. Chemiedozentagung, 1968.
[121] Ter Haar, G. L.; Dubeck, M. *Inorg. Chem.* **1964**, *3* (11), 1648–1650.
[122] Manriquez, J. M.; Fagan, P. J.; Marks, T. J.; Vollmer, S. H.; Day, C. S.; Day, V. W. *J. Am. Chem. Soc.* **1979**, *101* (17), 5075–5078.
[123] Fagan, P. J.; Manriquez, J. M.; Marks, T. J.; Day, C. S.; Vollmer, S. H.; Day, V. W. *Organometallics* **1982**, *1* (1), 170–180.
[124] Finke, R. G.; Gaughan, G.; Voegeli, R. *J. Organomet. Chem.* **1982**, *229* (2), 179–184.
[125] LeMaréchal, J. F.; Villiers, C.; Charpin, P.; Nierlich, M.; Lance, M.; Vigner, J.; Ephritikhine, M. *J. Organomet. Chem.* **1989**, *379* (3), 259–269.
[126] Wasserman, H. J.; Zozulin, A. J.; Moody, D. C.; Ryan, R. R.; Salazar, K. V. *J. Organomet. Chem.* **1983**, *254* (3), 305–311.
[127] Aleksanyan, V. T.; Lokshin, B. V. *J. Organomet. Chem.* **1977**, *131* (1), 113–120.
[128] Fischer, E. O.; Hafner, W.; Stahl, H. O. *Zeitschrift für Anorg. und Allg. Chemie* **1955**, *282* (1–6), 47–62.
[129] Wilkinson, G.; Cotton, F. A.; Birmingham, J. M. *J. Inorg. Nucl. Chem.* **1956**, *2* (2), 95–113.
[130] Fischer, E. O.; Hafner, W. *Zeitschrift für Naturforsch.* **1954**, *9 b*, 503–504.
[131] Bublitz, D. E.; McEwen, W. E.; Kleinberg, J. *Org. Synth.* **1961**, *41*, 96.
[132] Fischer, E. O.; Grubert, H. *Chem. Ber.* **1959**, *92* (9), 2302–2309.
[133] Tilley, T. D.; Andersen, R. A.; Spencer, B.; Ruben, H.; Zalkin, A.; Templeton, D. H. *Inorg. Chem.* **1980**, *19* (10), 2999–3003.
[134] Crisler, L. R.; Eggerman, W. G. *J. Inorg. Nucl. Chem.* **1974**, *36* (6), 1424–1426.
[135] Apostolidis, C. Unpublished results, 2014.
[136] Jutzi, P.; Leffers, W.; Hampel, B.; Pohl, S.; Saak, W. *Angew. Chemie Int. Ed. English* **1987**, *26* (6), 583–584.
[137] Fischer, R. D.; Ammon, R. V.; Kanellakopulos, B. *J. Organomet. Chem.* **1970**, *25* (1), 123–137.
[138] Wong, C. H.; Yen, T.; Lee, T. *Acta Crystallogr.* **1965**, *18* (3), 340–345.
[139] Raison, P.; Rebizant, J.; Apostolidis, C.; Lander, G. H.; Delapalme, A.; Kiat, J. M.; Schweiss, P.; Kanellakopulos, B.; Gonthier-Vassal, A.; Brown, P. J. *Zeitschrift für Krist. - Cryst. Mater.* **1994**, *209* (9), 720–726.
[140] Delapalme, A.; Raison, P.; Lander, G. H.; Rebizant, J.; Schweiss, P.; Kanellakopulos, B. *Zeitschrift für Krist. - Cryst. Mater.* **1994**, *209* (9), 727–732.
[141] Shannon, R. D. *Acta Crystallogr. Sect. A* **1976**, *32* (5), 751–767.
[142] Eggers, S. H.; Kopf, J.; Fischer, R. D. *Organometallics* **1986**, *5* (2), 383–385.
[143] Hinrichs, W.; Melzer, D.; Rehwoldt, M.; Jahn, W.; Fischer, R. D. *J. Organomet. Chem.* **1983**, *251* (3), 299–305.
[144] Zalkin, A.; Brennan, J. G.; Andersen, R. A. *Acta Crystallogr. Sect. C Cryst. Struct.*

Commun. **1988**, *44* (12), 2104–2106.
[145] Zegke, M. Reductive metalation of the uranyl oxo-groups with main Group-, d- and f-block metals, University of Edinburgh, 2015.
[146] Mougel, V.; Chatelain, L.; Pécaut, J.; Caciuffo, R.; Colineau, E.; Griveau, J.-C.; Mazzanti, M. *Nat. Chem.* **2012**, *4* (12), 1011–1017.
[147] Arnold, P. L.; Hollis, E.; Nichol, G. S.; Love, J. B.; Griveau, J.-C.; Caciuffo, R.; Magnani, N.; Maron, L.; Castro, L.; Yahia, A.; Odoh, S. O.; Schreckenbach, G. *J. Am. Chem. Soc.* **2013**, *135* (10), 3841–3854.
[148] Lam, O. P.; Heinemann, F. W.; Meyer, K. *Chem. Sci.* **2011**, *2* (8), 1538.
[149] Berthet, J.-C.; Le Maréchal, J.-F.; Nierlich, M.; Lance, M.; Vigner, J.; Ephritikhine, M. *J. Organomet. Chem.* **1991**, *408* (3), 335–341.
[150] Berthet, J. *J. Organomet. Chem.* **1993**, *460* (1), 47–53.
[151] Spirlet, M.-R.; Rebizant, J.; Apostolidis, C.; Dornberger, E.; Kanellakopulos, B.; Powietzka, B. *Polyhedron* **1996**, *15* (9), 1503–1508.
[152] Lukens, W. W.; Beshouri, S. M.; Blosch, L. L.; Andersen, R. A. *J. Am. Chem. Soc.* **1996**, *118* (4), 901–902.
[153] Berthet, J.-C.; Thuéry, P.; Ephritikhine, M. *Inorg. Chem.* **2010**, *49* (17), 8173–8177.
[154] Mougel, V.; Pécaut, J.; Mazzanti, M. *Chem. Commun.* **2012**, *48* (6), 868–870.
[155] Schnaars, D. D.; Wu, G.; Hayton, T. W. *Inorg. Chem.* **2011**, *50* (11), 4695–4697.
[156] Jones, G. M.; Arnold, P. L.; Love, J. B. *Chem. - A Eur. J.* **2013**, *19* (31), 10287–10294.
[157] Pedrick, E. A.; Wu, G.; Hayton, T. W. *Inorg. Chem.* **2014**, *53* (23), 12237–12239.
[158] Arnold, P. L.; Patel, D.; Pécharman, A.-F.; Wilson, C.; Love, J. B. *Dalton Trans.* **2010**, *39* (14), 3501–3508.
[159] Arnold, P. L.; Pécharman, A.-F.; Lord, R. M.; Jones, G. M.; Hollis, E.; Nichol, G. S.; Maron, L.; Fang, J.; Davin, T.; Love, J. B. *Inorg. Chem.* **2015**, *54* (7), 3702–3710.
[160] Zegke, M.; Nichol, G. S.; Arnold, P. L.; Love, J. B. *Chem. Commun.* **2015**, *51* (27), 5876–5879.
[161] Bagnall, K. W.; Payne, G. F.; Alcock, N. W.; Flanders, D. J.; Brown, D. *J. Chem. Soc. Dalt. Trans.* **1986**, No. 4, 783.
[162] King, D. M.; Tuna, F.; McMaster, J.; Lewis, W.; Blake, A. J.; McInnes, E. J. L.; Liddle, S. T. *Angew. Chemie Int. Ed.* **2013**, *52* (18), 4921–4924.
[163] Arnold, P. L.; Mansell, S. M.; Maron, L.; McKay, D. *Nat. Chem.* **2012**, *4* (8), 668–674.
[164] Hong, G.; Schautz, F.; Dolg, M. *J. Am. Chem. Soc.* **1999**, *121* (7), 1502–1512.
[165] Arnold, P. L.; Farnaby, J. H.; White, R. C.; Kaltsoyannis, N.; Gardiner, M. G.; Love, J. B. *Chem. Sci.* **2014**, *5* (2), 756–765.
[166] Arnold, P. L.; Farnaby, J. H.; Gardiner, M. G.; Love, J. B. *Organometallics* **2015**, *34* (11), 2114–2117.
[167] Ilango, S.; Vidjayacoumar, B.; Gambarotta, S. *Dalt. Trans.* **2010**, *39* (29), 6853.
[168] Baudry, D.; Bulot, E.; Charpin, P.; Ephritikhine, M.; Lance, M.; Nierlich, M.; Vigner, J. *J. Organomet. Chem.* **1989**, *371* (2), 163–174.
[169] Minasian, S. G.; Boland, K. S.; Feller, R. K.; Gaunt, A. J.; Kozimor, S. A.; May, I.; Reilly, S. D.; Scott, B. L.; Shuh, D. K. *Inorg. Chem.* **2012**, *51* (10), 5728–5736.
[170] Marks, T. J.; Seyam, A. M.; Wachter, W. A.; Halstead, G. W.; Raymond, K. N. In *Inorganic Syntheses: Reagents for Transition Metal Complex and Organometallic Syntheses*; Angelici, R. J., Ed.; Inorganic Syntheses; John Wiley & Sons, Inc.: Hoboken, NJ, USA, 1990; Vol. 28, pp 300–304.
[171] Panda, T. K.; Gamer, M. T.; Roesky, P. W.; Yoo, H.; Berry, D. H. In *Inorganic Syntheses: Volume 36*; Girolami, G. S., Sattelberger, A. P., Eds.; Inorganic Syntheses; John Wiley & Sons, Inc.: Hoboken, NJ, USA, 2014; pp 35–37.
[172] Nielson, A. J.; Rickard, C. E. F.; Smith, J. M.; Diel, B. N. In *Inorganic Syntheses*; Shreeve, J. M., Ed.; Inorganic Syntheses; John Wiley & Sons, Inc.: Hoboken, NJ, USA, 1986; Vol. 24, p 97.
[173] Streitwieser, A.; Mueller-Westerhoff, U.; Mares, F.; Grant, C. B.; Morrell, D. G.; Marks, T. J.; Miller, S. S. In *Inorganic Syntheses*; Shriver, D. F., Ed.; Inorganic Syntheses; John Wiley & Sons, Inc.: Hoboken, NJ, USA, 1979; Vol. 19, pp 149–

154.
[174] Evans, W. J.; Keyer, R. A.; Ziller, J. W. *J. Organomet. Chem.* **1990**, *394* (1–3), 87–97.
[175] Peterson, J. K.; MacDonald, M. R.; Ziller, J. W.; Evans, W. J. *Organometallics* **2013**, *32* (9), 2625–2631.
[176] Siemens 1997. Analytical X-ray Instruments Inc.: Karlsruhe, Germany 1997.
[177] Bruker (2007). Bruker AXS Inc.: Madison, Wisconsin, USA 2007.
[178] Sheldrick, G. **2008**.
[179] Sheldrick, G. M. *Acta Crystallogr. A.* **2008**, *64* (Pt 1), 112–122.
[180] Sheldrick, G. M. University of Göttingen, Germany 2013.
[181] Dolomanov, O. V.; Bourhis, L. J.; Gildea, R. J.; Howard, J. A. K.; Puschmann, H. *J. Appl. Crystallogr.* **2009**, *42* (2), 339–341.